



The
University
Of
Sheffield.

Access to Electronic Thesis

Author: Galal Mohamed
Thesis title: Dynamic deformation and fracture of aerospace structural materials
Qualification: PhD

This electronic thesis is protected by the Copyright, Designs and Patents Act 1988. No reproduction is permitted without consent of the author. It is also protected by the Creative Commons Licence allowing Attributions-Non-commercial-No derivatives.

If this electronic thesis has been edited by the author it will be indicated as such on the title page and in the text.

UNIVERSITY OF SHEFFIELD



Modelling damage and fracture of fibre metal laminates subject to blast loading

by

Galal Mohamed

A thesis submitted for the degree of
Doctor of Philosophy

in the
Composite Systems Innovation Centre
Department of Mechanical Engineering

February 2012

Declaration of Authorship

I, GALAL MOHAMED, declare that this thesis titled, ‘DYNAMIC DEFORMATION AND FRACTURE OF AEROSPACE STRUCTURAL MATERIALS’ and the work presented in it are my own. I confirm that:

- This work was done wholly or mainly while in candidature for a research degree at this University.
- Where any part of this thesis has previously been submitted for a degree or any other qualification at this University or any other institution, this has been clearly stated.
- Where I have consulted the published work of others, this is always clearly attributed.
- Where I have quoted from the work of others, the source is always given. With the exception of such quotations, this thesis is entirely my own work.
- I have acknowledged all main sources of help.
- Where the thesis is based on work done by myself jointly with others, I have made clear exactly what was done by others and what I have contributed myself.

Signed:

Date:

*“Winnie-the-Pooh read the two notices very carefully,
first from left to right, and afterwards,
in case he had missed some of it, from right to left.”*

A A Milne, *Winnie-the-Pooh*

Abstract

THE present thesis investigates the performance of current aerospace structural materials such as Glare, a fibre metal laminate, to the catastrophic consequence of sabotage-induced blast loadings on commercial aircraft. The aim is to quantify the effects of these blast events and establish if remedial action can in some manner increase the chances of aircraft survivability.

Within the EU funded VULCAN consortium, a coordinated effort has been devised to determine the dynamic deformation and fracture behaviour of structural materials subject to blast loadings using both experimental and numerical techniques. Test data from small-scale experimental blast trials have been verified and validated by the author using robust and efficient finite element models. Numerical studies have shown that Glare has potential to be a strong candidate for blast attenuating structures, exhibiting superior blast resistance compared to monolithic aluminium plates. Furthermore, a blast vulnerability and survivability analysis was devised to illustrate various failure scenarios in scaled fuselage structures.

To address the macroscopic crack propagation in large-scale shell structures to blast loadings, well-controlled dynamic fracture experiments have been performed. This configuration, which consists of closed-end pressurised barrels with a through-thickness crack, is designed to capture the underlying dynamic phenomena under investigation whilst keeping the computational effort manageable. Quantitative fracture metrics obtained from high speed imaging systems have shown that Glare exhibits much lower average crack velocities than Aluminium 2024-T3 and CFRP.

Experimental boundary and loading conditions served as well-defined input parameters to large-scale finite element models using cohesive elements. It has been shown that rate-independent cohesive models, initially verified using quasi-static fracture toughness tests, are insufficient to capture the dynamic crack growth rates. Alternative rate-dependent models have been discussed and implemented which take into account the influence of loading rate on the cohesive traction and energy dissipation. An inverse problem of cohesive zone modelling is performed to obtain mode-I cohesive zone laws. The comparison shows that both the experiments and the numerical simulations result in very similar crack initiation times and produce crack tip velocities of acceptable agreement.

Acknowledgements

I am sincerely and heartily grateful to my advisor Professor Costas Soutis for the encouragement, stimulating discussions and guidance he showed throughout my PhD. I am sure it would have not been possible without his help particularly pushing towards the final stages of dissertation writing. I would also like to gratefully acknowledge the support of my co-advisor, Dr Alma Hodzic, who has been a mentor since my early undergraduate years at Sheffield.

I would like to acknowledge the financial contribution of the EU VULCAN project and its partners for providing vital test data.

I have spent my most enjoyable, formative and constructive years at the Department of Mechanical Engineering in Sheffield and feel privileged to be part of such a dynamic and stimulating environment with friendly and enthusiastic people. It is impossible to mention them all, but some deserve special recognition. This dissertation would not have been possible without the modelling advice of my dear friend Renato Giannoccaro. He devoted many hours of his time during the latter stages of his PhD to assist me during the early stages of mine. I am also incredibly indebted to my research family of 'Office MD66' for their companionship and support; they are Akin, Zurina, Carlos, Mulyadi, Saravanan and Lino. Special thanks to Lizzy, Jen Rowson and Sofia; your sympathetic ear over a cup of tea, lunch or in the corridor was much appreciated! I would like to thank my other Sheffield 'family'; Jen, Steve, Robbie and Phil.

Finally, I want to express my love and gratitude to my wonderful parents and siblings for their support for what has been a challenging few years.

Galal Faysell Ahmed Mohamed
Sheffield, 2011

Contents

Declaration of Authorship	iii
Abstract	v
Acknowledgements	vi
List of Figures	xi
List of Tables	xv
Nomenclature	xx
1 Introduction	1
1.1 Introduction	1
1.2 Detailed description	3
1.2.1 Computational challenges	6
1.3 Problem statement	7
1.4 Aims and scope of this study	9
1.5 Outline	10
2 Fibre metal laminates	13
2.1 Introduction	13
2.2 Fibre Metal Laminates	14
2.3 Characteristics of Glare	17
2.3.1 Mechanical properties of Glare constituents	18
2.3.2 Corrosion and durability	21
2.3.3 Impact	21
2.3.4 Flame resistance	22
2.3.5 Blast	23
2.4 Applications of FMLs	25
3 Blast resistance and damage modelling of FMLs	27
3.1 Introduction	27
3.2 Performance of Glare panels subjected to intense uniform pressure pulse loading	29

3.2.1	Numerical methodology	30
3.2.2	High strain material properties	31
3.2.3	S2-glass/FM94	32
3.2.3.1	Damage initiation	34
3.2.3.2	Damage Evolution	36
3.2.3.3	Limitations	37
3.2.4	Aluminium 2024-T3	37
3.2.5	Modelling the blast load	39
3.2.6	Results	39
3.2.7	Comparison with Glare 5 and Aluminium 2024-T3	42
3.3	Numerical analysis of blast-induced wave propagation using FSI and ALE multi-material formulations	46
3.3.1	Far-field blast tests	47
3.3.2	Lagrangian formulation	48
3.3.3	Interlaminar delamination	49
3.3.4	Blast pressure characterisation	50
3.3.4.1	Empirical blast load	51
3.3.4.2	MMALE model	52
3.3.5	Results and discussion	55
3.3.5.1	Calibration of contact parameters in tie-break cohesive algorithm	55
3.3.6	Interaction results of Glare subjected to blast loading	57
3.3.6.1	Energy balance	60
3.3.7	Results: blast model comparison	60
3.4	Conclusions	61
4	Performance of scaled fuselage structures subjected to blast loadings	63
4.1	Blast performance of scaled fuselage demonstrators	63
4.2	Description of structures	64
4.3	Description of finite element models	68
4.3.1	LS-DYNA global lagrangian model	68
4.3.2	Blast load modellisation	70
4.4	Global model analysis results	72
4.4.1	Finite element model validation	72
4.4.2	Vulnerability analysis results	74
4.5	Conclusion	75
5	Dynamic fracture of aerospace structural materials	79
5.1	Introduction	79
5.1.1	Case study: Sudden centered crack on pre-stressed plates	82
5.1.2	How fast can cracks propagate?	85
5.2	Integrated experimental-numerical design approach	87
5.3	Pressurised barrel tests	89
5.4	Experimental results	92
5.4.1	Aluminium 2024-T3	92
5.4.2	Glare 3-3/2-0.4	94
5.5	Explanation of failure mechanisms in FMLs	96

5.6	Comparison with woven carbon-fibre reinforced plastics	100
5.7	Conclusion	101
6	Modelling of dynamic ductile fracture propagation using cohesive zone elements	103
6.1	Introduction	103
6.2	Introduction to cohesive elements	104
6.2.1	Motivation for applying cohesive zone models	104
6.3	The cohesive zone model	105
6.3.1	Traction-separation law	108
6.3.1.1	Modes of failure	108
6.3.2	Alternatives to using cohesive zones	111
6.4	Derivation of static cohesive parameters of Al 2024-T3	113
6.4.1	Identification procedure using numerical optimisation	113
6.4.2	Numerical model	115
6.4.3	Parameter identification	116
6.5	Simulation of dynamic fracture	119
6.5.1	Finite element model	119
6.5.1.1	Connecting shells to cohesive zone	122
6.5.2	Pressure load curves	123
6.6	Capturing the crack velocity	127
6.7	Comparison between experiments and simulations	128
6.8	Conclusion	134
7	Summary and Conclusions	139
7.1	Summary and Conclusions	139
7.2	Recommendations for future work	141
A	LS-DYNA/ABAQUS	145
A.1	ABAQUS	145
A.2	LS-DYNA	145
B	ABAQUS input files	147
C	LS-DYNA - MMALE input files	153
D	LS-DYNA - Scaled fuselage input files	167
E	RADIOSS - MMALE simulations	175
E.1	Interaction of pressurised cylindrical structures subjected to TNT blast loading	175
E.2	Influence of Barrel Length	175
E.3	Effect of pressurisation	178
F	LS-DYNA - Dynamic fracture files	181

Bibliography 187

Publications 197

Curriculum Vitae 199

List of Figures

1.1	Strain rates associated with different types of loading	2
1.2	Accident of Boeing 737 Aloha Airlines, 1988	4
1.3	A block diagram of the integrated approach for the validation of simulations of structures subjected to blast loadings.	6
1.4	Computational complexity and requirements on the accurate modelling of structural response to the blast phenomenon.	8
2.1	Typical lay-up of a fibre-metal laminate	14
2.2	Indexed specific static properties of Glare 3-3/2-0.3	20
2.3	A comparison of the impact performance of Glare 3 and other aerospace materials	22
2.4	Glare blast-resistant cargo container [34]	23
2.5	Graph of normalised displacement versus dimensionless impulse for Glare panels and steel plates	24
3.1	Configuration of Glare 3 & 5 laminates.	28
3.2	Schematic of experimental small scale blast trials.	29
3.3	Schematic of the 1/4 numerical model of fully clamped Glare 3 panel.	32
3.4	Definition of composite lay-up of Glare 3 using S4R elements.	32
3.5	Tensile stress-strain curves of Glare and its constituents.	33
3.6	Damage evolution for fibre-reinforced composites	37
3.7	Dynamic flow stress of Aluminium 2024-T3	38
3.8	Schematic of blast loading configuration and pressure distribution.	39
3.9	Comparison of experimental and numerical back face mid-span displacements	40
3.10	Response of Glare 3 panel at impulse 25.5 Ns showing displacement (in mm) in the z-direction.	41
3.11	Residual deflection of impulsively loaded Glare 3 panels.	41
3.12	Fibre and matrix tension damage in FML panel.	42
3.13	Predicted back face mid-point displacement of Glare 3 and 5 panels and monolithic aluminium plates.	43
3.14	Contours of equivalent plastic strain of Aluminium 2024-T3 and Glare 3	43
3.15	Partition of energies for Glare 3 subjected to impulse of 25.5 Ns	44
3.16	Graph of normalised mid-point back face deflection versus dimensionless impulse	46
3.17	Small-scale test used to assess relative blast resistance of typical aircraft materials	48
3.18	Multi-layered modelling approach of contact tie-break algorithm	49
3.19	Typical blast pressure-time history	51

3.20	Radial distribution of peak pressure-time pulse generated by the ConWep model	53
3.21	Blast pressure curves for 50g, 100g and 150g C-4 charge predicted by ConWep model	53
3.22	Description of MMALE arrangement of Glare flat panel simulation	54
3.23	Comparison of velocity profile for FML panel under pressure-pulse loading for one and multiple layers	57
3.24	Numerical predictions of mid-point deflection of Glare panels subjected to 75g and 100g C-4 explosive charge relative to the experimental results	58
3.25	Mid-point transverse velocity of each Aluminium layer of Glare 3 panel subjected to 100g C-4 charge at stand-off distance of 200 mm	59
3.26	Plot of delaminated area for each tie-break interface, where 1 is first tie-break interface located at the front of the panel (blast loaded face) and 6 is the back	59
3.27	Contours of blast pressure wave propagation using the MMALE approach at different time intervals (fringe levels in MPa)	61
3.28	Comparison of mid-point deflection of Glare panels using the ConWep and MMALE approach subjected to 75g C-4 explosive charge	62
4.1	CAD schematic of final metallic demonstrator	66
4.2	CAD schematic of final metallic demonstrator	66
4.3	Location of explosive charge and pressure gauges in demonstrator blast test	70
4.4	Experimental internal overpressure values taken at the top and bottom of the aluminium demonstrator for 20g explosive charge	71
4.5	Internal overpressure blast profile derived from ConWep empirical function for 20g and 50g Semtex load cases	71
4.6	Contours of out-of-plane displacement of metallic demonstrator subjected to an internal explosive charge of 20g Semtex	72
4.7	Mid-point out-of-plane displacement (z), and contour plots obtained from predictive simulations. Aluminium demonstrator, 20 gr explosive.	73
4.8	DIC contours of out-of-plane displacement of metallic demonstrator subjected to 20 gr Semtex explosive	74
4.9	DIC contours of out-of-plane displacement of metallic demonstrator subjected to 50 gr Semtex explosive	75
4.10	Contours of displacement of metallic demonstrator subjected to an internal explosive charge of 50g Semtex	76
4.11	Final damage state of metallic demonstrator tests subjected to an internal explosive charge of 50g Semtex	77
5.1	Experimental setup of sudden centered crack on pre-stressed plates	83
5.2	Quantitative fracture metrics obtained from high speed imaging system for SSCP aluminium plates	84
5.3	Crack propagation profile of sudden centered crack on pre-stressed plates	84
5.4	Schematic of the integrated approach for the validation of large-scale simulations of dynamic fracture	88
5.5	Experimental set-up of pressurised barrel tests	90
5.6	Location of experimental pressure gauges in pressurised barrel tests	91
5.7	High speed imaging system used to capture fast propagating crack	91
5.8	High speed camera images of dynamic crack propagation of Test A103	92

5.9	Quantitative performance crack metrics obtained from high speed images for Aluminium 2024-T3	93
5.10	Aluminium (TestA101) pressurised barrel tests subjected to internal blast loading	94
5.11	Pressure curves obtained from Test A103	95
5.12	High speed camera snapshots for mode-I crack propagation for GLARE panels	95
5.13	Quantitative performance crack metrics obtained from high speed images for GLARE 3-3/2-0.4	96
5.14	Comparison of crack velocity vs. crack advance of Glare barrel tests 01 and 02	97
5.15	Deformation characteristics taken from GLARE barrel tests	97
5.16	SEM image of ductile fracture surface	99
5.17	Ductile fracture process	99
5.18	High speed images of CFRP	100
5.19	Post-mortem view of CFRP fragments showing crack bifurcation	101
6.1	Cohesive model: Representation of the physical damage process by means of cohesive elements	107
6.2	Cohesive zone model: formulation according to Dugdale and Barenblatt	108
6.3	Typical traction-separation laws	109
6.4	Experimental crack data from B24LT-12 tests	114
6.5	Experimental data given for the characterisation of the deformation of Aluminium 2024-T3 material	115
6.6	Shape of the traction-separation law and 3D cohesive elements	116
6.7	3D finite element mesh for the M(T) specimen (1/8 of the structure).	117
6.8	Parameter identification for the 3D FE model of the M(T) specimen.	118
6.9	Tensile stresses at different time intervals during the propagation of the crack using hexahedral elements.	119
6.10	Details of the crack tunneling for the case modeled with 3D solid elements	120
6.11	Finite element details of explosive barrel tests	121
6.12	Tie formulation between shell edge and 3D cohesive elements (adopted by [21])	122
6.13	Plot of blast pressure profile for different internal pressures taken from the central perimeter of a closed barrel subjected to an internal explosive of 54g TNT charge	124
6.14	Numerical description of pressurised barrel tests	125
6.15	Typical pressure wave propagation within the pressurised barrel at different time intervals	126
6.16	Comparison of 54g TNT load case barrel test with ALE predictive model	126
6.17	Location (a) of the predicted pressure load curves (b) and their corresponding division in rings.	127
6.18	Comparison of the experimental crack tip position (from TestAL03) with that of simulations ($\Gamma=19 \text{ kJ/m}^2$ $T=931.5$).	130
6.20	Changes in static cohesive fracture parameters to match experimental results	131
6.21	Effect of the opening rate on the Perzyna visco-plastic cohesive formulation	132

6.22	Comparison of the experimental crack tip position (from TestAL03) with that of simulations obtained using the rate-dependent cohesive formulation.	135
6.23	Influence of Perzyna parameters on the TSL response extracted from a single element test	136
E.1	Distribution of blast (a) velocity (m/s) and (b) pressure shock wave at the same time for 1.4 and 2 m GLARE barrels for a 54g TNT charge (Pressure is in MPa)	176
E.2	Pressure profile extracted from lower perimeter for 1.4 and 2m GLARE barrels for a 54g TNT charge	177
E.3	Internal energy profile for 1.4 and 2 m GLARE barrels for a 54g TNT charge	178
E.4	Effect of pressurisation on the blast pressure profile for 1.4 m GLARE barrel for a 54g TNT charge	179
E.5	Effect of pressurisation on the internal energy of 1.4 m GLARE barrel for a 54g TNT charge	179

List of Tables

2.1	Details of commercially available Glare grades	19
2.2	Thermo-mechanical properties of the constituents of Glare	20
3.1	Uniformly distributed blast test results	30
3.2	Material property data used to represent S2-glass/FM94 laminates	33
3.3	Johnson-Cook material model parameters for Aluminium 2024-T3	38
3.4	Glare and Aluminium material properties, estimated using the MVF method	45
3.5	Summary of small-scale-blast trial results for various targets.	48
3.6	TNT equivalency for different explosives.	52
3.7	Explosive parameters used in air-blast simulations	55
3.8	Air parameters used in air-blast simulations	55
3.9	Model details for the air blast simulations	56
3.10	Results of air blast simulations using ConWep method	60
4.1	Description of structural components of metallic demonstrator	67
4.2	Johnson-Cook material model parameters for Aluminium 7178-T62 & 7075-T73	69
4.3	Vulnerability analysis of dynamic deformation for scaled fuselage structures subject to internal blast load	77
5.1	Blast loading regimes for aircraft explosions	80
5.2	Theoretic crack velocities in metallic, hybrid and composite mediums	86
5.3	Geometrical and loading parameters for numerical modelling	89
6.1	Definitions of 'thin-walled structure' which exist in the field of engineering	106
6.2	Reported cohesive properties of thin sheet aluminium 2024 T3	113
6.3	Experimental stress-strain data for the Al 2024 material	115
6.4	Perzyna parameters for Aluminium 2024-T3 barrel tests	134
E.1	Structural response of GLARE barrel lengths	178

Nomenclature

Roman Symbols

a_0	Initial fracture length	mm
a_i	Instantaneous fracture length	mm
A	Area	mm ²
$A_{N,TSL}$	Area under the normalised TSL curve	-
B	Strain hardening modulus	MPa
c	Wave speed in solid medium	m/s
c_D	Decompression wave speed	m/s
c_L	Longitudinal wave speed	m/s
c_R	Rayleigh wave speed	m/s
c_S	Shear wave speed	m/s
C_1, C_2	JWL constants of explosive	GPa
C	Strain rate coefficient	s ⁻¹
C_d	Damaged elastic matrix	GPa
C_p	Specific heat coefficient	J/(g · K)
d	Diameter of explosive	mm
d_B	Final displacements of the mid-span of the back panel	mm
d_k	Internal damage variable	-
D	Detonation velocity	m/s
E	Young's modulus	GPa
E_0	Initial specific energy	N/m ²
E_1	Young's modulus in fibre direction	GPa
E_2	Young's modulus in transverse direction	GPa
F_k^i	Fibre/Matrix damage loading function	-
G^c	Critical energy release rate	N/mm
G_{ij}	Laminate shear stiffness in ij direction	GPa
h	Thickness	mm
h_{pz}	Perzyna work hardening exponent parameter	-
I	Impulse	Ns
K_1	Loading stiffness	N/mm ³

K_2	Unloading stiffness or damaged stiffness	N/mm ³
l	Length dimension	mm
m	Thermal softening exponent	-
\mathbf{M}	Damage matrix operator	-
M	Mass	g
n	Strain hardening exponent	-
N_{pz}	Perzyna exponent parameter	-
P	Pressure	GPa
P_{CJ}	Chapman-Jouget pressure	GPa
q	Work hardening parameter	-
$q_{I,II,III}$	Work hardening in Mode I,II,III	-
R_1, R_2	JWL constants of explosive	-
S	Explosive stand-off distance	mm
$S_{LT,TT}$	In-plane shear strength	MPa
t	Time	s
t_0	Exponential time decay constant	s
T^*	Non-dimensional temperature, JC model	-
T_{0N}	Cohesive strength for normal fracture	N/mm ²
T_{0S}	Maximum cohesive traction for slant fracture	N/mm ²
T_{eq}	Equivalent cohesive traction according to Hill yield criterion	N/mm ²
T_{III}	Cohesive traction in Mode III	N/mm ²
T_{II}	Cohesive traction in Mode II	N/mm ²
T_I	Cohesive traction in Mode I	N/mm ²
V	Initial specific volume	m ³ /kg
w	Width dimension	mm
W_k	Energy component of global energy balance	Nmm
X_c	Longitudinal compressive strength in fibre direction	MPa
X_t	Longitudinal tensile strength in fibre direction	MPa
Y_c	Transverse compressive strength in fibre direction	MPa
Y_t	Transverse tensile strength in fibre direction	MPa

Greek Symbols

α_1	Thermal expansion coefficient in fibre direction	$\mu\text{m}/\text{m-K}$
α_2	Thermal expansion coefficient in transverse direction	$\mu\text{m}/\text{m-K}$
δ	Separation length or cohesive opening	mm
δ_0	Critical cohesive separation	mm
δ_1, δ_2	Shape parameters of TSL	mm
Γ	Cohesive energy	N/mm
Γ_{0N}	Cohesive energy for normal fracture	N/mm
Γ_{0S}	Cohesive energy for slant fracture	N/mm

ν_{ij}	Poisson's ratio	-
ω	JWL constants of explosive	-
ϕ	Non-dimensional impulse	-
ρ	Density	g/mm ³
$\bar{\sigma}_d$	Dynamic flow stress	MPa
σ	Stress	MPa
θ	Angle of incidence	rads
$\bar{\varepsilon}$	Equivalent strain	-
ε	Strain	-

Superscripts

0	Initiation of damage
<i>c</i>	Compressive
<i>f</i>	Final damage
<i>t</i>	Tensile

Subscripts

0	Reference state
1	Fibre direction
2	Transverse direction, perpendicular to the fibre direction
3	Out-of-plane direction
<i>al</i>	Aluminium
<i>comp</i>	Cross-plyed composite layers
<i>d</i>	Dynamic
<i>eq</i>	Equivalent
<i>f</i>	Fibre
<i>m</i>	Matrix
<i>pl</i>	Plastic
<i>ult</i>	Ultimate
<i>y</i>	Yield

Acronyms

<i>ARALL</i>	Aramid Reinforced ALuminium Laminates
<i>CFRP</i>	Carbon fibre reinforced plastics
<i>COD</i>	Crack opening displacement
<i>CTOD</i>	Crack tip opening displacement
<i>FML</i>	Fibre Metal Laminate
<i>FSI</i>	Fluid-structure interaction
<i>GLARE</i>	GLAss fibre REinforced laminate
<i>IED</i>	Improvised explosive devices
<i>MMALE</i>	Multi Material Arbitrary Lagrangian Eulerian
<i>MSD</i>	Multi-site damage

<i>MVF</i>	Metal volume fraction
<i>SOD</i>	Stand-off distance
<i>TSL</i>	Traction-separation law
<i>V&V</i>	Verification and Validation

To my mother and my father

Chapter 1

Introduction

THIS chapter provides a brief introduction to the research problem investigated in this thesis. An overview is given to the threat and possible failure scenario of sabotage-induced blast loadings to primary aerospace structures. A brief discussion is given to describe remedial measures to harden structures through innovative aircraft design and material selection. A review of relevant research in the open literature has identified limitations and areas of future work from which a statement of purpose is provided.

1.1 Introduction

The continuous threat of sabotage to primary aircraft structures has been a subject of considerable attention over the past few decades. Of particular concern is the aircraft fuselage, a thin-walled structure designed to withstand severe dynamic environments whilst maintaining a cabin pressure, at a level higher than the ambient pressure, at cruising altitude. Such structures have a relatively high susceptibility to damage in the form of fatigue cracks, environmental corrosion and impact/high strain rate damage. The damage in the form of the latter can appear in the form of foreign object projectiles (such as bird strikes, runaway debris and ballistic impact) or blast-type loading resulting from acts of sabotage (improvised explosive devices, IEDs) or engine malfunction. In the event of a high rate explosive event, extensive structural damage can occur over a very short time (μs - ms) period with macroscopic loading rates estimated to be as high as $50 \times 10^6 \text{ Ns}^{-1}$ [1] with corresponding local strain rates on the order of 10^6 - 10^7 s^{-1} [2]. These loading rates are significantly higher than quasi-static strain rates of 10^{-1} - 10^{-5} s^{-1} , as shown in Fig. 1.1. In the event of an explosion, due to the presence of multi-site damage (MSD), fatigue cracks can readily initiate from stress concentrations such as

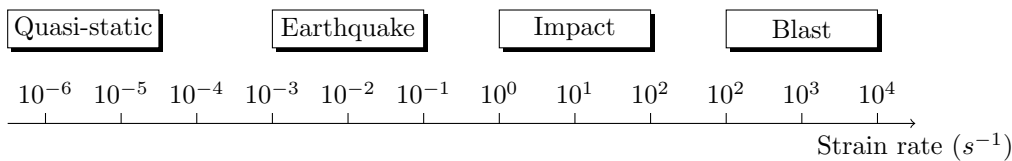


FIGURE 1.1: Strain rates associated with different types of loading

rivet holes, in the vicinity of the blast, and subsequently travel at velocities on the order of a few hundred meters per second [3, 4].

Cabin-pressurisation also pre-stresses the fuselage, which under the combined effects of inertia, may drive MSD cracks long after the initial dissipation of the explosion and subsequently travel large distances from the blast site. A similar crack in an un-pressurised fuselage would stop growing once the explosive pressure is spent. Therefore the combined effects of transient explosive forces and cabin pressurisation may result in severe degradation of structural integrity, posing serious risks to passengers and/or third parties.

Until recently, a large bulk of literature has accumulated in addressing blast mitigation for conventional metallic materials [1, 5–7]. Such remedial measures have involved crack arrest or deflection methodologies such as tear straps to limit the extent of crack growth [8]. Blast mitigation measures for fuselage structures have focussed on bay panels which prevent cracks from growing over large distances and are designed to break-off and vent the highly pressurised blast products [8]. Such designs allow the pressure in the cabin to reduce gradually and reduce the available energy to drive cracks even further.

However, over the past decade there has been a drive within the aerospace industry to replace conventional metallic materials in large scale components with composite materials, in applications where weight saving and structural integrity are of critical concern. In addition to conventional fibre reinforced polymer materials, such as carbon fibre reinforced polymer resins (CFRP), the search for new and improved materials in aerospace industry has stimulated the development of hybrid materials partly made out of composites, such as Fibre-Metal Laminates (FMLs).

These materials are composed of alternately stacked aluminium and fibre-reinforced composite layers, such that the best features of both constituents (i.e. high specific strength and improved machinability) are combined. FMLs are offered as a lightweight alternative over typical structural metals particularly in fatigue critical areas of aircraft [9]. The excellent fatigue resistance of the FML is achieved by the fibre bridging mechanism in the wake of the crack. Glare is currently the only commercially used FML, which comprises thin aluminium sheets and glass-fibre-reinforced epoxy (a thermoset),

to be implemented in civil aircraft primary structures [9]. The Airbus A380 jumbo jet makes extensive use of Glare in the manufacture of the upper fuselage panels and in the leading edges of the aircraft wing.

As we enter a new aircraft design philosophy with an evolving catalogue of advanced structural materials, it is imperative that the behaviour of such materials to high velocity deformation is known and effect of structural performance is established. This thesis attempts to address both of these challenges, by identifying measures that might reduce and mitigate the risks and effects of explosive devices and improve the tolerance of aircraft structures to explosive damage i.e. blast mitigation. This is achieved by following a systematic experimental-numerical approach which requires the development of efficient, reliable and novel predictive simulations based on minimal-well controlled experiments, to predict the response and performance of materials under dynamic loading conditions.

1.2 Detailed description

Modern aircraft fuselage systems were, and still are, typically fabricated using thin aluminum alloy sheets which are mechanically fastened to longitudinal stringers with rivets. Under normal operating conditions, fatigue cracks can emanate from regions of stress concentration and grow with repeated pressurization cycles associated with take-off and landing cycles [8]. Aviation accidents, such as the Aloha Airlines Boeing 737 aircraft incident in 1988, demonstrated that small cracks emanating from neighbouring rivet holes can interact with each other and critical lengths sufficient to trigger dynamic crack growth can be reached, see Fig. 1.2. Although the underlying cause of the accident was fatigue, the resulting fracture was dynamic in nature. In this incident, the fracture was contained by the frame of the aircraft riveted to the fracturing skin, and the aircraft was able to remain airworthy for the remaining of the flight until landing. In the event of an explosion, the pre-existing fatigue cracks, if oriented favourably with respect to the stress waves generated by the blast, may initiate even in areas of the structure far from the blast site. Furthermore, the resulting dynamic cracks may travel with speeds as high as 60-70 percent of the decompression wave speed, c_D , in air ($c_D \sim 300$ m/s) [3]. Under such conditions, as in the case of a pressurized pipeline, the driving force on the moving crack faces may be kept at sufficient levels (more than 50 percent of the cabin pressure) to propagate the cracks for distances much longer than current specifications allow, e.g. longer than 1-2 panels - two bay crack criterion [10].

Recent acts of unlawful interference with aircraft systems has stimulated interest in identifying measures that might mitigate the effects of explosive devices and improve



FIGURE 1.2: Accident with a Boeing 737 of Aloha Airlines in 1988 due to multiple site damage showing the importance of fatigue for ageing aircraft and of proper inspection and maintenance [11].

the damage tolerance of aircraft structures and systems to explosive damage. This approach was taken not long after the 1989 Pan Am tragedy in Lockerbie, Scotland, which resulted in significant loss of life. The UK Accident Investigation Branch (1990) reconstructed the damage of the aircraft, which was shown to have propagated both from the primary blast hole region and from other locations in the aircraft loaded by travelling stress waves [4]. It was concluded that the disintegration of the aircraft did not only result from the initial blast from the explosive charge, which caused small structural damage, but a large build-up of pressure still contained in the fuselage which triggered dynamic growth of cracks from the blast site [12].

However, air transport remains one of the safest forms of travel. According to the 2010 annual safety review published by the International Civil Aviation Organisation (ICAO), the current estimate of passenger fatalities per 100 million miles flown is **0.01**. This data excludes acts of unlawful interference and only relates to commercial civil aircraft. One source which sheds light on sabotage-related incidents is compiled by the British Civil Aviation Authority (CAA). This report states that between 1970-1993, with the exception of fire-related events, statistically it has been found that in cases where the loss of the fuselage structure has threatened or precipitated a catastrophic event, sabotage is as significant as structural failure from normal in-flight problems (such as degradation of fuselage structure by fatigue or corrosion) [6].

The same report offered blast mitigation measures that included intrinsic measures to improve the structure itself which included local reinforcement of skin and frames, improved attachment of fuselage stringers and selective placement of systems equipment. Additionally, extrinsic measures were suggested which included the use of hardened baggage containers and protective liners for the fuselage skin or spacing materials for the cargo hold which ensure an increased stand-off distance (SOD) between the device and

the skin. For example, in the mid-1990s, a series of hardened luggage containers made from materials such as glass/aramid fibre reinforced plastics and Glare were tested to meet Federal Aviation Administration (FAA) standards [13]. Glare (Galaxy Scientific ECOS3) was the only material to pass certification with no reported breaching of the container. The Glare structure was able to withstand and absorb the explosive energy, greater than that in the Lockerbie air disaster, and redistribute the impact load to the adjacent surface area rather than to one specific weak spot [13].

There are indications that the progressive nature of the failure mechanisms within a FML panel could be advantageous for containing blast loading compared to the sudden, catastrophic failure of metal containers that zip open (petalling failure) and allow the blast energy to escape [14]. More recently, there have been preliminary results on fully clamped Glare panels which have shown improved damage tolerance to impact and blast type loadings [15–17], relative to monolithic metal plates. However these observations are based on very limited experimental data, which are very expensive to conduct, highlighting the need for a more comprehensive research program with greater emphasis on predictive simulations.

In attempt to address some of these issues, VULCAN, an EU funded consortium of academia and industry, was setup within the European Framework 6 (Project No. AST5-CT-2006-031011), which focused on blast and fire mitigation through hardening strategies (material and design) aimed at near future composite/hybrid aero-structures. This would entail performing a limited number of benchmark experimental trials which would provide quantitative metrics and post-damage observations for numerical verification and validation (V & V). The validated numerical models would therefore enable the response of larger components (e.g. aircraft luggage containers) to be numerically modelled without the need to undertake a large number of expensive and time-consuming experiments and reduce the overall overhead costs. In order to fulfill these objectives, which are relevant to this study, the following steps are considered:

- Development of algorithms, materials models and failure criteria for high strain rate loading of composite and hybrid materials and calibration of these tools against numerical tools against experimental data,
- Dynamic analysis of the fracture phenomena and appropriate characterization of material properties
- Development of numerical tools for blast vulnerability analysis of composite and hybrid aeronautic structures.
- Blast vulnerability map of composite and hybrid scaled fuselage substructure for different charge locations and different locations.

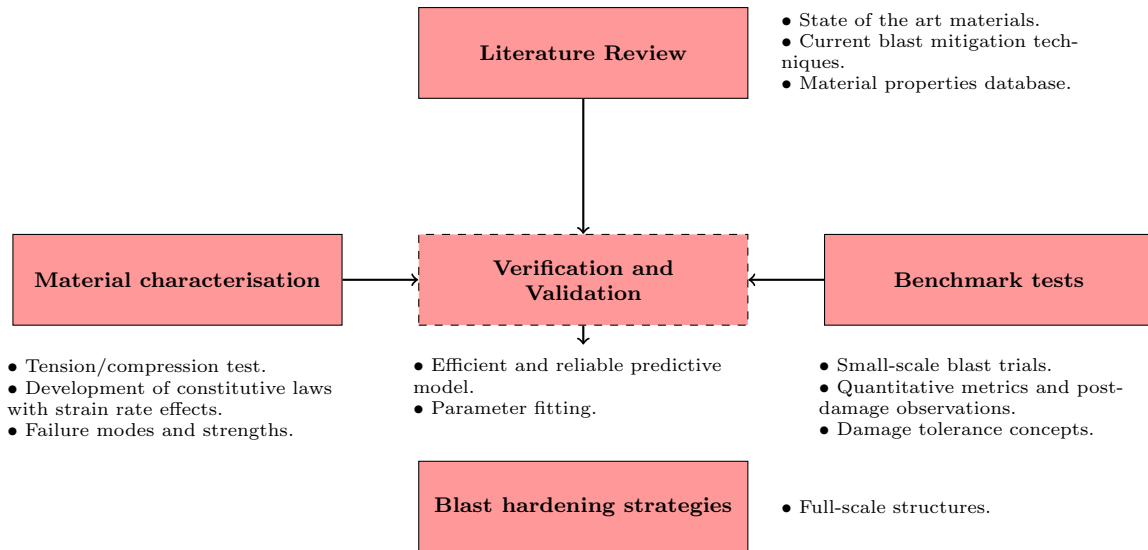


FIGURE 1.3: A block diagram of the integrated approach for the validation of simulations of structures subjected to blast loadings.

1.2.1 Computational challenges

Although, predictive simulations have proven to be a very useful tool to help understand and characterise the behaviour of structural aircraft materials to explosive blast loadings, its use remains challenging. Indeed, the actual predictive power of dynamic simulations is hindered by huge computational requirements and CPU, along with modelling uncertainties regarding the boundary and loading conditions. An extensive experimental program is preferable for initial model V & V to avoid unnecessary parameter fitting based on little or no physical meaning. This program should follow a hierarchical building block approach which covers small-scale test coupons for material characterisation to large-scale benchmark tests which takes into account the realistic kinematic boundary and loading conditions, as illustrated in Fig. 1.3.

Numerical work by Karagiozova et al. [18] and Soutis et al. [19] on locally blast-loaded FMLs has raised interesting computational issues. Since the problems are geometrically and materially nonlinear, the accuracy of the solutions was sensitive to several numerical algorithms: shock wave propagation through dissimilar materials, material anisotropy of the composite layers, air blast/structure coupling, progressive damage modelling and cohesive elements (see Chapter 3). Description of the damage and failure processes demanded high mesh resolution and often extremely small time steps. Since the localisation phenomenon of the blasts lead to large-scale plastic yielding in the aluminium layers and large deformations, the accuracy of the solution depended on the ability to capture the time and space resolved extreme gradients of stress, strain, and other internal state variables.

In dynamic fracture problems, these computational issues are further complicated. This is mainly due to phenomenal computational difficulty in describing the nucleation, propagation and branching of cracks with possibly complex topologies, and to effectively resolve the huge span of scales involved, from the sample size (metres) to the small-scale physical process at the crack tip (microns). A number of computational techniques have been proposed, which manage to qualitatively reproduce experimental observations. In particular FE implementation of cohesive zone models have been widely used to simulate the fracture processes for various materials, including polymers [20], metallic materials [21], and fibre reinforced plastic composites [22]. The references cited have been used to simulate fracture under static and dynamic loading conditions.

Researchers have resorted to various kinds of validation methodologies for dynamic fracture simulations [20, 21, 23]. In most studies, the numerical simulations are performed based on inputs taken from published experimental data. These inputs are often insufficient to completely setup a simulation, which therefore leaves room for the fitting of parameters. Then, the results of these simulations are validated against those of experiments published in the literature. These attempts highlight the need for integrated experiment-simulation approaches. This is discussed in much detail in Chapters 5 and 6. The premise of the PhD project, also implemented by other researchers in related topics, is that the development of a successful V & V program requires close collaboration between the experimentalist and the numerical analyst.

Figure 1.4 provides an illustration of the computational complexity and requirements in accurate advanced numerical simulation of structures under blast loading. The problems are generally geometrically and materially nonlinear. Accuracy of the solutions is sensitive to several numerical algorithms such as fluid-structure interaction coupling, contact algorithms and cohesive element. Description of the damage and failure processes demand high mesh resolutions and often extremely small time steps which can also suffer from mesh dependence during damage softening.

1.3 Problem statement

The author has identified two main issues which need addressing if successful prediction of structural integrity of composite based aircraft structures to blast loading is to be successful. They are:

- **Quantifying the performance of GLARE panels to realistic blast loading conditions.**

To date, no attempt has been made to determine the blast resistance of thin Glare



FIGURE 1.4: Computational complexity and requirements on the accurate modelling of structural response to the blast phenomenon.

panels to highly dynamic transverse loading. Small-scale blast trials with known kinematic boundary conditions will be performed to determine the relative performance of FMLs against its monolithic counterparts and other composite systems. The blast trials will also facilitate the setup of finite element models for model V & V. Such models will provide a quantitative description of the ability of FMLs to mitigate the effects of a small explosive charge, of similar magnitude and impact typically encountered in an IED event. Comparison with other variant configurations and monolithic aluminium of different geometry and loading conditions would also be of interest.

- **Dynamic fracture characteristics of typical aircraft structural materials**
Motivated by the limitations of previous validation studies and the need for more

systematic validation methods, a coordinated effort is attempted to validate experimentally large-scale finite element simulations of dynamic behaviour and fracture using finite element cohesive zone models. Within the financial and time constraints given in the project, the experiment should attempt to replicate, as much as possible, realistic kinematic boundary and loading conditions.

It is only through understanding and characterisation of both points that aircraft design may be improved to minimise catastrophic failure occurring as result of an on-board explosion.

1.4 Aims and scope of this study

The aim of the current research is to characterise the behaviour of typical aerospace structural materials to dynamic blast loading conditions. Of particular interest in this thesis are the commercially attractive FMLs, such as Glare, and its metallic counterpart, Aluminium 2024-T3 which have current applications in primary aerospace structures. To address this research problem, a profound understanding of these materials at both static and dynamic conditions is necessary for further improvement in the design philosophy of blast mitigation.

In line with previously mentioned trend in aircraft blast mitigation design from small-scale experimental tests/blast trials towards more advanced numerical methods, an experimental-numerical approach is developed based on the finite element (FE) method. These models are written in commercially available FE codes, such as ABAQUS [24] and LS-DYNA [25], rather than in-house finite element analysis tools to allow the transferability of skills, experience and more importantly subroutines ¹ to the wider industrial and academic community. Demonstrating and adapting existing codes to meet current technical challenges allows further transparency and better understanding of the computational methodology.

In order to fulfill these objectives the following phases are considered:

- The first phase of the research program is devised to determine the performance of FML structural materials to transverse dynamic (blast) loading. Via a number of benchmark blast trials for practical applications, a numerical model is devised and compared with the experimental test results. Strain rate dependency on the mechanical behaviour of the constituents of Glare is taken into consideration in

¹Subroutines are user-defined algorithms which can be implemented in existing finite element codes where such formulations and models are currently redundant or not available.

addition to the implementation of orthotropic damage model which accounts for the fibre and matrix damage in the glass fibre layers, i.e. the unidirectional glass-fibre epoxy layers in Glare. When necessary, numerical tools to simulate the interlaminar delamination are investigated and quantified relative to the global energy balance.

- Small-scale blast trials suffer from the idealised conditions in which the experiments are conducted (kinematic boundary and loading conditions) which may not be representative of real-life blast events, as a result of IEDs. Therefore more advanced numerical tools are explored to investigate the fluid-structure interaction (FSI) of cylindrical explosive charges compared to less computational expensive empirical blast algorithms. This will allow to incorporate the effects of internal pressurisation and curvature to the problem which are more akin to aircraft fuselage structures.
- Blast vulnerability map of composite and hybrid scaled fuselage substructure, with stringers/frame/ crack stoppers. Simulations of scaled fuselage substructures with crack stoppers will be performed to assess the damage tolerance to blast loadings. The results of this study will help numerical analysts studying the blast problem decide whether a certain amount of explosive could breach the structure and result in severe degradation of structural integrity.
- Another objective of this research is to explore the dynamic fracture characteristics of aerospace structural materials under blast loading conditions. The experimental program is designed specifically to facilitate the setup of complex large-scale simulations using cohesive finite elements with relatively few unknown parameters. The goal is to have a clear indication which material offers superior fracture resistance and lower crack growth rates. Well-controlled minimal experiments are performed which provide quantitative metrics (crack tip growth vs. time) from high speed imaging systems which are then compared *a posteriori* with the simulations. Qualitative differences in failure mechanisms and post-damage states are also given.
- Finally, blast hardening strategies for aircraft design to arrest dynamic fracture are suggested.

1.5 Outline

The research presented in the current thesis consists of numerical work performed by the author based on experimental data obtained within the framework of the EU-funded

program VULCAN (AST5-CT-2006-031011). Unless stated otherwise, all *numerical work* was performed at the Department of Mechanical Engineering at the University of Sheffield. Due to the sensitive nature of the project, all blast experiments were performed in secure facilities at the Royal Military College (RMA) in Belgium and TNO in the Netherlands.

In Chapter 2, the origins and evolution of FMLs are described in detail. Beside the development of FMLs (in particular Arall and Glare), the constituents, variants and main characteristics are given. Also, the impact and blast behaviour of FMLs are discussed, which will be the main focus of the present thesis.

In Chapter 3 robust and efficient computational models were developed for V & V which are capable of modelling the dynamic non-linear behaviour of Glare panels subjected to blast loadings. Numerical model validation was performed considering case studies of Glare panels subjected to a blast-type pressure pulse for which experimental data on the mid-point back face deflection and post-damage observations were available. In the first case study, excellent agreement of mid-point deflections and evidence of severe yield line deformation were shown and discussed against the performed blast tests. A further parametric study identified Glare as a potential blast attenuating structure, exhibiting superior blast potential against monolithic aluminium plates. The results were normalised and showed that for a given impulse, Glare exhibited a smaller normalised deflection, outperforming monolithic Aluminium 2024-T3 plates. In the second case study, the multi-material ALE formulation (MMALE) with fluid-structure interaction (FSI) was utilised to model the response of more complex blast loads. Cohesive tie-break contact algorithms are utilised to model interlaminar delamination between adjacent plies.

In Chapter 4 the vulnerability and survivability of scaled fuselage tests subjected to internal detonations is investigated and discussed. The purpose of this chapter was to develop survivability strategies to mitigate the effects of internal explosions. Vulnerability maps of the scaled demonstrator based on various failure scenarios, materials and charge location are developed for the purpose of examining airframe hardening options. All analysis results are compared and supported with experimental tests performed within the VULCAN consortium.

Motivated by the limitations of previous studies and the need for more systematic validation methods, a coordinated effort is reported in Chapters 5 and 6 to validate experimentally large-scale finite element simulations of dynamic fracture using cohesive zone models. To determine the interplay between cylindrical aircraft structures and the response of individual fatigue cracked panels (e.g. pre-existing MSD in aging aircraft), well-controlled and minimal experiments for dynamic fracture of blast loaded barrel tests

have been performed on three popular aerospace materials; Aluminium 2024-T3, Glare and CFRP [26]. The dynamic event induced crack growth speeds in order of magnitude of several hundred meters per second, metrics obtained via image processing of high speed images. Glare exhibited the lowest crack growth speeds and displayed a combination dynamic ductile behaviour and fibre bridging. The results also highlighted the poor blast attenuating qualities of CFRP, displaying crack speeds nearly ten times that of Glare with evidence of crack bifurcation-branching.

Finally, in an effort to model the dynamic ductile crack growth of Aluminium 2024-T3 from the previous barrel tests, a numerical cohesive zone approach is followed; a layer of interface elements which behave according to a traction-separation law are inserted along the fracture path. Static cohesive properties were extracted from standard fracture toughness tests and extrapolated to the aforementioned barrel tests. This method proved inaccurate to predict the rate of fracture as a considerable difference was found between the experiments and predictive results. This discrepancy was attributed to the rate-independence of the cohesive formulation which failed to take into account the influence of triaxiality and the opening rate on the local cohesive traction within the fracture process zone. To circumvent this problem, a Perzyna visco-plastic rate-dependent cohesive formulation is discussed and implemented which gave better representative results in terms of crack-growth rates. However the visco-plastic parameters were derived from one set of experimental data. It is acknowledge by the author that further small-scale fracture tests should be performed to (a) validate the derived parameters and (b) extract experimentally measured deformation fields to obtain accurate Mode I cohesive zone laws.

Chapter 2

Fibre metal laminates

THIS chapter gives an overview of the development of fibre metal laminates from its origins to current commercial applications. A brief description of the various compositions, manufacturing process and properties is given. Special attention is given to the development of Glare, a skin material for the A380 fuselage, and its favourable characteristic in fatigue, impact and blast applications.

2.1 Introduction

Over the past few decades, the application of fibrous composite materials in engineering structures has become increasingly popular, particularly in the aeronautic and space sector. Their plethora of uses in both military and civil aircraft also extends to more exotic applications such as unmanned aerial vehicles, space launchers, and satellites. Their growing uses have arisen from a drive within the aerospace industry to produce lighter aircraft, as the cost of fuel increases and environmental awareness becomes an important consideration [27]. Composites are preferred above conventional materials, such as steel and aluminium, because of their high specific properties (strength/stiffness versus weight ratio) and the ability to shape and tailor structures to produce more aerodynamically efficient structural configurations. However, reducing the weight whilst maintaining the structural integrity, affordability and durability continues to be a major issue in aircraft design. The manufacturing, assembly process and performance of composites are all intimately connected and have generated much attention and investment in developing new and improved "structural" materials.

However, metallic materials and their derivatives continue to have a fundamental role in applications where composites have yet to be exploited. This led to the development

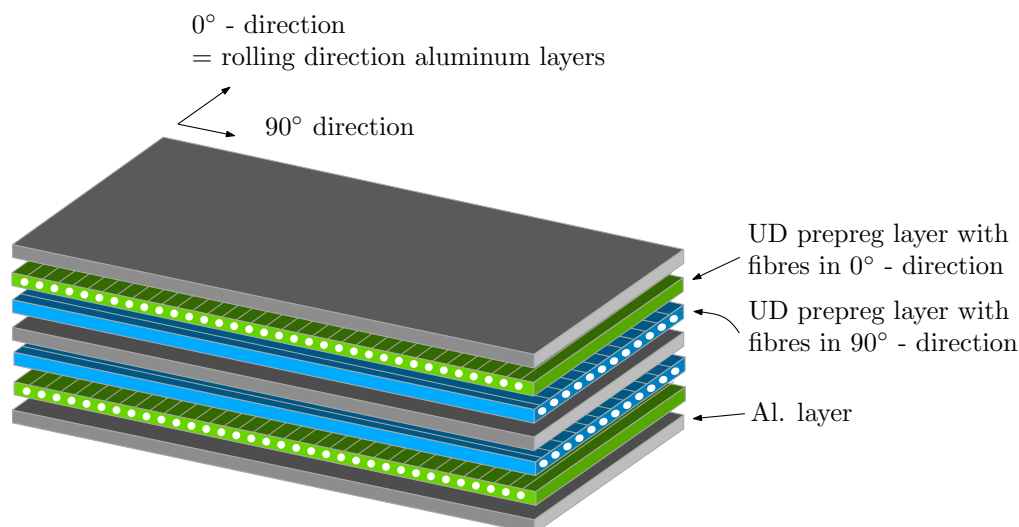


FIGURE 2.1: Typical lay-up of a fibre-metal laminate: Glare 3-2/1 laminate

of a hybrid system partly made of fibrous composites, known as fibre metal laminates (FMLs). FMLs consist of alternating layers of thin metallic sheets and fibre-reinforced plastics, see Fig. 2.1, such that the best of both qualities are exploited.

The history of the development of FMLs began in post-World War II Europe at the English aircraft manufacturer De Havilland, which was the first company to bond metal parts together. This metal bonding technology was later introduced to the Fokker facilities in the Netherlands, by Schliekelmann, who had worked as a trainee in De Havilland. The Fokker facilities had been left devastated in 1945 and no investment was available for large expensive milling machines, stimulating Fokker engineers to develop new manufacturing technologies to produce integrally stiffened panels. The optimisation in pre-treating the aluminium layers and improving the metal production process resulted in a new structural concept where built-up laminate structures could be developed that were tailored to its local strength, i.e. Fokker F-27. During this time, the use of composites, particularly fiberglass reinforced polyester, for structural and semi-structural parts was being explored and adopted. The combination of these two technologies was the initial spark in the development of FMLs [9]. A more comprehensive review can be found in Ref. [9]

2.2 Fibre Metal Laminates

Although metal bonding was developed as an alternative to machining with less investment costs and as an improvement of the compression properties, it was later discovered that bonded laminates structures appeared to have superior fracture toughness and fatigue properties relative to monolithic sheets. Following fatigue tests on F-27 centre

wings, it was shown that the crack growth was extremely slow due to the crack bridging effect; the fatigue crack of the outer layer was effectively bridged by the intact inner layers. This finding was particularly important since fatigue was becoming a major issue in aviation, due to the de Havilland DH 106 Comet jet airliner accident in 1952, which took place a few years after commercial introduction. Rivet holes near the window panels and escape/equipment hatches experienced catastrophic metal fatigue, which in combination with cabin pressurisation cycles, caused explosive decompression of the fuselage, tearing the aircraft apart in mid-flight.

The fatigue resistance of laminated structures was further improved by incorporating fibres in the adhesive. It was found that using unidirectional (UD) fibres in the adhesive effectively reduced the crack growth rates [9]. The stress in the loaded metal layers would be transferred to the fibres via the adhesive, thus unloading the metal layers and slowing down the crack growth in these layers. This phenomena is known as the 'fibre bridging mechanism'. This mechanism also encourages the adhesive, which is loaded in fatigue, to delaminate from the metal layers, relaxing the stresses at the fibre. Further fatigue tests on Arall (Aramid Reinforced ALuminium Laminates) conducted by Marissen [28] confirmed this behaviour and showed that the crack growth could be reduced by a factor of 10 to 100 compared to monolithic aluminium sheets. The 'crack bridging' mechanism responsible for the improved fatigue resistance is due to the intact fibres in the wake of the crack which considerably transfers a portion of the load in the aluminium layers over the crack, reducing the amount of load transferred around the crack tip. This result in a reduction of the effective stress intensity factor experienced at the crack tip. This can also be related to the crack opening which is constrained by the intact fibres, which also corresponds to a lower effective stress intensity factor at the crack tip. The presence of controlled delamination at the interface between the metal and fibre layers in the wake of the crack is also visible and advantageous to fatigue crack configurations, as it prevents fibre failure due to the relaxation of stresses.

The first generation of FMLs was Arall, an aramid/epoxy combined with aluminum sheets, which was primarily developed for wing structures. An extensive research program on full-scale Arall F-27 wing panels was conducted i.e. 270,000 flights. Tests revealed that Arall was quite sensitive to strength reductions caused by holes drilled in the material and that, although the material exhibited excellent fatigue properties, the presence of thickness steps (doubblers bonded on the structure to increase strength) would cause premature fatigue cracking. Nevertheless, despite these shortcomings, only minor surface cracks in the outer layers and in regions of thickness steps of the doublers was observed, whereas the aluminium equivalent would have failed catastrophically. Arall offered an increase weight saving of 33% compared to the original aluminium design.

Further tests on Arall on fuselage structures showed, however, that Arall was an unsuitable candidate for fuselage applications. Significant failure of aramid fibres was found to occur under realistic $R = 0$ fuselage skin loading due to the bad compression properties of the aramid fibres, as a result of which a reduction in the fatigue crack growth in the aluminium layers could no longer be warranted. This behaviour was partly attributed to the poor adhesive bonding of the aramid fibres which, under compressive loading, would result in fibre pull-out. The aramid fibres, due to the low compressive strength, are sensitive to buckling under compression. Furthermore as residual compressive stresses in the aramid layers are present at room temperature, after curing, due to the difference in coefficients of thermal expansions, cyclic compression of the aramid fibres will occur even if the minimum stress on the laminate is zero. Therefore to eliminate buckling under compression, the material needs to be post-stretched to reverse the stresses in the aramid/epoxy layer. This complicated and expensive process made Arall a less attractive candidate for fuselage skin applications.

During this period, fatigue related problems due to the ageing fleet of aircraft were becoming more prominent, which became apparent with the spectacular failure of the (presumed) damage tolerant Aloha Airline Boeing 737 in 1988. This ageing jet transport had flown nearly 90,000 flights when many small fatigue cracks, known as multi-site damage (MSD) in the same lap joint rivet row joined up into a single large crack, resulting in the loss of 4-6 meters, almost a third, section of the upper fuselage. This reinforced the view that damage tolerance is not simply structural design issue. Proper material selection (fatigue, corrosion and impact resistance alloys and durable bonding processes), qualified maintenance and better understanding of complex failure modes and damage tolerance evaluations of the aircraft structure appeared to be essential for safety.

By the late 1980s, the second generation of FMLs was introduced, specifically developed for fuselage skin applications. One variant which did not show fibre failure at all under fatigue loading conditions was Glare (GLAss fibre REinforced laminate), a second generation glass-fibre based FML which has a higher compressive strength and better damage tolerance than the aramid fibres in Arall [29]. This material system is suitable for both uniaxial and bi-axially loaded structures. Glare consists of thin aluminium 2024-T3 sheets bonded together with unidirectional or biaxially reinforced adhesive pre-preg of high strength glass fibres (S2-glass/FM94). This material, which was developed at the Delft University of Technology, is ideally suited for fuselage structure applications. Glare excels in all types of fatigue critical loading conditions (exhibiting crack growth rates 10 to 100 times slower than monolithic aluminium [10, 30]) and has damage tolerance built into the material as inspection of the structure for fatigue is not necessary for the entire operational life of the aircraft. Glare not only has excellent fatigue properties,

but also several other interesting material properties such as impact, residual and blunt notch strength, flame resistance and corrosion properties, all of which were found to be significantly better than those of monolithic aluminium.

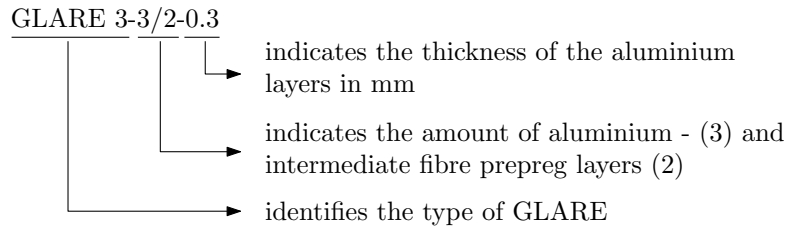
The road towards the application of Glare in primary aircraft structures began as a bonded patch repair installed on a C5-A Galaxy aircraft in the USAF at Kelly AFB [31]. The first commercial application was in a bulk cargo floor of the B777 of Boeing and the bulkhead of the Bombardier Learjet 125. By the early nineties, Airbus had initiated the next phase of its aircraft fleet to meet the growing and predicted growth in air traffic with a new family of very high capacity aircraft; the A3XX. However, this ambitious project presented new technical and economic challenges as reduction of production and operating costs were imperative to its success. To maintain the current number of accidents per year, the safety level of the aircraft has to increase significantly to counterbalance the growth of air transport and, yet, achieve a reduction in operating costs. Studies on fuselage structures of the A320 showed that with Glare a weight saving of 25.9% could be reached over aluminium. In addition, investigations on the Airbus A330 and A340 demonstrated a weight saving of 20% and 14-17%, respectively, as reported in Ref. [9]. The technological readiness of Glare as a potential candidate for fuselage skin application arrived with new production techniques, such as the splicing concept meant a major breakthrough for Glare. This allowed for larger panels, lower number of parts and thus reduced manufacturing costs. The philosophy was not to produce Glare as a sheet material, which has to be shaped and machined into a product as is done for aluminium, but as a *component*. Accordingly, the material is laid-up and cured in a curved mould such that after processing a product comes out of the autoclave with the right shape for a specific aircraft application. The final product thus includes the appropriate local fibre orientations and reinforcements with respect to the application it is meant for. With such a manufacturing procedure, the number of production steps, and thus the costs, is reduced significantly. This finally led to the application of Glare in a significant part of the Airbus A380 fuselage and in the leading edges of the vertical and horizontal tail planes.

2.3 Characteristics of Glare

Several Glare grades are currently available which are tailored to meet certain characteristics and structural requirements. These grades are based on various fibre-epoxy (prepreg) layers composed of either aluminium 7475-T761 and FM906 epoxy, which are the newest laminates designated as High Strength Glare, or aluminium 2024-T3 in combination with FM94 epoxy. In between each aluminium layer, a combination of two,

three or four unidirectional glass-fibre layers are arranged with different fibre orientations. The S2-glass fibres have a diameter of approximately $10 \mu\text{m}$, embedded in FM94 epoxy adhesive resulting in a nominally 0.127 mm thick prepreg with an average fibre volume fraction of 59%. As an example, the laminate build-up and stacking sequence of Glare 3, is presented in Figure 2.1. The direction of the fibres in the prepreg layers is related to the rolling direction of the aluminium sheets; 0° stands for fibres in the Longitudinal rolling direction (L) while 90° indicates fibres in the Longitudinal-Transverse direction (T). Details of the laminate building, thicknesses, aluminium grade and beneficial characteristics of all Glare grades, are listed in Table 2.1.

Since a large number of lay-ups are possible, a coding system is used to identify the grade and metal/composite arrangement. The cross-ply laminate, shown in Fig. 2.1, is referred to as Glare 3-3/2-0.3 and is defined as follows



Therefore Glare 3-3/2-0.3 has three aluminium layers of 0.3 mm thickness and two cross-ply intermediate glass-fibre layers.

2.3.1 Mechanical properties of Glare constituents

The mechanical behaviour of Glare is based upon the mechanical properties of its constituents, i.e., the aluminium and fibre-epoxy layers. The main properties of the constituents are listed in Table 2.2. Experimental studies have shown that the effective mechanical properties of Glare, in general, vary linearly with the Metal Volume Fraction (MVF)[10], which is defined by the ratio between the total thickness of the n aluminium layers, $\sum_i^n h_i$, and the laminate thickness h_{tot} , i.e.,

$$MVF = \frac{\sum_i^n h_i}{h_{tot}} \quad (2.1)$$

Figure 2.2 presents the main static and its corresponding specific material properties of Glare 3 compared to the currently most widely used aluminium alloy 2024-T3. The presented values are indexed, what means that they are presented as a percentage of the 2024-T3 properties (100 represents the 2024-T3 value). All static Glare parameters

TABLE 2.1: Details of commercially available Glare grades

Grade		Metal grade	Metal thickness (mm)	Fibre thickness (mm) ^a	Fibre orientation (°) ^{b, c}	Beneficial characteristics
Glare	1	7475-T761	0.3-0.4	0.25	0/0	fatigue, strength yield stress
	2A	2024-T3	0.2-0.5	0.25	0/0	fatigue, strength
	2B	2024-T3	0.2-0.5	0.25	90/90	fatigue, strength
	3	2024-T3	0.2-0.5	0.25	0/90	fatigue, impact
	4A	2024-T3	0.2-0.5	0.375	0/90/0	fatigue, strength in 0° direction
	4B	2024-T3	0.2-0.5	0.375	90/0/90	fatigue, strength in 90° direction
	5	2024-T3	0.2-0.5	0.5	0/90/90/0	Impact
	6A	2024-T3	0.2-0.5	0.5	+45/ - 45	shear, off-axis properties
	6B	2024-T3	0.2-0.5	0.5	-45/ + 45	shear, off-axis properties
	HS ^d	7475-T761	0.3-0.4	see 2-5	see 2-5	fatigue, strength yield

^a The thickness corresponds to the total thickness of a fibre-epoxy layer in between two aluminium layers.

^b The number of orientations in this column is equal to the number of unidirectional prepreg layers in each composite layer.

^c The (axial) rolling direction is defined as 0°, the transverse rolling direction is defined as 90°.

^d High Strength (HS) Glare has similar standard fibre lay-ups as in Glare 2 to Glare 5, but contains aluminium 7475-T761 and FM906 epoxy (instead of aluminium 2024-T3 and FM94 epoxy).

presented in Fig. 2.2 are lower than 2024-T3 except the ultimate strength and the gross blunt notch strength. The yield strength and the Young's modulus of the laminates are lower since the Young's modulus of the fibre prepreg is lower. The G modulus and the bearing strength are lower since the fibre-prepreg is not effective under these loading conditions. On the contrary, the blunt notch and ultimate strength are higher because of the higher ultimate strength of the fibre prepreg compared to 2024-T3. The large difference between the yield stress and the ultimate strength of the Glare laminate illustrates the extensive strain hardening that the materials exhibit. However, the specific weights or density of the Glare laminates are also lower. Figure 2.2 also presents all properties divided by the density, to allow a comparison towards the weight saving potentials.

TABLE 2.2: The thermo-mechanical properties of the constituents of Glare, as reproduced from [10]

Property	Unit	UD prepreg $V_f = 60\%$	Aluminium 2024-T3
Young's modulus, E_1	[GPa]	54.0	72.0
Young's modulus, E_2	[GPa]	9.4	72.0
Ultimate strength, σ_{ult}	[MPa]	2640.0	455.0
Ultimate strain, ε_{ult}	[%]	4.7	19.0
Poisson's ratio, ν_{12}	[-]	0.33	0.33
Poisson's ratio, ν_{21}	[-]	0.0575	0.33
Shear modulus, G_{12}	[GPa]	5.55	27.6
Density, ρ	[kg/m^3]	1980.0	2770.0
Thermal expansion coefficient, α_1	[$1/^\circ C$]	6.1×10^{-6}	23.4×10^{-6}
Thermal expansion coefficient, α_2	[$1/^\circ C$]	26.2×10^{-6}	23.4×10^{-6}

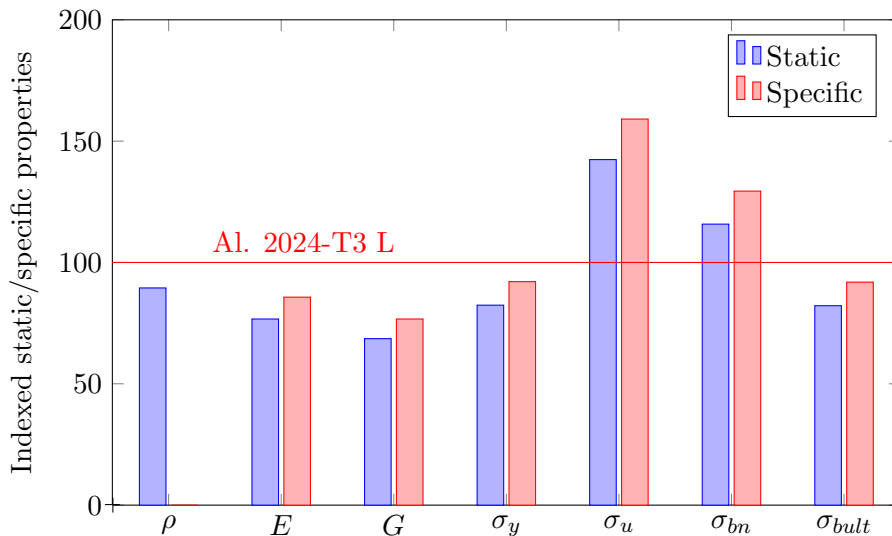


FIGURE 2.2: Indexed specific static properties of Glare 3-3/2-0.3

As shown in Table 2.2, the glass-fibre epoxy layers have a considerably lower weight than monolithic aluminium, 1.98 versus 2.77 g/cm³, respectively. As previously discussed, this can offer approximately 10% material and 20-30% structural weight reduction in primary structural applications. Although, in aircraft design the selection of a material is a compromise between technical, economic and environmental issues, weight is becoming an increasingly important factor in the material selection process. A lighter aircraft means that less lift has to be generated, which reduces the drag and fuel consumption, thus reducing the weight further, etc. This so-called 'snowball effect' has a large impact on the aircraft efficiency and operating costs.

2.3.2 Corrosion and durability

Aircraft structures are subjected to a wide spectrum of corrosion which is partly related to the vast number of different materials used in aircraft construction. However, it has been shown that Glare possesses good corrosion resistance [29]. Although it might appear that FMLs possess similar corrosion characteristics to monolithic aluminium, there are several aspects which distinguish FMLs from conventional, monolithic (thick) metal sheets. In Glare, the aluminium layers have a thickness of 0.2-0.5 mm, which is thinner than conventional metallic structures (2-4 mm). Following heat treatment during the rolling process, the aluminium sheets are quenched at a fast rate which results in less alloy elements at the crystal boundaries of the aluminium and thus superior corrosion resistance. Furthermore, all aluminium sheets used in the production of Glare are anodized and coated with a corrosion-inhibiting primer prior to bonding to the glass-fibre epoxy layers. To improve surface corrosion resistance, the outer aluminium layers can be supplied with a thin clad layer. Corrosion damage is also limited to the outer aluminium layer, since the fibre layers acts as corrosion barriers. Complementary to this, through-thickness corrosion is inhibited by the role of the thin aluminium sheets protecting the glass-fibre epoxy layers from degradation due to moisture and ultraviolet-radiation, which both can be a serious threat to the laminate strength and stiffness.

2.3.3 Impact

One of the key concerns in the application of FMLs to thin-walled structures, is their relatively high susceptibility to low and high velocity impact damage, such as runaway debris, hail, maintenance damage (i.e. dropped tools), bird-strike etc. Visible inspection for damage in Glare is easier than in brittle carbon fibre composites, due to clearly visible plastic deformation of the outer aluminium layers. Patch repair can be conducted using aluminium patches as they are similar in terms of stiffness mismatch and therefore does not require any special material to be in stock. Figure 2.3 compares the respective minimum impact energies to cause first failure [32]. It has been shown that, under low velocity impact (10 m/s), Glare exhibits comparable or superior (15%) better minimum cracking energy relative to monolithic aluminium of the same areal density and is superior (2–3.5 better) at high velocity impact (100 m/s) [15, 32]. An increase in the ballistic limit of 15% was also reported for Glare 5 [33]. The increase in energy absorption of Glare has been attributed to the high strain rate phenomenon that occurs in glass fibres, combined with their relatively high failure strain, since such an increase would not be as significant in monolithic aluminium [32]. On the other hand, brittle carbon fibre based composites are hampered by their low impact resistance and bad

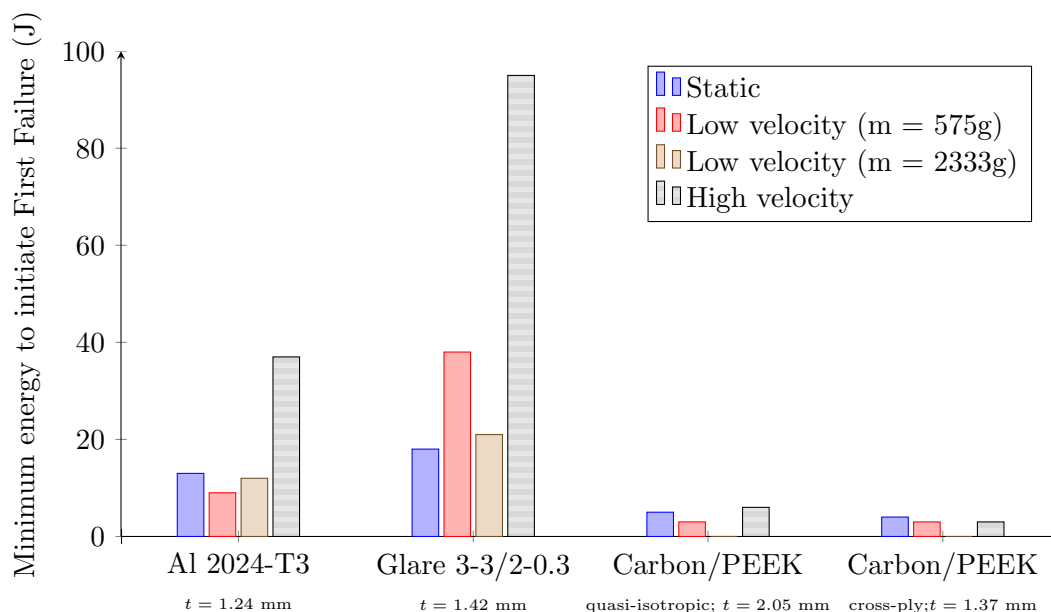


FIGURE 2.3: A comparison of the impact performance of Glare 3 and other aerospace materials

reputation concerning maintainability (i.e. complicated and expensive inspection and repair techniques are required).

2.3.4 Flame resistance

Glare has shown to have better fire resistance properties than monolithic aluminium alloys. Airworthiness regulations dictate that in the event of a fire, an escape time of 90 seconds for passengers must hold. However, as discussed in Ref [31], typical aircraft skins made from aluminium alloys will normally melt away in 20-30 seconds in the case of an outside kerosene fire. It has been shown, by fire resistance tests up to 1200° [31], that Glare can resist fire conditions for much longer time periods; preventing fire from penetrating for more than fifteen minutes. Although the outer aluminium layers and the adjacent matrix of the glass-fibre epoxy melts, the high melting temperature of the glass fibres (1500°C) is able to withstand the high temperature and remain intact and acts as a fire barrier. Therefore, the interior aluminium layers do not melt providing coherence to the structure (skin, stringers and frames) for a long period against an outside fire and ensuring that the structural integrity of the fuselage is intact during this period. A structure of monolithic equivalence would be more susceptible to melting, resulting in collapse and injury to passengers.

Both the blast and flame resistance of Glare was demonstrated by tests on blast-resistant cargo containers, performed by the FAA in 1995. The container was able to withstand the harmful effects of a blast and no breaching was reported, as shown in Fig. 2.4.



FIGURE 2.4: Glare blast-resistant cargo container [34]

2.3.5 Blast

On-board explosive devices can be particularly damaging to commercial aircraft due to the combined effects of transient explosive forces and normal cabin pressurization [3].¹

Until recently little work had been done to address damage in Glare structures in high-explosive events, such as that caused by on-board explosion. It has been reported in Ref. [13], that a series of hardened luggage containers made from a variety of materials, including reinforced aluminium, fibre glass, aramid fibres and polymers were tested to meet Federal Aviation Administration (FAA) standards, in response to the Pan Am Flight 103 Lockerbie disaster. Glare was the only material to pass certification with no reported breaching of the container. The Glare structure was able to withstand and absorb the explosive energy, greater than that in the Lockerbie air disaster, and redistribute the impact load to the adjacent surface area rather than to one specific weak spot [13]. Although significant deformation was present, the overall container remained intact. To the author's knowledge, no additional studies, neither experimentally nor numerically, have been performed to validate this study, since exact information about the precise design and the experiment details were not disclosed. Despite promising results, it has yet to come into use in most aircraft due to its increased cost compared to the currently aluminium containers.

¹Aircraft compression systems are designed to maintain sea-level atmospheric pressure inside the fuselage up to a given altitude at which a maximum pressure differential is reached. For flights at higher altitudes, a maximum pressure differential in the range of 51.7-62.0 kPa (7.59.0 psi) between the aircraft cabin and the ambient atmosphere is maintained [5].

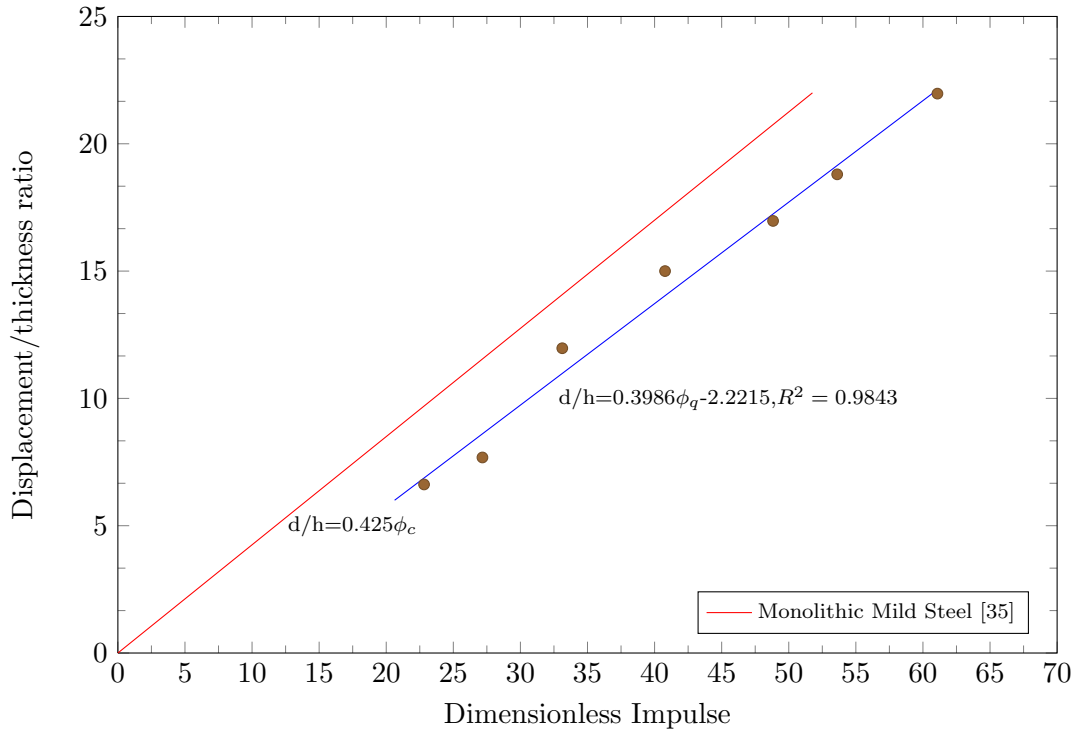


FIGURE 2.5: Graph of normalised displacement versus dimensionless impulse for Glare panels and steel plates [16]

To address the lack of experimental data in the blast response of Glare panels, Langdon et al. [16] presented some preliminary results of an experimental investigation of the blast response of Glare 3 panels. Results from preliminary blast tests on Glare panels indicated that the panels behaved similarly to monolithic metal plates, with the panels exhibiting large plastic deformation and yield line formation. The localised blast tests showed a trend of increasing normalised displacement with increasing non-dimensional impulse. Figure 2.5 shows a graph of displacement/thickness ratio against normalised impulse for Glare panels and results taken from Jacob et al. [35] on fully clamped circular steel plates. The panels appeared to offer higher blast resistance when compared to monolithic (ductile) metal plates. This is in contrast to a review by Langdon et al. [14], which found that the results from thermoplastic FMLs, showed no reduction in damage compared to steel plate data. However the study failed to determine the tearing threshold, which is an important parameter when assessing the ability of the structure to contain a blast load. Further work needs to be done to establish a better overview of Glare to blast loadings. Motivated by limitations and gaps in the current literature, numerical efforts have been performed to take into account different stacking-sequences, loading and boundary conditions and dynamic fracture characteristics, as discussed in the proceeding chapters.

2.4 Applications of FMLs

The feasibility of Glare as an aerospace material is determined by its potential to establish significant weight savings and reduce maintenance costs for a competitive price. The properties of Glare listed in the previous section allow for the applications listed below [10].

Fuselage skin: Glare has been optimised for fuselage skin application due to its excellent fatigue and high damage tolerance properties.

Upper and lower wing skins: Advancements in manufacturing of double-curved panels, amongst other positive attributes, have made Glare a cost-effective, attractive structural material for upper and lower wing skins. Furthermore, the strain sensitivity of the glass-fibres enhances the impact resistance in high strain rate events, such as bird strikes, fragmentation from engine failure and blast. For this reason, the application of Glare in the leading edge of an aircraft wing and cockpit roofs make use of the material's impact resistance and reparability.

Stringers and frames: The ability to tailor the stacking sequence of unidirectional Glare laminates makes it suitably ideal for applications with uni- or bi-axial loading direction, if an acceptable trade-off of weight saving and manufacturing costs is established.

Floors in passenger and cargo areas: Some areas of the aircraft are exposed to low velocity impact damage, such as the cargo area and flooring, as a result of human contact. Although many Glare grades exist, it is Glare 5 which has been specifically developed and optimised for impact applications. Glare possesses superior impact resistance to low and high velocity impact compared to monolithic aluminium and conventional composite materials.

Firewalls: In addition to excellent impact resistance and good formability, Glare has a superior flame resistance which has been proven in a number of qualification tests.

Bulkheads: The increase in diameter and reduction in thickness of fuselage structures in addition to cabin pressurisation imposes great loads to the fuselage skin material. Glare is currently used in the manufacture of the top-half of the fuselage skin for the Airbus A380, after reaching technological readiness, due to its excellent fatigue, damage tolerance and strength.

Cargo barriers: Cargo barriers are stiffened structures which separates the cargo from the pilot area. In the event of a crash, it is crucial that the cargo is prevented from crushing the cock-pit. The cargo area has also received considerable interest in blast

mitigation since the Lockerbie atrocity in 1989. The non-linear behaviour of Glare allows the glass fibres in the yielded area to still carry some of the load retaining its structural integrity. Its proven blast and impact resistance makes it an ideal candidate for cargo containers.

Chapter 3

Blast resistance and damage modelling of quadrangular FMLs

THE present chapter deals with investigating the performance of Glare to blast loadings compared to monolithic aluminium. Small-scale blast trials have been performed for numerical validation where back-face mid-span deflections and post-damage patterns were available. Secondly, the purpose of this chapter is also to validate the fluid-structure interaction (FSI) algorithms in Multi-Material ALE (MMALE) formulations against small-scale test results in anticipation of deployment for modelling of full-scale realistic scenarios. It has been shown that good agreement between the results of experimental and numerical simulation is obtained.

3.1 Introduction

As conventional metallic materials and their derivatives are increasingly being replaced in primary aerospace structures by fibre reinforced polymers, which offer lightweight and high specific properties; they continue to have a fundamental role in applications where composites have yet to be fully exploited [27]. As discussed in Chapter 2, Glare has attracted interest from industry as it has major advantages over conventional aluminium particularly better damage tolerance behaviour. In metal fatigue and impact applications, the elastic strain is larger than other metal material so it can consume more impact energy and have higher penetration resistance despite showing more visible impact damage (i.e. dents easier). Although various types of Glare configurations exist, depending on the structural requirement of the component, it is the cross-plyed Glare 3 and Glare 5 with bi-directional reinforcements [9] which are of interest in impact applications, see Fig. 3.1 for details.

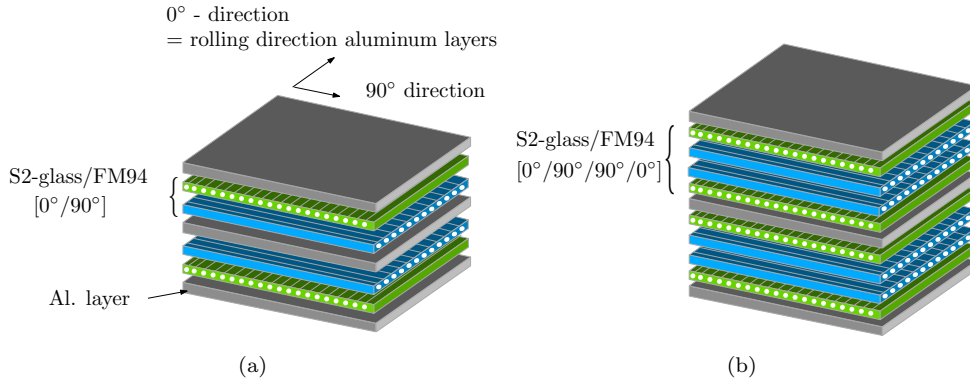


FIGURE 3.1: Configuration of Glare laminates:(a) 3-2/1 and (b) 5-3/2.

If Glare is to be considered as a blast mitigation structure it must demonstrate that it can absorb the destructive effects of IEDs and display favourable failure mechanisms which does not pose significant threats to passenger and/or third parties. To address these concerns, a series of small, precise blast trials have been completed and reported to investigate the performance of Glare to blast loadings. These tests will form part of a large building block to establish the structural response of hardened aircraft structures to realistic blast loadings.

Small-scale experimental trials are important in establishing benchmark behaviour of structural materials to blast-type loading. However, such experiments are expensive and time-consuming and are not amenable to cover different lay-up configurations, loading regimes and boundary conditions. Modelling the behaviour of these structural materials, using commercial finite element software, would be of great assistance as only a small number of experimental tests would need to be performed for model verification and validation. This requires developing efficient and reliable predictive techniques which take into account accurate material characterisation, appropriate failure criteria and description of the blast loads. This would enable the response of larger components (e.g. fuselage or aircraft luggage containers) to be modelled without the need to undertake a large number of experimental tests. Numerical work performed by Karagiozova et al. [18] on polypropylene based FMLs [36], has shown that it is possible to simulate and capture the response and failure mechanisms to localised blast loading using commercial finite element software.

The objective of this chapter is to present a robust and computationally efficient predictive model which can capture the dynamic non-linear behaviour of FMLs using the explicit finite element codes ABAQUS [24] and LS-DYNA [25], based on blast trials conducted within the VULCAN consortium and those reported in the open literature for

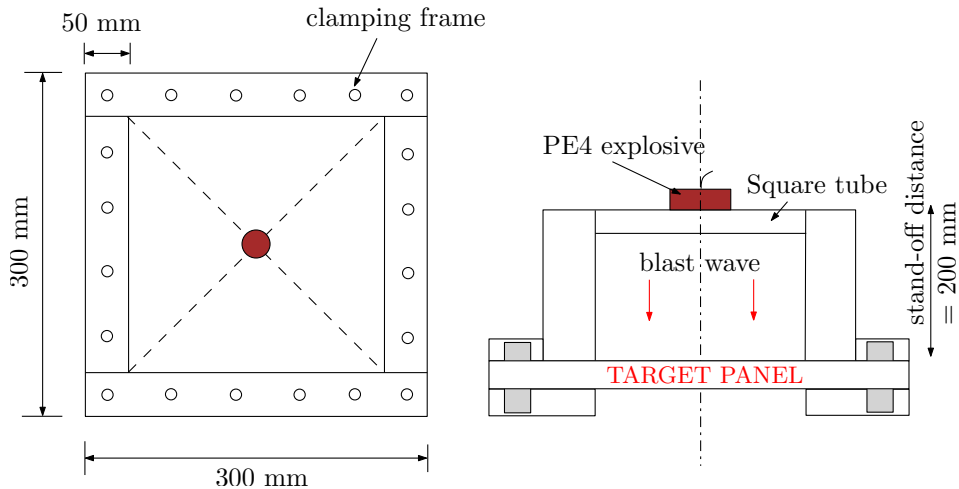


FIGURE 3.2: Schematic of experimental small scale blast trials.

which experimental data on the back face-displacement and post-damage information is available for model validation.

3.2 Performance of Glare panels subjected to intense uniform pressure pulse loading

The Glare 3 panels investigated by Langdon et al. [16] are 1.42 mm thick and comprise of three 0.3 mm thick aluminium 2024-T3 alloy sheets, with two cross-plyed ($0^\circ/90^\circ$) unidirectional S2-glass/FM94 between each pair of aluminium sheets. The square panels of dimensions 300 mm \times 300 mm were clamped between two steel frames and mounted onto a ballistic pendulum during blast testing, leaving an exposed area of 200 mm by 200 mm. The mass of the disc-shape PE4 plastic explosive, M , was varied between 4g to 14g to change the impulse, I , applied to the panels. Due to the low thickness of the Glare 3 panel, severe damage and petalling was observed for low impulses due to the localised nature of the blast load. To increase the spatial uniformity and decrease the intensity of the blast wave, a square tube, shown in Fig. 3.2, was employed to site the explosive 200 mm away from the panel. The explosive was detonated at the open end of the tube and the blast wave was directed down the tube towards the specimen. Two charge diameters, d , of 20 and 40 mm were used, both of which resulted in uniform type response of the Glare 3 panels. The results of the experiment are shown in Table 3.1 which are expressed in terms of the final displacements of the mid-span of the back panel, d_B .

TABLE 3.1: Uniformly distributed blast test results [16].

Test	ϕ [mm]	M_{PE4} [g]	I [Ns]	d_B [mm]	d_B/h [-]
001	40.0	14.0	31.9	31.2	22.0
002	40.0	11.0	28.0	26.7	18.8
003	40.0	9.0	25.5	24.1	17.0
004	40.0	7.0	21.3	21.3	15.0
005	40.0	5.0	17.3	17.0	12.0
006	20.0	5.0	13.1	10.9	7.7
007	20.0	3.0	11.0	9.4	6.6

3.2.1 Numerical methodology

FMLs are expected to fail under a multitude of failure mechanisms which are akin to those found in both metallic and composite structures. Such failure may involve severe plastic deformation, interlaminar delamination, and intralaminar damage such as fibre breakage and matrix cracking, all of which should be captured by the proposed computational model. The manifestation of these failure mechanisms will depend, amongst many others, on the nature of the dynamic loading (spatial intensity of the blast wave) and the applied edge boundary conditions which are imposed on the test panels as a result of clamping. The latter may prevent vibratory interference with the blast shock waves, resulting in more pronounced through-thickness perforation and shear damage. These factors will indeed influence and preclude the use of certain element formulations, constitutive models and require a different finite element modelling rationale.

The tested Glare panels have a nominal thickness of the order of a few millimeters, whereas the panels had a quadrangular geometry of the order of a few hundred millimeters ($h/L = 0.004$). Additionally, the blast load duration of the pressure-pulse loading is much higher than the transition time for through-thickness shock waves; hence the response of the panel is dominated by two-dimensional, transverse shear waves.

The uniaxial strain wave speed in cross-plyed $0^\circ/90^\circ$ orthotropic and homogeneous metallic plates can be expressed as [37]:

$$c_{comp} = \sqrt{\frac{(1 - \nu_{12})E_{33}}{[1 - \nu_{12} - \nu_{32}(\nu_{13} + \nu_{23})]\rho_{comp}}} \quad (3.1a)$$

$$c_{al} = \sqrt{\frac{E_{33}}{\rho_{al}}} \quad (3.1b)$$

giving $c_{comp} \approx 3700$ m/s and $c_{al} \approx 3130$ m/s. The wave transit time through each layer can be defined as $t = h/c_{comp,al}$. Furthermore, since all of the damaged Glare panels from the experiments underwent extensive panel deformation before tensile tearing, it is reasonable to assume that the through-thickness stress-waves can be considered negligible in thin FML panels. Due to this large aspect ratio with respect to the laminate thickness and two-dimensional transverse shear wave assumption, each layer can be assumed to be in state of plane stress, with all through-thickness normal and shear components of the stress tensor (σ_{13} , σ_{23} , σ_{33}) are assumed to be negligible in comparison with their in-plane counterparts (σ_{11} , σ_{22} , σ_{12}). As the mechanical properties of this hybrid system vary between each subsequent laminate, each layer can be represented by a unique set of integration points, as in the case of shell elements. Although this approach neglects delamination between adjacent layers, this assumption is acceptable if no significant delamination is observed from post-damaged cross-section samples [16].

The commercial finite element solver ABAQUS/Explicit 6.10 is used for the blast simulation. Four-node reduced integration shell elements with hourglass control, S4R, were selected to model each material constituent which were found to be comparable with SC8R, an 8-node 3D continuum shell, albeit at significant reduced computational cost. The cross-sectional behaviour of the shell was computed using the Simpson thickness integration method with three integration points in each layer of the composite system. The modelling approach for the Glare panel was as follows; a reference surface, which is also coincident with the mid-surface of the composite panel, is defined. In the composite lay-up model a material ID, orientation and thickness are assigned to each layer represented by at least three unique section points, as shown in Fig. 3.4.

In the experiments the panels are secured using two steel clamping plates. The bottom clamp is fixed whilst a downward force is applied to the rigid reference point of the top clamp to secure the Glare panel. The clamps are meshed using 4-node 3-dimensional discrete rigid brick elements (R3D4). General contact with separation is defined between the clamp and the panel. A friction coefficient of 0.5 is defined to simulate tangential contact behaviour [38]. The quarter symmetry, mesh density and boundary conditions is shown in Fig. 3.3.

3.2.2 High strain material properties

Typical quasi-static stress strain curves from static tensile tests for Glare 3 and its constituents are shown in Fig. 3.5. While quasi-static material data is widely available in the open literature, accurate high strain rate material characterisation for Glare 3 is

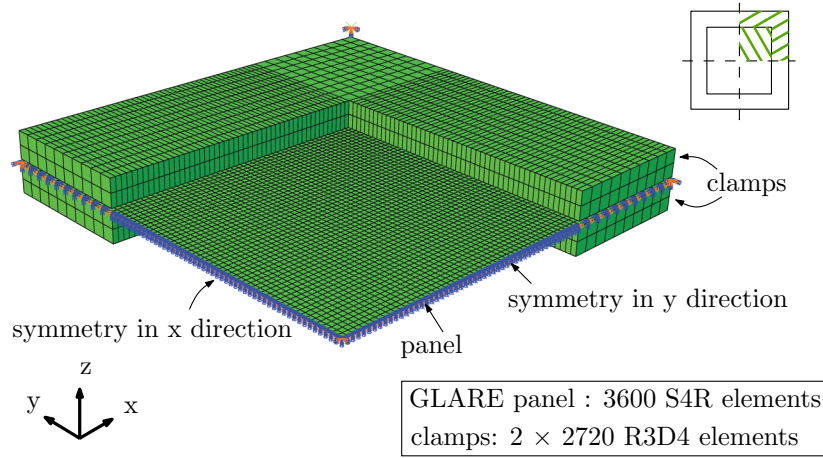


FIGURE 3.3: Schematic of the 1/4 numerical model of fully clamped Glare 3 panel.

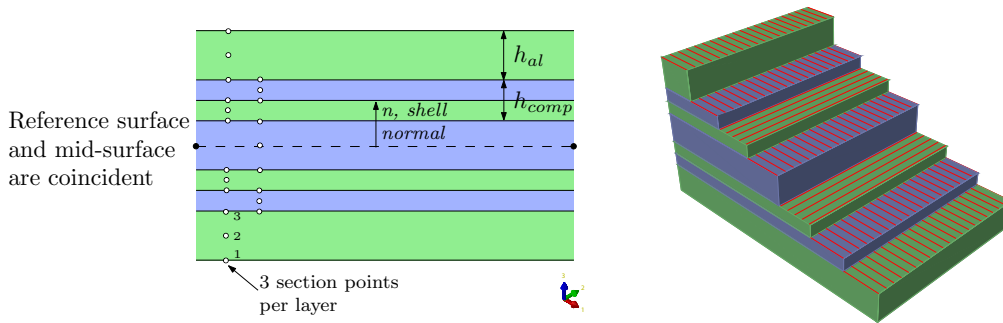


FIGURE 3.4: Definition of composite lay-up of Glare 3 using S4R elements.

scarce which poses challenges to the numerical analyst when defining input parameters for damage constitutive models.

3.2.3 S2-glass/FM94

In the open literature, high strain rate tensile tests on FML specimens (Glare 3-3/2-0.4) showed very little evidence for rate dependency (up to 3300 s^{-1}) for any of the in-plane elastic properties [39]. However tensile strength material results on waisted FML specimens exhibited positive strain rate sensitivity for both the 0° and 45° tests. In the 0° tests, an increase in ultimate load capacity (tensile strength) of 19% was observed for quasi-static to 3300 s^{-1} rates. The effect of strain rate on ultimate strength in the 0° direction was consistent with the findings of Vlot [40] who tested a similar cross-ply glass-based fibre metal laminate at a quasi-static rate and a rate of 20 m/s. To account for the strain rate effects observed in the experiments, McCarthy et al. [39] assigned a Dynamic Increase Factor (DIF) to the numerical strain rate model assuming that the transverse modulus, shear modulus and longitudinal fibre rupture strains were rate dependent and the longitudinal Young's modulus of the glass composite layers were

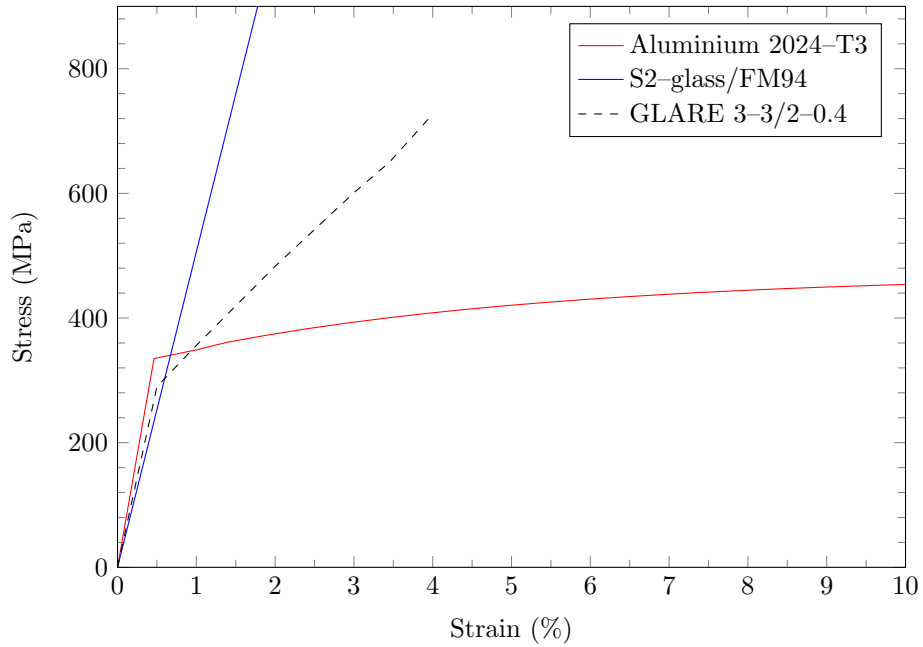


FIGURE 3.5: Typical tensile stress-strain curves of Glare and its constituents - Aluminium 2024-T3 and S2-glass/FM94.

not. Similarly, Hoo Fatt et al. [33] assumed that the in-plane elastic properties were 1.5 times that of the static values, although the Poisson's ratios remained equal to the static equivalent.

TABLE 3.2: Material property data used to represent S2-glass/FM94 laminates [41, 42].

Property	Units	Value	Property	Units	Value
ρ	kg/m^3	1980	S_{LT}^a	MPa	75
E_{11}	GPa	50.6	S_{TT}	MPa	50
E_{22}	GPa	9.9	X_c	MPa	2000
E_{33}	GPa	9.9	Y_c	MPa	150
ν_{12}	-	0.063	X_t	MPa	2500
ν_{13}	-	0.063	Y_t	MPa	50
ν_{23}	-	0.32			
G_{12}	GPa	3.7			
G_{13}	GPa	3.7			
G_{23}	GPa	1.65			

^a S_{LT} denotes the in-plane shear failure stress

Considering the incomplete data available for the individual constituents of the Glare (particularly the glass layers), and strain rate independent failure criteria available in ABAQUS, quasi-static in-plane elastic and strength properties were assumed, taken from

Refs. [41] and [42], respectively. However the maximum fibre rupture strain in tension was increased by a factor of 2.02 to correspond to the failure strain of Glare 3 at the maximum strain rate of 3300 s^{-1} (as performed by McCarthy et al. [39]), which is within the strain rate regime associated with blast loading.

In general, phenomenological strength criteria such as maximum stress, Hashin damage and Tsai-Wu criteria are used to detect the failure status of composite laminates. Due to the complexity of failure mechanisms in the Glare laminates, it is difficult to define an applicable failure criterion. In this study the readily available Hashin failure criteria were chosen [43], that can successfully predict damage initiation but it is recognised that a fracture based criteria should be used to model damage progression. Advantages and disadvantages in defining applicable failure criteria to composite structure can be found in [44–46]. Laminated shell theory was activated to properly model the transverse shear deformation. The material properties used are shown in Table 3.2.

3.2.3.1 Damage initiation

Hashins failure criteria [47] were chosen to predict damage initiation. In Hashins theory, the following four damage-initiation mechanisms are considered for a unidirectional laminate: fibre tension, matrix tension, fibre compression, and matrix compression. These are expressed in terms of principal stress σ_{ij} , material strengths, and the following failure parameters,

Fibre tension ($\hat{\sigma}_{11} \geq 0$):

$$F_f^t = \left(\frac{\hat{\sigma}_{11}}{X_T} \right)^2 + \left(\frac{\hat{\tau}_{12}}{S_L} \right)^2 \quad (3.2)$$

Matrix tension ($\hat{\sigma}_{22} \geq 0$)

$$F_m^t = \left(\frac{\hat{\sigma}_{22}}{Y_T} \right)^2 + \left(\frac{\hat{\tau}_{12}}{S_L} \right)^2 \quad (3.3)$$

Fibre compression ($\hat{\sigma}_{11} < 0$):

$$F_f^c = \left(\frac{\hat{\sigma}_{11}}{X_C} \right)^2 \quad (3.4)$$

Matrix compression ($\hat{\sigma}_{22} < 0$):

$$F_m^c = \left(\frac{\hat{\sigma}_{22}}{2S_T} \right)^2 + \left(\frac{\hat{\tau}_{12}}{S_L} \right)^2 + \left[\left(\frac{Y^c}{2S^T} \right)^2 - 1 \right] \frac{\hat{\sigma}_{22}}{Y^C} \quad (3.5)$$

where X^T and Y^T are the longitudinal and transverse tensile strength, X^C and Y^C are the longitudinal and transverse compressive strengths, S^L is the longitudinal shear strength, and S^T is the transverse shear strength. When $F_f^t = 1$, $F_m^t = 1$, $F_f^c = 1$, or $F_m^c = 1$, the corresponding damage mode initiates. $\hat{\sigma}_{11}, \hat{\sigma}_{22}, \hat{\tau}_{12}$ are components of the effective stress tensor, $\hat{\sigma}$, which is used to evaluate the initiation criteria. The effective stress tensor is computed from [48]:

$$\hat{\sigma} = \mathbf{M}\sigma \quad (3.6)$$

where σ is the true stress and \mathbf{M} the damage operator:

$$\begin{bmatrix} \frac{1}{1-d_f} & 0 & 0 \\ 0 & \frac{1}{1-d_m} & 0 \\ 0 & 0 & \frac{1}{1-d_s} \end{bmatrix} \quad (3.7)$$

d_f, d_m and d_s are internal (damage) variables that characterize fibre, matrix, and shear damage, which are derived from damage variables d_f^t, d_f^c, d_m^t , and d_m^c , corresponding to the four failure mechanisms

$$d_f = \begin{cases} d_f^t & \text{if } \hat{\sigma}_{11} \geq 0, \\ d_f^c & \text{if } \hat{\sigma}_{11} < 0, \end{cases} \quad (3.8a)$$

$$d_m = \begin{cases} d_m^t & \text{if } \hat{\sigma}_{22} \geq 0, \\ d_m^c & \text{if } \hat{\sigma}_{22} < 0, \end{cases} \quad (3.8b)$$

$$d_s = 1 - (1 - d_f^t)(1 - d_f^c)(1 - d_m^t)(1 - d_m^c). \quad (3.8c)$$

Prior to any damage initiation, i.e. d_f, d_m and d_s are equal to zero, the damage operator, \mathbf{M} , is equal to the identity matrix, so $\hat{\sigma} = \sigma$. Damage initiation occurs when one of the four aforementioned failure modes are satisfied, altering the corresponding damage parameters d_f, d_m or d_s , and so the damage operator matrix will be modified giving rise to a new effective stress tensor. The effective stress, $\hat{\sigma}$, is intended to represent the stress acting over the damaged area that effectively resists the internal forces.

3.2.3.2 Damage Evolution

In the post-damage initiation phase, damage evolves by the degradation of the plane stress orthotropic material's elasticity matrix. The response of the material in terms of stress is computed by relating the exhibited strain to the damaged elasticity matrix (\mathbf{C}_d) [48]:

$$\sigma = \mathbf{C}_d \varepsilon \quad (3.9)$$

where ε is the strain and \mathbf{C}_d is the damaged elasticity matrix, which has the form

$$\mathbf{C}_d = \frac{1}{D} \begin{bmatrix} (1 - d_f)E_1 & (1 - d_f)(1 - d_m)\nu_{21}E_1 & 0 \\ (1 - d_f)(1 - d_m)\nu_{12}E_2 & (1 - d_m)E_2 & 0 \\ 0 & 0 & (1 - d_s)GD \end{bmatrix} \quad (3.10)$$

where $D = (1 - d_f)(1 - d_m)\nu_{12}\nu_{21}$, d_f , d_m , d_s reflect the current state of fibre, matrix and shear damage, respectively. Stress-strain relationships for damage are prone to mesh dependency during material softening, leading to erroneous results; such as decreasing energy dissipation upon mesh refinement. A characteristic length, based on the element geometry and formulation, is introduced to alleviate mesh dependency, so that the constitutive law is expressed as a stress-displacement ($\sigma - \delta$) relation [48]. In this case, the damage variable will evolve in a bi-linear manner, as shown in Fig. 3.6(a) for each of the four failure modes. The positive slope of the stress-displacement curve, line OA , prior to damage initiation represents linear elastic orthotropic behaviour. At point A (i.e. equivalent displacement, δ_{eq}^0 , and stress, σ_{eq}^0 , at the onset of damage), damage is initiated and evolves via degradation of material properties, as indicated by the negative slope AC . Each increment is computed and stored so that unloading and re-loading of the partially damaged material can be accounted for, as shown by line OB . The energy dissipated due to failure, G^c , defines the equivalent displacement at final damage, δ_{eq}^f and is represented by the area under the triangle OAC . Hence,

$$\delta_{eq}^f = \frac{2G^c}{\sigma_{eq}^0} \quad (3.11)$$

After damage initiation (i.e., $\delta_{eq} \geq \delta_{eq}^0$), the damage variable for a particular mode of failure is given by the following expression

$$d = \frac{\delta_{eq}^f(\delta_{eq} - \delta_{eq}^0)}{\delta_{eq}(\delta_{eq}^f - \delta_{eq}^0)} \quad (3.12)$$

This relation is presented graphically in Fig 3.6(b).

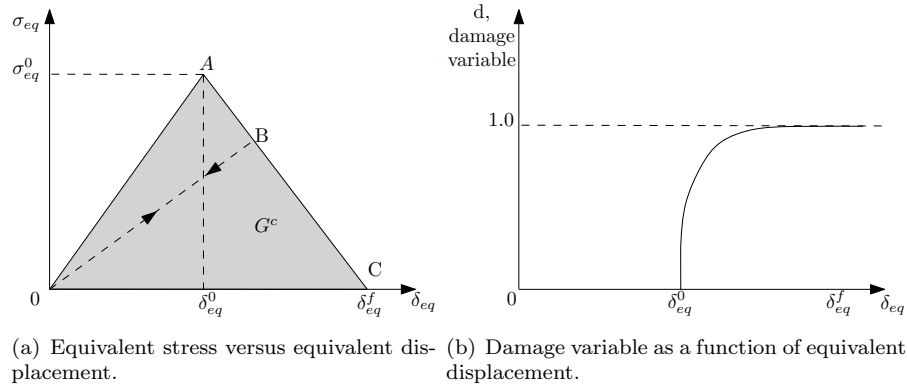


FIGURE 3.6: Damage evolution for fibre-reinforced composites

3.2.3.3 Limitations

The limitations of ABAQUS's Hashin based damage and failure model for fibre-reinforced composites lie in the fundamental inaccuracies of the Hashin criteria and simplifications imposed by ABAQUS. Firstly, the Hashin criteria presented (Eq.s 3.2 - 3.5) neglect the through-thickness stresses, and so, are essentially in a 2D form. For this reason, the model is limited to plane stress elements such as shells and continuum shells. Furthermore, the criterion does not predict the onset of delamination damage. Finally, although the Hashin criteria are commonly used in industry, studies have demonstrated their inaccurate failure prediction, especially in matrix and fibre compression modes.

3.2.4 Aluminium 2024-T3

To describe the elastic-plastic response of the Aluminium 2024-T3 layers, an isotropic constitutive model based on the Johnson-Cook (JC) material model [49] was implemented. The JC plasticity formulation defines the flow stress as a function of equivalent plastic strain, strain rate and temperature, was employed. The dynamic flow stress is expressed by the following relation [49]:

$$\bar{\sigma}_d = \left[\sigma_y + B(\bar{\varepsilon}^{pl})^n \right] \left[1 + C \ln \left(\frac{(d\bar{\varepsilon}/dt)_{pl}}{(d\varepsilon/dt)_0} \right) \right] (1 - T^{*m}) \quad (3.13)$$

where $\bar{\sigma}_d$ is the dynamic flow stress, $\bar{\varepsilon}_{pl}$ is the equivalent plastic strain, $(d\bar{\varepsilon}/dt)_{pl}$ is the equivalent plastic strain rate, and $(d\varepsilon/dt)_0$ is a reference strain rate (typically normalized to a strain rate of $1.0s^{-1}$). σ_y , B , n , m and C are material parameters and T^* is the

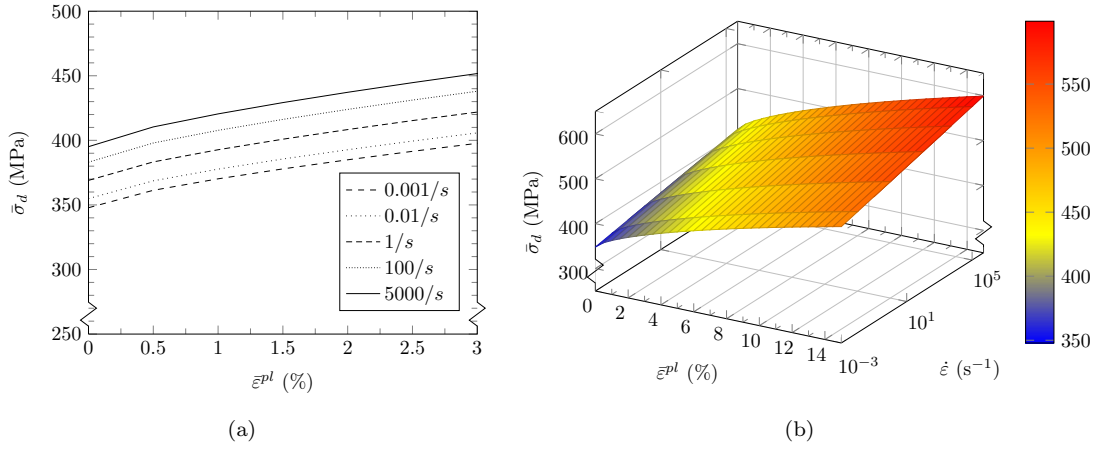


FIGURE 3.7: 2D (a) and 3D yield surface (b) of dynamic flow stress of Al 2024-T3 as a function of strain rate and equivalent plastic strain.

TABLE 3.3: Johnson-Cook material model parameters for Aluminium 2024-T3 [51]

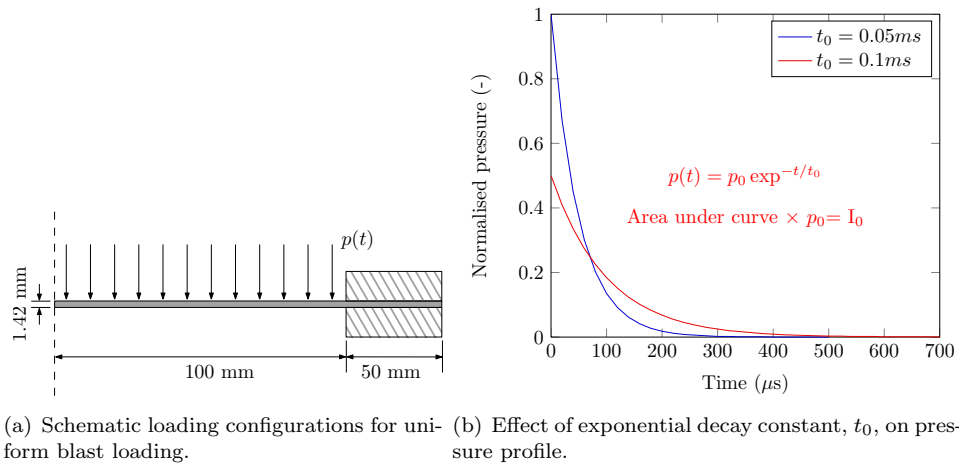
Property	ρ	ν	E	σ_y	B	n	C	m	T_0	T_{melt}
Units	kg/m^3	(-)	GPa	MPa	MPa	(-)	(-)	(-)	$^{\circ}K$	$^{\circ}K$
Value	2770	0.33	73.1	369	684	0.73	0.0083	1.7	294	775

non-dimensional temperature given by:

$$\begin{aligned}
 0 & & T < T_{transition} \\
 T^* \equiv (T - T_0)/(T_{melt} - T_0) & & T_0 \leq T \leq T_{melt} \\
 1 & & T > T_{melt}
 \end{aligned} \tag{3.14}$$

where T is the current temperature, T_{melt} is the melting temperature and T_0 is the temperature defined as the one at or below which there is no temperature dependence on the expression of the yield stress. The constant σ_y is the yield stress under quasi-static conditions, B and n are strain hardening parameters, m controls the temperature dependence and C the strain rate dependence.

Normally for high rate deformation problems, it is assumed that 90-100 % of the plastic work is dissipated as heat in the material [50]. However, in this study, temperature effects are ignored to reduce computational constraint, although significant thermal softening may occur during the initiation of the high explosive event. Material characterisation data for Aluminium 2024-T3 have been investigated and obtained at high strain rates and large strains using the split Hopkinson pressure bar (SHPB) methods [51], as shown in Table 3.3. The Johnson-Cook parameters have been determined for a strain rate validity range of $\dot{\epsilon} = 10^5 - 10^{-5} s^{-1}$. Figure 3.7 shows the influence of strain rate on the dynamic flow stress of the material.



(a) Schematic loading configurations for uniform blast loading. (b) Effect of exponential decay constant, t_0 , on pressure profile.

FIGURE 3.8: Schematic of blast loading configuration and pressure distribution.

3.2.5 Modelling the blast load

In this study, a uniformly distributed pressure pulse, similar to that adopted by Karagiozova et al. [18] given in Eq. 3.15, is analysed which is applied as a pressure pulse on the top surface of the Glare panel, see Fig. 3.8.

$$p(t) = p_0 \exp^{-t/t_0} \quad (3.15)$$

The pressure decays exponentially with a decay period of $t_0 = 0.05$ or 0.1 ms for the 20 and 40 mm charge diameter, respectively. It is assumed that different charge diameters will affect the rate of energy, as defined by the slope of the impulse-time curve, transferred to the target structure which also controls the strain rate experienced by the target material. The effect of changing the exponential decay time constant is shown on a normalised pressure-time curve, given in Fig. 3.8(b). The term p_0 is defined as the maximum overpressure of the blast wave which is evaluated based on the momentum conservation equation:

$$I = A \int_0^{\infty} p(t) dt \quad (3.16)$$

3.2.6 Results

The transient displacement contour plots of a Glare 3 panel subjected to an impulsive load of 25.5 Ns is shown in Fig.3.10. The results show that the panel deforms with plastic hinges first developing at the boundary and then moving towards the centre of the plate. A comparison of the results of the numerical analysis was obtained by investigating the deformed mid-point deflection of each back face layer. The predicted and experimental final displacements of the mid-span of the back panel of the clamped Glare 3 panels

for the entire tested range of impulses between 11 Ns and 31.9 Ns are given in Fig. 3.9. Although the predictive model slightly overestimates the experimental mid-span displacements, reasonable agreement is obtained for all load cases.

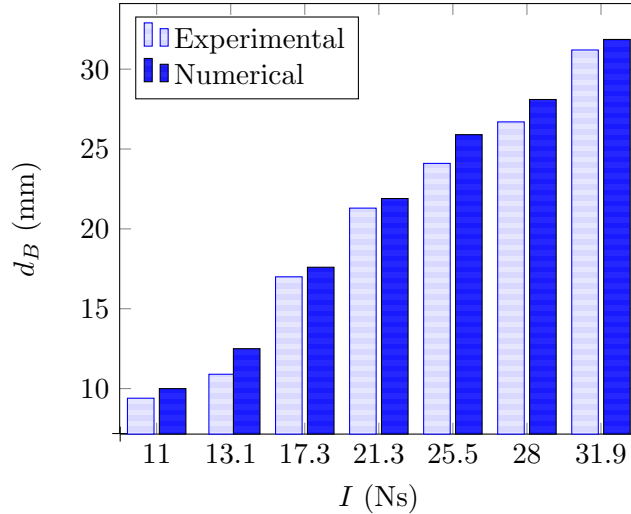


FIGURE 3.9: Comparison of experimental and numerical back face mid-span displacements ($I= 11$ Ns - 31.9 Ns at 200 mm stand-off distance)

The deformed quadrangular panel profile along its diagonal lines of symmetry was also investigated. Typical plate profile plots along the centre lines of the flat panel are shown in Fig. 3.11. Experimental observations on the post-damage panels at higher impulses saw the appearance of debonding and pulling in (i.e. tearing at the bolt holes) along the boundary edges. These observations are partly related to the interaction of the nuts, bolts and clamping conditions which influence the impulse transfer to the panel. The pulling-in effect is an undesirable feature which corresponds to inadequate clamping conditions as it delays the onset of tensile perforation of the panel. Therefore the results shown in Fig. 3.11 need to be interpreted in terms of the experimental set-up in which they were obtained, as one might not expect such a steep rise in the deflection profile emanating from the clamped boundary edges.

The ABAQUS/Explicit finite element program was run using Hashin's failure criteria for damage initiation. Figure 3.12 shows fibre and matrix tension damage at the bottom 0° glass fibre facesheet. Fibre tension damage was initiated near the center of the panel which extended in size with increasing applied impulse. However, the damage is rather limited to the centre of the panel which indicates that the glass-fibres in this layer still have load-bearing capacity retaining the structural integrity and support of the panel. Tensile matrix damage was also very extensive across the panel which extended across the clamped boundary. The predictive model showed that no tearing or perforation of the panel occurred up to an impulse of 35 Ns. It is important to comment at this point,

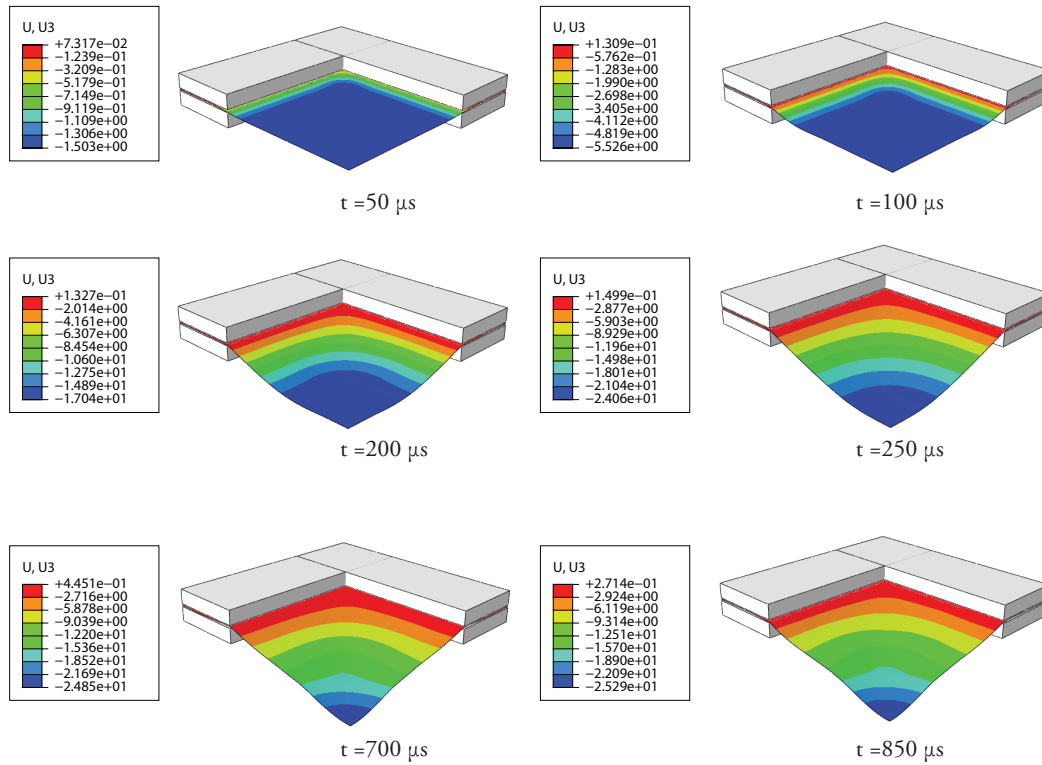


FIGURE 3.10: Response of Glare 3 panel at impulse 25.5 Ns showing displacement (in mm) in the z-direction.

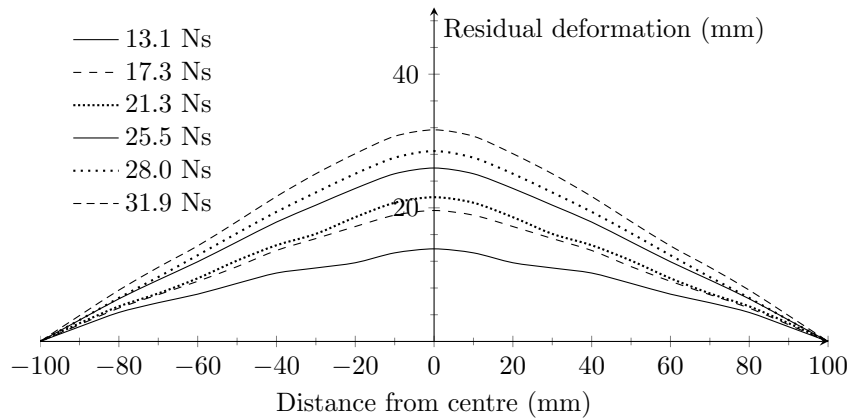


FIGURE 3.11: Residual deflection of impulsively loaded Glare 3 panels ($I= 11 \text{ Ns} - 31.9 \text{ Ns}$ at 200 mm stand-off distance).

that matrix cracks in the cross-plyed laminate will give rise to high interlaminar shear stresses at the boundary which will induce extensive debonding at the interface.

This model also highlights the success in approximating the blast load as a uniformly distributed pressure pulse, expressed as a function of some exponential time decay constant, which corresponds to the mass/diameter of the explosive.

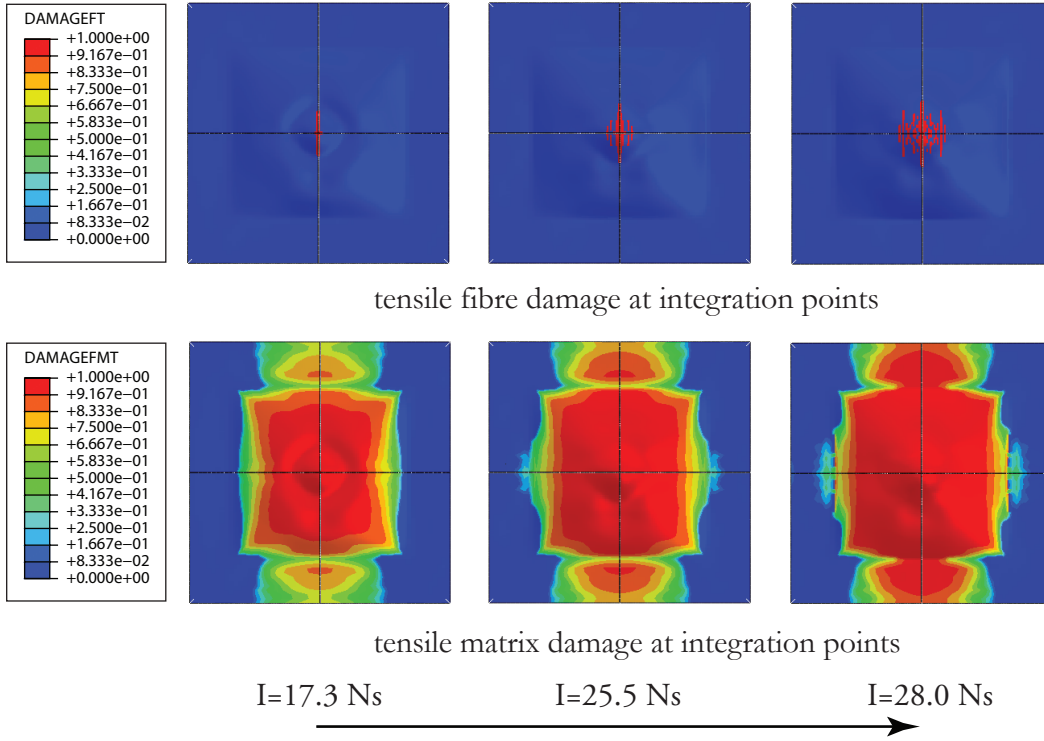


FIGURE 3.12: Fibre and matrix tension damage at bottom 0° facesheet using Hashin's failure criteria for increasing applied impulse.

3.2.7 Comparison with Glare 5 and Aluminium 2024-T3

A further objective of this study was to compare the performance of Glare against monolithic aluminium panels of equivalent areal density and Glare 5, a variant of Glare which is used in impact applications, see Table 2.1 for details on stacking sequence.

The results of this parametric study are given in Fig. 3.13, which shows mid-point displacement against applied impulse. For a given impulse, it appears that Glare exhibits smaller mid-point displacements than monolithic aluminium panels. Considerable inelastic deformation occurred in the panels where yield line formation (the formation of plastic hinges) is clearly seen in Fig. 3.14, which is typical of the response of a monolithic metal panels subjected to uniformly distributed pressure loading.

The deformation of the damaged Glare panels suggests that the energy imparted on the panel from the blast load can be dissipated in global deformation including panel bending and membrane stretching; extensive delamination within the glass/epoxy plies or debonding between the aluminium and glass/epoxy layers; and tensile fracture of the glass/epoxy and aluminium. Assuming that energy contributed to delamination and debonding is negligible, a simple energy balance of the numerical model is thus given by:

$$W_{total} = W_{int} + W_{ke} + \cancel{W_{vd}} + \cancel{W_{fd}} - W_{wk} = constant \quad (3.17)$$

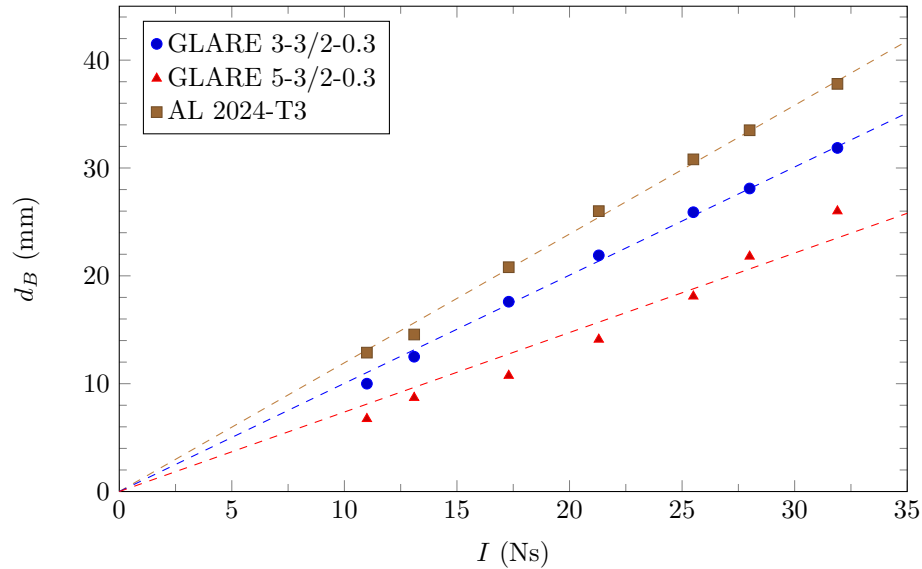


FIGURE 3.13: Predicted back face mid-point displacement of Glare 3 and 5 panels and monolithic aluminium plates.

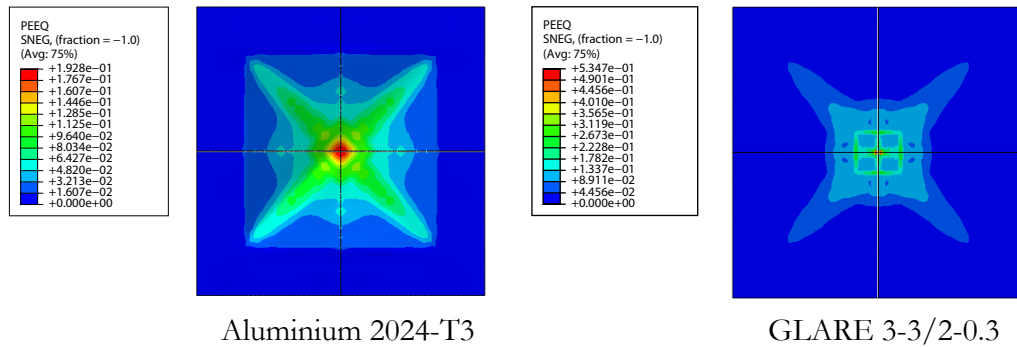


FIGURE 3.14: Contours of equivalent plastic strain of Aluminium 2024-T3 and Glare 3 of same areal density

where

$$W_{int} = W_{el} + W_{pl} + W_{dmg} \quad (3.18)$$

where the subscripts, int , ke , vd , fd and wd refer to the internal, kinematic, viscous, frictional dissipation and external work, respectively. Artificial energies due to hourglass modes of deformation in addition to viscous and frictional effects are negligible compared to the internal energy of the system, i.e. $< 1\%$. It can be shown in Fig. 3.15 that 87% of the internal energy is dissipated as non-recoverable plastic deformation in the thin aluminium layers of the Glare system. The remaining energy is due to elastic recoverable energy and fibre-reinforced damaged, 10% and 3% respectively. This is in contrast to an aluminium plate of equivalent areal density, where almost all of the energy is dissipated as plastic deformation, leaving no recoverable elastic deformation. The contribution of the glass fibres clearly enhances the blast mitigation of the Glare system, which is

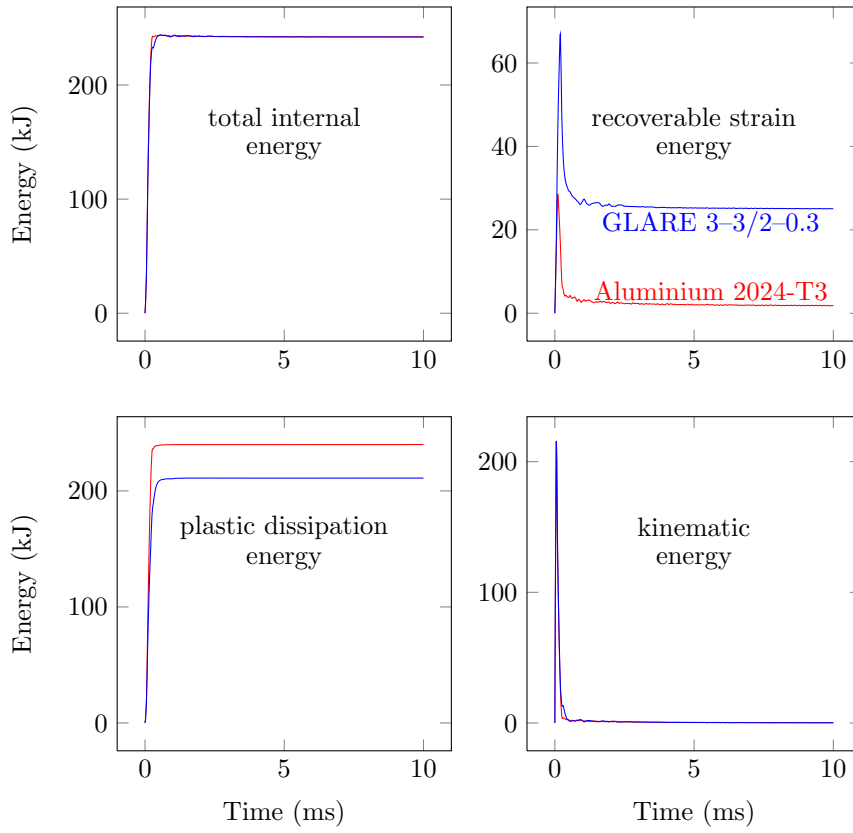


FIGURE 3.15: Partition of energies for Glare 3 subjected to impulse of 25.5 Ns

expected to improve at higher strain rates, due to their positive strain rate sensitivity.

However, direct comparison between all three materials is not possible, due to the inherent differences in density, material properties and configuration. An approach commonly adopted in the literature is to use non-dimensional parameters which allows for comparison of blast-loaded panels of different materials (densities and characteristic stresses), geometries (lengths, widths and thickness's) and loading conditions to be treated similarly. Nurick and Martin [52], initially derived an expression based upon Johnson's damage number [53], shown in Eq. 3.19 for quadrangular plates,

$$\phi_q = \frac{I}{2h^2(wl\rho\sigma)^{1/2}} \quad (3.19)$$

where w and l refer to the width and length of the panel, respectively. It has been subsequently modified by Nurick and co-workers [35, 54] for localised blast loading as shown in Eq. 3.20

$$\phi_{qt} = \frac{I \left(1 + \ln \frac{4wl}{\pi d^2}\right)}{2h^2 (wl\rho\sigma)^{1/2}} \quad (3.20)$$

TABLE 3.4: Glare and Aluminium material properties, estimated using the MVF method

	Units	Glare 3-3/2-0.3	Glare 5-3/2-0.3	Al 2024-T3
ρ	(kg/m ³)	2495.0	2360.0	2780.0
σ_y	(MPa)	305.8	276.0	369.0
E	(GPa)	57.3	48.6	72.4

and stand off distance, shown in Eq. 3.21.

$$\phi_{qt} = \frac{I \left(1 + \ln \frac{4wl}{\pi d^2}\right)}{2h^2 \left(1 + \ln \frac{2S}{d}\right) (WL\rho\sigma)^{1/2}} \quad (3.21)$$

S is the distance that the blast wave has to travel before it impinges onto the edge of the panel and α_q is known as the non-dimensional impulse.

The characteristic stress used in Eq. 3.19 to Eq. 3.21 is defined as the static yield stress for monolithic metal plates, however it has also been defined as the global ultimate tensile strength for locally loaded thermoplastic-based FML panels [14] due to the different stress-strain behaviour of the component materials. The relative proportions of metal and composite were used to compute "smeared" average values for stress and density. Following the approach taken in [16], smeared stress and density values for Glare 3 and Glare 5 were calculated based on the MVF method and the properties of the component materials given in Table 3.4.

The results from the parametric blast study were converted to dimensionless form and displayed graphically as displacement-thickness ratio versus dimensionless impulse, as shown in Fig. 3.16. It is evident that the Glare 5 panels exhibit a smaller normalised displacements (approximately 11% lower) than the monolithic aluminium plates for a given dimensionless impulse.

The case study highlights the favourable resistance of Glare compared to its metallic counterpart. The set-up of the small-scale blast trials, from the kinematic boundary conditions of the panel to the blast load response were well defined and controlled which greatly facilitated the computational effort. Such blast trials are a useful precursor study in the early stages of blast mitigation which allows the structural analyst to determine the feasibility of implementing new structural materials; vulnerable to acts of sabotage or high strain rate events. Naturally, the next phase of the chapter is to consider blast loading conditions which are reminiscent of IEDs (which are non-uniform in a temporal and spatial dimension) using more advanced computational techniques which are discussed in the following section.

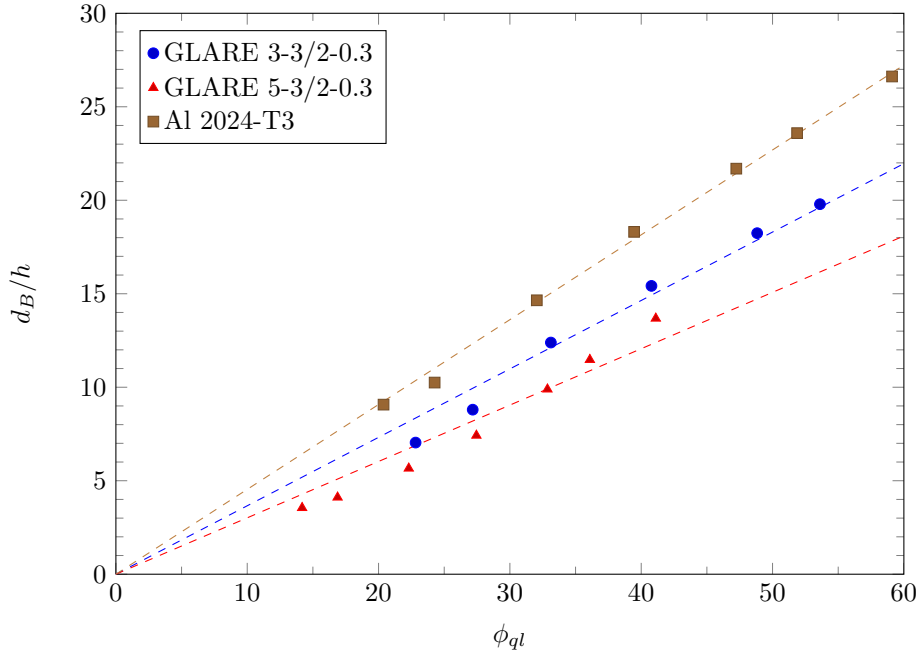


FIGURE 3.16: Graph of normalised mid-point back face deflection versus dimensionless impulse

3.3 Numerical analysis of blast-induced wave propagation using FSI and ALE multi-material formulations

The pressure imparted on the target surface will depend on the shape of the explosive, stand-off distance and angle of incidence. In such cases, simple pressure functions are not appropriate and may produce conservative results. Slightly higher fidelity could be gained using empirical blast load functions such as the ConWep algorithm [55] which is also implemented in the commercial finite element (FE) code LS-DYNA based on work done by Rahnders-Pehrson and Bannister [25, 56]. This makes it possible to simulate blast loads acting on structures representing spherical and hemispherical explosive shapes of TNT with reasonable computational effort. The ConWep blast model has produced satisfactory results, as shown by Neuberger et al. [57], where a good agreement between numerical simulation predictions of mid-point deflections and test results was obtained. However, other authors have produced negative results such as Forghani et al. [58], who showed that the experimentally determined mid-point velocities were underestimated by the predictive model.

In situations where the set-up of the problem makes it unsuitable to use empirical load functions, an alternative approach may be to use the multi-material Arbitrary Lagrangian Eulerian (MMALE) approach to simulate the shock wave phenomenon of an air-blast event. Air and the detonation products may be described with an Eulerian

formulation in a gaseous domain, while the structure response is treated in a structural domain. A coupling algorithm for the fluid-structure interaction is then used to connect the two domains. This has been performed, for example by Soutis et al. [59] who investigated the response of closed cylindrical barrels subjected to an internal blast load of different longitudinal lengths and pre-pressurisation conditions. The numerically obtained internal energies were then used to provide a qualitative discussion on the expected extensive structural damage of pressurised cylindrical structures to blast loading.

The objective of this section is to develop efficient and reliable predictive techniques which can accurately model the dynamic behaviour of Glare. Case studies of Glare panels subjected to a blast-type loading for which experimental data on the back face-displacement and post-damage information is available for model validation. A comparison between the MMALE approach and the less computationally expensive ConWep algorithm is performed to determine the suitability and performance of each method.

3.3.1 Far-field blast tests

Within the EU-funded VULCAN programme (AST5-CT-2006-031011), three aerospace structural materials were selected for blast assessment using small-scale blast trials, see Table 3.5 [17]. In addition to providing an early indication of the most promising solutions, the small-scale trials provided valuable experimental data for model validation. The relative performance of the candidate materials was assessed in terms of the threshold charge weight for a fixed stand-off distance, defined as the charge weight of explosive required to cause maximum damage without through-thickness rupture. Small-scale testing was undertaken using 800 mm \times 800 mm fully clamped targets. The relative level of resistance to blast loading was assessed on a thickness by thickness basis, against a benchmark 1.7 mm Glare 3 laminate with an areal density of approximately 4.35 kg/m². In order to replicate the highly focussed loading associated with an on-board explosion event and minimise the influence of boundary effects, a stand off distance of 200 mm was employed, as illustrated in Fig. 3.17. The level of blast loading was controlled by varying the mass of the spherical charge.

The results of the small-scale blast tests, shown in Table 3.5, reveal that for a given explosive charge weight, Glare 3 panels outperformed Aluminium 2024-T3 and CFRP panels. The Aluminium plates indicated a failure limit between 80g and 85g. For Glare, the authors claim a failure limit greater than 150g C-4, although pulling-in of the panel edges was reported, which was proceeded by some tearing of the bolt holes. This

TABLE 3.5: Summary of small-scale-blast trial results for various targets [17].

Material	Charge mass				
	50g	75g	85g	100g	150g
Aluminium 2024-T3	✓	✓	✗	-	-
CFRP	✗	-	-	-	-
Glare 3-3/2-0.4	✓	✓	✓	✓	✓

✓ no through-thickness rupture (pass), ✗ fully ruptured target (fail)

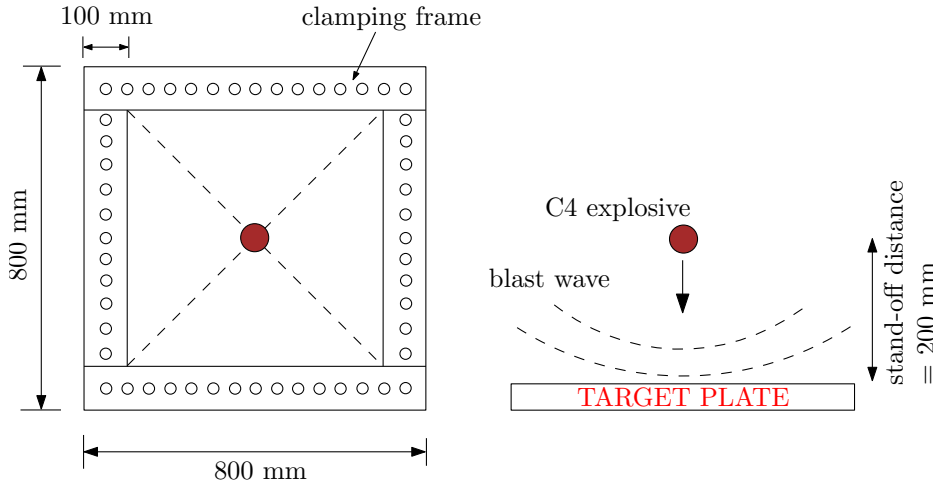


FIGURE 3.17: Small-scale test used to assess relative blast resistance of typical aircraft materials ([17])

raises doubts about the load charge required to cause through-thickness rupture as these features may have delayed the onset of tearing at the clamped boundary conditions.

3.3.2 Lagrangian formulation

This study was conducted within the framework of the VULCAN consortium where the FE code of choice was LS-DYNA, a commercially available explicit code developed by Livermore Software Technology Corp and is widely distributed and used in industry and academia [25]. Therefore from this point forth, LS-DYNA is used for all numerical studies ¹.

One of the areas of interest in this study is to investigate the severity of interlaminar delamination under blast loading conditions. Therefore, a multi-layer shell element model with cohesive tie-break capabilities was developed to simulate the hybrid composite target. As the mechanical properties of Glare vary between each subsequent layer, a unique

¹Please refer to Appendix A for further discussion and comparison of ABAQUS/Explicit and LS-DYNA.

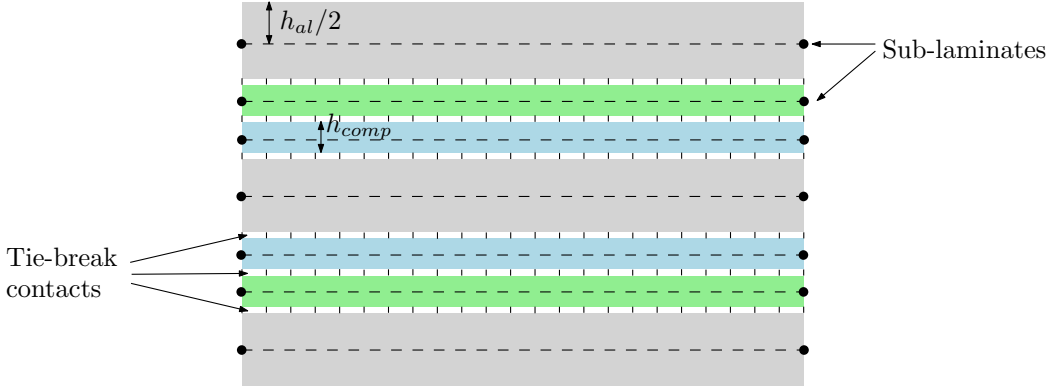


FIGURE 3.18: Multi-layered modelling approach of contact tie-break algorithm

layer of fully integrated shell elements (Type 16) was defined to represent the 7 plies with four integration points associated with each layer, as shown in Fig. 3.18.

3.3.3 Interlaminar delamination

Cohesive tie-break algorithms [60] available in LS-DYNA are employed to model interlaminar delamination between the metal/composite and composite/composite interface [25], as shown in Fig. 3.18. Tie-break contacts are penalty-based algorithms which model the connections of surfaces, allowing the transmission of both compressive and tensile forces (*a tie*). Before failure, the tie-break contact works by resisting the separation of the slave node from the master segment. After failure, the tensile coupling is removed and the contact behaves in a traditional surface to surface contact with thickness offsets. Additionally, all tie-break contacts have an optional failure criterion depending on the nature of the connection. In this study, to simulate interlaminar debonding the *CONTACT_AUTOMATIC_SURFACE_TO_SURFACE_TIEBREAK - DYCOSS Option 9 was chosen [61]. This cohesive contact criteria are based on the cohesive fracture model defined in *MAT_138 (COHESIVE_MIXED_MODE) [25]. This card includes a bilinear traction-separation law with quadratic mixed mode delamination criterion and a damage formulation [25]. In the interface cohesive model, the ultimate displacement in the normal and tangential directions are the displacements at the time when the material has failed completely. The bilinear traction-separation law gives a linear stiffness for loading followed by the linear softening during the damage and provides a simple relationship between energy release rates, the peak tractions and the ultimate displacements [25]:

$$G_{IC} = \frac{T_N \cdot \delta_I^f}{2} \tag{3.22a}$$

$$G_{IIC} = \frac{T_T \cdot \delta_{II}^f}{2} \tag{3.22b}$$

where T_N is the peak traction in normal direction, T_T is the peak traction in tangential direction, δ_I is the ultimate displacement in the normal direction, δ_{II} is the ultimate displacement in the tangential direction, G_{IC} is the mode I energy release and G_{IIC} is the mode II energy release rate.

If the peak tractions are not specified they can be computed from the ultimate displacements. In the cohesive material model, the total mixed mode relative displacement δ_m is defined as $\delta_m = (\delta_I^2 + \delta_{II}^2)^{1/2}$, where $\delta_I = \delta_3$ is the separation in normal direction (mode I) and $\delta_{II} = (\delta_1^2 + \delta_2^2)^{1/2}$ is the separation in tangential direction (mode II). The mixed mode damage initiation displacement δ_0 (onset of softening) is given by

$$\delta^0 = \delta_I^0 \delta_{II}^0 \left[\frac{1 + \beta^2}{(\delta_{II}^0)^2 + (\beta \delta_I^0)^2} \right]^{1/2} \quad (3.23)$$

where $\delta_I^0 = T/K_N$ and $\delta_{II}^0 = S/K_T$ are the single mode damage initiation separation lengths, K_N is the stiffness normal to the interface plane, K_T is the stiffness into the interface plane and β is the 'mode mixity'. The ultimate mixed mode displacement δ_F (total failure) for the Benzeggagh-Kenane law is

$$\delta_F = \frac{2}{\delta^0 \left(\frac{1}{1+\beta^2} K_N + \frac{\beta^2}{1+\beta^2} K_T \right)} \left[G_{IC} + (G_{IIC} - G_{IC}) \left(\frac{\beta^2 K_T}{K_N + \beta^2 K_T} \right)^{XMU} \right] \quad (3.24)$$

where XMU is the exponent of the mixed mode criteria. The effect of contact parameters on the dynamic behaviour of seven-layered Glare 3 panels was investigated and discussed in the results section. A maximum nominal stress of 60 MPa was assumed and an interlaminar fracture energy of 2.5 N/mm was chosen [62].

3.3.4 Blast pressure characterisation

The initial detonation and subsequent blast wave propagation which impinges and interacts with boundaries is a complex process. It is well known that the detonation of the explosive creates a shock wave in the surrounding fluid, which is known as a blast wave. The fluid (air) applies a very short but intense pressure field whose shape depends on the explosive geometry, its chemical composition, its distance from the structure and the fluid properties such as density and wave speed. When the explosive is detonated, its volume expands significantly and moves outwards with a velocity that is initially close to the detonation velocity of the explosive (7-10 km/s). The radially expanding shock wave interacts with the structure and the surrounding fluid. The blast wave produced is characterised by an extremely high peak pressure and short duration, see Fig. 3.19.

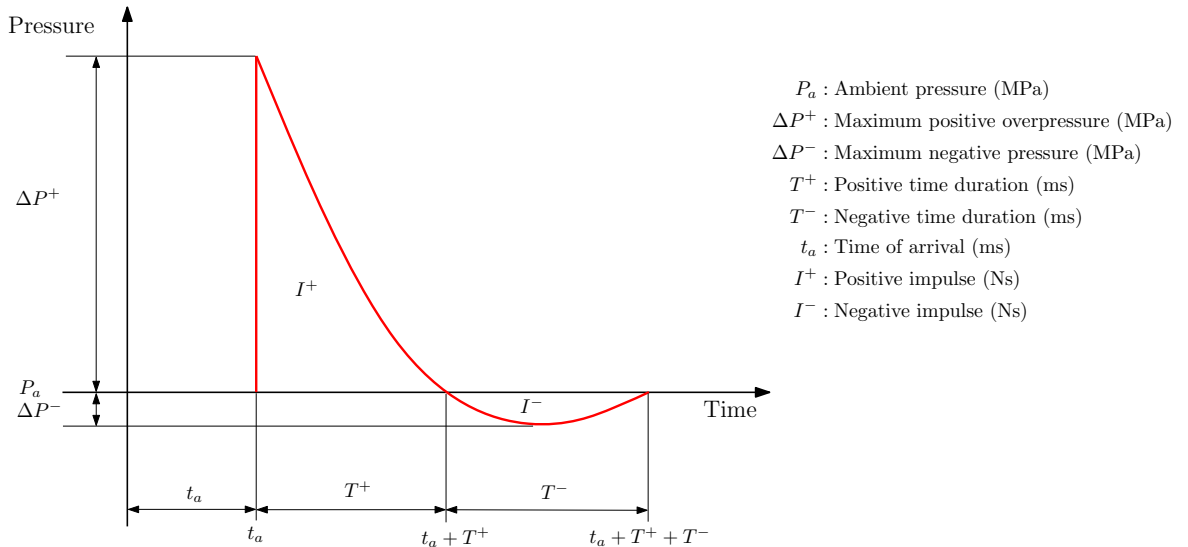


FIGURE 3.19: Typical pressure-time history. At the arrival time, following the explosion, the pressure suddenly increases to a peak pressure value. The pressure then decays to an ambient level at time $(t_a + T^+)$ and decays further to an under-pressure (creating a partial vacuum) before returning to ambient conditions at time $(t_a + T^+ + T^-)$.

Two approaches were used to simulate the blast loads: a Lagrangian model with ConWep load function and a multi-material ALE (MMALE) model. The latter was performed for the 75g load case only due to the computational effort and time this formulation imposes on the numerical analyst.

3.3.4.1 Empirical blast load

A comparison with the aforementioned MMALE model is made with the less computationally expensive ConWep algorithm [63]. This enables an opportunity to simulate and compare blast loading on a Lagrangian structure without having to simulate the blast load in an Eulerian domain. In LS-DYNA, based on user input parameters regarding the location and mass of the explosive charge, ConWep automatically calculates the correct distance and angles of incidence and assigns pressures accordingly to the surface of the target.

Most semi-empirical models, such as ConWep, of free-field blast express the data with reference to the blast output of TNT. Different explosives are generally compared by means of their TNT equivalency both in terms of peak pressure and impulse. The TNT equivalency of an explosive is the ratio of the mass of TNT to the mass of the explosive such that both yield equal pressure or impulse. It is known that 1 kg TNT releases the energy of 4.520×10^6 J. The TNT equivalent is available for standard explosives, some of which are summarized in Table 3.6. The TNT equivalency of C-4 is not unique and

TABLE 3.6: TNT equivalency for different explosives. C-4 explosive used in this study is highlighted in grey

Explosive	Mass specific energy (kJ/kg)	TNT equivalency
TNT	4520	1
Torpex	7540	1.667
C-4	6057	1.37
Semtex 1A	4980	1.102

typically varies from 1.15 to 1.6 depending on how it is measured. As a reference, an equivalency of 1.37 for pressure and 1.19 for impulse is used [63].

The pressure load which acts on a set of pre-defined segments, i.e. a surface of solid elements or shell elements acts on a segment account for angle of incidence of the pressure wave, θ , is determined according to:

$$p = p_i (1 + \cos\theta - 2\cos^2\theta) + P_r \cos^2\theta \quad (3.25)$$

where p_i is the incident pressure and p_r the reflected pressure [56]. The blast load corresponds to a free air detonation of a spherical charge with a TNT weight equivalence of 1.3 to account for the C-4 explosive charge. The blast pressure profile generated by the ConWep algorithm at different locations of the plate, corresponding to a C-4 charge of 50g is shown in Fig. 3.20. A comparison of the maximum overpressure predicted by the ConWep algorithm for 50g, 75g, 100g and 150g C-4 charge is given in Fig. 3.21. The delay in the pressure-time plots reflect the time taken for the blast wave to arrive at the plate surface after the explosion is initiated.

3.3.4.2 MMALE model

In MMALE approach, both a Lagrangian (Glare 3 target) and an Eulerian (air + explosive) domain are simulated, together with a coupling algorithm for fluid-structure interaction (FSI). The composite target is modelled in quarter symmetry, while the explosive and air (solid ELFORM=1) is represented in 1/8 symmetry. As shown in Fig. 3.22, symmetry conditions for the 3D gas domain illustrates where the three symmetry planes are defined; at the bottom of the model and the two planes along the centre axis of the explosive. The 75g spherical C-4 charge (radius 2.2 cm) is modelled with 1,764 hexahedral finite elements and is ignited at its centre. The spherical charge is surrounded with the air mesh so there is one-to-one node match at the boundary between the explosive and the air. Non-reflecting boundary conditions are also imposed on the outer lateral and top boundaries to prevent artificial pressure wave reflections generated

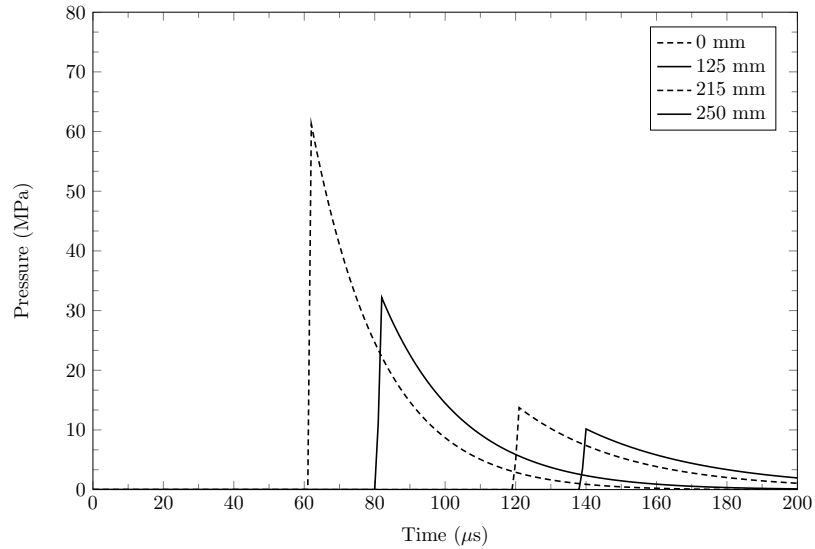


FIGURE 3.20: Radial distribution of peak pressure-time pulse generated by the ConWep model (radial distances r from the center) corresponding for a charge of 50g C-4 at a stand-off distance of 200 mm

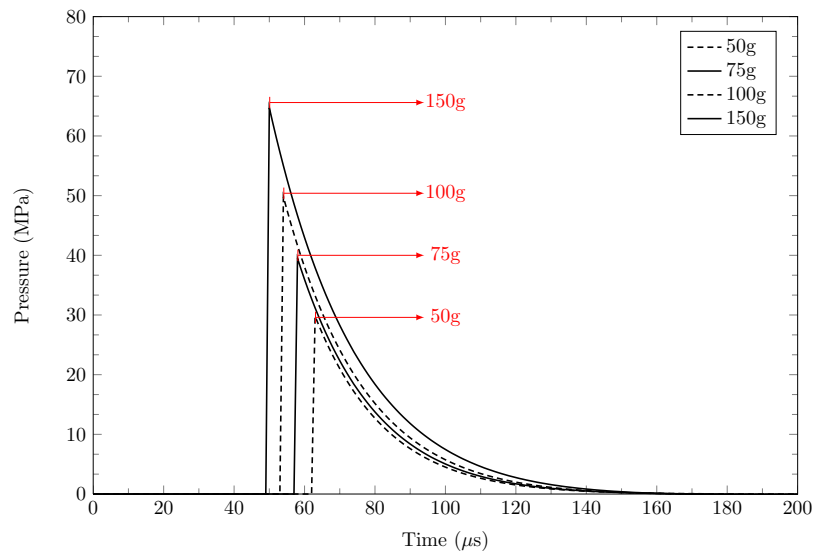


FIGURE 3.21: Blast pressure curves for 50g, 100g and 150g C-4 charge predicted by ConWep model

at the model boundaries from re-entering the model and contaminating the results. The boundary conditions for the plate are considered as being perfectly clamped.

The TNT explosive charge was modelled via *MAT_008 (HIGH_EXPLOSIVE_BURN) and the Jones-Wilkins-Lee (JWL) semi-empirical equation of state (*EOS_JWL) [25]. The pressure field is given by:

$$P = C_1 \left(1 - \frac{\omega}{R_1 V}\right) e^{-R_1 V} + C_2 \left(1 - \frac{\omega}{R_2 V}\right) e^{-R_2 V} + \frac{\omega E_0}{V} \quad (3.26)$$

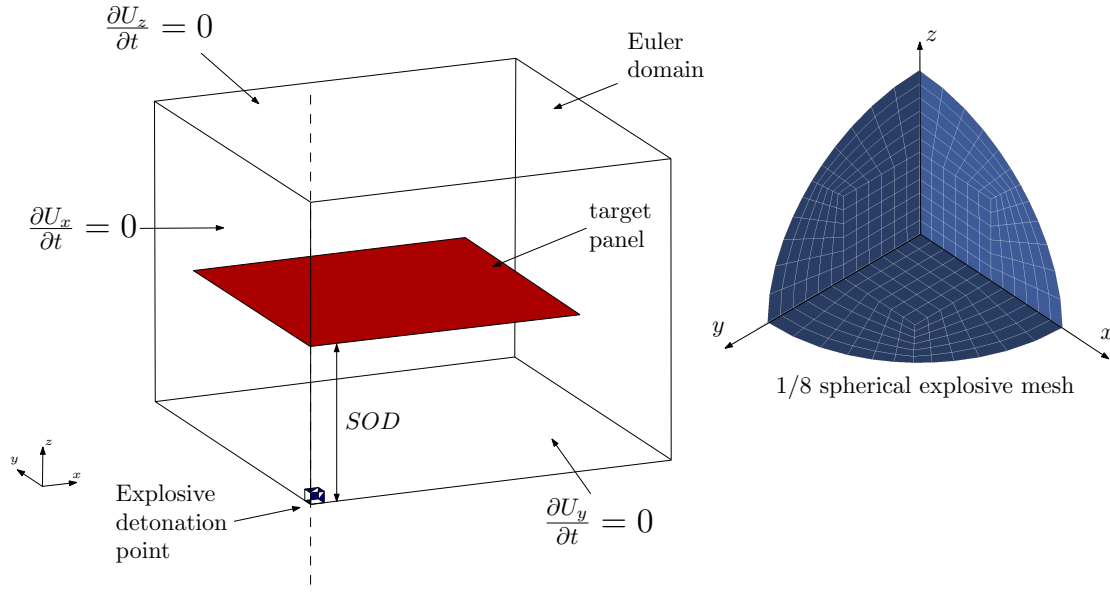


FIGURE 3.22: Description of MMALE arrangement of Glare flat panel simulation

where $C_1, C_2, R_1, R_2, \omega$ are material constants: their values C-4 (explosives), according to Alia and Souli [64] are presented in Table 3.7. $V = v/v_0$ is the relative volume of the gas products to the initial explosive state, and E_0 is the energy per unit volume.

The medium in which the blast wave propagates (air) was modelled with *MAT_009 (NULL) and a linear polynomial EOS (*EOS_LINEAR_POLYNOMIAL) for linear internal energy. Pressure for a perfect gas assuming the gamma law EOS was used which simplifies to:

$$P = (\gamma - 1) \frac{\rho}{\rho_0} E_0 \quad (3.27)$$

where ρ is the current density, and ρ_0 the initial density while E_0 is the internal energy per unit reference volume. Also γ is defined as the ratio between the specific heat at constant pressure and volume, respectively. Specific heat capacities are functions of temperature and pressure which can give rise to significant errors if the temperature range of the process it pertains is ignored. It is assumed that $\gamma = 1.4$ is a constant during the explosive event. This rather restrictive assumption can be problematic for explosives which expel large pressures and higher temperatures. Under such conditions, the air starts to ionize and dissociate, and the property of the gas changes so that the ratio of specific heats is no longer a constant [65]. However, without the knowledge of the dependence of specific heat capacity on the overpressure for a given load case, a constant value is assumed. With initial density 1.2 kg/m^3 , the initial pressure is 1 bar which results in an initial internal energy E_0 of 250 kJ/m^3 . Additional parameters such as density, a pressure cut-off and viscosity coefficient (within the *MAT_NULL card) are also required for complete definition of the air medium. The viscosity and pressure

TABLE 3.7: Explosive parameters used in air-blast simulations, C-4 explosive properties taken from [64](mm, kg, ms)

ρ (kg/m ³)	D (m/s)	P_{CJ} (GPa)	C_1 (GPa)	C_2 (GPa)	R_1 (-)	R_2 (-)	ω (-)	E_0 (GPa)
1601	8040	29.5	598.155	13.75	4.5	1.5	0.32	8.7

TABLE 3.8: Air parameters used in air-blast simulations

ρ_0 (kg/m ³)	γ (-)	T_{ref} (K)	C_p (kJ/kg K)	E_0 (kJ/m ³)
1.22	1.4	288.2	1.012	250

cut-off are set to zero because it cannot be negative and the viscosity forces are assumed equal to zero, see Table 3.8 for details.

FSI is simulated using a coupling algorithm within the *CONSTRAINED_LAGRANGE_TO_SOLID card in LS-DYNA. The FSI thus couples the blast pressure of the moving fluid and the deformation of the composite structure. The penalty-based coupling algorithm is used in this study, which conserve internal energy rather than momentum. This formulation applies nodal forces explicitly by tracking the relative motion of a given point [66]. The purpose of using these algorithms is so that the fluid material, i.e. shock wave, flows around and along but not through the structure. During the course of the simulation, if a fluid particle should penetrate through a Lagrangian mesh, a resisting force is applied to both the fluid particle and the structure node to prevent penetration from occurring. The penalty method applies a resisting force to the slave node, proportional to the penetration, through the mesh segment [67]. Poor definition of parameters within this card may result in large non-physical interface (sliding) energy which is not only dependent on the penalty stiffness, but also the leakage control and the time step (TSSFAC). Material transport in the MMALE elements is controlled by the first order (donor cell) advection technique defined in the *CONTROL_ALE card.

Table 3.9 provides details of the numerical components employed in this study.

3.3.5 Results and discussion

3.3.5.1 Calibration of contact parameters in tie-break cohesive algorithm

A sensitivity study was conducted to investigate the effect of the tie-break on the dynamic behaviour of laminated systems and hence develop a model whose response is independent of the number of sub-laminates. To eliminate uncertainties involving the

TABLE 3.9: Model details for the air blast simulations

Part	Material	Element type	Element length (mm)	No. of elements	Model size		
					X-dir (mm)	Y-dir (mm)	Z-dir (mm)
Target plate	Glare	Shell	10	864	300	300	0
Euler domain ^b	Air	MMALE	3 ^a	172,368	400	400	300
Euler domain ^b	Explosive	MMALE	1.8 ^c	1,764	22	22	22

^a Minimum element size at the radius of explosive

^b Omitted for ConWep blast loads

^c Minimum element size

blast pressure phenomena, a uniformly distributed triangular pressure pulse is applied for simplicity:

$$p(t) = \begin{cases} p_0 \left(1 - \frac{t}{t_0}\right), & 0 \leq t \leq t_0 \\ 0, & t \geq t_0 \end{cases} \quad (3.28)$$

where p_0 is the peak pressure and t_0 is the load duration. In this example the panel was subjected to a triangular pulse of 17.3 MPa ($t_0 = 0.05ms$), which is the equivalent to an impulse of 156 Ns. When the blast wave drops to zero upon reaching the blast duration, t_0 , momentum is transferred to the panel, which has become impulsively loaded with a uniformly distributed velocity field. Conservation of momentum gives the initial velocity of the panel as:

$$v_i = \frac{p_0 t_0}{2(\rho_{comp} h_{comp} + \rho_{al} h_{al})} \quad (3.29)$$

where $\rho_{comp,al}$ and $h_{comp,al}$ are the density and thickness of the composite and aluminium layers respectively. For an impulse of 17.3 Ns, the initial velocity of the panel is calculated as 99 m/s. The maximum back face velocity is extracted from the numerical analysis, as a method of verifying if momentum is being transferred from the front face to the back. The plate is modelled using one and seven layers of shell elements tied together with the tie-break interface, see Fig. 3.18.

It can be seen from Fig. 3.23 that the back-face velocity depends on the penalty scale factor for the tie-break algorithm. When the default penalty stiffness factor of 0.1 is used, the back-face velocity deviates from the expected value giving spurious oscillations which does not converge. The reason for this is that the default value of the penalty stiffness is not enough to 'tie' the layers together, i.e. the layers do not move together. The momentum of the blast load is transferred from one layer to another sequentially. Thus, instead of the structure carrying the momentum together, the momentum is carried by the first layer and then transferred to the second layer up to the last layer. Consequently,

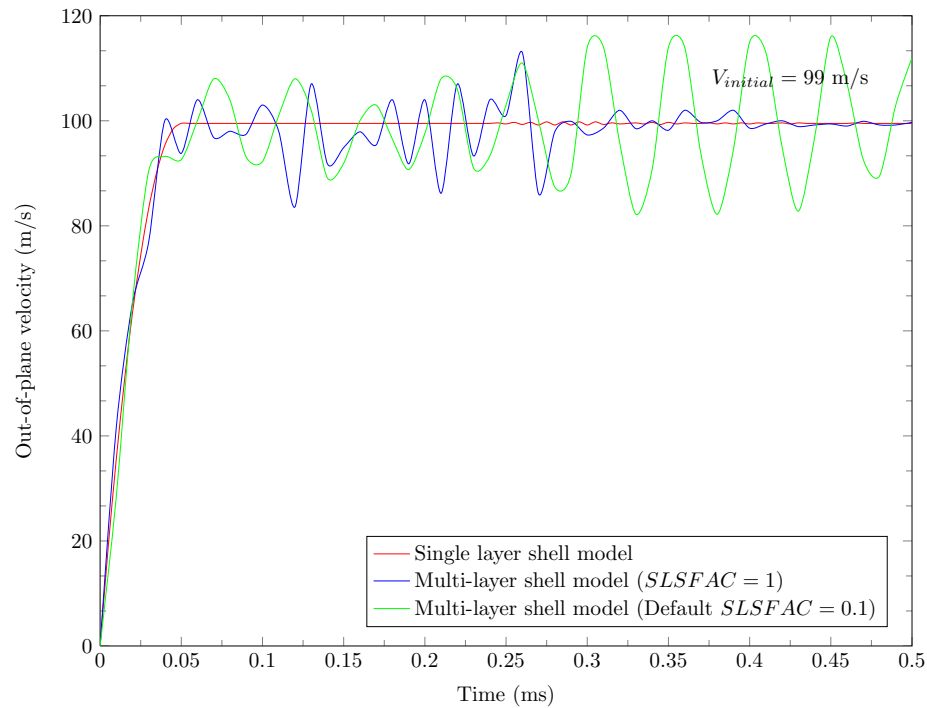


FIGURE 3.23: Comparison of velocity profile for FML panel under pressure-pulse loading for one and multiple layers. SLSFAC is the scale factor for sliding interface penalties

the maximum velocity of each layer will depend on the amount of transferred momentum and the mass of each layer. This effect is eliminated when a penalty stiffness factor of 1 is used.

3.3.6 Interaction results of Glare subjected to blast loading

This section presents the numerical results for the air blast events, where the blast loads have been calculated using the empirical blast function, ConWep for the 75g and 100g C-4 load charge. The simulation cases with results regarding the maximum mid-point deflections, δ_{max} for the air blast simulations are shown in Table 3.10.

A comparison between the numerical simulations with the experimental maximum mid-point deflection is also shown in Fig. 3.24. The numerically determined quantities show a difference of 1-5 % compared to the experimental quantity, which shows that the two results are in good agreement.

Fig. 3.25 shows the time-history of the transverse velocity at the centre of each aluminium layer for an explosive charge of 100g C-4 and stand-off distance of 200 mm. The structural response, in terms of transverse velocity, has been assessed for this load case which can be described in three phases. The first phase begins during the first 2.5 ms when the blast shock wave strikes the Glare panel. In this phase, the dynamic

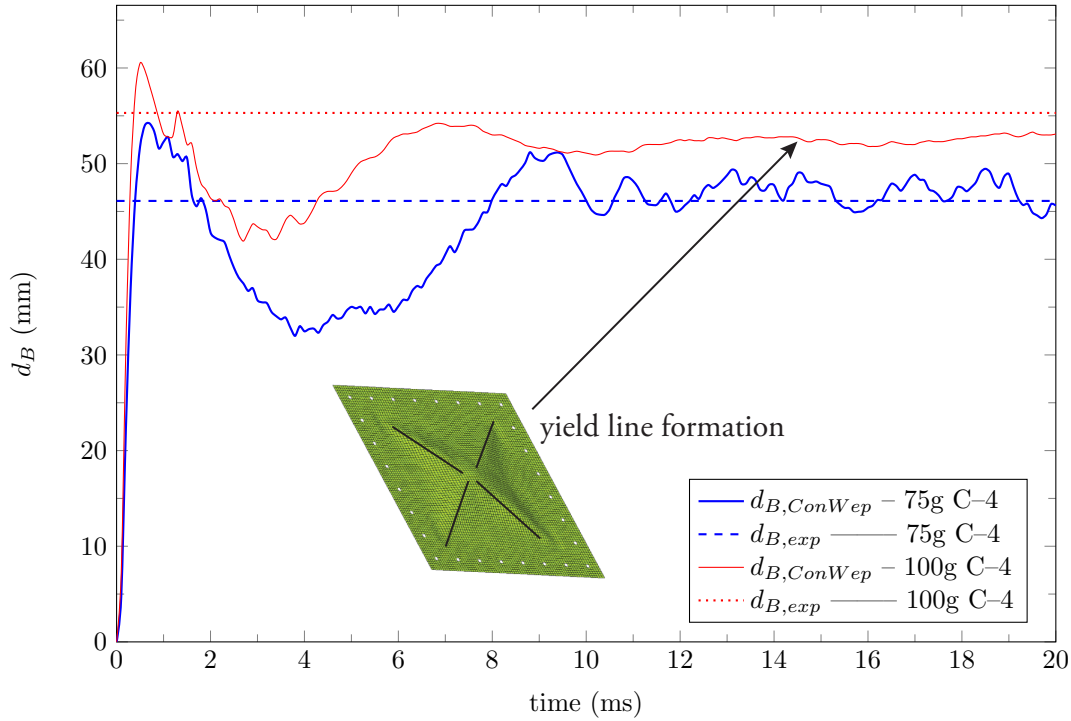


FIGURE 3.24: Numerical predictions of mid-point deflection of Glare panels subjected to 75g and 100g C-4 explosive charge relative to the experimental results [17]

response is governed by the balance of the momentum induced by the blast. As shown in Equation 3.29, the velocity of the system strongly depends on the thickness of each constituent layer and corresponding densities, and the intensity of the blast shock wave.

The second phase starts about 2.5 ms after the blast hits the plate. In this phase, due to the deformation of the plate, strains and consequently stresses develop and the structure starts to resist the blast loads. The velocity reduces (giving negative accelerations) and deflects contrary to the deflection of the blast wave. This is mainly due to the elastic contribution of the glass-fibres which are resisting the blast load. There is only enough energy for a couple of vibratory oscillations of the panel.

The final phase begins about 6 ms after the blast initiation, at which point the blast load has totally decayed to zero, and the panel is regaining some structural stability and reaching its permanent deflection (i.e. zero velocity).

To investigate and quantify the energy absorbing mechanisms in the FML system, the time histories of the total delaminated area and dissipated interlaminar energies for each tie-break contact were written to a text file. The time histories of total delaminated area for each tie-break contact followed by slave node data (damage, mode-mixity and stresses) for a 100g C-4 charge is given in Fig. 3.26. Interface **1** is the first tie-break interface located towards the bottom of the panel (blast loaded face) and interface **6** is

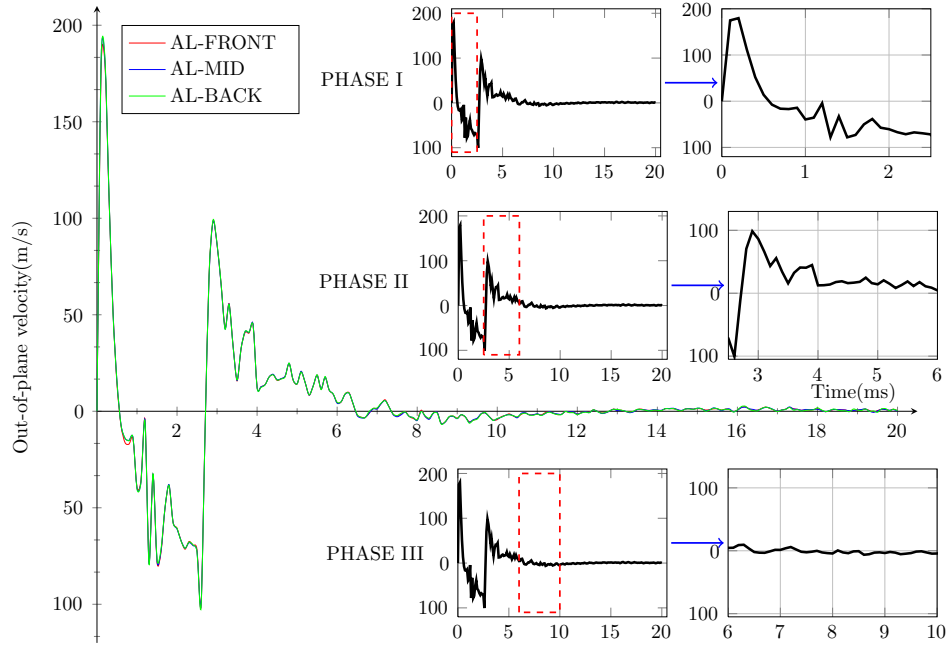


FIGURE 3.25: Mid-point transverse velocity of each Aluminium layer of Glare 3 panel subjected to 100g C-4 charge at stand-off distance of 200 mm

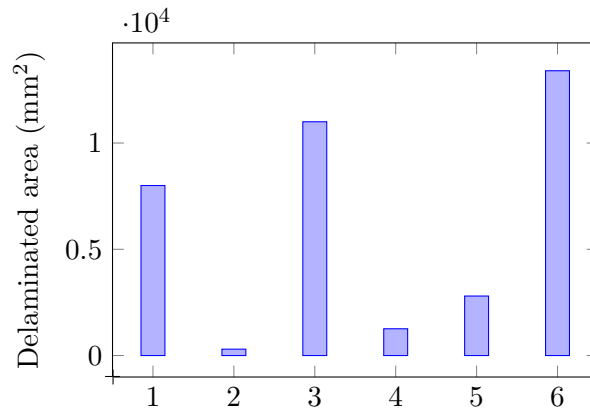


FIGURE 3.26: Plot of delaminated area for each tie-break interface, where 1 is first tie-break interface located at the front of the panel (blast loaded face) and 6 is the back

the last sub-laminate at the top of the panel (distal face). It is apparent that the back and middle layers debonded the most, compared to the front layers which experience the blast load more severely. An explanation for this however may arise from the fact that the shock wave initially propagates as a compression wave through the multi-layered material which is subsequently reflected as a tensile wave, resulting in the debonding of the back-layers. Also, the debonded areas predicted by the simulations, shown in Fig. 3.26, cannot be compared to the experiments as no cross-sectional analysis was performed.

TABLE 3.10: Results of air blast simulations using ConWep method

C-4 charge (g)	Stand-off distance (mm)	Comparison	d_B (mm)	% difference
75	200	Experimental	46.1	1.1
		ConWep	45.6	
100	200	Experimental	55.3	3.98
		ConWep	53.1	

3.3.6.1 Energy balance

The deformations of the damaged Glare panels suggests that the energy imparted on the panel from the blast load can be dissipated in global deformation including panel bending and membrane stretching; extensive delamination within the glass/epoxy plies or debonding between the aluminium and glass/epoxy layers; and tensile fracture of the glass/epoxy and aluminium. A simple energy balance is thus given by:

$$W_{tot} = W_{bm} + W_{del} + W_{deb} + W_t + W_p \quad (3.30)$$

where W_{bm} is the strain energy and plastic work in bending and membrane stretching; W_{del} is the delamination energy within glass/epoxy layers; W_{deb} is the energy dissipated in debonding aluminium and glass/epoxy layers; W_t is the tensile fracture energy of the glass/epoxy, W_p is the fracture energy in petalling of aluminium layers (≈ 0). The results from the analysis of the 100g C-4 load case, show that the energy dissipated in interlaminar debonding was approximately 2 – 3% of the total absorbed energy.

3.3.7 Results: blast model comparison

In this section, a comparison between the two methods of describing the blast load takes place. The result from the ConWep calculations was presented in the previous section. Fig. 3.27 shows iso-surface contours of the fluid pressure at different time intervals. The blast pressure propagates outwardly in a radial manner, as expected for spherical explosives. At $t = 100 \mu s$, the point of impact of the blast wave with the composite target is clearly shown which is larger than that expected in a completely free-air blast event (the incident wave reinforced by the target surface). It is clearly shown that no fluid leakage (penetration) has occurred through the target plate which provides confidence in the implemented FSI penalty parameters within the MMALE card. Results of mid-point deflection from the air blast simulation for a C-4 charge of

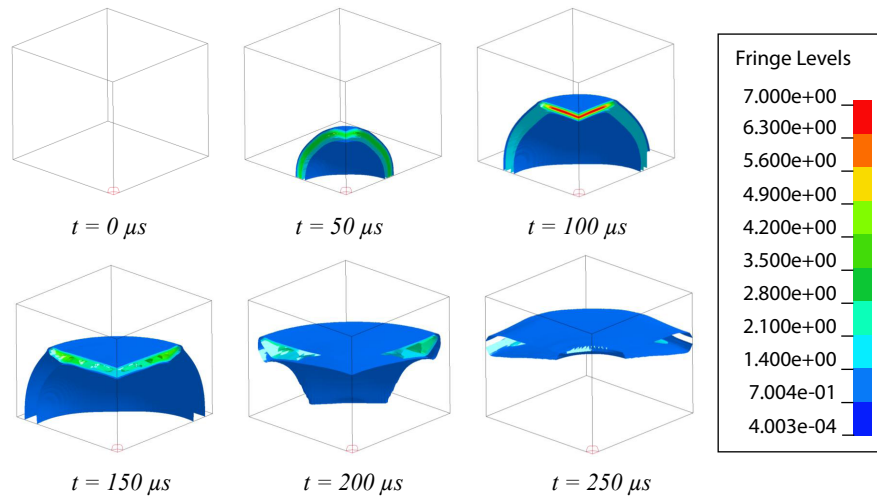


FIGURE 3.27: Contours of blast pressure wave propagation using the MMALE approach at different time intervals (fringe levels in MPa)

75g is given in Fig. 3.28, both for the Eulerian and ConWep simulations. It is shown that excellent agreement with the mid-point experimental value is obtained with the MMALE approach, with evidence of better structural stability than the ConWep approach. This may be attributed to the TNT equivalence for C-4 implemented in the ConWep blast model and stand-off distance, hence slightly over-estimating the blast pressure imparted on the composite target. Nevertheless, in terms of CPU time, the ConWep calculations results in considerably shorter CPU times, nearly 10 times faster than the MMALE approach.

3.4 Conclusions

A robust and efficient computational model has been developed in the commercial FE code LS-DYNA to investigate the structural response of fully clamped Glare panels to C-4 blast loads. Numerical model validation have been performed considering case studies of Glare panels subjected to a blast-type pressure pulse for which experimental data on the back face-displacement and post-damage observations were available. Excellent agreement of mid-point deflections and evidence of severe yield line deformation were shown and discussed against the performed blast tests. The performance of both the ConWep and MMALE methods of simulating the blast loads were also performed and assessed.

The suitability of using cohesive tie-break algorithms in blast-type problems involving hybrid composite systems was also assessed. Due to the mismatch in stiffness of the composite and aluminium layers, a penalty stiffness approach was used to ensure that

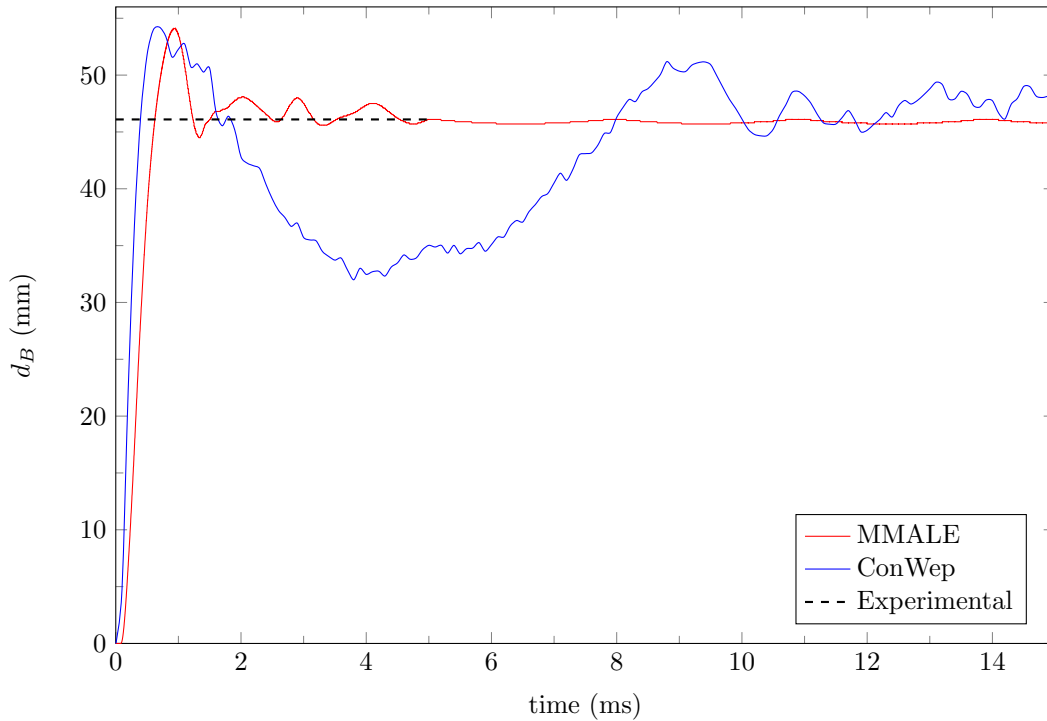


FIGURE 3.28: Comparison of mid-point deflection of Glare panels using the ConWep and MMALE approach subjected to 75g C-4 explosive charge

the panel behaved as a single unit, to ensure that momentum from the blast wave to the panel was accurately captured during the initial blast durations. A sensitivity study showed that default values would give erroneous results as the momentum transferred from the blast load would not be carried by the whole laminate; rather it is carried by one or some of the layers at any given time.

Future work should include temperature effects in the Johnson-Cook material model as thermal softening may be significant on the blast face of the panels. Of particular interest, is the effect of cabin pressurization on the elastic and plastic deformation of fuselage skin under blast loading. Cabin pressurization pre-stresses the fuselage and thus may alter the structural response to an internal explosion, work that will be discussed in the succeeding chapters. In such problems, it is the opinion of the author, that given the current modelling capabilities and results, the MMALE would give higher fidelity in capturing the complex blast wave phenomenon. However, in circumstances where the explosive charge is close to the target panel and the effect of geometrical non-linearity is minimal, the ConWep algorithm is acceptable in such cases.

Chapter 4

Performance of scaled fuselage structures subjected to blast loadings

THE purpose of this chapter is to investigate the extent of the immediate damage of scaled fuselage structures due to a bomb blast event situated near the target skin. Assessment of immediate damage was conducted using LS-DYNA models of existing fuselage demonstrator tests trials taking into account composite and metallic damage, bolted joint analysis and stiffening elements. The initial predictive fuselage data was in reasonable agreement with test data. Further analysis on Aluminium 2024-T3 tests revealed that maximum allowable charge load is approximately 50g SEMTEX. Glare 3 structures did not report such breaching or tearing of the target skin at the charge load although it was on the borderline of reaching the failure limit.

4.1 Blast performance of scaled fuselage demonstrators

The concept of hardening aircraft structures has gained momentum since the advent of lightweight but high strength composites. However, before hardening strategies can be implemented it is imperative that a comprehensive understanding of what happens when an explosive is detonated on an airplane is established. As discussed in Chapter 3, full-scale testing of realistic blast scenarios related to IEDs is often prohibitively expensive and time consuming. Practical alternatives, which can dramatically reduce the time and financial constraints to deliver results, include small-scale experiments and numerical simulation. The performance and numerical validation of small quadrangular Glare panels have been performed. However, aero-structures are very complex in structural

and material design which operate under severe dynamic environments. Thus, under assumed flying conditions it is important to understand the failure scenario and sequence of damage of an in-flight explosion for a given size and location of explosive. This will help develop survivability strategies to mitigate the effects of internal explosions with the aid of blast vulnerability maps which examine hardening options based on various failure scenarios.

In the event of an explosion, there are two issues which should be considered: One is the extent of damage immediately after the explosion and its survivability. The second, and equally important, issue is the aircraft's ability to complete the flight and land safely. These two aspects require distinct approaches and strategies which have been attempted in the past [7]. The purpose of this chapter is to investigate the former issue. Finite element models have been developed to simulate and understand the effects of bomb blast on simplified scaled aircraft structures using LS-DYNA for nonlinear transient dynamic analysis.

4.2 Description of structures

A typical aircraft fuselage shell is normally a semi-monocoque type structure composed of skin, longitudinal stringers (longerons), circumferential frames and bulkheads. A typical method of constructing an all-aluminum fuselage is to firstly arrange a series of frames in the shape of the fuselage cross section which are held in position on a rigid fixture. These frames prevent the structure from buckling and maintaining its cross section. These frames are then joined with lightweight longitudinal elements called stringers. These are in turn covered with a skin of thin aluminium sheets (typically several large sections are constructed which are then joined with fasteners to form the complete fuselage), attached by riveting or adhesive bonding. The fixture is then disassembled and removed from the completed fuselage shell, which is then fitted out with wiring, controls, and interior equipment such as seats and luggage bins.

Both monocoque and semi-monocoque are referred to as "stressed skin" structures as all or a portion of the external load (i.e. from wings and empennage, and from discrete masses such as the engine) is taken by the surface covering. In addition, the entire load from internal pressurization is carried (as skin tension) by the external skin. The frames and stringers acts as crack stoppers in the presence of multi-site damage, arresting and slowing down cracks as they reach the stiffening barriers. Reference openings such as doors, windows and escape hatches are also included in the construction of the fuselage. Furthermore, a typical fuselage structure consists of two floors. One is the passenger floor dividing the fuselage into an upper chamber for passengers and a lower chamber

for cargo. The passenger floor beams support seats tracks upon which the passenger seats are mounted. The cargo floor is a relatively rigid member. The cargo bay consists of the passenger floor on the top, a cargo floor at the bottom, right and left side wall, bulkheads at both end, and a cargo door at the right. Traditionally, aluminium has been the material of choice in airframe structure due to its excellent fatigue characteristics and favourable higher ductility.

Within the framework of the VULCAN programme, a series of scaled fuselage demonstrator tests were designed to encompass realistic structural design features which reflect commercial aircraft fuselage structures [68]. During the early stages of the programme, structural details such as flooring, luggage compartments and windows were included in the technical designs with funds assigned to meet manufacturing and labour costs. However, due to the economic climate (2009/2010) some of the technical designs were scaled back to keep operational and manufacturing costs to a minimum whilst maintaining the overall essential features, mainly the stiffening elements. Unfortunately, cutbacks in this technical work-package did exempt the proposed FML based structural designs.

Nevertheless, the final demonstrator design, albeit compromised, is shown in Fig. 4.1. It is a fully metallic structure of internal diameter 1230 mm and 1300 mm long. The skin consists of four equal quadrants of 2.2 mm thick Aluminium 7178-T63 sheets. The plates were rolled and assembled with the addition of internal and external doublers, mechanically fastened using EN6114 countersunk bolts and protruding head bolts of type EN6115. The corresponding nut fastener was chosen as ASNA2528. To reduce the stresses induced by the blast explosion at both ends of the structure, the skin is reinforced with additional aluminium sheets of 4 mm thickness. Each skin quadrant is stiffened and mechanically fastened by four 'Z' stringers of material Aluminium 7075-T73511. The rest of the framework consist of three 'L' shaped frames, each of which is manufactured as two parts, fastened together with stiffening doublers. The distance between the frames is kept to 480 mm. To offer stability to the frames and skin, cleats are fabricated and fastened to both components. Figure 4.2 and Table 4.1 provides an overview of the dimensions and part-list of each structural component. The manufacture of the demonstrators were performed at the Hellenic Aerospace Industry (HAI) facilities in Greece. Subsequent explosive testing and experimental stress analysis were performed at the testing facilities at TNO, The Netherlands.

The metallic demonstrator tests were pressurised to 2 bars and an explosive was detonated inside. A spherical explosive is placed offset from the centre of the barrel, 200 mm from the demonstrator wall, to ensure that failure is induced on one side of the wall. The explosive of choice was Semtex, an explosive which share some similarities with the previous plastic explosive C-4, such malleability. It is able to operate over a greater

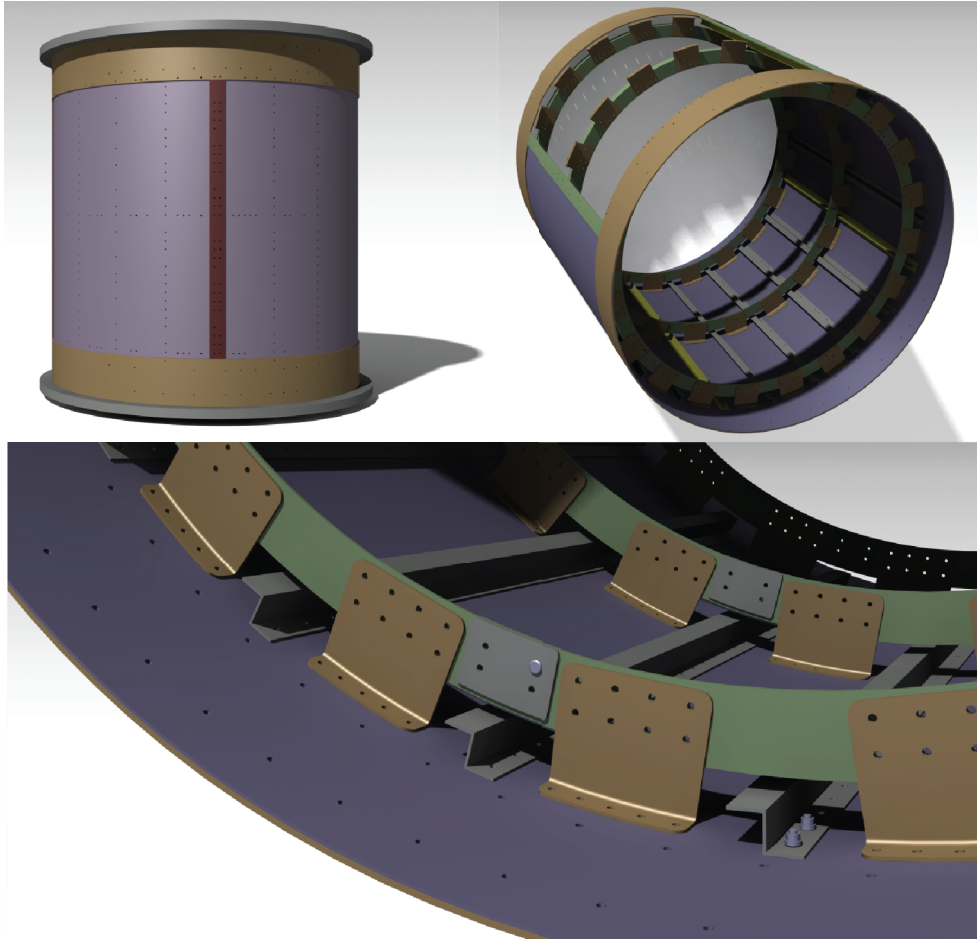


FIGURE 4.1: CAD schematic of final metallic demonstrator

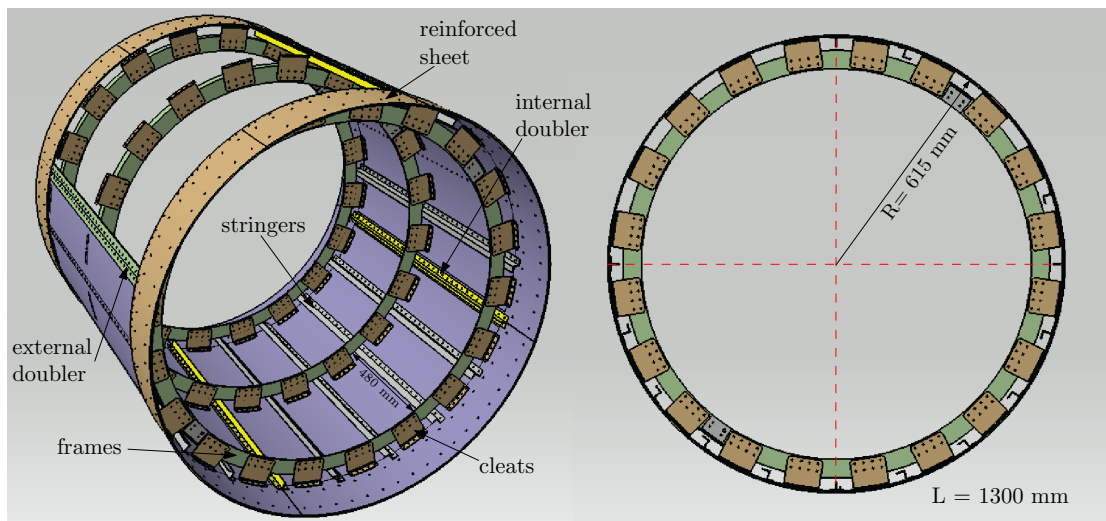
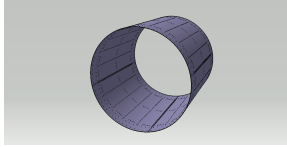
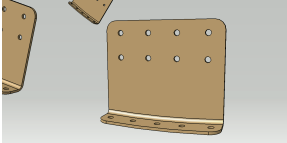
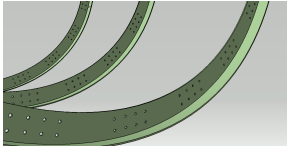
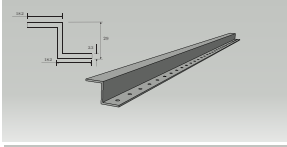
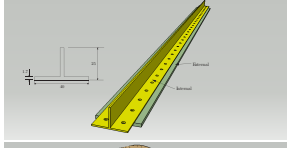

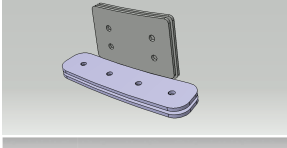
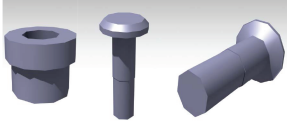


FIGURE 4.2: CAD schematic of final metallic demonstrator

TABLE 4.1: Description of structural components of metallic demonstrator

Skin		Aluminium 7178-T62 2.2 mm thick Consists of 4 equal quadrants
Cleats		Aluminium 7178-T62 2.2 mm thick
Frames		Aluminium 2024-T3 2.2 mm thick
Stringers		Aluminium 7075-T735 2.3 mm thick
Internal and external doubler		Aluminium 2024-T3 Internal :2.3 mm thick External : 4 mm thick
Reinforced sheet		Aluminium 2024-T3 4 mm thick
Frame doublers		Aluminium 7178-T62 2.2 mm thick
Nuts and bolts		Bolts: EN6114, EN6115 Nuts: ASNA 2528

temperature gradient and is waterproof. Furthermore, whereas C-4 is off-white in colour, Semtex is red or brick-orange and has a high TNT equivalency of 1.66 ($C-4=1.34$). This means that for a given mass of explosive, the intensity of the blast overpressure shock wave is different and therefore not directly comparable.

The previous small-scale tests suffered from lack of real-time data acquisition as only the post-damage state was measured. Therefore, at the testing facilities at TNO (The Netherlands), 3D measurements of surface displacements (in-plane and out-of plane displacements) during the explosive event were obtained by means of the popular optical method, Digital Image Correlation (DIC). A gray speckle pattern is applied to the target skin surface which is monitored and tracked by two cameras situated at either

side. The method tracks the gray value pattern in small neighbourhoods called subsets (pixel intensity array subsets) during deformation. This technique is predicated on the maximisation of a correlation coefficient that is determined by applying a grey speckle pattern and examining the pixel intensity array subsets (small neighbourhoods of patterns) on two or more corresponding images (undamaged and damaged state). From this data the deformation mapping function that relates the images can be extracted and interpreted in terms of displacements and strains. During the explosive event, it is anticipated that DIC will provide some insight into the magnitudes of displacement and time-dependent response. Finally, akin to the previous barrel tests, sensitive pressure gauges are placed at the top and bottom centre of the structure.

Due to unforeseeable circumstances, the skin structure was manufactured using Aluminium 7178-T63 rather than Aluminium 2024-T4 at the HAI facilities in Greece. The latter material is a high strength structural aluminium alloy which was used in the first commercially successful jetliner, Boeing 707. It was concluded that this particular Aluminium grade was prone to stress corrosion cracking, particularly in thick mill products, which inhibited its use in future fuselage applications. However, these design modifications do not deter from the original objectives of this thesis as the tests are a benchmark to which qualitative and quantitative data on failure modes and structural dynamic behaviour can be derived and compared *a posteriori* with the simulations. Further simulations can therefore be performed on Aluminium 2024-T3 and GLARE 3 systems without the need to undertake further experimental tests.

4.3 Description of finite element models

This section covers the development of finite element models used for the analysis. The LS-DYNA model, based on the aforementioned demonstrator design, is a global lagrangian model for the construction of the vulnerability map to study the overall behaviour of the structure after the explosion.

4.3.1 LS-DYNA global lagrangian model

The metallic demonstrator was modelled using approximately 360,000 quadrilateral fully integrated shell elements (Type 16) with an average element size of approximately 5 mm x 5 mm. The demonstrator is fixed at both ends via thick steel end caps which are assumed to remain rigid through the simulation.

Aluminium 7178-T62 and 7075-T735 do not exhibit strong strain-rate sensitivity, and, as a result, strain rate hardening has a minimal influence on the material flow stress.

TABLE 4.2: Johnson-Cook material model parameters for Aluminium 7178-T62 & 7075-T73 [69, 70]

Property	ρ	ν	E	σ_y	B	n	C	m	T_0	T_{melt}
Units	kg/m^3	(-)	GPa	MPa	MPa	(-)	(-)	(-)	$^{\circ}K$	$^{\circ}K$
Al 7178-T62	2830	0.33	71.7	538	200	0.2	0	-	-	-
Al 7075-T73	2780	0.33	71.0	434	303.58	0.390	0	-	-	-

For this reason, the power-law (first term) expression of the Johnson-Cook law is solely used which is expected to perform comparably to the full strain-rate formulation. The Aluminium 7178-T62 skin part of the structure fail when the effective plastic strain, $\bar{\epsilon}_f^p$, reaches 10% [69]. Input constants are summarized in Table 4.2.

The main structure consists of four parts: the skin and frame model, connecting cleats and the longeron components. The four models are combined together, but the nodes are not equivalenced. Shear clips (cleats) are made of Al 7075-T6 and their function is to connect the skin and the frames by means of rivets. The external and internal doubler and stringer are also connected to the skin by means of rivets. The mechanically fastened joints were modelled based on a tie-break contact algorithm with a force based failure criteria in shear and tension satisfying the following criterion:

$$\left(\frac{f_N}{NFLF}\right)^2 + \left(\frac{f_S}{SFLF}\right)^2 \geq 1 \quad (4.1)$$

where f_N and f_S are the developed normal and shear forces respectively and NFLF and SFLF are the corresponding failure forces. The NFLF failure force was set to a value of 2.16 kN and the SFLF failure force to 2.58 kN with these values retrieved from [5].

The joints described above are primarily permanent fasteners such as rivets. The main disadvantage of these joints is that the tensile and fatigue strengths of rivets are lower than bolts and screws. Therefore high tensile loads may pull out the clinch, or severe vibrations may loosen the fastening. When a blast pressure is applied on the walls of the skin, essentially a large tensile force is applied to the rivets, possibly causing the rivets to fail in succession (unzipping effect).

The concept of the vulnerability map is based on the premise that the vulnerability of the structure varies depending on the location and size of the explosive charge. Associated with a fixed point in the structure, a charge size that triggers failure when exploded is the basis for the vulnerability map. This model is intended for analysing global effects on the aircraft such as overall stress/strain distribution, deformation pattern and generating a vulnerability map. This overall behaviour of the structure for post explosion flight can be well simulated using the global model.

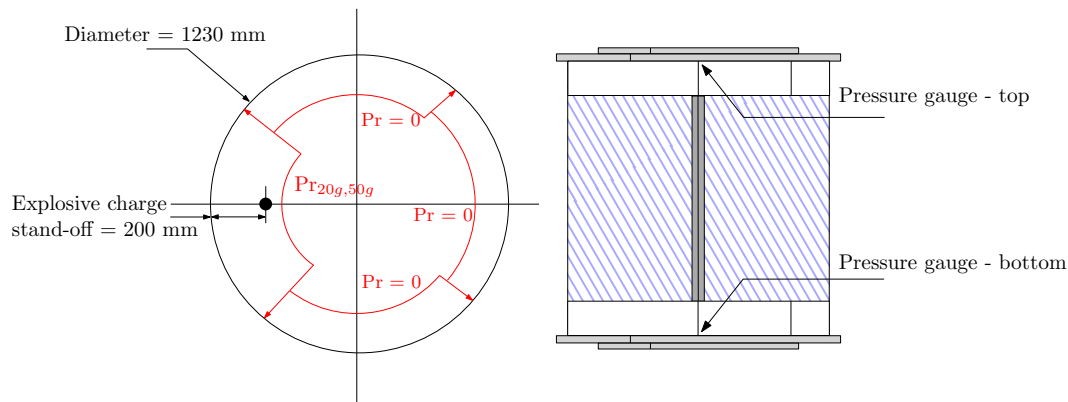


FIGURE 4.3: Location of explosive charge and pressure gauges in demonstrator blast test

4.3.2 Blast load modellisation

For the metallic demonstrator tests, the explosive charge was offset from the centre of the structure to ensure failure on one side of the skin quadrant. A radially expanding shock wave propagates throughout the structure impinging on the skin quadrant nearest the charge before the other quadrants. The pressure distribution is therefore considered to be non-uniform, both spatially and temporally, and implies that the skin nearest the charge will experience the most severe pressure. Data from the pressure gauges for the 20g load case, situated at the top and bottom of the structure, as shown in Fig. 4.3, show a relatively small instantaneous pressure peak and prolonged duration which remains at the initial internal pressure. This shows that the top and bottom of the structure is largely unaffected by the explosive charge, as most of the blast energy is spent in deforming the critical skin quadrant. Although the MMALE approach would provide an accurate description of the pressure profile at every point the structure, albeit at huge computational and labour cost, it is assumed that pressure load curves derived from the empirical load function, ConWep, is sufficient given the explosive stand-off distance and charge mass.

Therefore in this study, the purely lagrangian structure is subjected to an intense pressure whereby the skin quadrant closest to the explosive charge is subjected to two load cases derived from empirical blast functions, as shown in Fig. 4.5.

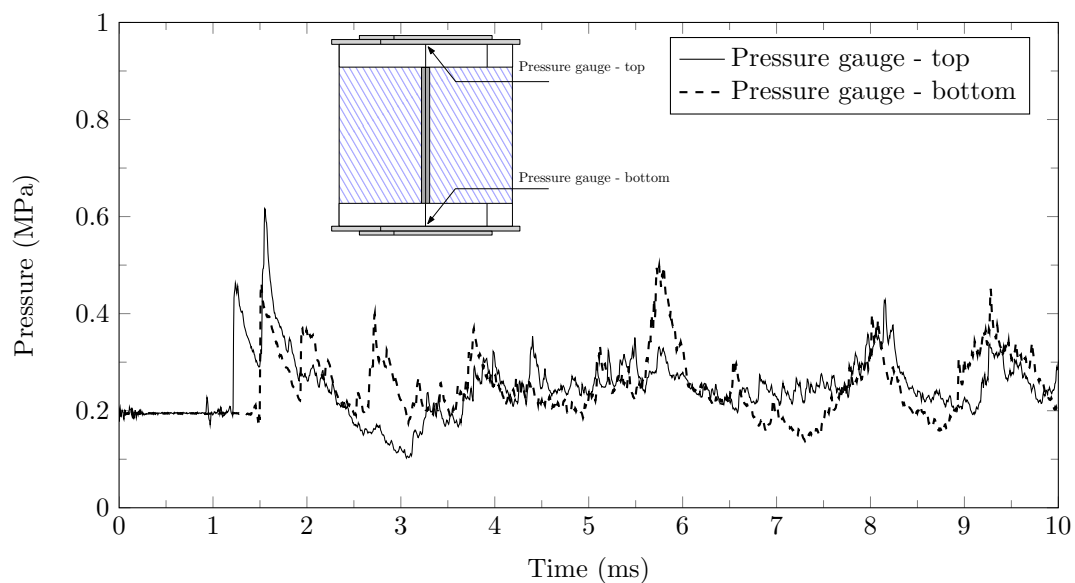


FIGURE 4.4: Experimental internal overpressure values taken at the top and bottom of the aluminium demonstrator for 20g explosive charge

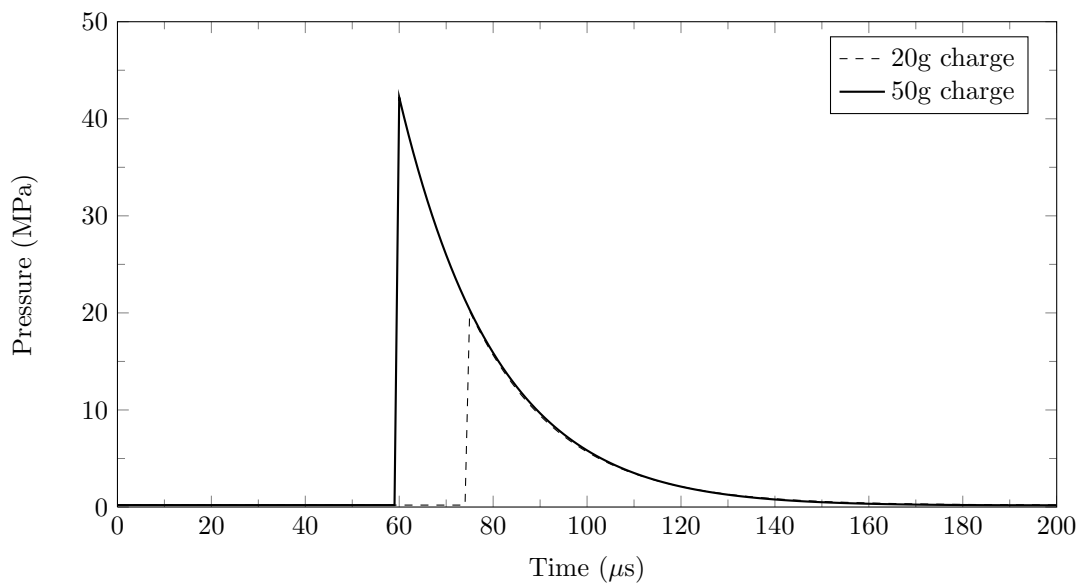


FIGURE 4.5: Internal overpressure blast profile derived from ConWep empirical function for 20g and 50g Semtex load cases

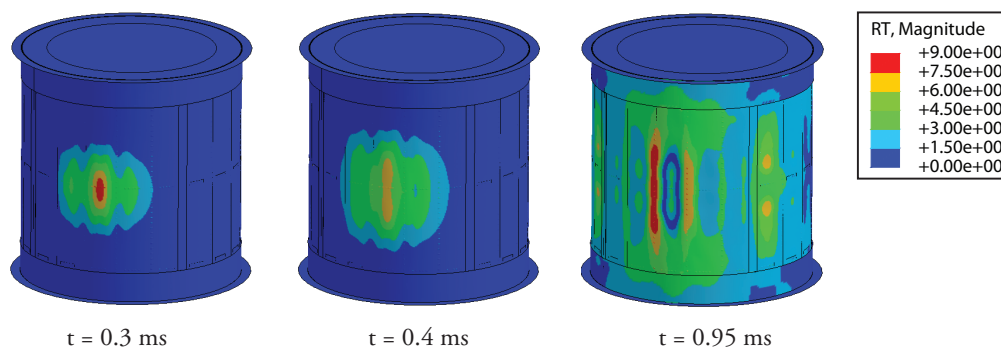


FIGURE 4.6: Contours of out-of-plane displacement of metallic demonstrator subjected to an internal explosive charge of 20g Semtex

4.4 Global model analysis results

4.4.1 Finite element model validation

The only tests data available are those blast tests that were conducted using one explosive charge location and size. Therefore, the validation of the LS-DYNA finite element model was performed, first of all, by comparing the results of the demonstrator tests performed by TNO [68], which is discussed below.

It was anticipated that the demonstrator would not withstand an **explosive charge of 20g** due to the very small stand-off distance and high TNT equivalency of Semtex. However, the predictive results show that the structure withstood the explosive event with no indications of breaching or significant damage to the skin, stiffening elements and reinforcements. Figure 4.6 shows the evolution of out-of-plane displacement of the structure at different time intervals obtained from the predictive simulation. The maximum displacement occurs at the centre of the skin (where the explosive charge is located) and evolves with time along the structure. The displacement contours evolve in a non-uniform manner due to the presence of the stringers and frames which add resistance in these regions. Displacement data from the middle of the skin was obtained and showed that the skin wall vibrated elastically during this explosive event, as shown in Fig 4.7.

These results are further supported by experimental data obtained from the DIC apparatus. Out-of-plane displacements on the demonstrator surface were obtained at different cross-sections and time intervals, given in Fig. 4.8. For the 20 gr charge, the demonstrator wall vibrates elastically in both the positive and negative direction which eventually regains stability with time (i.e. displacement fades to zero).

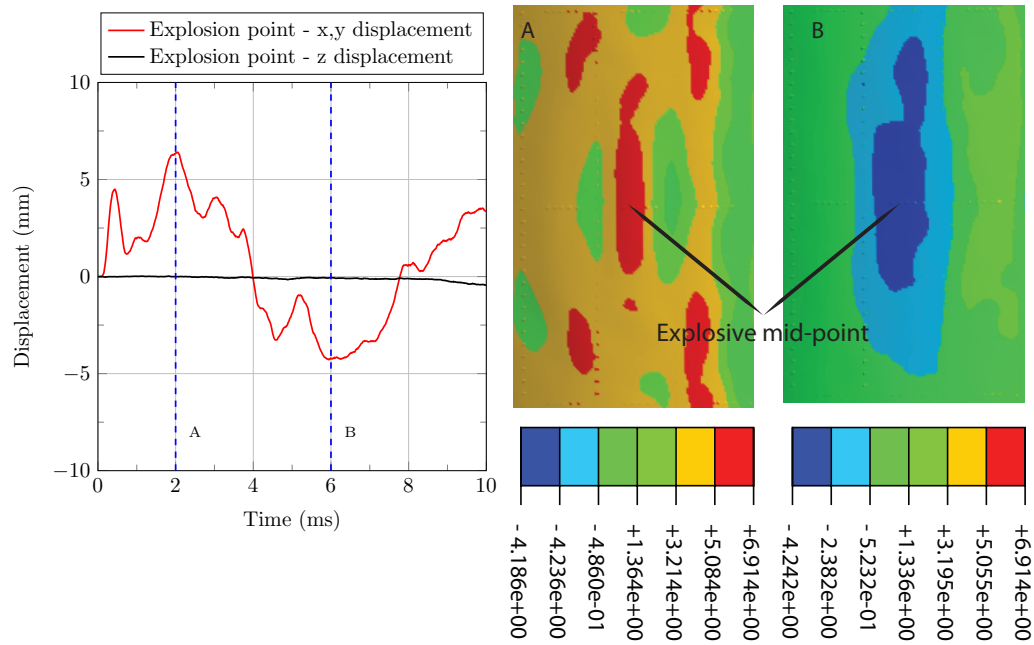


FIGURE 4.7: Mid-point out-of-plane displacement (z), and contour plots obtained from predictive simulations. Aluminium demonstrator, 20 gr explosive.

A second simulation was performed with a 50 gr explosive charge at the same stand-off distance. The intensity of the shock wave ($P_{max}=45$ MPa) was severe enough to cause breaching of the critical skin quadrant. The sequence of failure begins with the appearance of high stresses developing along the boundary edges of the stringers which increases with magnitude. When the equivalent plastic strain for failure is reached, cracks initiate and grow along these boundaries, as shown in Fig 4.9. The stringers at this point are still structurally sound and continue to resist the outward pressure exerted on the skin quadrant and corresponding stiffening elements. The failure criteria assigned to the mechanically fastened rivets have been satisfied resulting in failure of this contact interaction which allows the skin quadrant and stringer to deform more severely. Catastrophic failure is reached when the propagating cracks reach the upper and lower region of the bulkhead which directs the cracks to continue along the circumference of the structure. This concludes with very high bending stresses developing at the boundary of the stringers resulting in complete failure. The only structural component to remain intact in this region is the frame, albeit severely deformed. These observations are further supported by DIC measurements in Fig 4.11.

The 20 gr and 50 gr blast tests were carried out on the same structure. It is shown that the 50 gr load case induces damage in the form of severe plasticity with significant breaching of skin. Furthermore, from visual observations, and the displacement measurements, it can be concluded that the aluminium demonstrator remained fairly intact after the 20 gr blast (no plasticity, no damage). From visual and acoustic inspection,

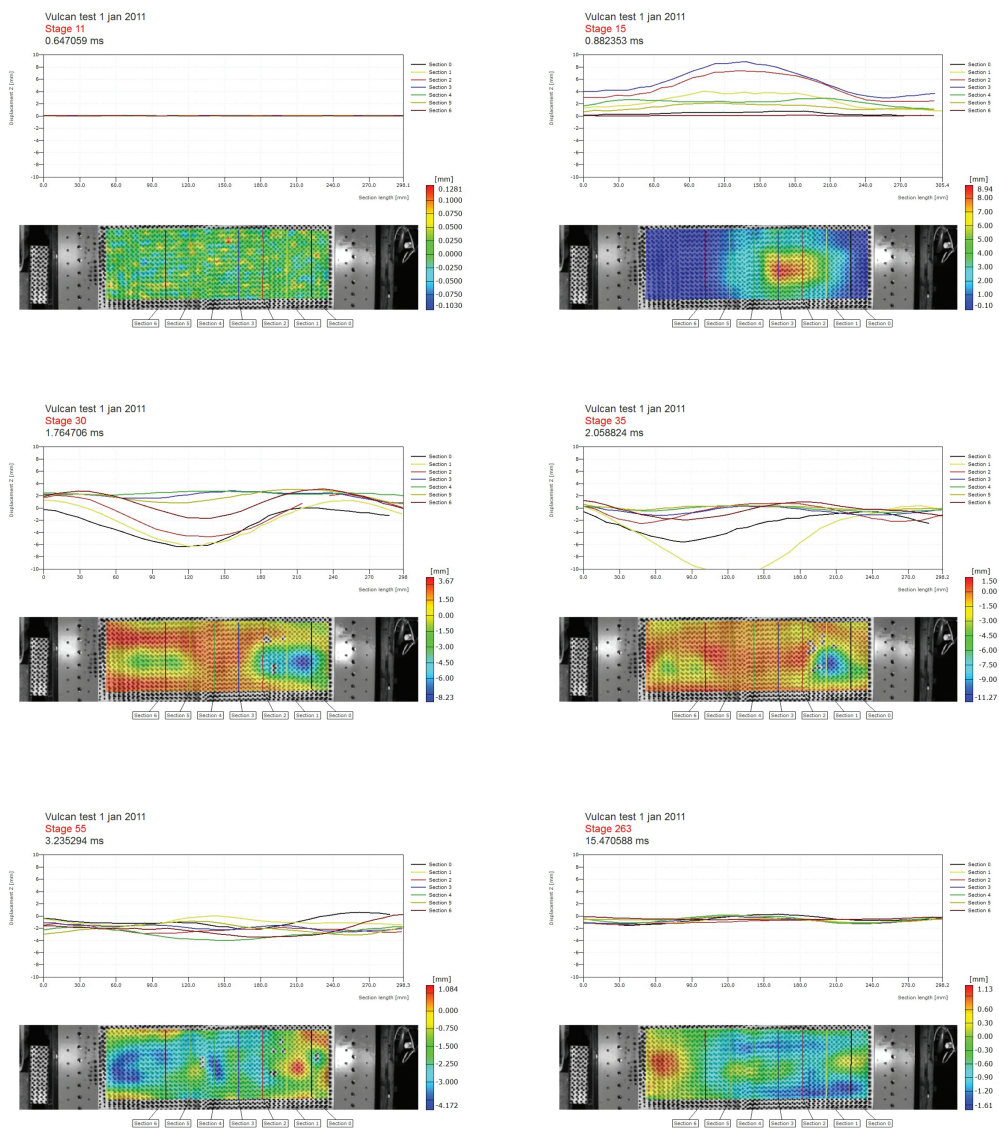


FIGURE 4.8: Out-of-plane displacement z at different cross sections and times. Aluminium demonstrator, 20 gr explosive. Displacements obtained with DIC [68]

the CFRP demonstrator did not manifest any damage on the skin after the 20 gr charge, although the middle frame was fractured. The DIC technique in combination with high speed cameras has proven to be extremely useful to obtain displacements (strains are also possible). This together with the pressure measurements provides valuable material to validate computer models.

4.4.2 Vulnerability analysis results

This modelling program was extended to Aluminium 2024-T3 and Glare 3 scaled fuselage structures. As expected, Aluminium 2024-T3 displayed identical damage observations

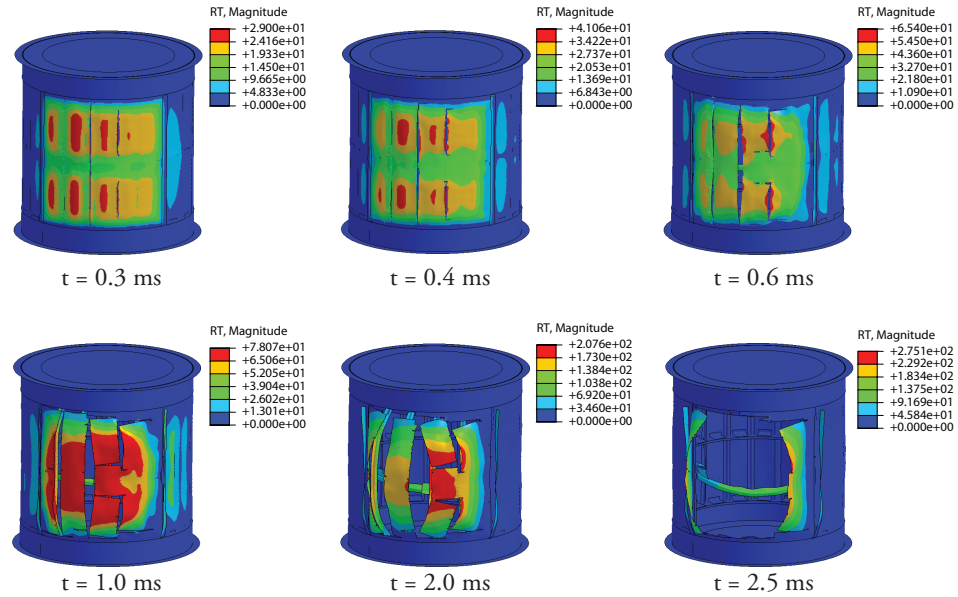


FIGURE 4.9: Out-of-plane displacement z at different cross sections and times. Aluminium demonstrator, 50 gr explosive.

and tearing thresholds as the previous simulations due to similar mechanical properties for both the 20 and 50g charge load. In the case of Glare 3, one should be cautious how results are interpreted. In the shell multi-layered approach adopted in this Glare model, if the composite failure criteria are satisfied, for example maximum strain for fibre tension, the layer in the *element is completely removed*. This element is deleted from the analysis even if adjacent composite or aluminium plies are still within their failure limit. Therefore additional computational effort was required to determine the damage state of all seven layers in the hybrid system to establish if complete failure had been satisfied. Complete failure was defined when the front and back aluminium layers had reached the equivalent plastic failure strain of 18%.

The results therefore show that Glare 3 showed no significant breaching/tearing of the structure at the maximum charge load of 50g. Very high composite damage was observed at the stinger/frame interface and within close vicinity of the blast. The results of these simulations are given in Table 4.3.

4.5 Conclusion

The purpose of this chapter is to investigate the extent of the immediate damage of scaled fuselage structures due to a bomb blast event situated near the target skin. Assessment of immediate damage was conducted using LS-DYNA models of existing fuselage demonstrator tests trials taking into account composite and metallic damage,

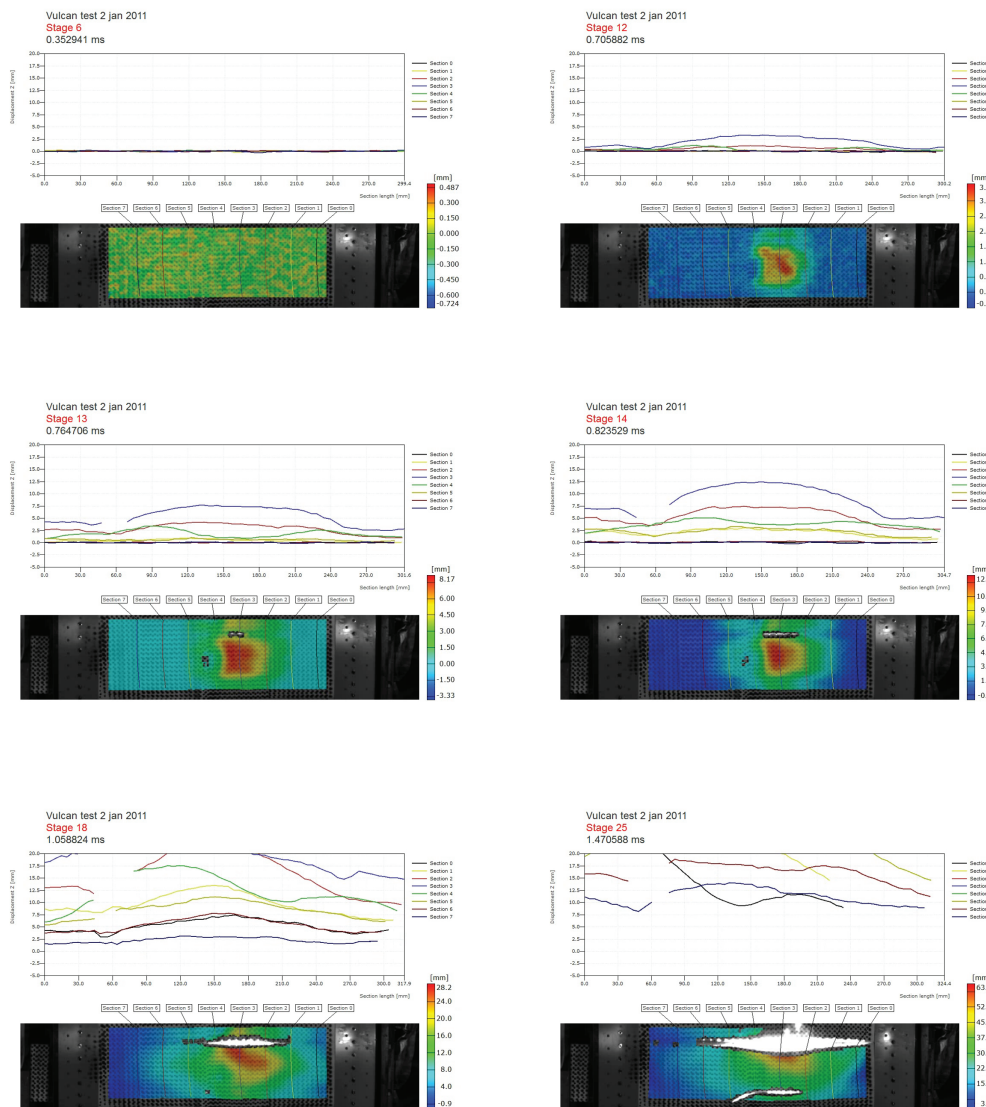


FIGURE 4.10: Contours of out-of-plane displacement of metallic demonstrator subjected to an internal explosive charge of 50g Semtex [68]

bolted joint analysis and stiffening elements. The initial predictive fuselage data were in reasonable agreement with test data. Further analysis on Aluminium 2024-T3 tests revealed that maximum allowable charge load is approximately 50g SEMTEX. Glare 3 structures did not report such breaching or tearing of the target skin at the charge load although it was on the borderline of reaching the failure limit.

The data from the scaled fuselage designs need further assessment to cover more charge designation points and different amounts of charge sizes. Furthermore, these tests also reveal the deficiency of small-scale blast trials in fuselage blast mitigation analysis. It is clear that the interaction of stiffening elements, bolted joints and frames have an immense impact on the structural behaviour of fuselage structures, which are not reflected in small-scale blast trials. These trials approximated the panel of fuselage skins as fully

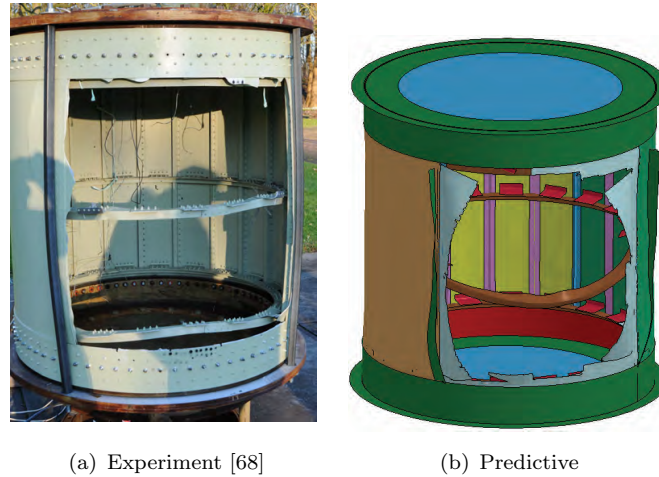


FIGURE 4.11: Final damage state of metallic demonstrator tests subjected to an internal explosive charge of 50g Semtex

TABLE 4.3: Vulnerability analysis of dynamic deformation for scaled fuselage structures subject to internal blast load

Material	Charge designation	Charge mass	Observed damage
Aluminium 2024-T3	200 mm from target skin	20g	Minor internal structural damage. Dent, irreversible plastic damage to stiffening elements.
		50g	Fractured stringers. Severe damage to stiffening elements. Extensive cracking.
Glare 3-3/2-0.4	200 mm from target skin	20g	Minor structural damage to stiffening elements. Minor composite damage in vicinity of blast load and along skin/stringer boundary.
		50g	Increased internal damage Ripped stringers No significant breaching of target skin.

clamped. These kinematic boundary conditions clearly are not transferable to full-scale designs since the sequence of failure and damage scenario is different. Future airframe damage assessment should to incorporate curvature, stiffening elements and bolted joints in the experimental trials.

Finally, the objective of this chapter is to establish failure scenarios for the purpose of examining airframe hardening options. It is clear that existing crack arresting features such as crack straps have been successful in mitigating the effects of blast. However, Glare, compared to monolithic aluminium, has demonstrated to offer superior blast resistance.

The question remains whether the design of metallic structures can be transferred to Glare and other hybrid composite systems. This need to be investigated further as slight modifications may need to be considered to obtain a more favourable damage scenario (i.e. arrangement of stringers and frames, interaction of metallic bolts with composite structures etc.).

Chapter 5

Dynamic fracture of aerospace structural materials

THIS chapter describes efforts to address the large-scale damage propagation and crack growth of fuselage-like structures to blast loadings in the presence of multi-site damage. Motivated by the limitations of previous dynamic fracture tests which were ill-designed for the setup of simulation models, a coordinated effort is reported here that not only focusses on the underlying fracture phenomena but also makes the computational effort manageable. To determine the interplay between cylindrical aircraft structures (global dynamic loading due to internal explosive) and the response of individual fatigue cracked panel (e.g. pre-existing multi-site damage in aging aircraft), well-controlled and minimal experiments for dynamic fracture of blast loaded barrel tests with a pre-existing notch have been performed by TNO [26], for typical aircraft materials; Aluminium 2024-T3, Glare and CFRP. High speed imaging systems and pressure gauges were implemented to obtain useful, quantitative physical fracture metrics, such as crack tip velocity. The results have shown that crack growth speeds were in the order of magnitude of several hundred meters per second, with Glare exhibiting much lower average crack velocities than its metallic counterpart. CFRP indicated brittle behaviour with very high crack speeds and crack bifurcation-branching.

5.1 Introduction

The catastrophic consequences of sabotage-induced blast loadings on commercial aircraft have been a topic of interest for the past three decades. Events such as the Lockerbie tragedy in 1989 promoted a review of blast protection measures on aircraft which

TABLE 5.1: Blast loading regimes for aircraft explosions

Loading regime	Characterisation	Time scale (ms)	Analysis methodology
1	Explosive detonation	0-0.2	Eulerian
2	Blast wave propagation through surroundings	0.2-1	Eulerian
3	On-set of structural deformation and damage	0.5-5	MMALE
4	Large scale damage propagation by crack growth initiation and fluid-structure interaction	5-100	Coupled structural and fluid mechanics codes.

included the feasibility of manufacturing Glare based aircraft luggage containers. Furthermore, while airport security screening measures now ensure that large quantities of explosive will not pass through security, small amounts of explosives such as IEDs can still be difficult to detect and have devastating effects. It is desirable to quantify these effects and to establish if remedial action can in some manner increase the chances of aircraft survivability. For example, consideration has been given to venting the explosive through designated panels to vent off the blast products and ensure safe decompression, a procedure misleadingly called "aircraft hardening". Results from Chapter 4 show that during an explosive event in a scaled fuselage structure, there are a number of possible processes which can take place at different moments in time, long after the detonation of the explosive. These four regimes have been summarised as in Table 5.1.

Of course each regime presents its own unique set of technical challenges and problems which from a numerical simulation viewpoint can manifest and accumulate in each subsequent step, if not properly addressed. Chapters 3 and 4 assessed the computational capability and suitability of using hydrocodes such as LS-DYNA to address the first three regimes which simulate, amongst other factors, the initial detonation and subsequent blast wave propagation in the structure using an Eulerian formulation. As the blast wave impinges on the structure, a fluid-structure interaction algorithm is defined to transfer the blast energy to the structure based on a MMALE formulation. However, blast reflections and other interactions that were considered to be secondary events were not included. More importantly the regime (Regime 4) of large scale damage propagation by dynamic crack growth has hitherto largely remained absent from structural analysis. The presence of multi-site damage and the large build-up of high pressure still contained in the fuselage after the initial explosion can trigger the growth of small cracks which will link up and form large cracks resulting in fast fracture (Regime 4). Assuming that the link-up process takes place, the configuration on an elementary level may be considered as a long crack in a pressurised cylinder. A number of interesting challenges

arise from this configuration, such as:

- The curved geometry and pressure differential causes the pre-existing longitudinal crack to bulge out or protrude from the original contour. Under static loading conditions this change in geometry, or bulging effect, significantly increases the stress intensity factor at the crack tips which can trigger different types of failure mechanisms.
- The contribution of non-linear elastic-plastic behaviour in the fracture process zone and surrounding medium.
- The combined contribution of inertia (which enhances the stress state) and dynamic effects (fast motion which reduces the resistance to crack growth).
- Blast wave reflections from the non-linear boundary and build-up of high pressure.
- Under pressurised conditions (or at atmospheric conditions), crack growth will result in high pressure leakage which will further drive the crack to grow.

Both theoretical and experimental studies on dynamic crack propagation in polymers [20] and ductile materials [21] under dynamic loading conditions have received considerable attention in recent years. An understanding of the opening mode I crack initiation and the subsequent crack growth phenomenon in Aluminium 2024-T3 have also been extensively studied [3]. Although dynamic fracture is to some extent well understood, predictive simulations remain a challenge. Indeed, the actual predictive power of dynamic fracture simulations is hindered by huge computational requirements, along with modelling uncertainties such as kinematic boundary and loading conditions and fracture parameters.

Researchers have resorted to various kinds of validation methodologies for dynamic fracture simulations. In some studies, the numerical simulations are performed based on inputs taken from published experimental data. These numerical inputs are often insufficient to completely setup a simulation, which therefore leaves room for modelling assumptions or the fitting of parameters. Then, the results of these simulations are validated against those experiments published in the literature. These attempts highlight the need for integrated experiment-simulation approaches. In addition to loading conditions, there are uncertainties in the cohesive properties of the material. The current opinion in the field of cohesive zone modelling of fracture is that the cohesive zone law can be described by two independent parameters out of the following three parameters; cohesive energy, Γ , cohesive strength, T_0 , and the separation length, δ [20]. In

most cases, the first two parameters are obtained from the global standard experimental measurements for a given material, which is discussed later in this chapter.

An ill-designed large-scale experiment can result in uncertainties regarding kinematic boundary and loading conditions which can result in many unknown parameters and provide quantitative data which cannot be captured by the predictive model. This chapter and the one that succeeds it illustrate this approach in detail. The outline is as follows: the first section of this chapter highlights a case-study in which the planning and design of dynamic fracture experiments was made without taking into account numerical concerns, appropriate extraction of fracture metrics etc. The unsatisfactory outcomes of this experiment became the catalyst for a more integrated, two-way approach which is explained, investigated and evaluated throughout this chapter.

5.1.1 Case study: Sudden centered crack on pre-stressed plates

Designing and executing large-scale dynamic fracture experiments is non-trivial and requires expensive apparatus and measuring instruments. The term 'large-scale' is an important one and refers to the size of the sample which ideally should embody the scale and essential features of fuselage structures. Furthermore, the sample size should be large enough to prevent or at least delay the interference of reflected blast waves with the crack tip, but not too large to overwhelm testing machinery and make the computational effort unmanageable.

As a first step, a configuration was derived which consisted of a large pre-stressed plate mounted on a loading frame with anti-buckling plates positioned below and above the plane of crack growth, similar to a M(T) fracture toughness test [26]. The crucial difference is that the initial crack of length, a_0 , was initiated by means of a line explosive charge placed against the plate and a fixed anvil on the other side, see Fig. 5.1. This configuration was informally referred to as Sudden Centred Crack on Pre-stressed Plates (SCPP). Once detonated, the intensity of the explosive charge will instantaneously conflict with the fixed anvil causing a through-thickness crack corresponding to the length of both the explosive and anvil. The combined effects of the pre-loaded plate and the dynamic effects of the explosive will cause the crack to grow towards the longitudinal boundaries. The time scale of such an event is of the order of ms which cannot be captured using standard photographic equipment. Therefore a high speed imaging system capable of providing temporal resolutions of up 70,000 frames per second (fps) was used. Tests were performed at TNO, Netherlands on Aluminium 2024-T3 ($h = 1$ mm), Glare 3-3/2-0.4 ($h = 1.7$ mm), CFRP (woven, $h = 2$ mm).

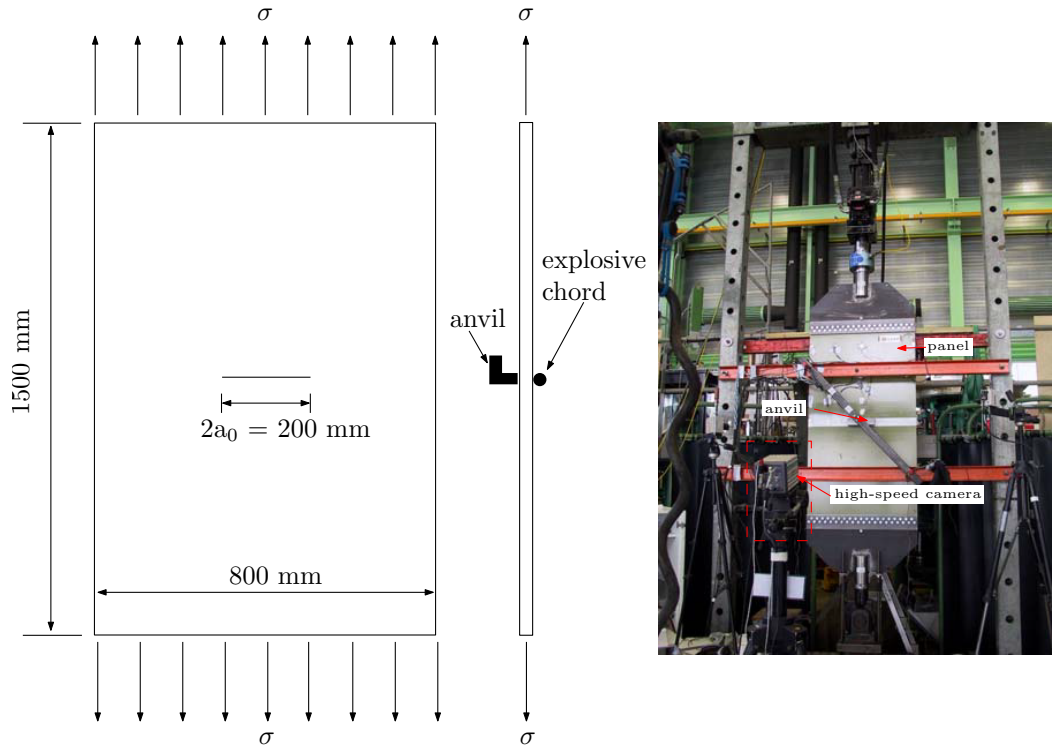


FIGURE 5.1: Experimental setup of sudden centred crack on pre-stressed plates [26]

Fig. 5.2(left) shows the results of the experiment taken from high speed images of the dynamic fracture event ($0-300\mu s$) of 1 mm thick SSCP Aluminium 2024-T3 plates. The images were sent to Sheffield and were quantified digitally using Matlab Imaging Processing Toolbox where a reference length, i.e. initial fracture length, was defined and measured in terms of 'points'. All subsequent measurements were taken relative to this reference which included the following metrics: horizontal and vertical distances relative to the global coordinate system (x and y axes), absolute distances and angular deviation. The derived quantitative metrics of crack length vs. time are given in Fig. 5.2(right). It is clear from this figure that both sides of the crack tip fails to propagate in the same manner, as the left crack tip reaches the boundary of the plate before the right crack tip. It is also worth noting that the areas of white in the high speed images are due to bulging of the plate, causing out-of-plane displacements. Furthermore, the two crack tips do not advance at the same rate failing to reach an asymptotic value i.e. doesn't reach a constant velocity, but rather accelerate and decelerate. This may be due to the stress waves reflecting from the plate boundaries and interacting with the crack tip. The crack does not progress in Mode-I, but rather deviates from the plane of crack in a curved like manner. It is clear from Fig. 5.2(left) that the right crack tip, before deviating from its straight path, is arrested until the left side crack tip reaches the boundary of the plate. The remaining un-fractured ligament of the plate is suddenly pulled apart after some delay.

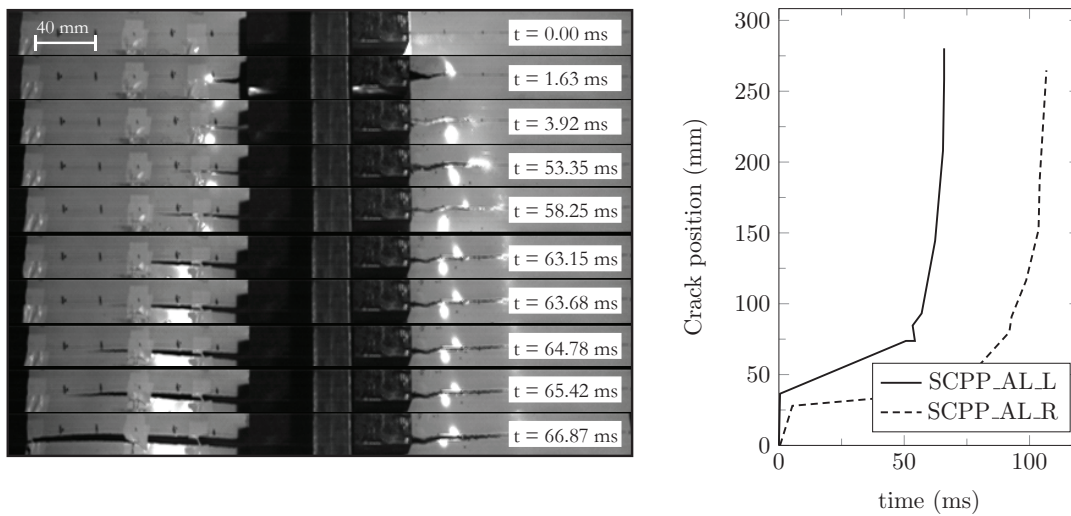


FIGURE 5.2: Description of (left) high speed images for dynamic crack propagation of 200 MPa pre-stressed SCPP aluminium plates and (right) corresponding crack length as a function of time

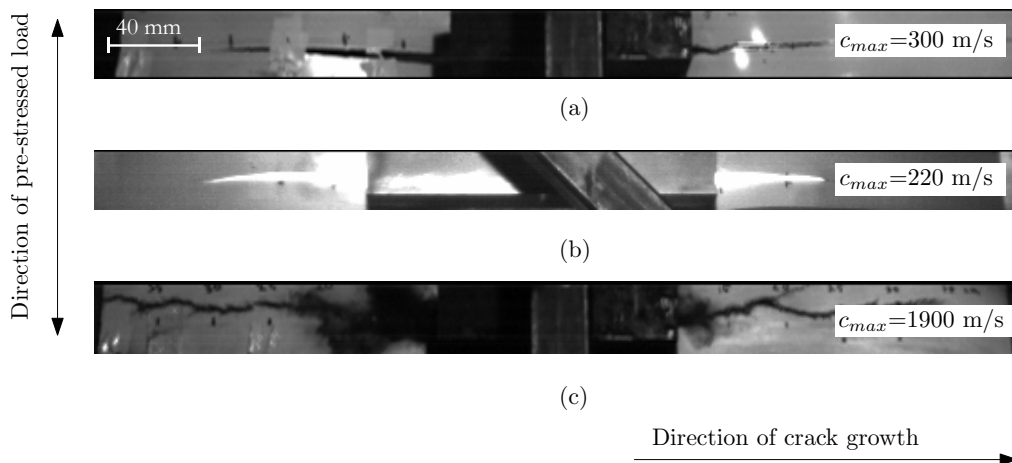


FIGURE 5.3: Crack propagation of (a) Aluminium 2024-T3 (b) Glare 3-3/2-0.4 (c) CFRP [26]

Figure 5.3 shows crack growth profiles obtained from high speed images of Aluminium, Glare and CFRP, with corresponding maximum instantaneous crack velocities. Compared to Aluminium, Glare exhibited a blunter crack tip, which is attributed to the fibre bridging mechanism, and lower crack growth rates. Fig. 5.3(c) shows the brittle dynamic behaviour of CFRP, displaying crack branching, bifurcation and significantly higher maximum crack speeds. Fibre splitting and matrix cracking alters locally the direction of the propagating crack. However overall the crack path appears almost perpendicular to the direction of the applied load.

5.1.2 How fast can cracks propagate?

Theoretical bounds to the rate of fracture exist based on the theory of elastodynamics of brittle solids. The speed of the surface stress waves in an elastic fracturing medium is generally known as the Rayleigh wave speed, c_R , expressed as [71]:

$$c_R = c_S \frac{0.862 + 1.14\nu}{1 + \nu} \quad (5.1)$$

where c_S is known as the shear wave speed:

$$c_S = \sqrt{\frac{G}{\rho}} \quad (5.2)$$

where G is the shear modulus which can be obtained from the Young's modulus, E , and the Poisson's ratio, ν , by

$$G = \frac{E}{2(1 + \nu)} \quad (5.3)$$

Generally speaking, experimentally observed terminal fracture speeds is only around half of the theoretically predicted value which is crudely attributed to the observation that rapidly moving cracks develop roughened fracture surfaces. Alternatively, an estimation of the crack speed which propagates in an unstable manner was derived using the Griffith energy concept; this states that the surplus of energy during the fracture process can be converted to the kinetic energy of the material elements in the crack path as they move apart from each other. This is expressed as [72]:

$$c = \sqrt{\frac{\pi}{\kappa}} \sqrt{\frac{E}{\rho}} \left(1 - \frac{a_0}{a_i}\right) \quad (5.4)$$

where κ is a constant, a_0 is the initial crack length and a_i is the crack length at every time instant. A more detailed analysis of the crack tip stress field has given an estimation of 0.38 for the first term on the right hand side of the above equation. The second term on the right is the speed of propagation of longitudinal waves, c_L , in the material, thus:

$$c = 0.38 c_L \left(1 - \frac{a_0}{a_i}\right) \quad (5.5)$$

It can be observed that the limit: $\lim_{a_i \rightarrow \infty} \left(1 - \frac{a_0}{a_i}\right) = 1$. Therefore for $a_i \gg a_0$, Equation 5.5 becomes:

$$c = 0.38 c_L \quad (5.6)$$

Based on the above expression, it is clear that there is a limit to the crack speed in every material. Nevertheless, the speed of unstable crack growth is comparable with the speed of propagation of sound waves in the material. This has catastrophic implications in the

event of unstable crack growth of an initial crack of a few millimeters as entire fuselage structures can be destroyed in a matter of moments.

Additionally, a geometry dependent limit to the fracture propagation speed in pipes was derived by Kanninen [4]:

$$c = \frac{c_L}{\sqrt[4]{3(1-\nu^2)}} \sqrt{\frac{2h}{d}} \quad (5.7)$$

Where h denotes the pipe wall thickness and d is the pipe diameter. A similar expression by the same author was given in [73], in the form of:

$$c = 0.75 c_L \sqrt{\frac{2h}{d}} \quad (5.8)$$

Table 5.2 shows the theoretical crack speeds of growing cracks for the three aerospace structural materials. Of course, they should be considered as upper bound velocities as the underlying assumption is that the medium obeys linear elastic, isotropic, brittle behaviour. The two formulae by Kanninen do not differ substantially from each other in outcome and only Eq. 5.7 is included. As the formulae are geometry dependent, an example geometry based on the *VULCAN barrel tests*, introduced later in this chapter is assumed.

TABLE 5.2: Theoretic crack velocities in metallic, hybrid and composite mediums

Material	Rayleigh, (m/s) Eq. 5.1	Griffith, (m/s) Eq. 5.6	Kanninen, (m/s) Eq. 5.8
Aluminium 2024-T3	2929	1939	171.2
GLARE 3-3/2-0.4	2753	1821	209.6
CFRP	3025	2001	249.8

Table 5.2 shows a considerable difference between the upper bound fracture rates of Rayleigh and Griffith and the predictions of the Kanninen formula. Equation 5.7 is somewhat empirical in nature since it is based on a simple model calibrated with experimental data. Although the range of validity is not indicated, this empirical formula was derived for oil pipeline applications and pressure vessels, nuclear reactor design etc. In applications such as this, the ratio $\frac{2h}{d}$ is typically in the range $\frac{1}{30} - \frac{1}{60}$, considerably lower than the value of $\frac{1}{500}$ for the barrel tests. It is clear from Eqs. 5.7 and 5.8 that it cannot hold for arbitrarily high $\frac{2h}{d}$ ratios; this would imply that un-curved plates could never fracture. Whether a large thin-walled cylindrical structure falls within the range of validity is doubtful as it does not resemble the typical geometry the formula is used for.

5.2 Integrated experimental-numerical design approach

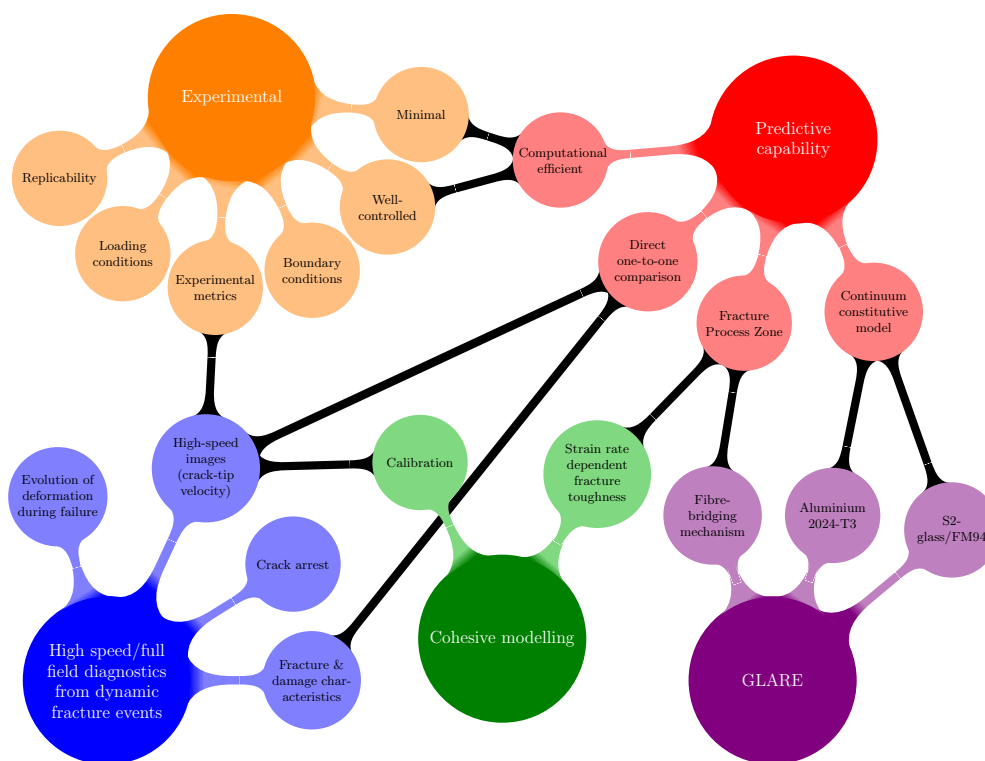
Despite the obvious shortcomings of this case study, the tests did provide a conservative measure of the dynamic fracture characteristics of the aforementioned materials. One of the main concerns was that the tests lacked practical applicability to aircraft cylindrical structures. Passenger aircraft have insulation and panelling making an explosive placed directly against the skin by a passenger an unlikely scenario, as the stand-off distance of the explosive will have a significant influence. An additional consideration was the effect of cabin pressurization on the elastic and plastic deformation of the fuselage skin under blast loading. Cabin pressurization pre-stresses the fuselage and thus may alter the structural response to an internal explosion. Although it would be ideal to utilize full-scale explosive testing on aircraft for this evaluation, the cost and size of such an endeavour were not amenable in this study. Furthermore, the experiments must also facilitate the setup of finite element models based on controlled kinematic boundary and loading conditions with few unknown parameters. The asymmetry of the previous SSCP test setup, uncertainties regarding loading conditions (particular the damaged induced by the explosive charge) and out-of-plane movements of the plate makes this arrangement very difficult and unsuitable for V & V simulations.

Motivated by the limitations of this study and the need for more realistic structural configurations which favour the V & V process, a more intimate collaboration between the experimentalist and numerical analysts was needed.

The inspiring guidelines in this effort were as follows:

- An integrated design of the experiments and the simulations with the premise of avoiding unnecessary challenges to the computational model while probing the essential dynamic fracture features;
- Direct one-to-one comparison based on a set of relevant predefined experimental metrics;
- Avoid case-specific parameter fitting which have no physical/useful interpretation;
- Reduction of uncertainty levels through well-defined kinematic boundary and loading conditions and, *if possible*, independent experimental parameter determination (e.g. cohesive law).

A schematic of the requirements and rationale behind the integrated approach is given in Fig. 5.4. Key aspects in carrying out this program include on the experimental side high-resolution full-field diagnostics, and well controlled and well instrumented reproducible



1

FIGURE 5.4: Schematic of the integrated approach for the validation of large-scale simulations of dynamic fracture

loading. The quantitative performance metrics, such as crack-tip velocity, provided by the experiments are compared *a posteriori* with the predictive simulations.

Within the VULCAN consortium, a well-controlled, minimal and representative experimental scheme for dynamic fracture was designed specifically for the validation of large-scale simulations using cohesive finite elements. The rationale is taken from the concept that multi-site cracks in a pressurised fuselage are subjected to internal pressure loads and can link up to form longer cracks, i.e. a long crack in a pressurised cylinder. A new test design based on a closed pressurised barrel set-up was identified as the best design candidate which closely resembles the structure of a commercial aircraft fuselage, such as curvature and pressurisation, while still allowing cost-effective parametric studies. A series of explosive pressurised barrel tests were performed by the Dutch defence company TNO, under the EU funded VULCAN project [26]. The responsibility of the author, although not directly involved in the development of this experimental program, was to develop complex finite element models which would validate and give further insight into the blast-induced response of Glare/Aluminium structures in the presence of cracks.

TABLE 5.3: Geometrical and loading parameters for numerical modelling

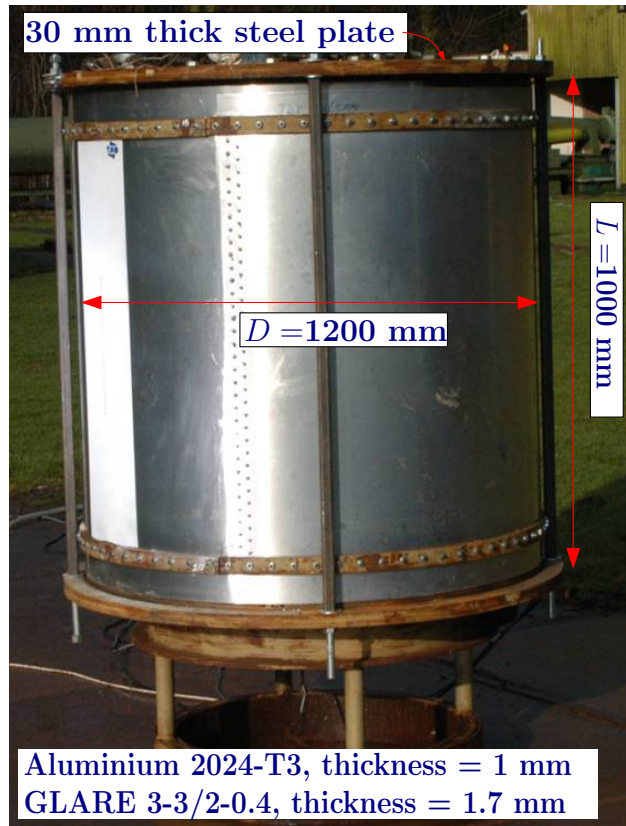
Material	Diameter, d (mm)	Length, l (mm)	Thickness, h (mm)	Pressure (kPa)	Amount of TNT (g)
Aluminium 2024-T3	1225	1000	1	200	54
Glare 3-3/2-0.4			1.7		

5.3 Pressurised barrel tests

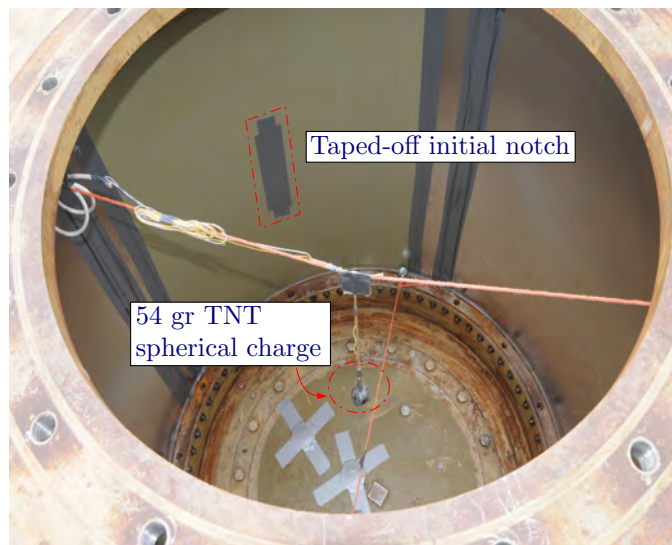
The barrel consists of two plates, front and back, which are mechanically fixed with bolts. The perimeter of the front plate relative to the back is approximately 1:3 and is varied throughout the test program to encompass different structural materials. The back plate material remains constant as Aluminium 2024-T3 material of 1 mm thickness. The overall dimensions are approximately 1.2 m diameter and 1 m height and the top and bottom of the barrel are firmly fixed using massive steel plates, relative to one another in the vertical direction, as shown in Fig. 5.5(a). In order to provide accurate loading conditions to the simulations, a loading set-up is designed where a pre-notched barrel is pressurised and crack propagation is triggered by the detonation of a TNT charge placed inside in the middle of the barrel, see Fig. 5.5(b) for details. This barrel setup does not have the shortcoming of the previous one (no damage on the barrel skin, symmetric blast and standoff distance larger than zero).

To simulate aircraft operating conditions, a pressure valve is connected to the top of the barrel and an initial internal pressure of 200 kPa is applied. To monitor the pressure profile during the blast explosion, a series of pressure gauges are situated at the top and bottom of the barrel, as shown in Fig. 5.6.

A through-thickness pre-notch of 56 mm length is saw-cut on the front plate and taped off using an industry foil adhesive tape to avoid de-pressurisation, as shown in Fig. 5.5(b) for details. The pre-notch length has been obtained by means of FE simulations [21], so that a crack does not propagate under the static pressure alone. Table 5.3 shows the geometrical and loading parameters for the Aluminium and Glare barrel tests. The crack path was recorded using high speed cameras which can capture up to 40,000 frames per second, depending on the level of resolution required. In order to achieve the best possible exposure, the front plate of the barrel was illuminated in white and the pre-notch was clearly marked in black with a series of grid lines extending in intervals of 10 mm, as shown in Fig. 5.7.



(a) Geometry of pressurised barrel tests indicating 30 mm thick steel end cap plates



(b) Location of spherical TNT charge and initial notch

FIGURE 5.5: Experimental set-up of pressurised barrel tests [26]

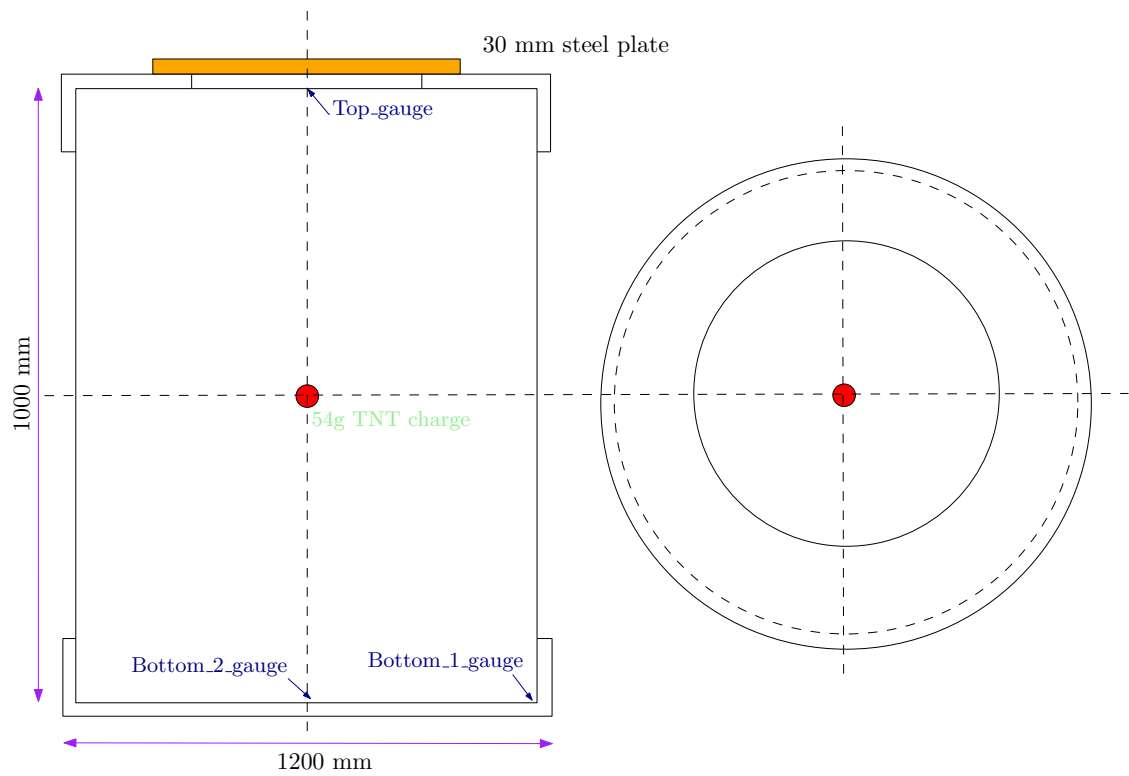


FIGURE 5.6: Location of experimental pressure gauges in pressurised barrel tests.

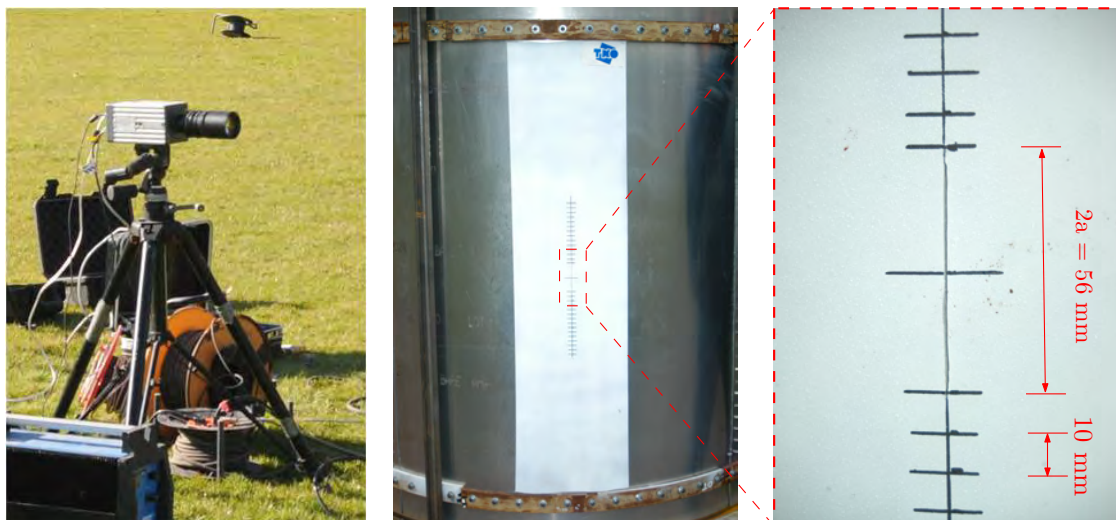


FIGURE 5.7: High speed imaging system used to capture fast propagating crack, capable of reaching 40,000 fps [26]

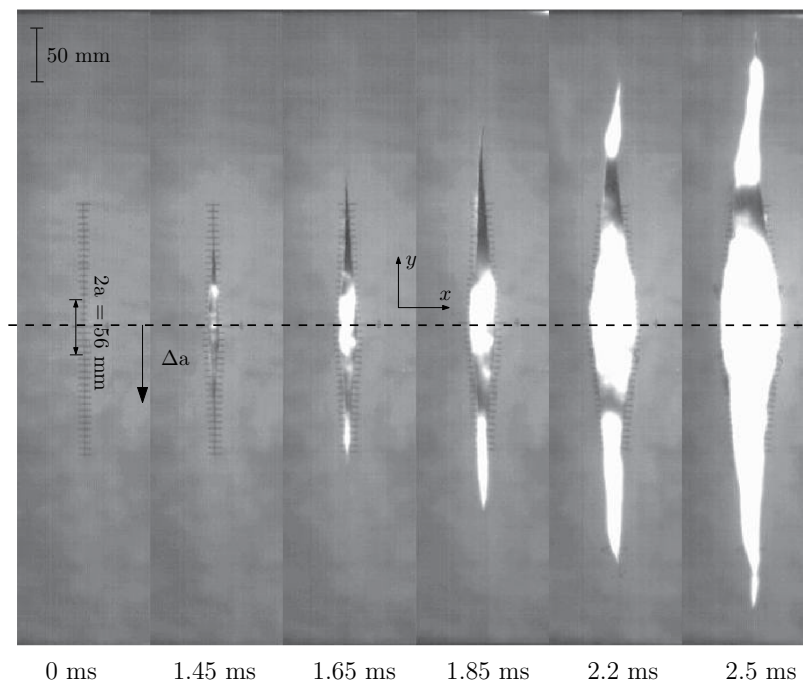


FIGURE 5.8: High speed camera images of dynamic crack propagation of Test AL03

5.4 Experimental results

5.4.1 Aluminium 2024-T3

The choice of quantitative metrics is at the heart of any V & V effort, which must reflect the aims and objectives of the experiment and have real, physical significance to the underlying phenomena and be amenable to accurate experimental instrumentation. Moreover, they should be easily executable from simulation results. In the problem of dynamic crack propagation considered here, the following set of validation metrics are employed: crack initiation time, crack tip position and crack tip velocity. This choice satisfies the above requirements and gives the ability of one-to-one direct comparison of the simulation results with the experimental data.

The real-time records of the high speed images associated with the propagation of a crack along the vertical crack plane is shown in Fig. 5.8. Although the front notch face is somewhat unclear due to the high contrast flash of the internal explosion, both top and bottom notch crack tip locations can be inferred from the images and show a clear, symmetrical continuous crack extension.

These high speed images provide a set of quantitative measures which were identified and measured from the crack tip position and frame number. Typical crack tip metrics on both the top and bottom notch faces for this test (Test AL03) are shown in Fig. 5.9.

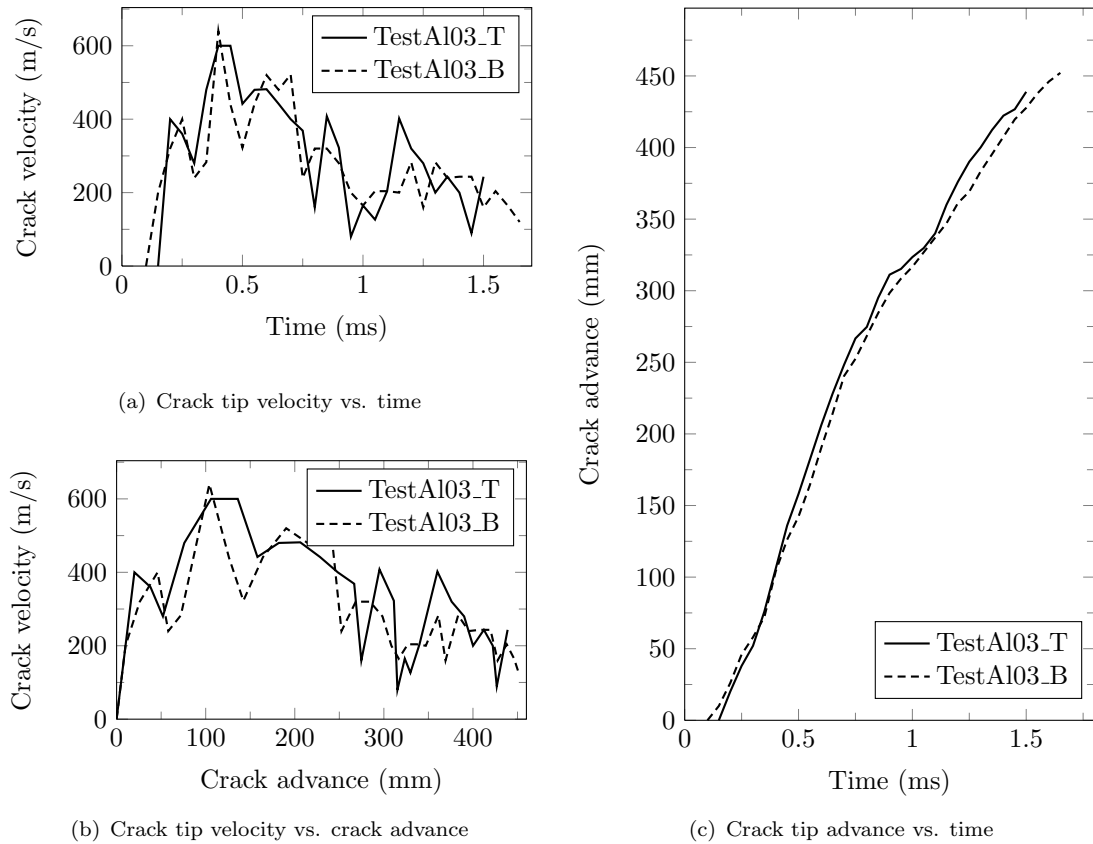


FIGURE 5.9: Quantitative performance crack metrics obtained from high speed images for Aluminium 2024-T3

As shown in this figure the crack takes $t=150 \mu\text{s}$ to initiate upon loading and propagates with an average velocity of 300 m/s.

Both crack speeds follow the same pattern, an indicator of the uniform loading and constraints giving to the favourable symmetrical behaviour. There is an initial peak velocity of approximately 600 m/s which then decreases to a mean value between 200 and 300 m/s. These results are reasonably close to the values published in [26] and the speed of fracture is still much lower than the Rayleigh wave speed of aluminium (2929 m/s).

The fracture profile shows that fracture was initiated at the initial notch and continued in both vertical directions, thus fracturing in Mode I until reaching the end of the barrel. This was preceded by Mode III fracture which occurred along the circumference of the barrel creating an opening up of the barrel in two apertures, see Fig 5.10(a). The profile of the crack path indicates a clean fracture reminiscent of fracture in thin walled structures, showing significant plastic deformation and bulging due to the outward expulsion of the explosion, see Fig 5.10(b).



FIGURE 5.10: (a) Pressurised barrel after the explosion, (b) Profile of crack path

The pressure curves are presented below in Fig. 5.11. Pressure gauges `Top` and `Bottom_2` show very similar pressure profiles showing an initial instantaneous rise in pressure followed by a decay in pressure below that of atmospheric pressure. This initial overpressure is preceded by further reflections of the shock wave on the boundary of the barrel, resulting in periodic peaks of pressure with time. The pressure profile gradually decays to atmospheric pressure, over a few milliseconds, indicating total expulsion of the blast pressure. Pressure gauge `Bottom_1` shows a similar behaviour with an exception of a significantly larger second peak overpressure which is more than double of the initial peak overpressure. The pressure gauge located near the boundary of the circumference of the barrel shows that more severe magnitudes of pressure occur in this region. This behaviour reveals the complex shock wave phenomena of the explosion within the barrel which includes a number of periodic shock wave reflections occurring over a few milliseconds. These findings reiterate the knowledge that cabin pressurisation, which pre-stresses the fuselage, under the combined effects of inertia, will drive MSD cracks long after the initial dissipation of the explosion and subsequently travel large distances from the blast site. A similar crack in an un-pressurised fuselage would stop growing once the explosive pressure is spent.

5.4.2 Glare 3-3/2-0.4

High speed images taken from the first barrel test are shown in Fig. 5.12. A distinct feature of the crack profile is the bluntness of the crack tip during the initial phase of crack extension, $t = 1.35 - 2.8$ ms. During this period there is evidence of crack arrest, shown in frames 2 and 3. This is in contrast to Aluminium which exhibited a consistent

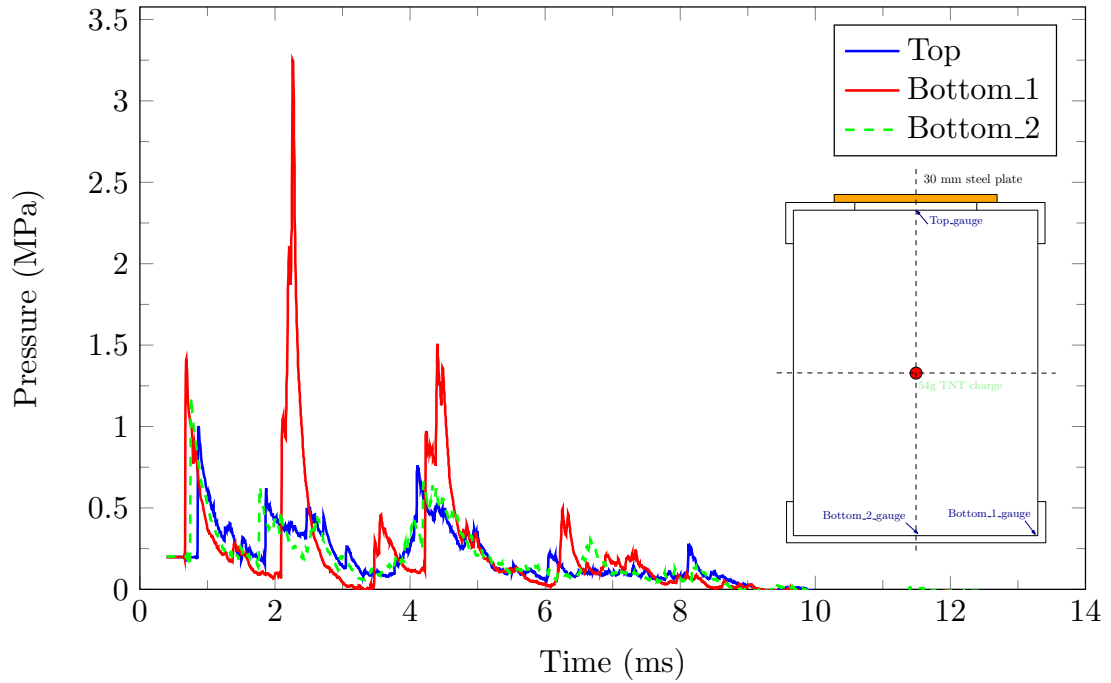


FIGURE 5.11: Pressure curves obtained from Test A103

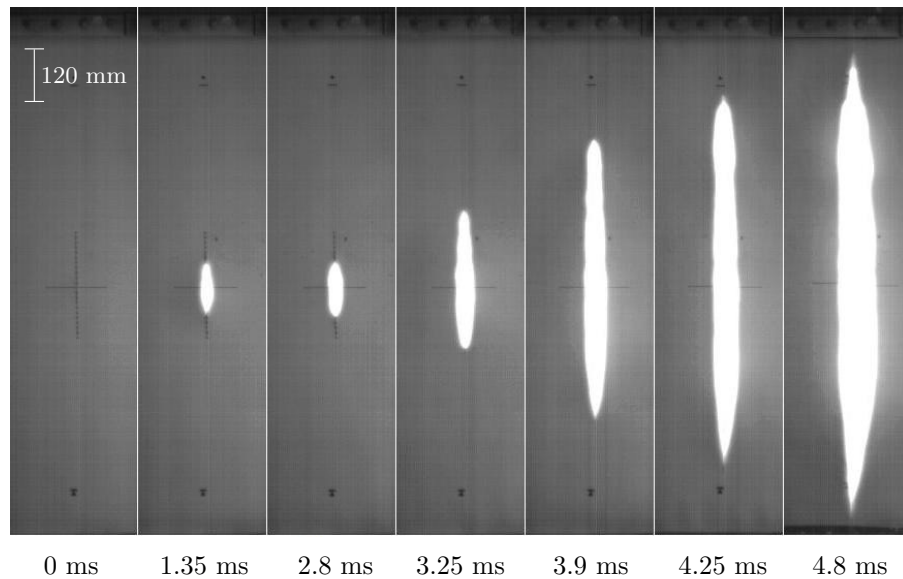


FIGURE 5.12: High speed camera snapshots for mode-I crack propagation for Glare panels [26]

sharp crack tip throughout the test. The fracture metrics obtained from the sequence of high speed images are shown in Fig. 5.13, and show an average crack velocity of 200 m/s, which is lower than the average crack velocity found in Aluminium 2024-T4 (300 m/s).

No evidence of crack arrest was found in the second barrel test which may raise questions about the repeatability of the test, however the results in terms of average crack velocity

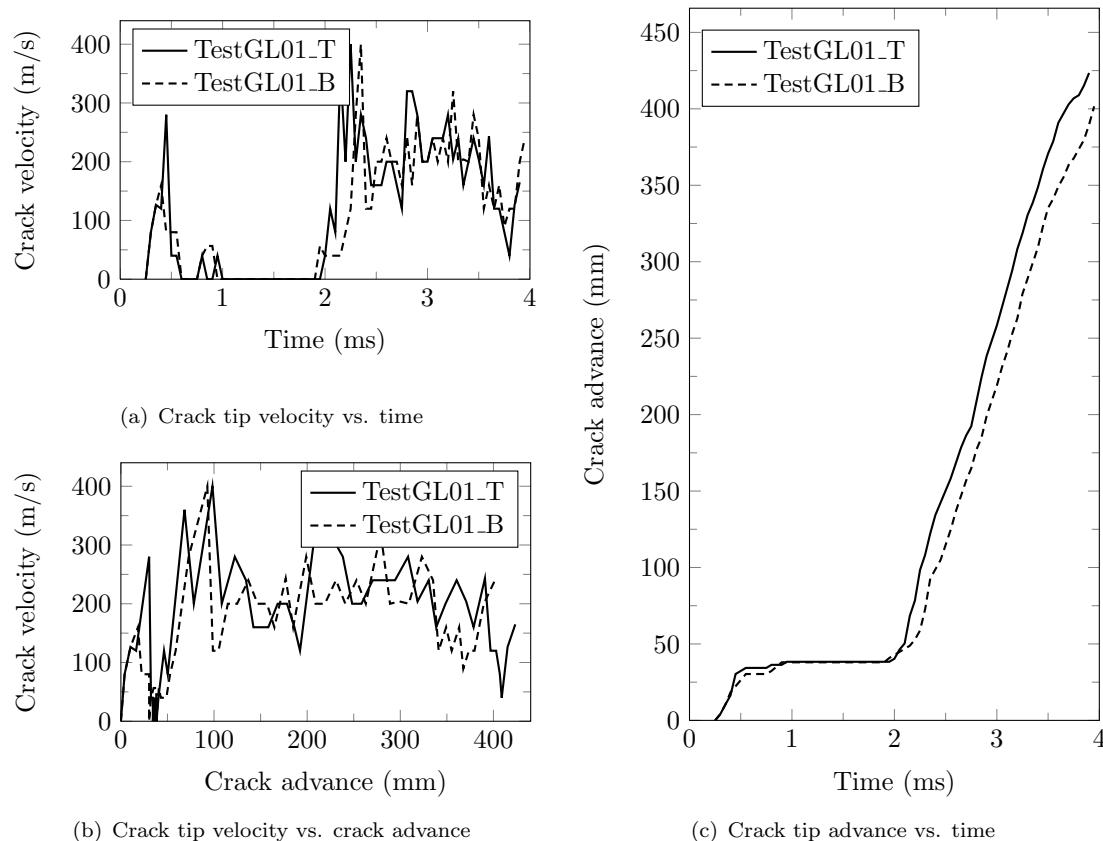


FIGURE 5.13: Quantitative performance crack metrics obtained from high speed images for GLARE 3-3/2-0.4

are deemed consistent with the first test. Figure 5.14 shows a comparison of crack velocities vs. crack advance of both Glare barrel tests.

5.5 Explanation of failure mechanisms in FMLs

Damaged samples from these tests were sent to Sheffield for further inspection which revealed a multitude a failure mechanisms which are both metallic and composite in nature. This includes interlaminar delamination at the metallic/composite interface, extensive fibre splitting and failure and ductile tearing of the aluminium layers, as shown in Fig. 5.15.

The lower average crack velocity exhibited by Glare compared to monolithic aluminium may be attributed to these complex failure mechanisms. Of particular interest is the transition from blunt to sharp notch profiles which seems to be indicative of cracked Glare structures subject to dynamic loading. Vermeeren [74] and De Vries [10] provided a detailed description of the quasi/static failure sequence in Glare. The presence of a through-thickness crack, or saw-cut, causes the stress intensity to increase at the crack

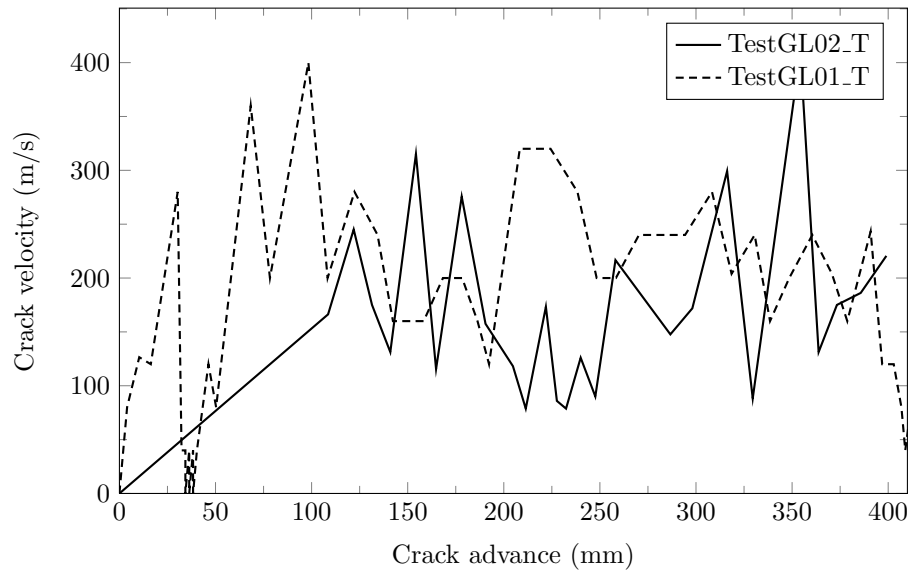


FIGURE 5.14: Comparison of average crack velocity of GLARE barrel tests 01 and 02

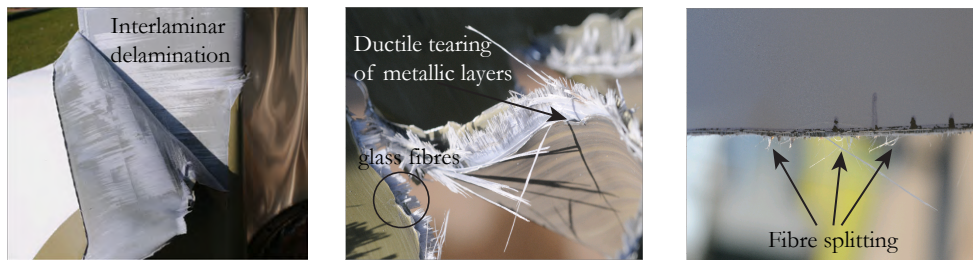


FIGURE 5.15: Deformation characteristics taken from GLARE barrel tests [26]

tip. Due to the pre-pressurisation phase, a hoop stress is applied to the barrel which results in a local plastic zone in front of the crack tip in the metal layer which also induces crack tip to blunt. This has also been observed in centre-crack flat panels, further details can be found in Ref. [10]. Since both metal and glass fibre layers are equally strained in the far field, a complex shear stress state takes place at the metal/fibre interface due to the occurrence of plasticity. Superposition of the shear stresses due to plasticity and crack blunting can result in local shear stresses that exceed the critical shear stress of the resin. When the shear stress reaches a critical value, interlaminar delamination can occur at the metal/fibre interface. With increase applied load, fibre failure can occur when the ultimate fibre failure strain (which is approximately 4.5 %) is reached. Fibre failure causes a re-distribution of stresses to the still intact part of the structure. It is expected, that the elastic energy of the glass fibres is released into the matrix and causes delamination at the resin-rich metal/fibre interface. However, it is anticipated in the barrel tests that, due to the very high dynamic loads, the surrounding metal layers will be severely yielded. Therefore the strain field in front of the crack tip will influence the load carrying capability of the structure. In this scenario, the vicinity of the crack tip

which experiences very high plasticity may lose its capability to carry the load and part of the load is transferred to both the elastic fibre layers and the remaining elastic part of the metal layers. This complex mechanisms ensures higher performance of FMLs with respect to an equivalent monolithic metal panel when high static loads are applied. This may help explain the blunt to sharp notch transition observed in these experiments. This feature is supported by work done by De Vries [10], who observed flat centre-cracked Glare panels under quasi-static loading. During crack extension, the crack-tip opening angle (CTOA) was investigated and was found to be strongly dependent on crack tip blunting. It was demonstrated that the critical CTOA, which represent the amount of blunting, reduces for large crack extension, and hence the shear stresses resulting from blunting also reduces.

This raises rather interesting questions which seem to indicate that failure mechanisms observed under quasi-static loading could be extended to those of a dynamic nature. It is prudent of course to consider that under high strain rate loading condition, there are other issues which should be taken into account, mainly:

- Strain rate sensitivity of the glass fibres and the epoxy resin, resulting in change in fracture surface due to high rate of material separation.
- Reflected shock waves from the boundaries of the specimen interfering with the crack growth.
- Dependence of fracture toughness on loading rate etc.

Post-damage inspection of the fracture surfaces of the Aluminium samples revealed the dominant fracture to be ductile transgranular fracture by microvoid coalescence. This is typically characterised by a dimpled appearance on the fracture surface where the voids and ligaments have coalesced, as shown by a scanning electron microscope image in Fig. 5.16. The dimple shape is strongly influenced by the type of loading and, in the case of local uniaxial tensile loading, the formation of equiaxed dimples can be seen in this figure. The microvoids that form these dimples nucleate at various internal discontinuities such as intermetallic particles, precipitates, second phase particles and grain boundaries (Figs. 5.17(a) and 5.17(b)) [75]. These voids grow as the local stress continues to increase (Fig. 5.17(c)), until the local stress is too large for the remaining ligaments between the voids and the material fractures completely in void coalescence (Fig. 5.17(d)).

This is in contrast to brittle materials which tend to fracture intergranularly [75]. In this process the fracture follows the grain boundaries, or in cleavage, where the separation occurs along specific crystallographic planes, and through the grains.

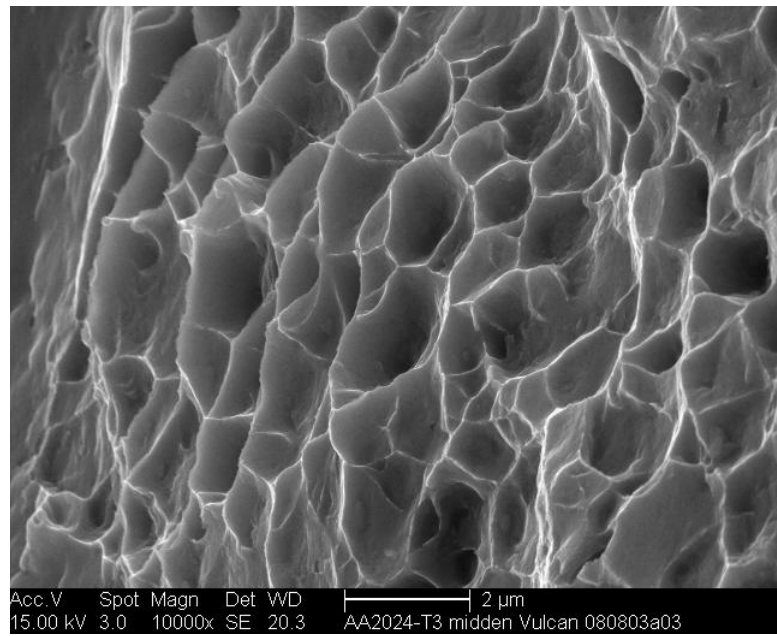


FIGURE 5.16: SEM image of ductile fracture surface [26]

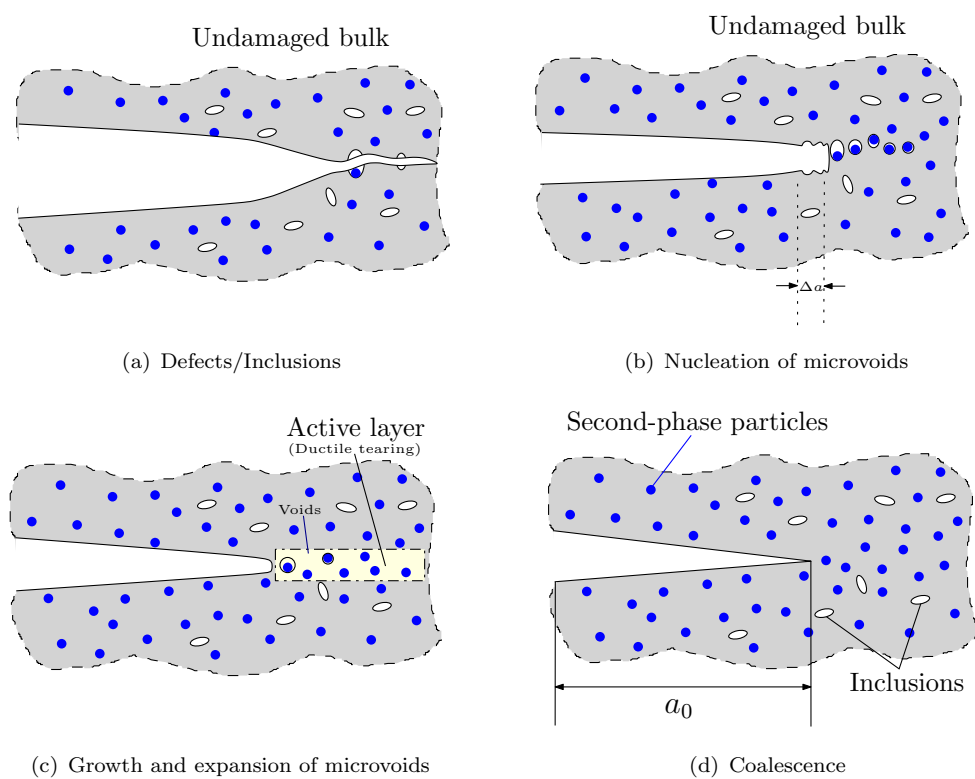


FIGURE 5.17: Ductile fracture process

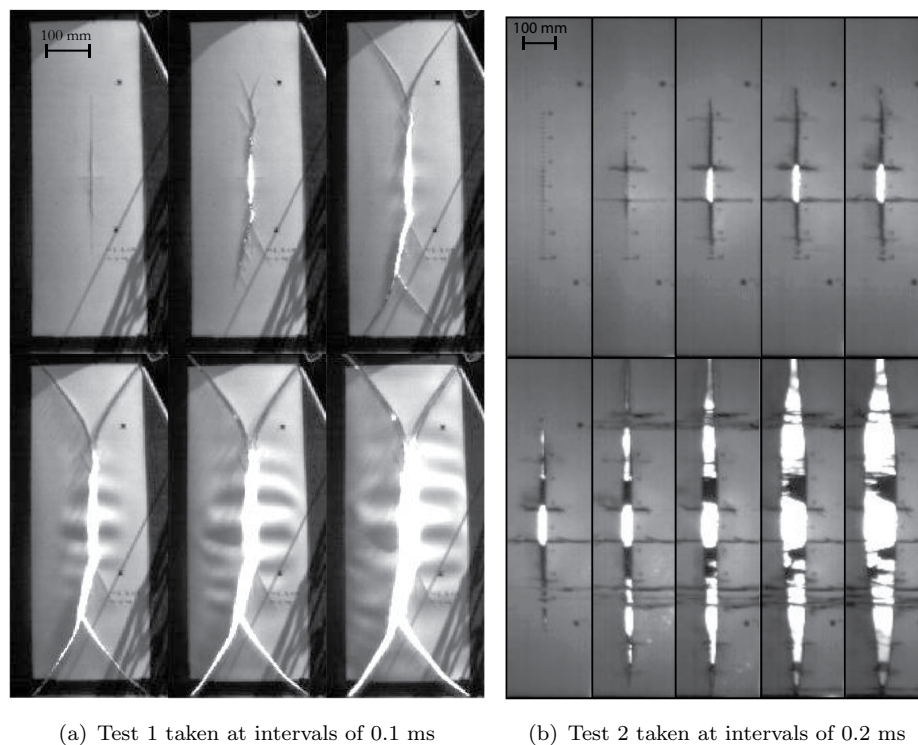


FIGURE 5.18: High speed camera snapshots during crack propagation of CFRP. Test 1 (a) and 2 (b).

5.6 Comparison with woven carbon-fibre reinforced plastics

Finally, two pressurised explosive barrel tests were performed on woven carbon-fibre reinforced plastic (CFRP), a multi-layered brittle elastic material system with higher stiffness compared to Aluminium and Glare. In Figs. 5.18(a) and 5.18(b), taken from both tests, the high speed camera images clearly show the evolution of failure with crack bifurcation and multiple crack branching. The V shape of the cracks near the top and bottom of the barrel, in Fig. 5.18(a), are probably due to a boundary effect. In both tests, there is strong evidence of rear surface interlaminar delamination and fracture, although the fibres at the front remain intact resulting in fibre bridging. In Fig. 5.18(b), extensive fibre splitting occurs across the circumference of the barrel, increasing in size during the explosion. The poor failure threshold of CFRP to blast loading conducted previously by RMA-VULCAN [17] also suggests that these systems do not absorb significant energy in fracture mechanisms such as delamination and fibre fracture. The average crack speed is approximately 2500 m/s, not far from its theoretical limit, the Rayleigh wave speed (3000 m/s).

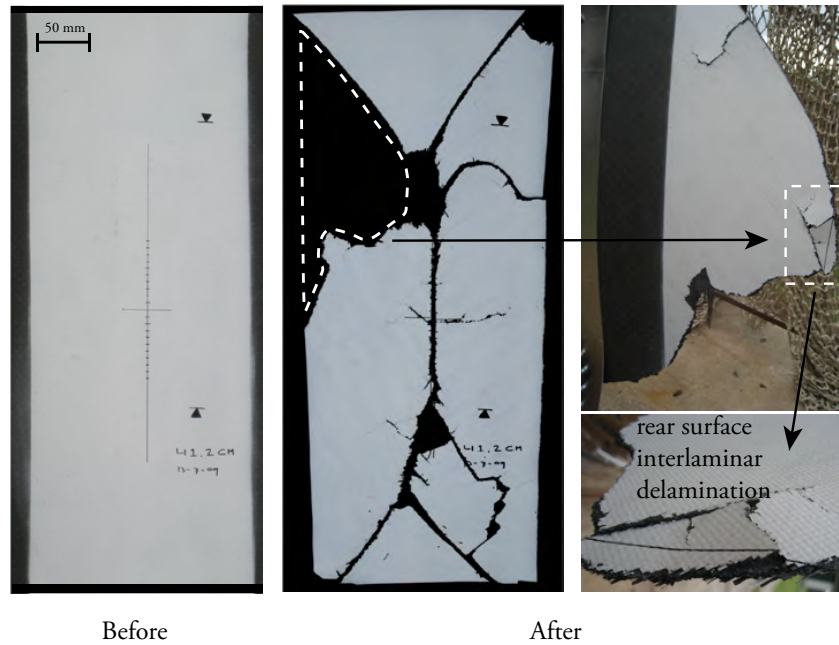


FIGURE 5.19: Post-mortem view of CFRP fragments showing crack bifurcation [26]

5.7 Conclusion

A coordinated effort is reported in this chapter to establish an experimental design which not only addresses the underlying dynamic fracture phenomena and key features of aircraft fuselage elements but also makes the computational effort manageable. Previous experimental efforts on pre-stressed flat plates were ill-designed with many uncertainties regarding kinematic and boundary conditions. The results of the test were inconsistent showing asymmetric crack growth from both crack notches and significant damage in the vicinity of the crack due to the manner in which the explosive was detonated. Uncertainties regarding the setup of the experiment hindered the use of numerical models. However, the results did appear to show that Glare exhibits superior resistance to fast fracture growth compared to monolithic aluminium and traditional woven CFRP systems.

To address the shortcomings of the previous experiment, an integrated experimental-numerical approach was devised within the VUCLAN consortium to incorporate features such as cabin pressure, curvature and multi-site damage. Pre-notched cylindrical structures were manufactured and tested under an explosive charge of 54g TNT placed in the centre of the structure. High speed imaging systems and pressure gauges were implemented to capture and record this high speed event. From this data, quantitative metrics were employed which expressed the crack-tip position as a function of time. Due to the hybrid multi-layered nature of Glare and the bridging of glass-fibres in the wake of the crack, Glare showed to have much lower average crack velocities than Aluminium

2024-T3 and CFRP. The brittle nature of the CFRP tests was highlighted by the very high crack speeds reaching almost $2/3$ of its theoretical Rayleigh value. This resistance to crack growth was further displayed by the clear surplus of energy needed to create new fracture surfaces resulting in multiple crack paths, known as crack branching. The crack bifurcation and brittle-like shattering of the CFRP panels make it an unsuitable candidate for blast attenuating structures particular as such blast-induced debris can cause secondary injuries to third parties.

The blast pressure profile taken from the pressure gauges showed multiple reflected shock waves from the boundary and substantial pressure leakage during the fast fracture phase. The internal pressure and hence the pressure differential relative to atmospheric conditions drives the crack long after the initial explosion (which is of a fraction of a millisecond). Furthermore, the blast pressure profile and boundary conditions proved to be consistent and reproducible. The next phase is to use these well-controlled experiments for the validation of large-scale FE models using cohesive finite elements.

Chapter 6

Modelling of dynamic ductile fracture propagation using cohesive zone elements

DYNAMIC fracture experiments are simulated in this chapter using cohesive elements inserted along the crack path. Validated MMALE models are developed to extract a full blast pressure profile of the blast event which are subsequently transferred to the lagrangian fracture model. Current capabilities in LS-DYNA precludes the use of shell cohesive elements, therefore a shell-solid transition interface was defined. It will be shown that the existing rate independent cohesive zones over predict the rate of crack propagation dramatically. Alternative rate dependent models are discussed and implemented.

6.1 Introduction

In this section, the dynamic fracture experiments described in Chapter 5 are simulated using the explicit finite element solver, LS-DYNA. As previously discussed, the role of the experiments in the integrated experimental-numerical approach is twofold. On the one hand, the experiments provide well-controlled, minimal experiments which facilitate the setup of the numerical model with very few unknown parameters. On the other hand, quantitatively derived experimental metrics (crack tip velocity) are derived from the experiments which are compared *a posteriori* with the developed numerical model. This is achieved through the implementation of cohesive zone elements (CZE) which are inserted in the plane of crack growth and behave according to a traction-separation law.

The formulation of rate independent CZE's which exist in the material library of LS-DYNA with respect to quasi-static and dynamic loading rates are discussed, simulated and analysed. The parameters for the cohesive model have to be identified first, which will be performed by reproducing the experimental F(COD) curve and the COD(da) curve of standard fracture M(T) tests which are reported in the literature.

The outline of this chapter is as follows: firstly, the origins of the cohesive zone model and its role in the field of fracture mechanics and structural integrity assessment are given. Secondly, the concept of traction-separation law (TSL) to describe the behaviour of cohesive elements and the various formulations which have been postulated in the open literature are introduced. The term 'thin walled structure' is acknowledged and defined to establish the appropriate modelling rationale and guidelines. The extraction of static cohesive properties is then investigated and transferred to the explosive barrel tests. Finally, the degrees of success in which these elements can capture the dynamic crack growth rates are discussed with recommendations for future work.

6.2 Introduction to cohesive elements

6.2.1 Motivation for applying cohesive zone models

Structural components are vulnerable to damage which can arise during the manufacturing process and/or throughout its operation lifetime. Damage in the form of crack-like flaws is commonly assessed using the concepts of classical fracture mechanics, a concept which arguably has reached technological maturity since its infancy in the A.A. Griffith era. Today, the characterisation of structural materials and structural integrity assessment methods can be found in national and international standards and codes. However, the field of classical fracture mechanics becomes somewhat limited when assessing the structural integrity of thin-walled structures, such as the fuselage, and when a higher exploitation of mass in engineering structures is needed [76].

It is important at this point to clarify the term 'thin-walled structure', a term which has resonance in several engineering contexts. Three different types of definitions exist which are given in Table 6.1. Considering the above definitions in relation to the performed VULCAN barrel tests, it is assumed that the skin is thin-walled and will be, from herein, treated as such in numerical analyses.

Traditionally, the field of classical fracture mechanics approaches fracture problems in a two-dimensional manner, notwithstanding the fact that three-dimensional FE models of structural components or test pieces exist and can be performed with varying degrees

of success. In industry, structural engineers prefer to deal with single, manageable, fracture parameters which can be interpreted using charts or tables. Such parameters may be a single-valued property such as fracture toughness, or a relationship between the crack extension resistance and the amount of crack extension, all of which have been determined under pre-defined circumstances describing the near crack-tip stresses and strain fields under limiting conditions. These conditions are commonly considered to be in a state of plane strain, a condition where the principal strain in the direction of the longest dimension (which is very large compared to the others) is constrained and can be assumed as zero. On the other hand, in thin-walled structures a state of plane stress arises which must be acknowledged and accounted for in structural assessment exercises. However, in reality the conditions a structure are under is difficult to establish and can substantially deviate from the lab-based tests conditions. This poses problems for the determination of the fracture parameters to be used for the assessment of the components.

This transferability problem in classical fracture mechanics led to the advent of numerical damage models which gave a new perspective on structural assessment procedures. In these models, the damage within the fracture process zone is computed and embedded in the global finite element model of the component which is under a prescribed loading condition. If the three-dimensionality of the analyses is taken in to account and the damage model parameters are given as functions of the triaxiality of the stress state, then the transferability problem is somewhat solved [77]. In this thesis, the phenomenological damage model of cohesive zone elements are used for the experimental validation of the previously mentioned barrel tests of dynamic fracture.

6.3 The cohesive zone model

The cohesive zone (CZ) model is a phenomenological damage model which describes the fracture process zone and fracture by means of a separate interface layer of cohesive elements, which obey a traction-separation law (TSL), embedded between the continuum elements of the global FE model. The TSL relates the displacement jump vector between the two surfaces of the element, δ , to the traction vector, $T = f(\delta)$, acting on the surface. The CZ elements exert a traction between the surfaces of the fracture until a certain maximum displacement between the flanks, or maximum opening, δ_0 , is reached. Therefore the traction-separation law describes the loss of load bearing capacity of the material as a function of a separation, irrespective of the physical details of damage occurring in the actual material. This formulation can be applied to both ductile and brittle damage failure processes [22, 78–80]. A drawback of the cohesive model is that

TABLE 6.1: Definitions of 'thin-walled structure' which exist in the field of engineering

Definition	Description
Geometrical	A structure is called thin-walled, if the thickness is significantly smaller than all other relevant dimensions (normally 10 times smaller). This is sometimes expressed in terms of its slenderness ratio, β . All Aluminium and Glare panels and structures described in this thesis satisfy this definition.
Mechanical	A structure can be regarded as thin-walled, if the stresses in the thickness direction are negligible compared to all other in-plane stress components (plane-stress assumption). This definition raises many interesting questions. In the case of the pressurised barrel tests this condition is satisfied. However, in stiffened fuselage structures, cracks may occur at the boundary of the skin-stringer. In this region, complex three dimensional stress states may develop due to the local constraint precluding the application of conventional shell elements in the numerical analyses.
Structural	The term 'thin walled' is commonly used by design engineers to describe structures which can only carry the applied load by stiffening elements either by use of extra material (reinforcements or frames) or by design principles in order to avoid buckling problems. See scaled fuselage demonstrators tests in Chapter 4.

the crack path has to be defined *a priori* which is sometimes not known to the numerical analyst. Figure 6.1 shows a schematic of the physical damage process using cohesive elements.

The cohesive zone model was inspired by the work of Dugdale [81] and Barenblatt [82], both of whom considered the idea of a cohesive traction preventing a crack from extending. Both authors considered a fracture to have a stress free actual length, and a fracture process zone ahead of the physical crack tip. A cohesive traction was postulated to exist of some constant quantity, σ_0 , (Dugdale, Fig. 6.2(a)) or a traction as a function of the distance from the crack tip (Barenblatt, Fig. 6.2(b)). These concepts were implemented to develop cohesive models which define the tractions as functions of the separation length within the cohesive zone. Material degradation and separation are concentrated in a discrete plane, represented by cohesive elements which are embedded in the continuum elements representing the tests piece or structural component. This allowed the elastic stress singularity in the crack tip to disappear [83]. Figure 6.1(a) shows how the physical process can be represented by the cohesive model. The first application of CZM to the fracture behaviour of a material was performed by Hillerborg et al. [84] to describe the damage behaviour of concrete.

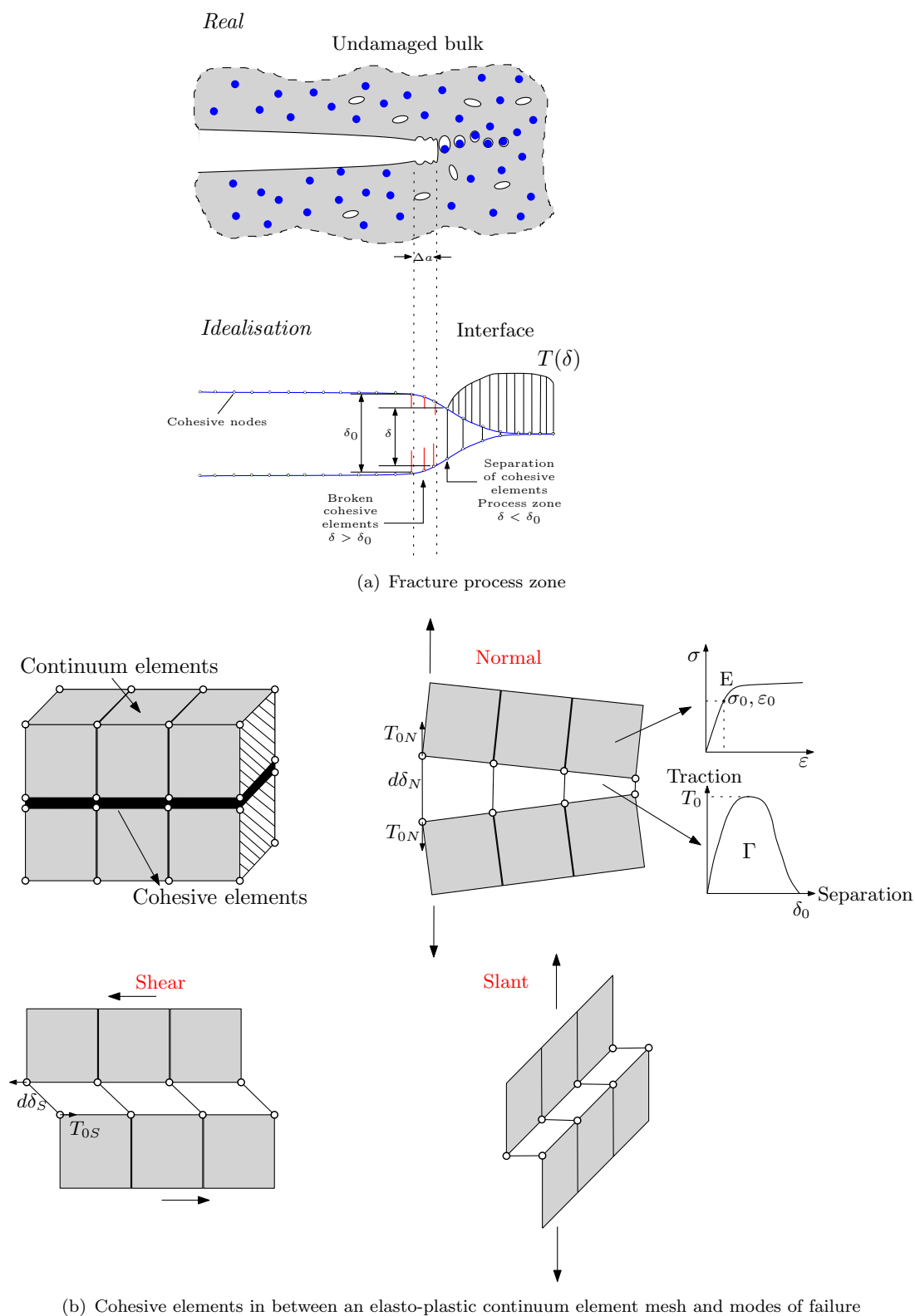


FIGURE 6.1: Cohesive model: Representation of the physical damage process by means of cohesive elements

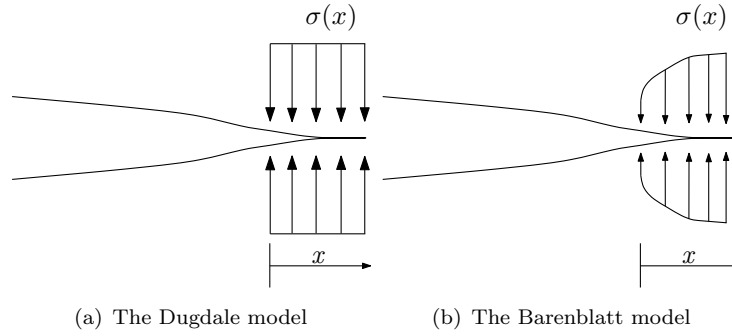


FIGURE 6.2: Cohesive zone model: formulation according to Dugdale [81] and Barenblatt [82]

6.3.1 Traction-separation law

6.3.1.1 Modes of failure

In the field of fracture mechanics, three modes of failure are distinguished, each of which can act in isolation or a combination of the three. The discriminating feature of these failure modes is that they fail to identify the presence of shear lips which can occur in plane strain fracture problems (i.e. theoretical smooth surface). Mode I operates normal to the failure plane and acts in the direction of the normal tractions. Mode II and III are associated with in- and out-of-plane shear respectively. Various criteria exist to account for the mixed-mode interaction of failure and assign different cohesive properties (weighting) for mode I and II/III.

The constitutive behaviour of the cohesive model is formulated as a traction-separation law (TSL), which relates the traction, T , to the separation, δ , the latter representing the displacement jump within the cohesive element. A cohesive element fails when the separation attains a material specific value, δ_0 . The maximum stress reached in a TSL, the cohesive strength, T_0 is a further material parameter. For a given shape of the TSL, the two parameters, δ_0 and T_0 , are sufficient for modelling the complete separation process. In practice, it has been proven useful to use the cohesive energy, Γ_0 , instead of the critical separation. The cohesive energy is the work needed to create a unit area of fracture surface (in fact twice the unit fracture surface because of the two cohesive surfaces) and is given by:

$$\Gamma = \int_0^{\delta_0} T(\delta) d\delta \quad (6.1)$$

A host of TSL have been suggested where the exact shape may vary according to the fracture behaviour of the material. A typical TSL for ductile fracture as depicted in Fig. 6.3(d), has three phases, a semi-linear elastic start where tractions increase with

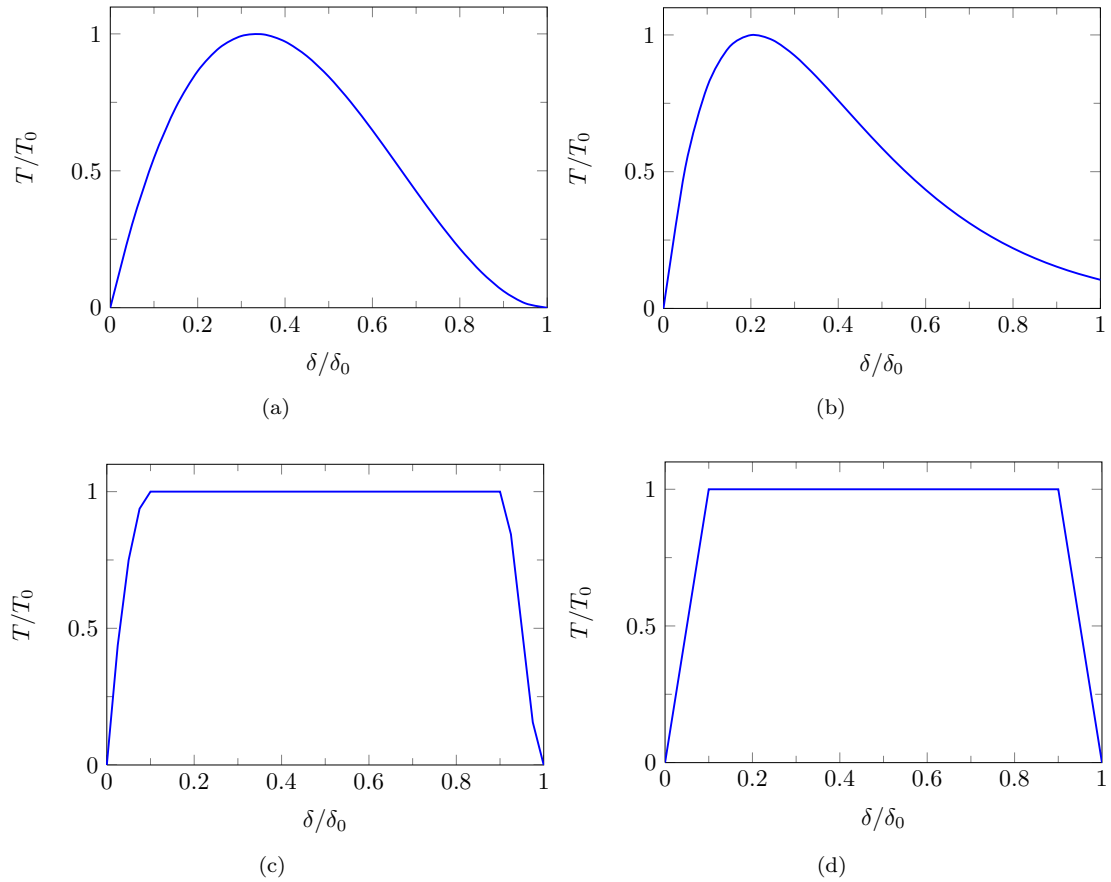


FIGURE 6.3: Typical traction-separation laws: (a) Needleman (1987), (b) Needleman (1990), (c) Scheider, (d) Tvergaard and Hutchinson

increasing opening. This is followed by a constant level of cohesive traction level caused by plastic yielding of the intervoidal ligaments. The last part describes a decreasing traction as the ligaments begin to fail. The increasing and decreasing slopes of the TSL are also present to avoid the numerical problems associated with a step function TSL approach. The exact shape of the normalised TSL is often reported to have no or little effect [85, 86], while others do report an influence [87], but mostly in the area of fracture branching. In this study the recommended Scheider model [83] (Fig. 6.3(c)) is used. Some of the most widely used TSL are discussed below and shown in Fig. 6.3.

Needleman

Needleman [88] (1987) proposed an intrinsic cohesive law formulated as cohesive energy density ϕ of the following form:

$$\begin{aligned} \phi(\Delta_n, \Delta_t, \Delta_b) = & \frac{27}{4} T_0 \delta_n \left\{ \frac{1}{2} \left(\frac{\Delta_n}{\delta_n} \right) \left[1 - \frac{4}{3} \left(\frac{\Delta_n}{\delta_n} \right) + \frac{1}{2} \left(\frac{\Delta_n}{\delta_n} \right)^2 \right] \right. \\ & + \frac{1}{2} \alpha \left(\frac{\Delta_t}{\delta_n} \right) \left[1 - 2 \left(\frac{\Delta_n}{\delta_n} \right) + \left(\frac{\Delta_n}{\delta_n} \right)^2 \right] \\ & \left. + \frac{1}{2} \alpha \left(\frac{\Delta_b}{\delta_n} \right) \left[1 - 2 \left(\frac{\Delta_n}{\delta_n} \right) + \left(\frac{\Delta_n}{\delta_n} \right)^2 \right] \right\} \end{aligned} \quad (6.2)$$

which for mode I is reduced to:

$$T = \frac{27}{4} T \frac{\delta}{\delta_0} \left(1 - \frac{\delta}{\delta_0} \right) \quad (6.3)$$

This TSL is depicted in Fig. 6.3(a).

Needleman [86] also proposed a second exponential model in 1990 to simulate a ductile fracture process. This TSL does not have a zero traction at the moment of failure as can be observed in Fig. 6.3(b). Equation 6.4 defines it, where $z = \frac{16}{9}e$.

$$T = zT e^{\frac{\delta}{\delta_0}} e^{-z \frac{\delta}{\delta_0}} \quad (6.4)$$

Tvergaard

Tvergaard et al. [78] proposed a tri-linear TSL with a stable traction level for most of the opening profile. It is shown in Fig. 6.3(d). It is defined by Eq. 6.5.

$$T = T_0 \begin{cases} \left(\frac{\delta}{\delta_1} \right) & \delta < \delta_1 \\ 1 & \delta_1 < \delta < \delta_2 \\ \left(\frac{\delta - \delta_2}{\delta_0} \right) & \delta_2 < \delta < \delta_0 \end{cases} \quad (6.5)$$

Scheider

An adaptation to the Tvergaard model was published by Scheider & Brooks [89], making the TSL continuously differentiable in order to avoid numerical problems. Equation 6.6 defines the TSL and is illustrated in Fig. 6.3(c). The model is the one used in the non-rate sensitive cohesive simulation performed for this research.

$$T = T_0 \begin{cases} 2 \left(\frac{\delta}{\delta_1} - \frac{\delta}{\delta_1} \right)^3 & \delta < \delta_1 \\ 1 & \delta_1 < \delta < \delta_2 \\ 2 \left(\frac{\delta - \delta_2}{\delta_0 - \delta_2} \right)^3 - 3 \left(\frac{\delta - \delta_2}{\delta_0 - \delta_2} \right)^3 + 1 & \delta_2 < \delta < \delta_0 \end{cases} \quad (6.6)$$

The parameters δ_1 and δ_2 are set to $\delta_1 = 0.01 \delta_0$ and $\delta_2 = 0.75 \delta_0$.

The TSL is unequivocally determined by any two out of the following three parameters

1. Cohesive stress, T_0 .
2. Cohesive energy, Γ_0 .
3. Critical separation, δ_0 .

According to Equation 6.6, the area under the curve in Figure 6.3(c) is given by

$$\Gamma = T_0 \left(\frac{1}{2} - \frac{1}{3} \frac{\delta_1}{\delta_0} + \frac{1}{2} \frac{\delta_2}{\delta_0} \right) \delta_0 \quad (6.7)$$

Consequently, two cohesive parameters are sufficient to describe the TSL, of which T_0 and Γ_0 have been chosen for this procedure. In LS-DYNA the traction-separation law is given by a tabular input of data points of the curve. According to Ref [83](GKSS), the following procedure is recommended:

1. The initial slope, K_{ini} , of the TSL should be as steep as possible. As a rule of thumb, $T_0/K_{ini} < 0.05 \delta_0$ should hold.
2. A constant stress part should terminate at $\delta \leq 0.75 \delta_0$, then the cohesive stress should decrease to zero at δ_0 .
3. If possible the corners of this multi-linear representation should be rounded by additional points.

6.3.2 Alternatives to using cohesive zones

Simulating the fracture process in commercial finite element codes can be achieved through means other than cohesive zone elements. This section offers an overview of the available fracture analysis techniques.

Element erosion

The element erosion technique is similar to that used in Chapter 4 whereby elements are completely removed after a certain criterion is met according to a maximum principal strain or stress value. The main advantage of this technique is that it does not need special meshing or modelling techniques for embedding cohesive elements or special elements for capturing crack-tip singularities. The failure criteria are easily implemented within the constitutive model card of the bulk finite element model. However, element deletion can result in mesh convergence issues particularly in non-linear elastic-plastic problems. It has been reported that such problems can be overcome, as is done in [90], where a Rice-Tracey failure criterion is used with a correction for element size. Furthermore, the loss of mass and inertia ahead of the propagating crack tip can influence the rate of fracture which may yield conservative results.

Nodal release

Nodal release is a technique commonly used in ABAQUS Standard (not too common in LS-DYNA) to simulate crack propagation by duplicating nodes along element boundaries of fracture surfaces which obey a certain crack propagation criterion. Once a criterion is met, such as critical crack opening displacement (COD), the nodes are released and separated from both side of the duplicated boundary and advance to the next crack-tip position. A drawback of this techniques is the need to pre-define the crack path and hence does not allow arbitrary crack paths.

Mesh independent crack propagation - XFEM

In recent years XFEM has emerged as a powerful numerical procedure for the analysis of crack problems. In traditional formulations, the existences of crack are simulated by requiring the crack follow a pre-defined path (or element edges). In contrast, the XFEM does not require such a path since the crack geometry need not be aligned with the boundaries of elements. This provided huge flexibility and versatility in modelling. This is achieved by enriching the nodes of the elements intersected by the crack with additional degrees of freedom (DOFs) and functions that reproduce the asymptotic LEFM fields. This allows the modelling of crack discontinuity within the crack tip elements allowing for cracks to follow arbitrary paths under a variety of loading conditions. This has yet to be implemented into LS-DYNA, although it is available in ABAQUS Standard with some limitations which rendered it unsuitable to tackle this dynamic problem.

Other techniques are available which are not discussed here such as continuum softening (i.e. Gurson-void model and smeared crack approached) in addition to the Virtual Crack Closure Technique (VCCT).

TABLE 6.2: Reported cohesive properties of thin sheet aluminium 2024 T3

Source	Thickness (mm)	Γ_N (kJ/m^2)	T (N/mm^2)
[92]	1/2.3	19	$2.7 \cdot \sigma_y = 2.7 \cdot 345 = 931.5$
[93]	2.3	17	$2.0 \cdot \sigma_y = 2.0 \cdot 285 = 570.0$

6.4 Derivation of static cohesive parameters of Al 2024-T3

6.4.1 Identification procedure using numerical optimisation

A two parameter optimisation method is adopted in the present procedure. The experiments for the parameter identification were performed on standard fracture specimens which conform to ASTM standards. The size, thickness and stress state of the specimen for parameter identification has been chosen so that it is similar to that of a thin fuselage (thin-walled) structure in order to ensure the same failure mechanism.

The fracture properties of the material were determined by experimental data on a M(T) centre-cracked panel with anti-buckling plates, performed by the TU-Delft [91], with a width of $2W = 400mm$, a thickness $t = 1.00mm$ and an initial crack length of $2a_0 = 103mm$ (Test B24LT-10), as illustrated in Fig. 6.4(a). From this test, in addition to the cross-head displacement, three different values are measured: the force, F , the crack mouth opening displacement, COD , and the crack extension, Δa , averaged over the thickness according to ASTM standard and determined by multi specimen technique. Based on these values a $F(COD)$ curve, Fig. 6.8(b), and the average applied stress versus cross-head displacement, Fig. 6.4. Fracture resistance curves were provided $K(\Delta a)$, but since the use of K for a thin-walled specimen under large scale yielding conditions is questionable, it is not used for the determination of the cohesive parameters and a $F(\Delta a)$ curve is used for numerical identification instead.

In the beginning, the fracture extends as a function of stress, but as the stress increases, the fracture releases more potential energy per unit of fracture increase until this becomes equal to the amount of energy needed to fracture the same unit length of fracture. At this point, no additional external energy is needed to propagate the fracture and the fracture accelerates independently of the externally applied load.

The object of this section is to derive the cohesive energy Γ_N and traction T for a mode I opening. No data or estimates were found for the other modes. These are set equal to the mode I parameters therefore in the simulations. As is pointed out in [83], the two parameters are not independent from one and another, but need to be derived together. Two sources give estimates of these values. they are given in Table 6.2.

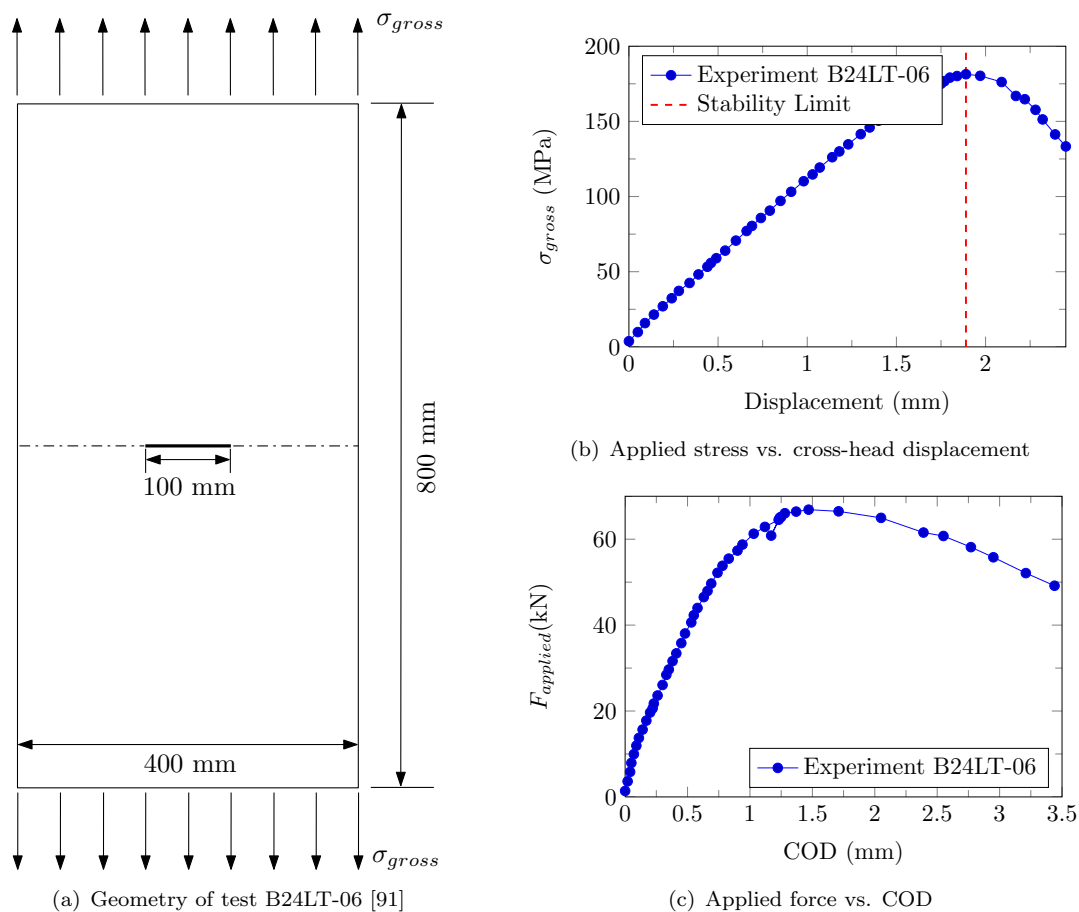


FIGURE 6.4: Experimental crack data from B24LT-12 tests [91]

The trial and error procedure adopted to identify the cohesive parameters was determined by running a number of simulations using varied cohesive properties until a reasonably good approximation of the experiment was attained. This procedure can be quite time consuming and may require up to 10-20 simulations until the objective target function for the minimisation of the error is fulfilled. Figure 6.8(b) shows the applied force versus the crack opening displacement and the point of instability.

The elastic-plastic properties have been described by three distinct values, given for two different material directions which are given in Fig. 6.5. The data was obtained from Ref [91] of six tensile tests according to ASTM E8. The tests were performed on a 3 tonnes Zwick tensile machine at the Structures and Materials Laboratory of the Delft University of Technology. The same batch of materials used in the tensile tests was also used in the $M(T)$ fracture toughness tests. Although though it is known that the cohesive model is very sensitive to changes in elasticplastic properties and the values given in Table 6.3 are by far not sufficient for a precise description of the stress state around the crack tip, no alternative was possible from generating a material flow curve from these values. From the table, one can see that the orientation dependence regarding yield strength

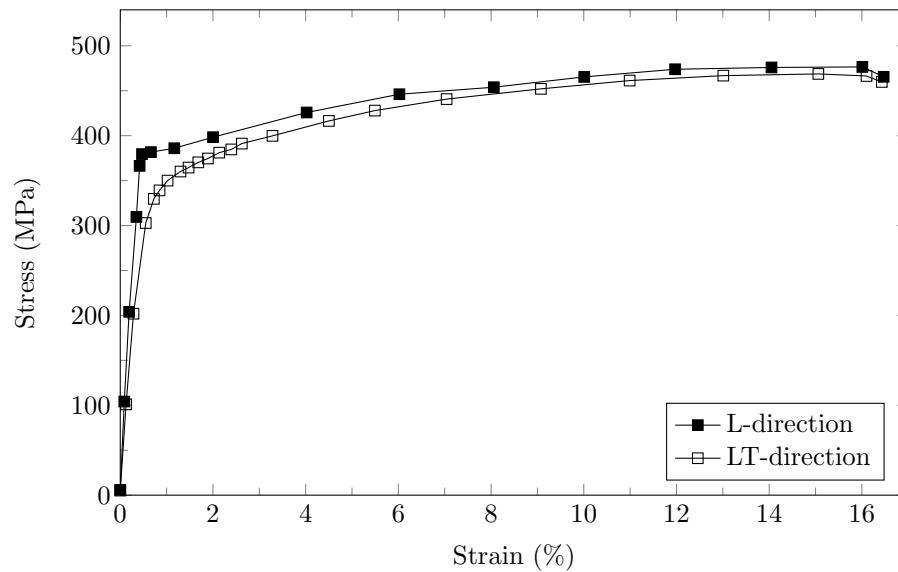


FIGURE 6.5: Experimental data given for the characterisation of the deformation of Aluminium 2024-T3 material

TABLE 6.3: Experimental stress-strain data given by M705 technical report for the Al2024 material [91]

	σ_y (MPa)	σ_{ult} (MPa)	$\varepsilon @ \sigma_{ult}$ (%)	E (GPa)	$\nu_{12} = \nu_{21}$ (-)
L-direction	380	475	16.47	76	0.33
LT-direction	330	470	16.43	70	0.33

and hardening is rather pronounced. However, in LS-DYNA, only Hills anisotropic yield function is available, which does not account for an orientation dependent hardening. Since no appropriate model is available and the aim of the study is to predict the residual strength with the lowest effort possible, isotropic von Mises plasticity is used in all simulations.

6.4.2 Numerical model

As outlined previously, the cohesive model is utilised for the numerical crack extension analyses. Arbitrary material decohesion processes are idealised in this model by reducing the fracture process zone to an interface with zero width. Cohesive elements are available for 2D (plane strain and plane stress), axisymmetric, shell and 3D finite element models. In this study, 3D cohesive elements (MAT_138) have been implemented using existing formulations within the material library of the finite element code LS-DYNA ¹.

¹The current version of LS-DYNA precludes the use of 2D cohesive elements although user defined elements have been implemented successfully in the open literature [94]

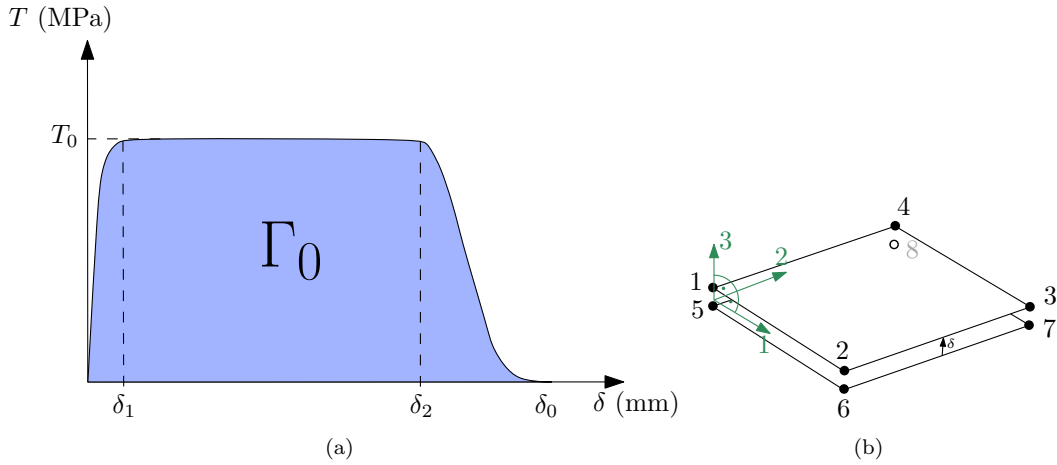


FIGURE 6.6: Shape of the traction-separation law as described by Eq. 6.6 (right) and cohesive elements for three-dimensional models (left)

In the present investigation the shape of the traction-separation law is described by Eqn. 6.6 [89] as recommended by Ref. [83].

The shape of Eq. 6.6 is shown in Fig. 6.6(a), which is given in tabular form in LS-DYNA. It is assumed that the traction-separation law has a high stiffness in the beginning, $\delta_1 = 0.01 \delta_0$, and contains a significant part with a constant stress, $\delta_2 = 0.75 \delta_0$. The 3D cohesive elements implemented in LS-DYNA can handle interface elements with a finite volume in the undeformed state, see the right sketch of Fig. 6.6. However it is recommended that, for mesh generation guidelines, the height of the cohesive element is significantly lower than the thickness, critical opening displacement and general geometrical properties. To avoid computational problems, zero thickness cohesive element were defined by generating finite volume interface elements as per usual, and then shifting the nodes such that the top and bottom nodes coincide.

6.4.3 Parameter identification

The 3D FE model of the M(T) specimen represents one eighth of the panel with three symmetry planes and consists of 29016 linear 3D elements within the uncracked domain (LS-DYNA 8 node elements with nodal rotations), see Fig. 6.7. Six layers of solid elements over the half thickness are generated in the ligament, with a constant length width of $150 \mu\text{m}$ in the cracked domain and their length being $170 \mu\text{m}$ in order to keep the aspect ratio of the elements close to 1.0. The cohesive surface consists of $6 \times 200 = 1200$ cohesive elements (MAT_138), thus allowing for a maximum crack extension of 30 mm. The whole model has 113,472 degrees of freedom. 3D elements were used to describe the interfacial separation and the continuum behaviour of the material.

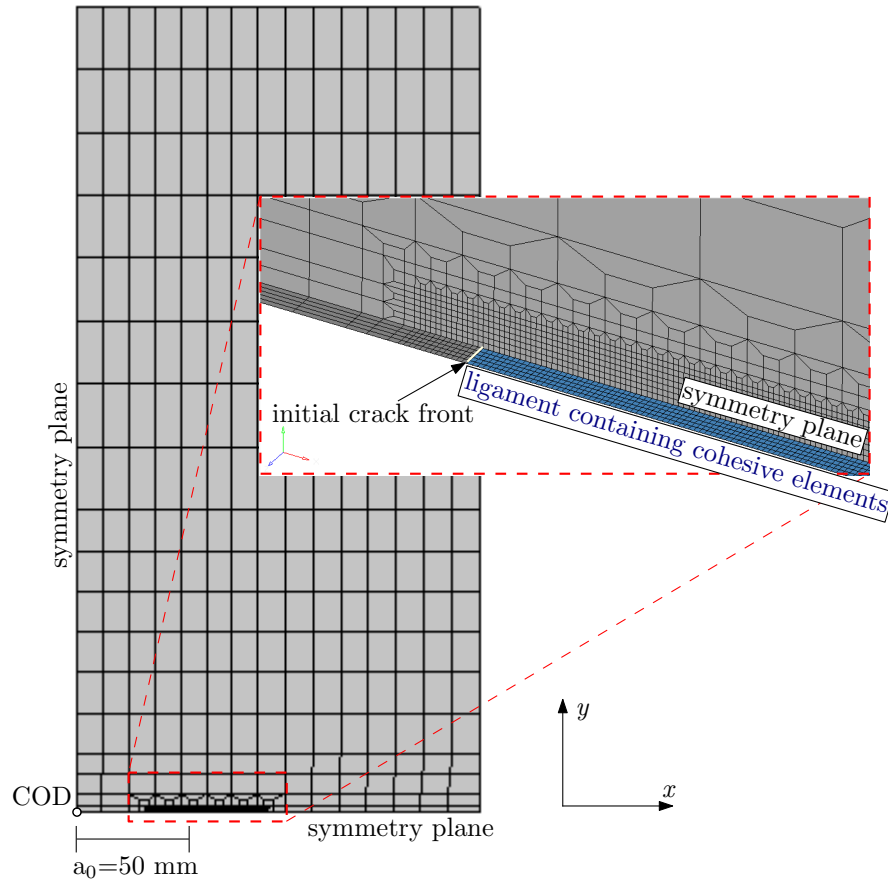
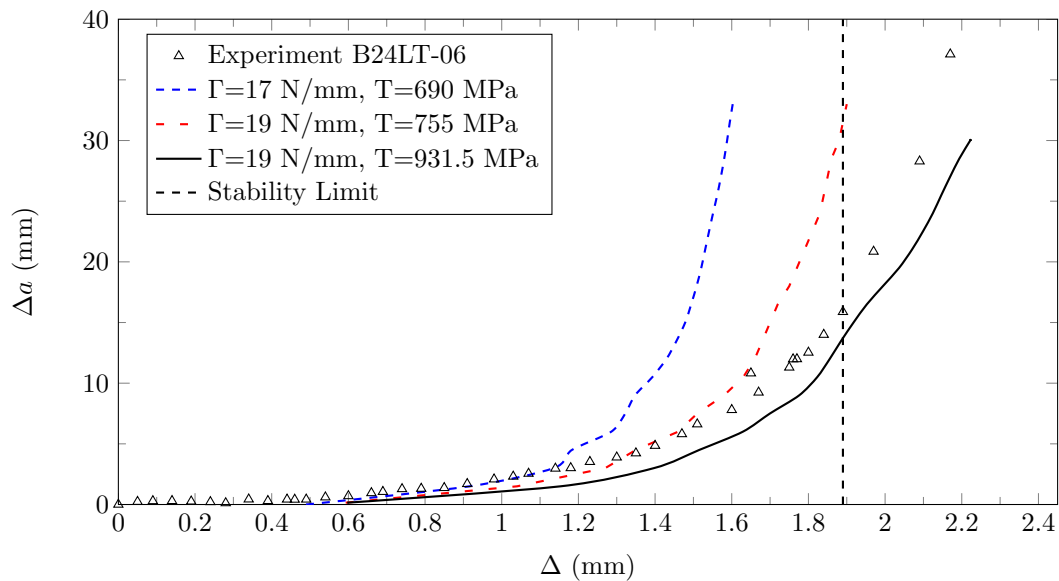


FIGURE 6.7: 3D finite element mesh for the M(T) specimen (1/8 of the structure).

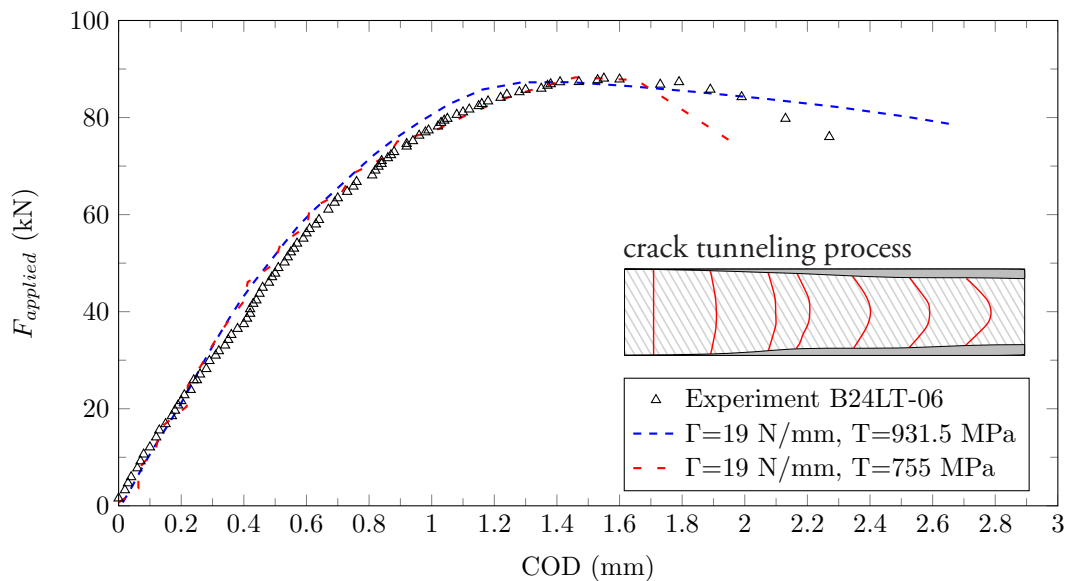
Using 3D elements can vastly increase the model size and thus computation time compared to shell elements. A small reduction of the problem may be achieved by coupling a 3D mesh for the crack tip region to a shell mesh for the global structure [94], but since approximately 90% of all elements are placed along the ligament, the savings are not worth the additional meshing effort.

In order to simulate the quasi-static test with displacement control loading using an explicit codes such as LS-DYNA, uniform low velocities are applied at the nodes on the top boundary. Previous calculations demonstrated that applied nodal velocities of about 500–750 mm/sec are slow enough to prevent inertia effects in the calculation and satisfactorily fast to improve CPU efficiency. The loading is applied by a prescribed displacement at the top of the specimen. As a result, the total force, F , COD and the crack extension, Δa , are determined. The latter is calculated based on the total area of the failed cohesive elements divided by the original thickness.

The comparisons between simulation and experiment for a range of cohesive parameters with respect to the crack tip position (Δa) as a function of the applied displacement (Δu) and the applied force $F(COD)$ vs. $COD(\delta a)$ curves are shown in Fig. 6.8. Even



(a)



(b)

FIGURE 6.8: Parameter identification for the 3D FE model of the M(T) specimen. Comparison of simulation and experiment for the respective optimised parameter sets. [91]

though there is excellent agreement to the point of instability, there is a noticeable disagreement beyond this point.

To support the findings of this model, further efforts were made to investigate the fracture characteristics and behaviour of this thin-walled specimen. Figure 6.9 shows the initiation and evolution of crack growth in term of the Von Mises yield criterion, where the crack propagates from the centre of the initial crack (i.e. only 1/2 predictive model

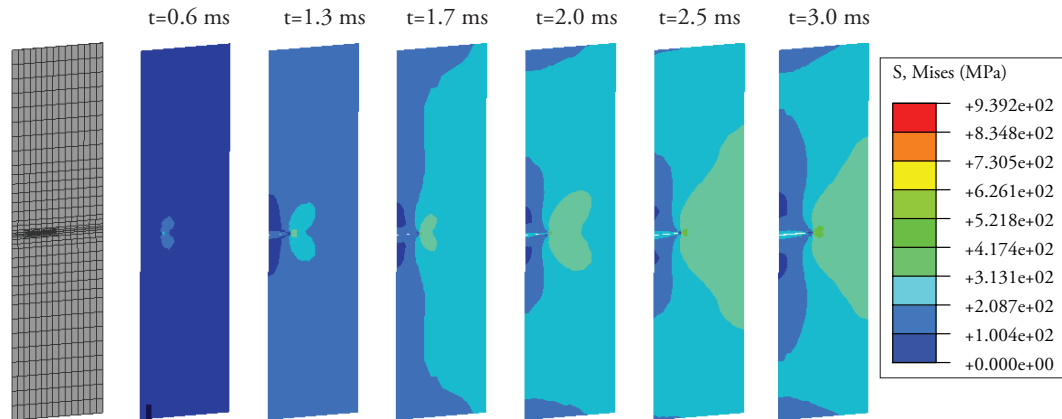


FIGURE 6.9: Tensile stresses at different time intervals during the propagation of the crack using hexahedral elements.

is shown). Further verification of the developed predictive model is made by observing the crack surfaces during crack propagation. It has been widely reported that during ductile crack propagation of thin metals, a characteristic phenomenon called tunneling is observed. Crack tunneling is when the crack front appears straight at the early stages of crack growth and progresses more rapidly in the centre of the thin-walled specimen leading to the formation of the rounded crack front profile. This is clearly shown in Fig. 6.10, which illustrates the progression of crack tunneling obtained directly from the finite element model. As a result of this process, additional out-of-plane components of shear stress become significant as the highly plastic deformation takes place near the crack region. However, the study of this phenomena (as well as slant fracture) is outside the scope of this analysis and was mentioned merely to further support the verification of this model. Thus, we will restrict the current study to determine the optimum fracture parameters for Aluminium 2024-T3 of 1 mm thickness.

In conclusion, the optimal parameter set for the 3D simulation is $\Gamma_0 = 19 \text{ kJ/m}^2$ and $T_0 = 931.5 \text{ MPa}$, the critical separation resulting in $\delta_0 = 0.024 \text{ mm}$.

6.5 Simulation of dynamic fracture

6.5.1 Finite element model

The barrel tests exhibit two planes of symmetry which can be exploited to reduce the number of elements and hence computational time and power. However, it transpired that the plane of symmetry which cuts through the circumference of the barrel in two was difficult to exploit and proved problematic as the analysis would go unstable and result in infinite nodal velocities belonging to the cohesive elements. As a result only the

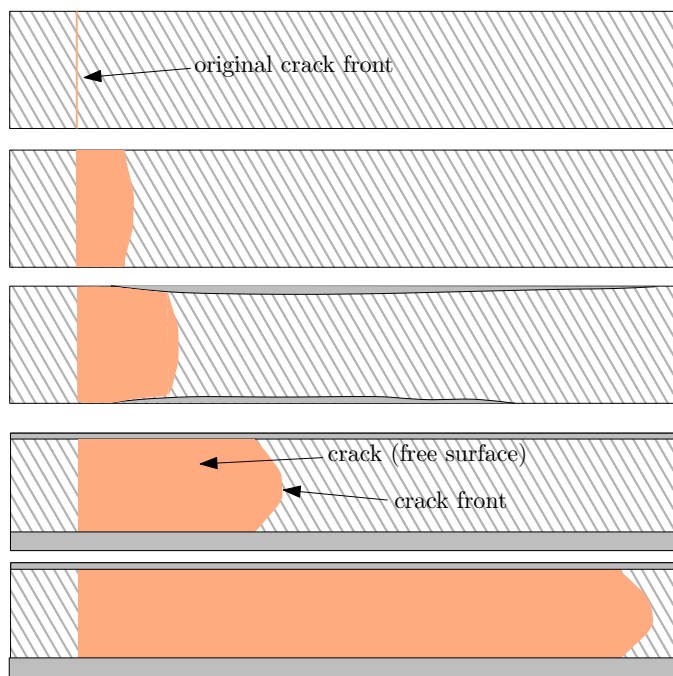
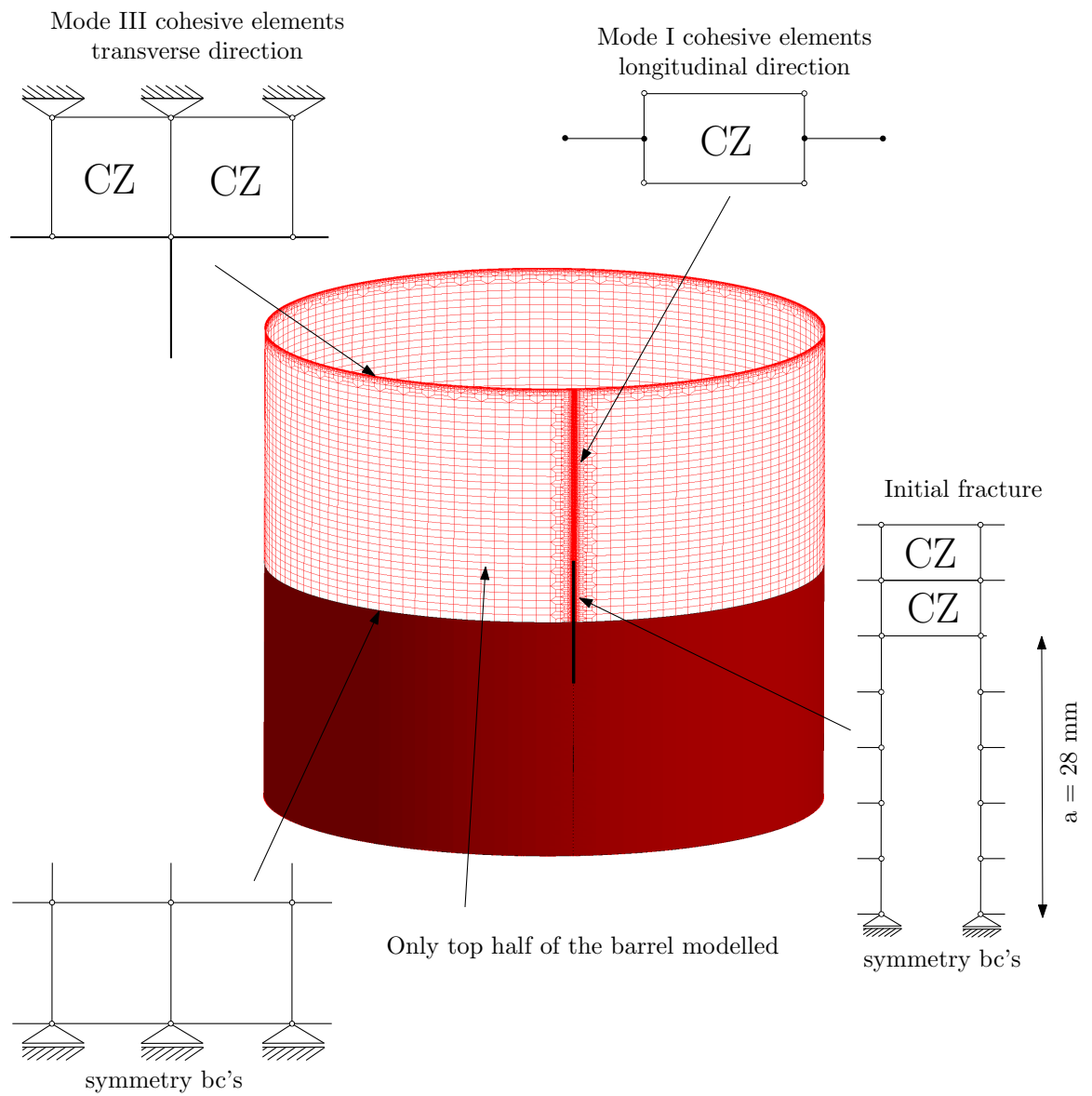


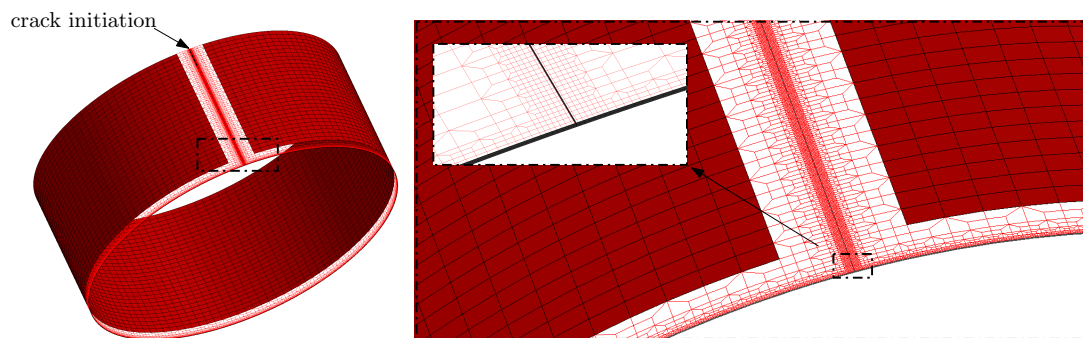
FIGURE 6.10: Details of the crack tunneling for the case modeled with 3D solid elements. The red region indicates where $\Gamma_{disp}/\Gamma_I = 1.0$.

symmetry through the longitudinal direction of the barrel was exploited. Figure 6.11 gives modelling details of the explosive barrel tests which include symmetry boundary conditions, insertion of cohesive zone elements and overall mesh design. The complexity of the mesh design is clearly illustrated in order to have an acceptable mesh size within the fracture process zone (typically 0.625 mm). Experimental observations gave a clear sequence of fracture which began at the initial notch of the barrel which propagated along the longitudinal length of the barrel. Upon reaching the top and bottom part of the barrel, fracture continued along the circumference of the barrel resulting in a double door effect, as shown in Fig. 5.10. Therefore, two different fracture paths were implemented to account for this observation which significantly increased the complexity and mesh design of the problem.

Furthermore, in contrast to the previous flat fracture model in which the continuum and cohesive elements were 3D dimensional, the scale and complexity of the problem precludes the use of these elements in the continuum domain and were defined by fully integrated shell elements. As only solid cohesive zone elements are currently supported within LS-DYNA, a transition between the shell elements of continuum domain and the solid cohesive elements was defined.



(a) Setup of finite element model of explosive barrel tests



(b) Closeup of mesh refinement within the fracture zone (cohesive elements are shown in black)

FIGURE 6.11: Finite element details of explosive barrel tests

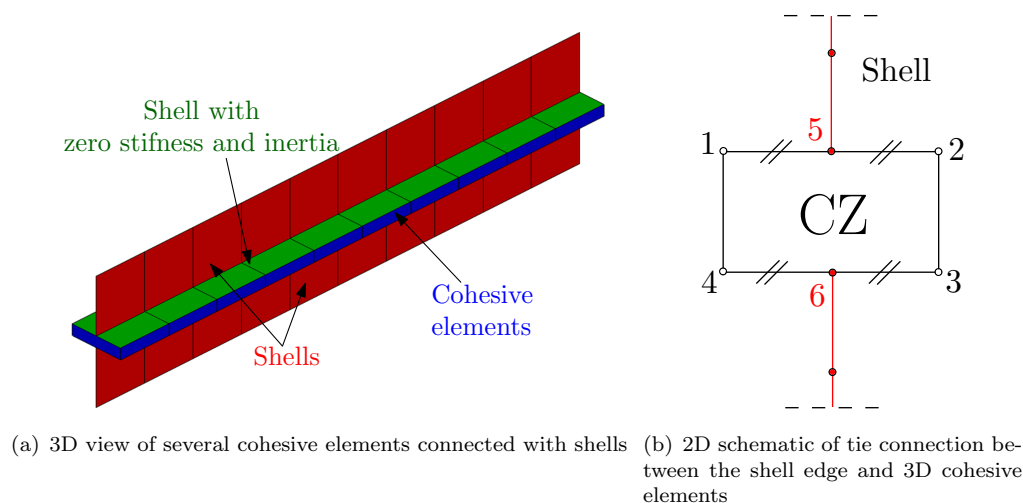


FIGURE 6.12: Tie formulation between shell edge and 3D cohesive elements (adopted by [21])

6.5.1.1 Connecting shells to cohesive zone

A robust solution to this problem was proposed which took advantage of the *CONSTRAINED card in LS-DYNA to define a shell-brick interface by constraining nodal degrees of freedom in such a way that the shell/brick translates and rotates in a certain way. The CONSTRAINED_SHELL_TO_SOLID card is a nodal constrain algorithm which ties the node of a shell element to an orthogonal line of nodes belonging to a solid element. A schematic of this, reproduced from Ref. [21], is given in Fig 6.12 which shows a method of a single brick element tied to a pair of shells. Nodes 1, 2, 3 and 4 are nodes on the cohesive element that defines a line on that solid part which are constrained to remain linear throughout the simulation. Shell nodes 5 and 6 are tied to the solid part and maintain the same relative spacing between the first and last brick node (1,2 & 3,4). Nodes 5 and 6 are free to rotate as imposing additional constraints are not possible since this procedure is limited to one constraint per node in LS-DYNA.

Moreover, to avoid error messages in the solution phase relating to the fact that the cohesive elements are not explicitly connected to other elements, i.e.

```
*** Warning: The top/bottom of cohesive element 1
            is not attached to an adjacent element.
```

, zero stiffness and inertia shells are additionally placed on the upper and lower surface of the cohesive elements, see Fig. 6.12(b). They do not have any effect in the results and are not included in the stiffness matrix.

An additional set of boundary conditions are defined at both ends of the geometry which refer to the steel lid of the barrel. It is assumed that the steel lids behave in a rigid, fixed manner and are not affected by the explosive event. Therefore the nodes corresponding to the top and bottom of the steel lid are constrained in all translational and rotational degrees of freedom.

6.5.2 Pressure load curves

Upon detonation, the explosive charge transmits a fast moving pressure wave to the barrel walls under an internal pressure of 200 kPa. Thus, there are two factors which need to be addressed here; one is the description of the pressure profile at each point of the cylindrical barrel, and secondly establishes the intimate relationship between internal pressurisation and the explosive shock wave.

The latter has been investigated in Ref. [95] in which the MMALE formulation within the explicit finite element solver, RADIOSS, was used to successfully model the complex blast wave phenomena in cylindrical structures as a function of longitudinal length and internal pressure. In this study, a pressurised cylindrical structure similar to that described in Chapter 5 is modified such that the parameters within the interior Eulerian mesh (air) accounts for both atmospheric and pressurised (200 kPa) loading conditions. It is clear from Fig. E.4, which is taken from the central perimeter of that barrel, that both loading cases are characterised by an instantaneous rise in pressure, albeit of different magnitudes of maximum overpressure and times of arrival. The additional internal energy per unit volume drives the shock wave to travel faster and imparts a higher pressure on the barrel walls. Furthermore, a second peak in pressure is observed (reflected pressure) which again is significantly advanced than in the non-pressurised case. This result is significant as it implies that under the combined effects of inertia and cabin pressurisation, additional energy can be spent to drive multi-site damage long after the initial dissipation of the explosion. The reader is encouraged to refer to Appendix E for a more extensive discussion and analysis.

The results of this study give credence to the idea that the MMALE formulation can provide a comprehensive description of the pressure distribution within the *pressurised* cylindrical structure. Following this study, the explosive barrel tests were simulated using LS-DYNA to obtain pressure-time curves at different locations of the structure. Although the original barrel tests contained a pre-notch to initiate dynamic crack propagation, this feature added unnecessary complications and was outside the scope of this task. Due to the inherent symmetry of the barrel problem, only one-eighth of the barrel was modelled using the appropriate boundary conditions along the symmetry planes

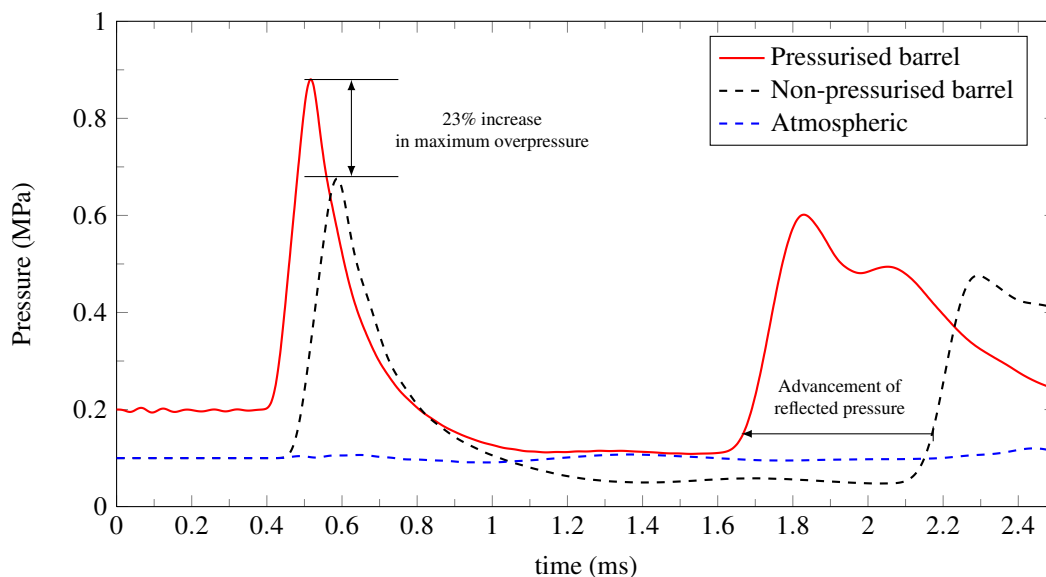
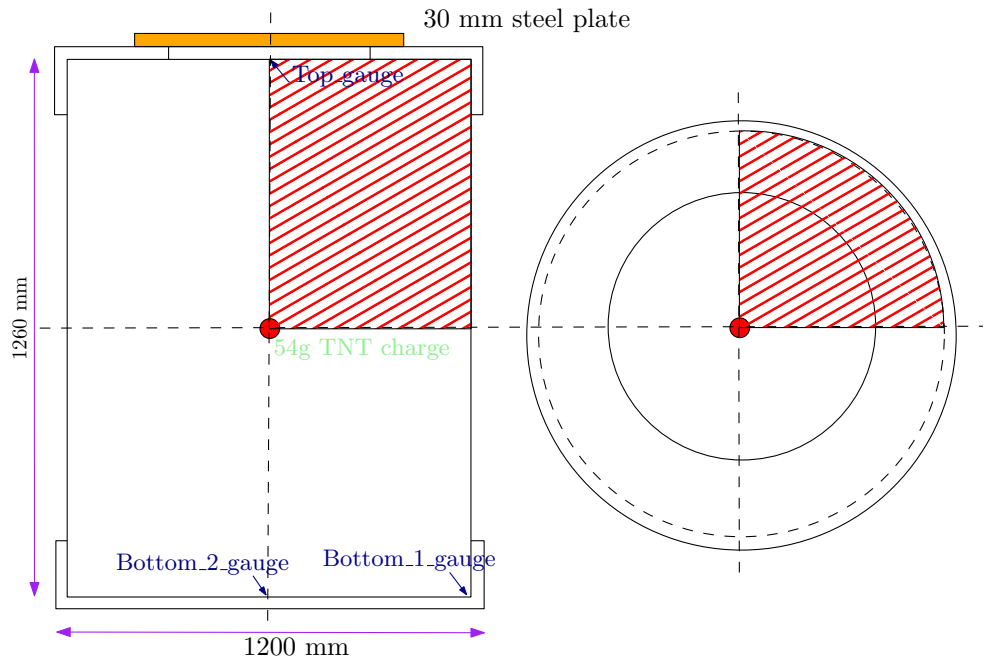


FIGURE 6.13: Plot of blast pressure profile for different internal pressures taken from the central perimeter of a closed barrel subjected to an internal explosive of 54g TNT charge

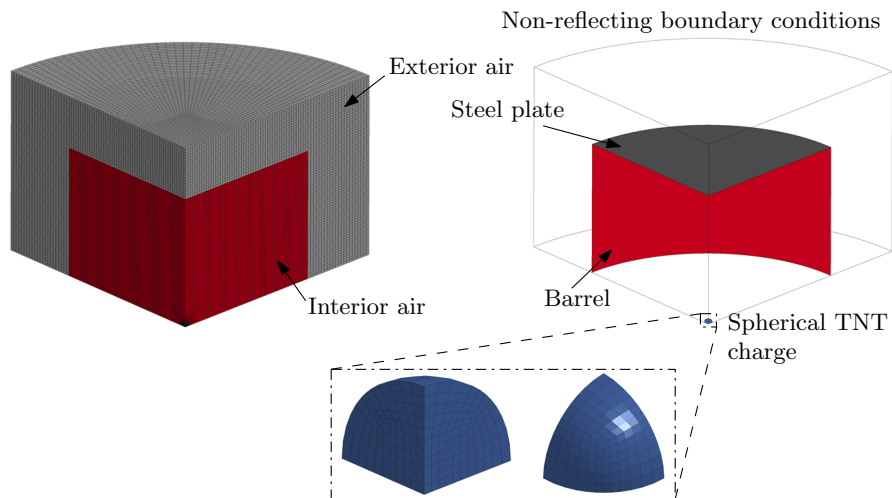
as shown in Figs. 6.14(a) and 6.14(b). Similarly to the model used to simulate the flat panels, it is imperative that the model could capture a reasonably accurate shock peak pressure due to the sharp discontinuity in the pressure wave. Therefore a fine mesh resolution is required, where the spherical explosive mesh and its corresponding air components are fine enough to match accurately the shock pressure that originates from the explosive. As shown in Fig. 6.14(b), the ignition point is placed in the centre of the cylindrical barrel. For TNT, the radius is 20 mm and its weight is 54g. Seven elements are needed to span the radius of the sphere to adequately build up the detonation pressure during the explosive burn.

The initial detonation and subsequent propagation of the 54g TNT charge is shown in Fig. 6.15, where contours of fluid iso-surfaces clearly illustrate the radial distribution and impact on the boundary of the pressurised barrel tests. The pressure distribution at the top of the barrel is compared with that obtained from the experimental tests using pressure gauges.

Clearly, as shown in Fig.6.16, there is excellent agreement concerning the first initial peak pressure suggesting that the assumptions and simplifications introduced in the analysis can accurately represent the blast event. A slight discontinuity in the post-peak decaying region is observed that may be attributed to the close proximity of the point of interest with the boundary of the barrel where the numerical coupling algorithm is applying nodal forces to resist penetration. This can also be due to the discontinuity of the mesh within the barrel where the air elements within the explosive charge region



(a) Schematic of pressurised barrel tests condition



(b) Description of 1/8 explosive-air model mesh and barrel arrangement

FIGURE 6.14: Numerical description of pressurised barrel tests

are mainly of quadrangular orientation and diverge radially to account for the cylindrical perimeter of the barrel. As the ALE formulation in high explosive events is sensitive to mesh density and shape, this discontinuity may influence the shock wave velocity of the explosive. However, the relative errors in arrival time and initial peak magnitude are negligible and this represents an excellent approximation for the problem. Comparison of the pressure profile beyond the initial pressure profile is misleading and clearly shows lack of agreement. This is due to the fact that in the actual experiment a pre-notch was present and propagated during the high explosive event, venting pressure during the process which in turn will help drive the propagating crack long after the initial blast

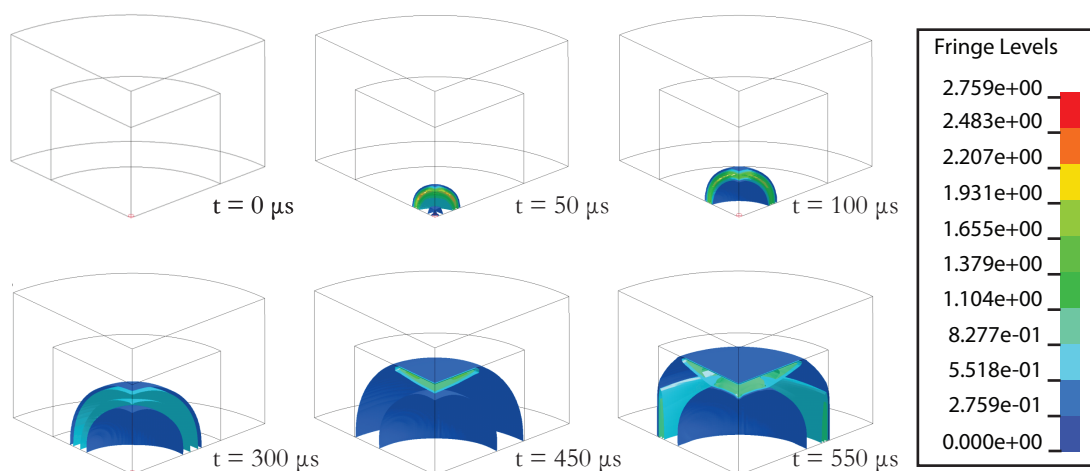


FIGURE 6.15: A typical pressure wave propagation within the pressurised barrel at different time intervals (fringe levels in MPa)

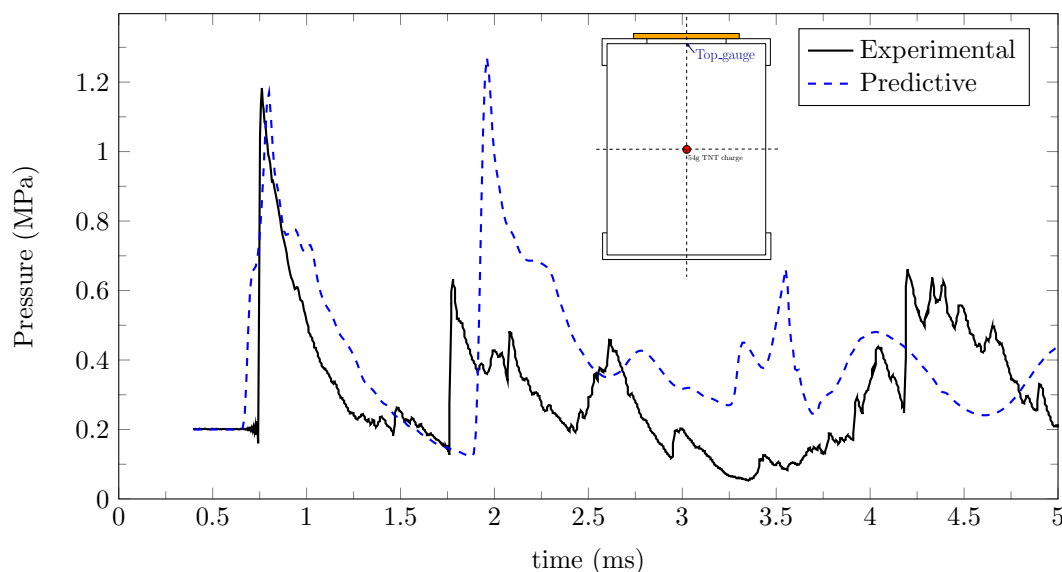


FIGURE 6.16: Comparison of the experimental [26] and the LS-DYNA model for an internal charge of 54g TNT. The experimental curve presents an initial pressure peak of 1.2 MPa at about $t = 0.75$ ms

event.

Finally, five pressure-time curves were extracted from various points of the barrel. Figure 6.17 shows the geometry of the barrel tests and the five points where the pressure was calculated, which are given in Fig. 6.17(b). The pressure curves differ in time of arrival and scale factor in the peak maximum overpressure, as the shock wave radially expands with increasing distance. The close proximity of points 1 and 2 results in coincident load curves, in contrast to the others which are displaced by a few milliseconds (takes longer to arrive at the top of the barrel). The load curves were subsequently exported

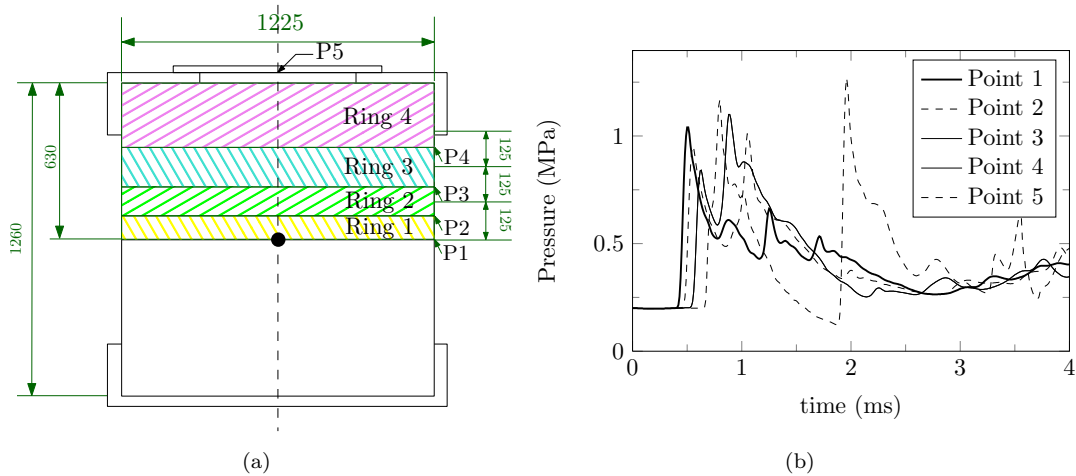


FIGURE 6.17: Location (a) of the predicted pressure load curves (b) and their corresponding division in rings.

in the numerical model and were applied to each shell set which represents each of the four 'ring' domains.

6.6 Capturing the crack velocity

LS-DYNA is not the obvious FE code of choice in dealing with fracture problems as its origins lie in highly nonlinear dynamic problems such as crash analysis. Therefore the code does not have specific modelling and post-processing capabilities for fracture mechanics analyses, unlike ABAQUS/Explicit. However, LS-DYNA allows the user to manipulate the post-processing of results via third-party software such as MATLAB or FORTRAN.

During the analysis, the status of each time step is written to a message file which includes error messages and time of element deletion. When the cohesive elements satisfy the failure criteria, the element fails in its path and LS-DYNA in the analysis terminal reports elements failure in its message log. An example error message would be:

```
solid element 2077 failed at time 1.60019E+00
```

As shown, only the element ID and time of failure is reported. Therefore, it is possible to obtain the time of fracture which passed certain points along the fracture path at known distances from the initial fracture front. Of course there are several ways to accomplish this, but the method of highest fidelity is to consider each element deletion increment separately. The file is interpreted by a MATLAB code which scans the failure

message and reads the coordinates of the failed element number/ID from the mesh file. The relevant distance to the crack tip position is then assigned to this element with its corresponding time of failure. The crack-tip position vs. time can therefore be obtained. Furthermore, to derive a crude value of the crack-tip velocity profile, simple numerical differentiation of this data can be performed:

$$c_n = \frac{a_{n+1} - a_n}{t_{fail,n+1} - t_{fail,n}} \quad (6.8)$$

However, this method can result in numerical instability and smoothing problems, since the dependent variable in this case is 'time'. During very fast fracture events, it is possible that a number of elements will fail at the same discrete time step, therefore Eq. 6.8 will report infinite values of crack-tip velocity as the time increment between consecutive failure reports approaches zero. A way of circumventing this problem is to lump and add all the fracture increases into a single event per time step, preventing local displacement jumps and obtaining crack-tip positions curve which are continually differentiable.

If the number of time increments chosen by the user is insufficiently high, an unstable, almost discrete velocity profile will be produced. Therefore the decision was taken to artificially increase the time increment at the cost of computation time to obtain an acceptable level of smoothness. It should be stated that either method does not alter the shape or magnitude of the velocity profile, merely improves its smoothness and visual interpretation.

6.7 Comparison between experiments and simulations

Figure 6.18 shows a comparison of the simulated longitudinal crack growth rate with those obtained experimentally. Figure 6.18(b) shows the calculated crack position versus time and Fig. 6.18 plots the terminal crack velocity (c_{crack}/c_R) against crack position. It is clear that significant differences exist between the simulated and experimental fracture metrics. The rate-independent cohesive zone model in LS-DYNA using the cohesive fracture parameters overestimates the crack velocity by an order of magnitude. The predicted maximum crack velocity is approximately 1500 m/s (nearly 50% of the Rayleigh wave speed) which is far greater than the experimental value (\approx 300 m/s).

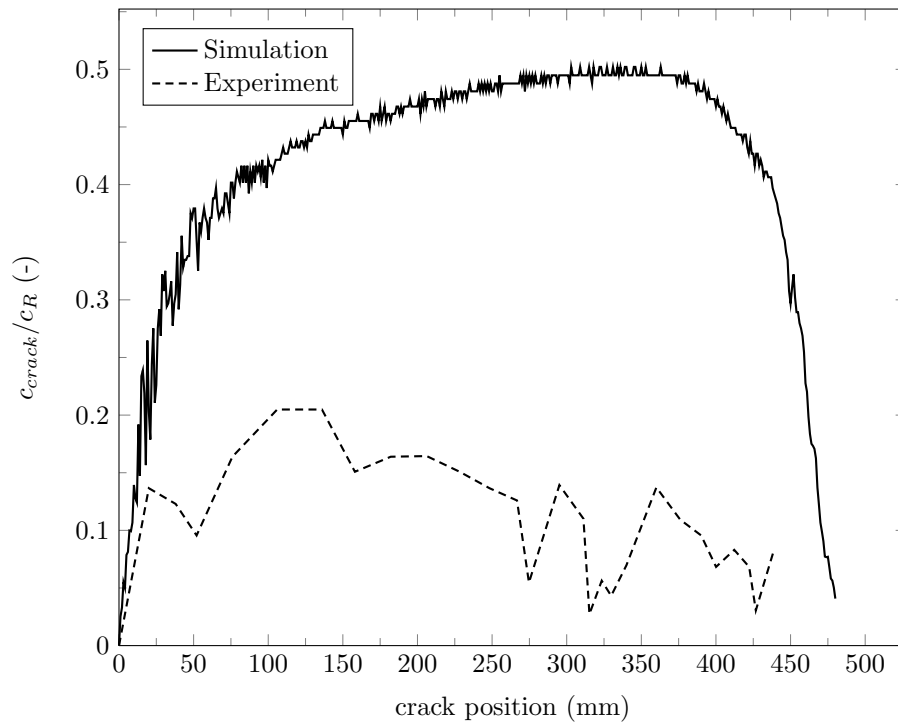
Figure 6.19 presents the von-Mises stress plots at different simulation times where it is observable that the crack grown in the longitudinal direction first followed by the opening of the crack along the circumference of the barrel. Only one half of the barrel is shown. Furthermore, the region in the vicinity of the crack tip clearly shows the

appearance of plasticity due to the ductile behaviour of the material during the crack propagation.

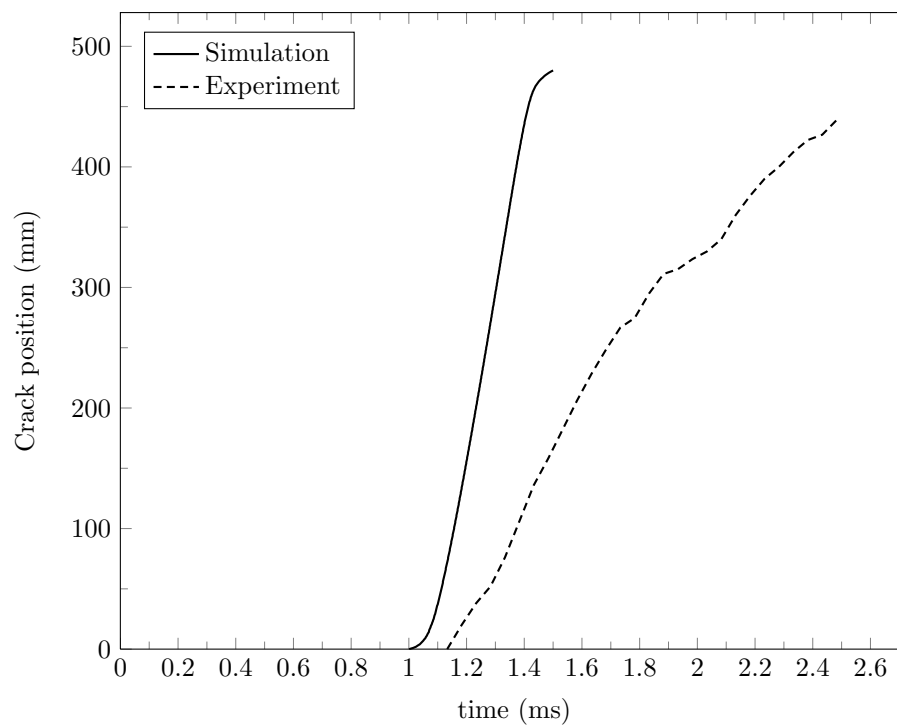
It is well known that high speed deformation in solids introduces stress waves into the structure and hence inertia effects become rather significant and in many cases can affect the energy absorption of the structure. As discussed in Chapter 3, the strain rate effects can increase the flow stress and strain hardening of a metal. Furthermore, dynamic deformation and fracture during a blast event can include high local temperature increases due to adiabatic heating which reduces the flow strength and counteracts the strain-rate hardening effect. These so-called phenomena can significantly affect the fracture toughness and hence crack-tip velocity, factors which are not taken into account in the present analysis. An excellent discussion on dynamic fracture by Freund [71] states that 'as the crack advances more rapidly, the material is deformed more rapidly and a larger cohesive stress is required in order to achieve the requisite crack tip opening displacement.' A larger cohesive stress leads to a higher cohesive energy (area under TSL curve), which suggests that a strengthening of the material at the crack-front may develop, resulting in greater dissipation of energy.

To investigate this issue further, a study was performed by varying the cohesive stress, T , and energy, Γ . Considering that the cohesive element has an initially high stiffness, the area under the non-dimensional TSL is close to being equal to unity. Therefore, an increase in the maximum traction, T_O , proportionally increases the cohesive energy, Γ , for a given maximum opening, δ_0 . A number of simulations have been performed to match the predicted crack-tip position data with the experimental observed fracture propagation rates. The initial values of the cohesive properties are set equal to the static cohesive properties obtained in the previous section. The results of these simulations are given in Fig. 6.20. It is clear from this figure that as the cohesive properties increase by the same factor, the time at which unstable crack growth initiates also increases. The stresses needed for crack propagation are higher compared to the case with static cohesive properties, which in turn reduces the crack growth rate. Higher values of cohesive stress led to fracture arrest in the initial fracture phase. A good match was achieved with a cohesive stress and energy factor of 1.3.

However, this explanation trivialises the complexity of the dynamic phenomena which is developing in the fracture process zone. The triaxiality of the stress state in the fracture process zone influence the cohesive zone behaviour, a factor which is not considered in the present analysis. An increase of triaxiality leads to a higher cohesive energy, therefore in dynamic analysis, the presumption of ductile fracture will be inaccurate if the change of triaxiality is ignored. Due to limitations of LS-DYNA it is not possible to obtain information regarding the triaxiality from within the cohesive zone elements nor



(a) velocity as a function of crack position



(b) crack position as a function of time

FIGURE 6.18: Comparison of the experimental crack tip position (from TestAL03) with that of simulations ($\Gamma=19$ kJ/m² $T=931.5$).

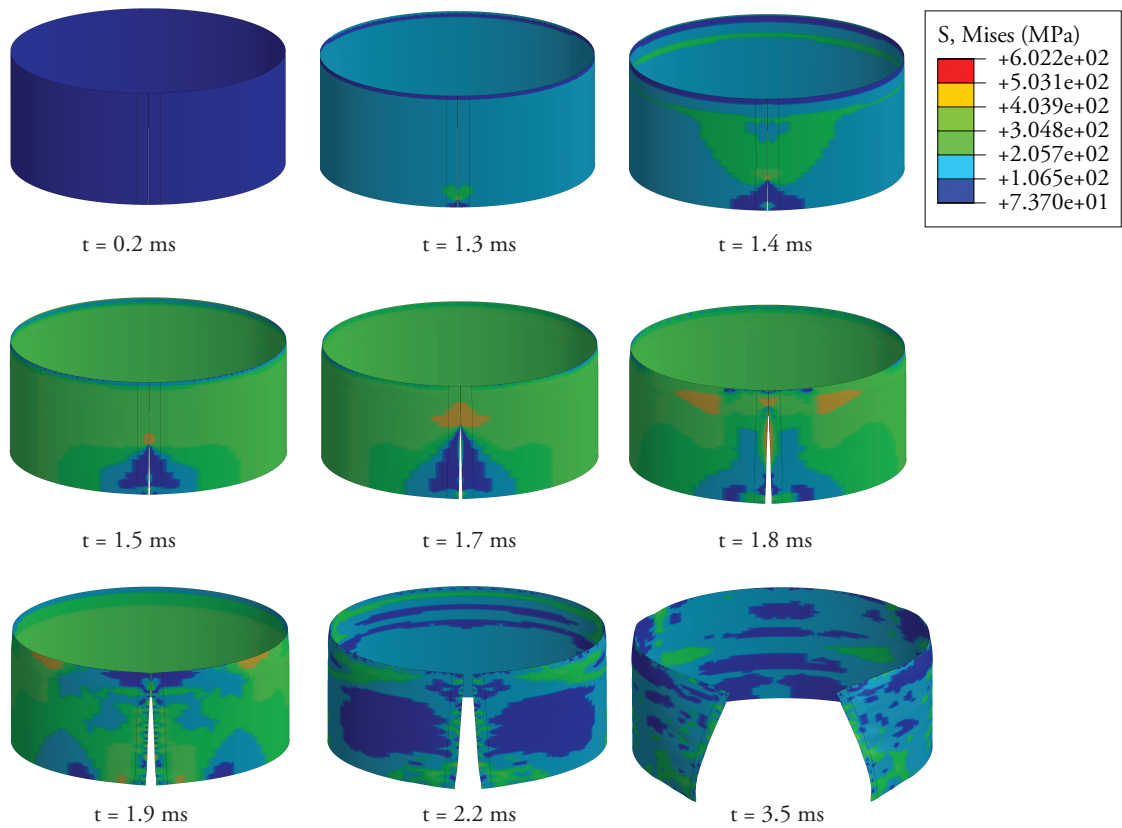


FIGURE 6.19: Von Mises stresses for different simulation time of testAl03

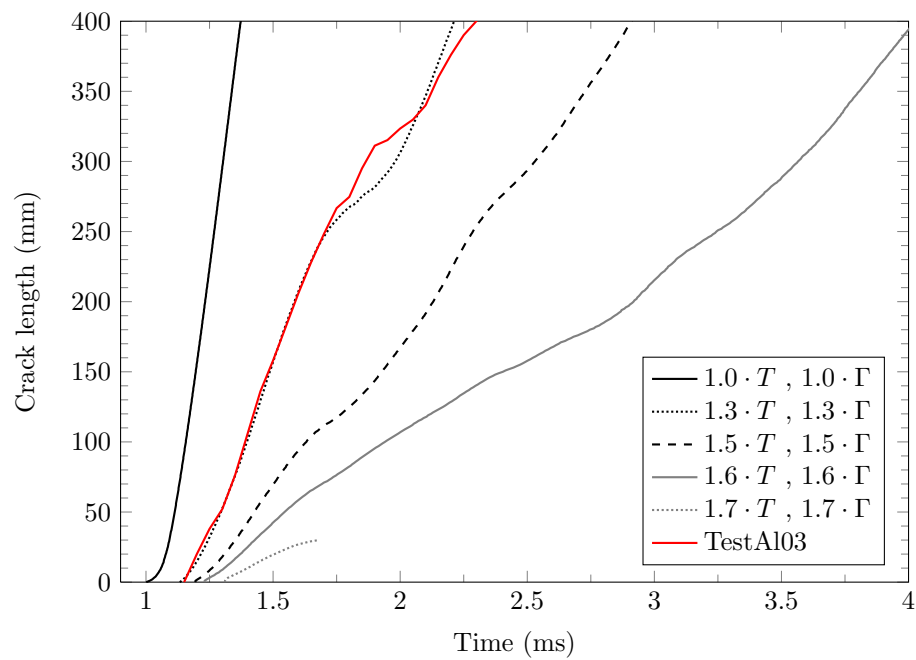


FIGURE 6.20: Changes in static cohesive fracture parameters to match experimental results

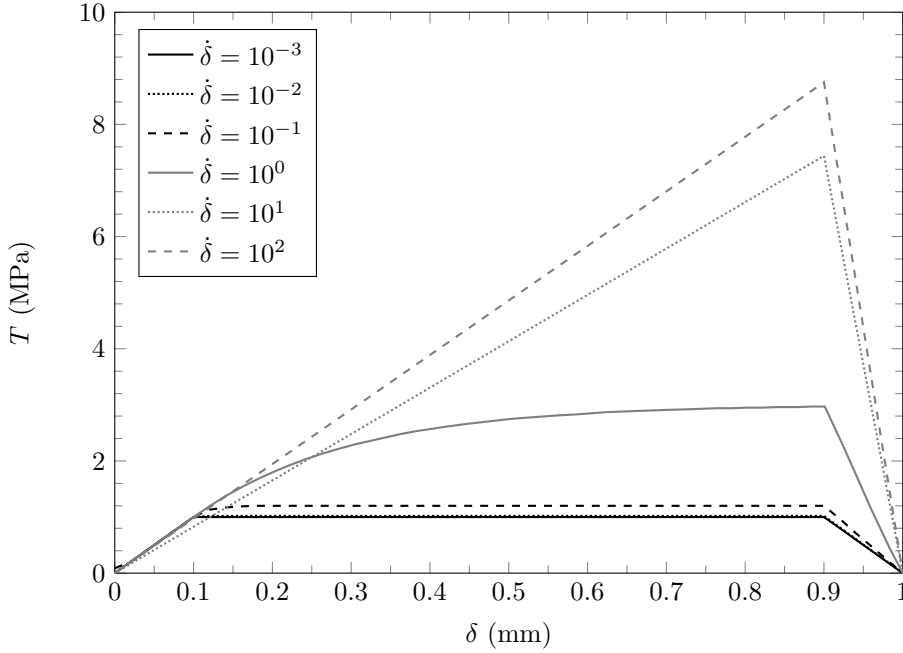


FIGURE 6.21: Effect of the opening rate on the Perzyna visco-plastic cohesive formulation

bulk material.

It is therefore clear that the use of strain-rate independent cohesive models is inadequate for dynamic fracture analysis. Efforts have been made to simulate dynamic ductile crack growth using strain-rate dependent cohesive elements, such as Anvari et al. [96] and Zhang et al. [97].

A brief description here is given to show how strain-rate dependent cohesive elements are used to simulate crack growth under dynamic loading condition. This cohesive formulation is an extension of the Perzyna continuous visco-plastic continuum model [21, 98]. This formulation is sensitive to the opening rate of the cohesive elements which, at higher loading rates, increases the cohesive stress and thus the area under the TSL curve (increase in cohesive energy). This is shown graphically in Fig 6.21.

The original Perzyna model was a strain-rate sensitive model for continuum elements which have been rewritten and modified so that 'stresses' and 'strains' were expressed in terms of 'tractions' and 'openings'. This formulation is defined by the following set of partial differential equations:

$$\psi(T_{eq}) = \left\langle \frac{T_{eq}}{T_{0N}} - 1 \right\rangle^{N_{pz}} \quad (6.9a)$$

$$\bar{m} = \frac{\partial T_{eq}}{\partial T} \quad (6.9b)$$

$$\dot{\delta}_{vp} = \frac{1}{\eta}(T_{eq}) \bar{m} \quad (6.9c)$$

$$\dot{q} = \dot{\delta}_{vp} \bar{m} \cdot h_{pz} \quad (6.9d)$$

$$\dot{T} = K(\dot{\delta} - \dot{\delta}_{vp}) \quad (6.9e)$$

The term T_{eq} is a single traction parameter which describe the three-dimensional state T . It is based on a modification of the quadratic, anisotropic Hill yield stress criteria, and has been modified to take into account the work hardening \dot{q} . Thus, T_{eq} is defined as:

$$T_{eq} = T_{0N} \sqrt{\frac{\left(\frac{T_I}{q_I}\right)^2}{T_{0N}^2} + \frac{\left(\frac{T_{II}}{q_{II}}\right)^2}{T_{0S}^2} + \frac{\left(\frac{T_{III}}{q_{III}}\right)^2}{T_{0S}^2}} \quad (6.10)$$

this is the variable of the over-traction function, ψ , given in Eq. 6.9a, a function which describes the relative traction level above the yield traction, defined as the maximum traction in Mode I, i.e. T_{0N} ². The term $\dot{\delta}_{vp}$ represents how much the opening of the cohesive surfaces increase due to plasticity. Again, when this term is below the yield limit, this value is equivalent to zero, which indicates that the response is within the elastic region. Beyond its traction limit, this term increases gradually which implies a decrease in the material stiffness until the visco-plastic opening rate, $\dot{\delta}_{vp}$, is equal to the actual opening rate, $\dot{\delta}$, and thus the material is fully plastic. Equation 6.9d represents the evolution of work hardening, an expression which influences the yield traction of the material and plays a significant role in cyclic loading applications. This term has been omitted in this study, as it is not expected to have an effect on the fracture behaviour of the pressurised barrel tests.

An inverse modelling procedure was conducted to determine the Perzyna parameters, K , η and N_{pz} as described in Ref [21], which has a complete study of effects of each one of these parameters. The derived parameters for the pressurised barrel tests are shown in Table. 6.4.

²The brackets in this equation are McCauley brackets which mean that the function is equal to zero if T_{eq} is below T_{0N} .

TABLE 6.4: Perzyna parameters for Aluminium 2024-T3 barrel tests

T_{ON} (N/mm ²)	T_{OS} (N/mm ²)	Γ_{0N} (N/mm)	Γ_{0S} (N/mm)	$K_{1,2}$ (N/mm ³)	N_{pz} (Nms/mm ²)	η (-)
931.5	931.5	19	19	$2 \cdot 10^6$	3.125	0.32

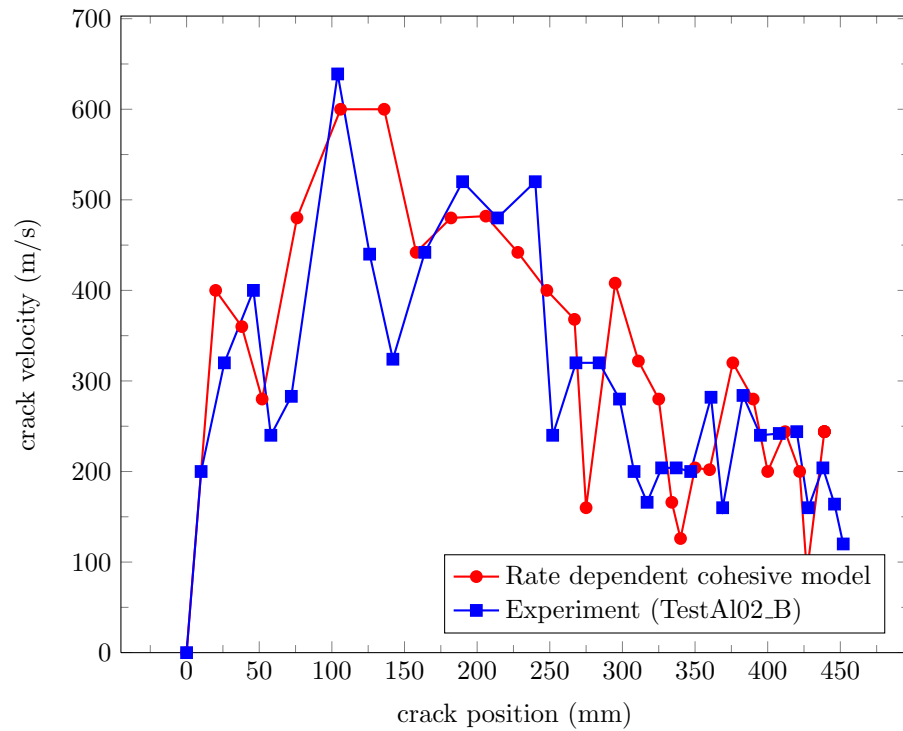
The Perzyna model has been implemented in the LS-DYNA code as a user-defined material model and calibrated against the pressurised barrel tests.

A comparison of the experimental fracture metrics (testAl02) with that of the rate dependent cohesive simulations is shown in Fig 6.22. A very good agreement is found based on the derived fracture parameters which have clearly reduced the rate of crack propagation compared to the rate-independent cohesive model. However, this model is still in its infancy and it would be premature at this stage to extract many conclusions, as the derived parameters are based on very limited experimental data. More independent fracture tests are required to support and perhaps recalibrate the parameters. Furthermore, the physical meaning of the Perzyna parameters are somewhat dubious and is unclear how such parameters, η & N_{pz} , could be derived from experimental data or experimental stress techniques. This impacts the fidelity of the Perzyna and requires more extensive investigation. Simulations on singular element tests reveal that η influences the maximum dynamic traction as function of the opening rate, see Fig. 6.23³. At higher values of η , the plastic yield part disappears and the TSL curve reduces to a tri-linear expression. Furthermore, the Perzyna exponent parameter N_{pz} appears to have a similar effect, although the effect is rather less pronounced.

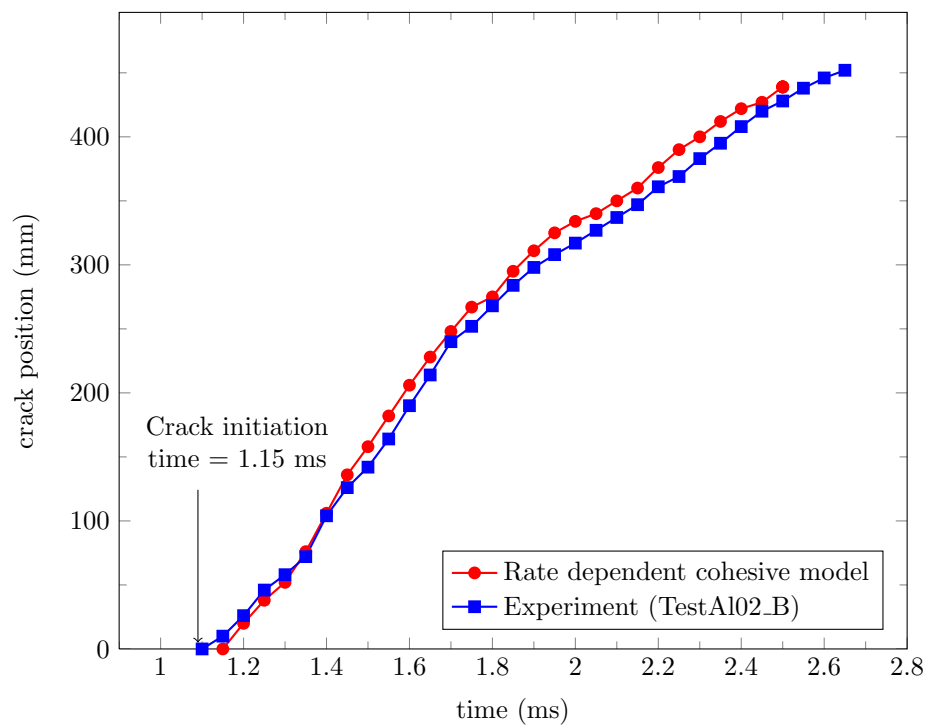
6.8 Conclusion

An integrated experimental design is devised to provide appropriate input parameters for conducting and validating large-scale dynamic fracture simulations. The loading and kinematic boundary conditions were reproducible with minimum unknown parameters. The experimental setup provided high quality qualitative fracture metrics, which are representative of the dynamic phenomena under investigation, from high speed imaging systems which could be compared with the numerical model. However, the highly complex blast wave phenomena in the cylindrical structure required third party data from MMALE/FSI models for a complete setup of the dynamic fracture model. These pressure curves were loaded to a separate lagrangian fracture model which contained cohesive elements. These elements were inserted in the FE discretization of the global

³In this study the maximum opening δ_0 and T_0 was set to 1 and $K_{1,2}=10$



(a) velocity as a function of crack position



(b) crack position as a function of time

FIGURE 6.22: Comparison of the experimental crack tip position (from TestAL03) with that of simulations obtained using the rate-dependent cohesive formulation.

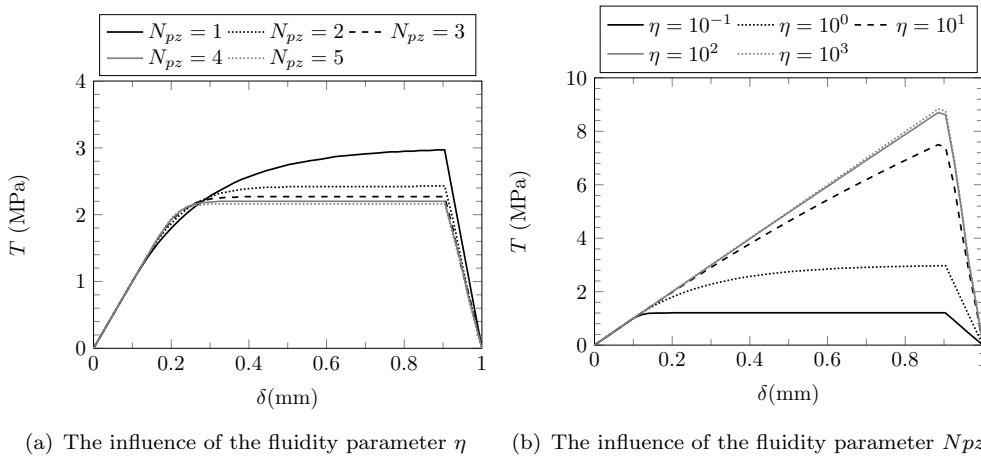


FIGURE 6.23: Influence of Perzyna parameters on the TSL response extracted from a single element test

body to simulate fast growing cracks. The formulations of the cohesive elements govern the manner in which the crack flanks separate according to a traction separation law. The cohesive parameters were initially derived from small-scale quasi-static fracture toughness experiments. The modelling procedure was not straightforward, as the mesh design of the problem and the transition between shell and solid elements proved rather challenging. Numerical results showed that using rate-independent cohesive models in LS-DYNA were insufficient to capture the rate of crack propagation as it did not take into account the influence of loading rate on the cohesive traction within the fracture process zone. A modified visco-plastic rate-dependent Perzyna model was implemented which required the derivation of certain parameters. These visco-plastic parameters were derived from a single pre-notched barrel test subject to an internal explosion of 54g TNT, through an inverse modelling procedure to obtain the optimum solution with the experimental data. The results in the Perzyna rate dependent model showed good agreement and consistency with respect to the crack initiation time and average crack tip velocity. However, it is premature to deduce that these parameters are independent of geometry and scale as they were derived from only one set of experimental data. This is a topic of future work.

This chapter has highlighted the numerous challenges which hinder the validation of dynamic fracture experiments. However, the computational effort has been considerably reduced thanks to the integrated philosophy adopted early on in the project to produce well-controlled, minimal experiments. It is clear that separate small-scale dynamic fracture experiments are needed to extract accurate cohesive laws under dynamic loading conditions. The challenge remains how this data translate to individual rate dependence cohesive models, of which there are a few. It is clear that the current modelling

capabilities in LS-DYNA have not reached technological maturity to make dynamic fracture problems cost effective, both in terms of computational time and labour. Future work may involve more advanced crack propagation techniques such as XFEM which eliminates the shell-solid transition and allows the crack to follow an arbitrary path. Furthermore, current XFEM formulations consider rate-dependence although they are still in its infancy. Modelling the dynamic fracture of Glare still remains an elusive goal as there are a multitude of failure mechanisms operating at once which should be captured by the proposed model. Further work should attempt to model Glare as a homogeneous structure using 'smeared' mechanical properties and assume the fracture path obeys a traction separation law which takes into account the glass-fibre bridging mechanisms. Therefore, the shape of the TSL may have more of an influence than in the case of isotropic ductile crack growth.

Chapter 7

Summary and Conclusions

7.1 Summary and Conclusions

THE growing threat of sabotage to thin-walled structures, such as the fuselage, is a topic which has gained considerable momentum in recent years. During this period, there has also been a drive within the aerospace industry to produce lighter and more fuel efficient aircraft by replacing conventional metallic materials in large scale components with novel composite materials, in applications where weight saving and structural integrity are of critical concern. The present thesis describes the behaviour of Glare and its metallic counterpart, Aluminium 2024-T3, under dynamic blast loading conditions. These structural materials have current applications in primary aerospace structures although their full potential has yet to be exploited, particularly in blast mitigation.

In line with previously mentioned trend in aircraft blast mitigation design from small-scale experimental tests/blast trials towards more advanced numerical methods, an experimental-numerical approach is presented based on the finite element (FE) method. Commercially available FE codes, such as ABAQUS [24] and LS-DYNA [25] were used, rather than in-house finite element analysis tools to allow the transferability of skills, experience and more importantly subroutines to the wider industrial and academic community. Demonstrating and adapting existing codes to meet current technical challenges allow further transparency and better understanding of the computational methodology,

The research presented in the current thesis consists of numerical work based on third-part experimental tests performed within the framework of the EU-funded program VULCAN (AST5-CT-2006-031011). Due to the sensitive nature of the project, all blast experiments were performed in secure facilities at the Royal Military College (RMA) in

Belgium and TNO in the Netherlands.

In Chapter 2, an introduction to FMLs was given and described in detail. Beside the development of FMLs (in particular Arall and Glare), the constituents, variants and the main characteristics were given. These constitutive parameters would formulate a large bulk of input data to describe the mechanical response of Glare in the numerical analyses. Also, the impact and blast behaviour of FMLs were discussed which showed early indications of the potential of Glare as a blast attenuating structure.

In Chapter 3, robust and efficient computational models were developed for the purpose of V & V which successfully modelled the dynamic non-linear behaviour of Glare panels subjected to blast loadings. Numerical model validation was performed considering case studies of Glare panels subjected to a blast-type pressure pulse for which experimental data on the mid-point back face deflection and post-damage observations were available. In the first case study, excellent agreement of mid-point deflections and evidence of severe yield line deformation were shown and discussed against the performed blast tests. A further parametric study identified Glare as a potential blast attenuating structure, exhibiting superior blast potential against monolithic aluminium plates. The results were normalised and showed that for a given impulse, Glare exhibited a smaller normalised deflection, outperforming monolithic Aluminium 2024-T3 plates. In the second case study, the multi-material ALE formulation (MMALE) with fluid-structure interaction (FSI) was utilised to model the response of more complex blast loads. Cohesive tie-break contact algorithms are implemented to model interlaminar delamination between adjacent plies. The energy dissipated to create new interlaminar fracture surfaces was determined to be 2-8 % of the total internal energy. The remaining energy was dissipated in irreversible damage mechanisms within the aluminium and composite plies, although plastic deformation in the aluminium layers was the dominant energy-absorbing mechanism.

In Chapter 4, the next phase of the thesis moved towards the vulnerability and survivability of scaled fuselage demonstrators subjected to internal detonations. The purpose of this chapter was to develop survivability strategies to mitigate the effects of internal explosions. Vulnerability maps of the scaled demonstrator based on various failure scenarios, materials and charge location were developed for the purpose of examining airframe hardening options. All analysis results were compared and supported, to an extent, with experimental test data within the VULCAN consortium.

Motivated by the limitations of previous studies and the need for more systematic validation methods, a coordinated effort is reported in Chapters 5 and 6 to validate experimentally large-scale finite element simulations of dynamic fracture using cohesive

zone models. To determine the interplay between cylindrical aircraft structures and the response of individual fatigue cracked panels (e.g. pre-existing MSD in aging aircraft), well-controlled and minimal experiments for dynamic fracture of blast loaded barrel tests have been performed on three popular aerospace materials; Aluminium 2024-T3, Glare and CFRP [26]. The dynamic event induced crack growth speeds in order of magnitude of several hundred meters per second, metrics obtained via image processing of high speed images. Glare exhibited the lowest crack growth speeds and displayed a combination dynamic ductile behaviour and fibre bridging. The results also highlighted the poor blast attenuating qualities of CFRP, displaying crack speeds nearly ten times that of Glare with evidence of crack bifurcation-branching.

Finally, in an effort to model the dynamic ductile crack growth of Aluminium 2024-T3 from the previous barrel tests, a numerical cohesive zone approach is followed; a layer of interface elements which behave according to a traction-separation law is inserted along the fracture path. Static cohesive properties were extracted from standard fracture toughness tests and extrapolated to the aforementioned barrel tests. This method proved inaccurate to predict the rate of fracture as a considerable difference was found between the experiments and predictive results. This discrepancy was attributed to the rate-independence of the cohesive formulation which failed to take into account the influence of triaxiality and the opening rate on the local cohesive traction within the fracture process zone. To circumvent this problem, a Perzyna visco-plastic rate-dependent cohesive formulation is discussed and implemented which gave better representative results in terms of crack-growth rates. However the visco-plastic parameters were derived from one set of experimental data.

7.2 Recommendations for future work

In order to define some interesting areas of further research, it is useful to present first a perspective of this research in relation to the main aims and objectives.

Blast mitigation of structural materials to withstand acts of sabotage require a fundamental understanding of its use in real-life applications, whether military, civil or in urban areas. This thesis focusses on thin-walled structures which are predominantly used in aircraft applications where stiffness and weight are driving performance factors. It has been shown that if a cylindrical thin-walled structure, such as the fuselage, is explosively detonated then the combination of internal pressurisation and the explosively driven blast impulse can cause severe structural damage and generate cracks that propagate along the length of the aircraft at supersonic speeds. According to the author's opinion based on the numerical work performed in Chapter 4, a small amount of

explosive (IED) can lead to catastrophic failure (both in wide-body and narrow bodied aircraft) posing great threats to passengers and ground civilians. It is very difficult to quantify the amount of explosive charge (impulse) which is needed to breach the fuselage as there are a multitude of scenarios which could take place on-board an aircraft. As shown in the pressurised barrel tests, the blast pressure reduces rapidly with distance ($1/2$ metre) and so the implications for aircraft security is that the explosive charge has to be in close proximity to the skin of the fuselage or be of large size/quantity to cause breaching of the structure. It is assumed in this research that current baggage screening capabilities in airports can detect large amounts of explosive and therefore only small amounts, such as IEDs, should be considered. However, the smaller the explosive the more difficult it is to detect. Further work needs to be done to quantify these issues, such as how much explosive could bring down an aircraft, for a multitude of vulnerable locations such as the passenger and luggage cabin sections. Ideally, this should be done for large-scale aircraft (wide and narrow bodied) which encompass all of the elements which were neglected in this thesis, such as flooring, window openings etc.

The present work has focussed on Glare, a fuselage skin material for the Airbus A380, which has shown to outperform monolithic aluminium in blast events. Nevertheless, it would be useful to the wider community if the tearing threshold of this material in relation to other conventional structural materials was determined.

Moving away from Glare, there are also many other promising material variations (such as Titanium-CFRP laminates) which should be explored. Although it is recognized that such materials will seldom reach technological maturity for fuselage applications, efforts could focus on blast mitigated luggage containers. Such containers can help reduce the blast pressures at vulnerable locations on the airframe. This is by no means a trivial feat, since economics (manufacturing, materials) and weight are crucial driving factors. Furthermore, if successful, such designs must be retro-fitted to existing aircraft to reduce costs and meet the demand of passenger security in this ever changing climate.

It is acknowledged by the author that further small-scale fracture tests for Glare should be performed to (a) validate the derived cohesive parameters and, if possible, (b) extract experimentally measured deformation fields to obtain accurate Mode I cohesive zone laws. The traction-separation law should encompass the fibre bridging mechanism and the process of stress transfer between the aluminium layers and glass-fibre in the wake of the crack. Furthermore, a revision of the numerical methodology should be performed to generate models (mesh design generation, boundary and loading input parameters, cohesive zone element formulation) which are more manageable for the numerical analyst, particularly in industry. One such area of further research is the development and implementation of shell cohesive zone elements which can be integrated seamlessly to

the global shell structure. This would preclude the use of shell-solid connections and significantly reduce the computational effort. To help alleviate some of the shortcomings of the finite element method in relation to crack growth (where the direction of the path must be known to the user), the XFEM (partition of unity) method should be considered to model the propagation of discontinuities in large-scale shell structures. These enriched elements can reproduce the challenging features of fracture without the user knowing or tracking the crack path. Moreover, treating problems with discontinuities with the XFEM method suppresses the need to define time-consuming mesh refinement in the vicinity of the crack tip and avoid re-meshing the discontinuity surfaces. These factors can alleviate the computational cost and errors associated with conventional finite element methods.

Appendix A

LS-DYNA/ABAQUS

A.1 ABAQUS

ABAQUS [24] is a multipurpose finite element analysis code. The ABAQUS product consists of three core products: ABAQUS/Standard, ABAQUS/Explicit and ABAQUS/CAE. ABAQUS/Standard is more efficient for solving smooth nonlinear problems (i.e. general and linear perturbation procedures) using a stiffness-based solution technique that is unconditionally stable. ABAQUS/Standard must iterate to determine the solution to a nonlinear problem. However ABAQUS/Explicit is more suited for dynamic problems such as wave propagation analysis. ABAQUS/Explicit determines the solution without iterating by explicitly advancing the kinematic state from the previous increment. For dynamic problems ABAQUS/Explicit is computationally more efficient than ABAQUS/Standard. ABAQUS/CAE is the complete ABAQUS Environment that allows the definition and generation of geometry, material models and applying boundary conditions etc. ABAQUS is very attractive for blast modelling as it gives the user more freedom to define blast functions/loads via the implementation of subroutines (FORTRAN programming).

A.2 LS-DYNA

LS-DYNA [25] is a general purpose multi physics finite element solver commercialized by the Livermore Software Technology Corporation or LSTC. It has its roots in the public domain finite element solver, DYNA3D, which was developed by John O. Hallquist, who worked for the Lawrence Livermore National Laboratory and was released in 1976. The source was declassified in 1978 by the US military and released into the public

domain. Work on the public domain code was performed solely by Hallquist up to 1984. In 1989, Hallquist ceased work on DYNA3D development and founded LSTC. LSTC commercialized the code and continued development on it under the name LS-DYNA.

Later versions of LS-DYNA include a, somewhat limited, implicit solver as an option, but the main part of the code is aimed at explicit time integration. The advantage of explicit code over implicit code lies in its ability to describe highly non-linear, transient and dynamic phenomena. The ability to effectively solve non linear problems is necessary when either the material behaves non-linear, for example concrete at high strain rates, or when geometric non-linearities arise such as buckling of sheets. A third type of non-linearity comes from changing boundary conditions, for example as a result of contact. Transient Dynamic problems are characterized by the large influence of inertia. Examples of these are found where loads are large, sudden and short in nature such as explosions car crashes and metal extrusion.

LS-DYNA simulations are completely described by an input text file called a keyword file. This may link to other files. It is convenient for larger simulations to have the mesh made by a preprocessor and have it saved in a separate file with the nodal and elemental definitions. The statements following the stars (*) are known as keywords and the information on the lines following them are cards.

Appendix B

ABAQUS input files

Representative input files from the ABAQUS FE analysis conducted throughout this work are presented in this Appendix. Files created using the ABAQUS/CAE preprocessor are large because all the elements and nodes of the model are listed. This information has therefore been omitted.

```
*Heading
** Job name: glare3_s4r_hshn_17_3Ns Model name: glare3_s4r_hshn_17_3Ns
** Generated by: Abaqus/CAE 6.10-1
*Preprint, echo=NO, model=NO, history=NO, contact=NO
**
** PARTS
**
*Part, name=clamp
*Node
    1,      100.,      100.,      10.
    2,      100.,      150.,      10.
    3,      100.,      150.,       0.
    4,      100.,      100.,       0.
    5,       0.,      150.,       0. ...
*Element, type=R3D4
    1,  1,  17, 525,  36
    2, 17,  18, 526, 525
    3, 18,  19, 527, 526
    4, 19,  20, 528, 527
    5, 20,  21, 529, 528...
*End Part
**
*Part, name=glare3_panel
*Node
    1,      150.,      100.,       0.
    2,      100.,      100.,       0.
    3,      100.,       0.,       0.
    4,      150.,       0.,       0.
    5,       0.,      100.,       0. ...
*Element, type=S4R
    1,  1,  10, 358, 125
```

```
2, 10, 11, 359, 358
3, 11, 12, 360, 359
4, 12, 13, 361, 360
5, 13, 14, 362, 361 ...
** Region: (glare3_panel-1: Generated From Layup)
*Elset, elset=glare3_panel-1, generate
    1, 3600, 1
** Section: glare3_panel-1
*Shell Section, elset=glare3_panel-1, composite, layup=glare3_panel
0.3, 3, al2024-t3, 0., Ply-1
0.13, 3, s2-glass/fm94, 90., Ply-2
0.13, 3, s2-glass/fm94, 0., Ply-3
0.3, 3, al2024-t3, 0., Ply-4
0.13, 3, s2-glass/fm94, 0., Ply-5
0.13, 3, s2-glass/fm94, 90., Ply-6
0.3, 3, al2024-t3, 0., Ply-7
*End Part
**
**
** ASSEMBLY
**
*Assembly, name=Assembly
**
*Instance, name=glare3_panel-1, part=glare3_panel
*End Instance
**
*Instance, name=clamp-1, part=clamp
    0., 0., 1.
*End Instance
**
*Instance, name=clamp-2, part=clamp
    0., 0., -11.
*End Instance
**
*Node
    1, 150., 150., 15.
*Node
    2, 150., 150., -15.
*Nset, nset=xsymm, instance=glare3_panel-1
    5, 6, 8, 175, 176, 177, 178, 179, 180,
    181, 182, 183, 184, 185, 186, 187...
*Elset, elset=xsymm, instance=glare3_panel-1
    550, 600, 650, 700, 750, 800, 850, 900,
    950, 1000, 1050, 1100, 1150, 1200, 1250, 1300...
*Nset, nset=ysymm, instance=glare3_panel-1
    3, 4, 6, 68, 69, 70, 71, 72, 73,
    74, 75, 76, 224, 225, 226, 227...
*Elset, elset=ysymm, instance=glare3_panel-1
    491, 492, 493, 494, 495, 496, 497, 498, 499,
    500, 2951, 2952, 2953, 2954, 2955, 2956...
*Nset, nset=fix_bndry, instance=glare3_panel-1
    1, 4, 7, 8, 9, 77, 78, 79, 80,
    81, 82, 83, 84, 85, 86, 87...
*Elset, elset=fix_bndry, instance=glare3_panel-1
    1, 11, 21, 31, 41, 51, 61, 71,
```

```

      81, 91, 101, 111, 121, 131, 141, 151...
*Nset, nset=mid_node, instance=glare3_panel-1
  6,
*Nset, nset=top_ref
  1,
*Nset, nset=bot_ref
  2,
*Nset, nset=top_clamp, instance=clamp-1, generate
  1, 2700, 1
*Elset, elset=top_clamp, instance=clamp-1, generate
  1, 2720, 1
*Nset, nset=bot_clamp, instance=clamp-2, generate
  1, 2700, 1
*Nset, nset=bot_clamp
  2,
*Elset, elset=bot_clamp, instance=clamp-2, generate
  1, 2720, 1
*Nset, nset=comp_panel, instance=glare3_panel-1, generate
  1, 3721, 1
*Elset, elset=comp_panel, instance=glare3_panel-1, generate
  1, 3600, 1
*Elset, elset=_blast_surface_SPOS, internal, instance=glare3_panel-1, generate
  501, 3000, 1
*Surface, type=ELEMENT, name=blast_surface
  _blast_surface_SPOS, SPOS
** Constraint: bot_clamp
*Rigid Body, ref node=bot_ref, elset=bot_clamp
** Constraint: top_clamp
*Rigid Body, ref node=top_ref, elset=top_clamp
*Element, type=MASS, elset=bot_ref_mass_bot_
  1, 2
*Mass, elset=bot_ref_mass_bot_
  0.97875,
*Element, type=MASS, elset=top_ref_mass_top_
  2, 1
*Mass, elset=top_ref_mass_top_
  0.97875,
*End Assembly
*Amplitude, name=blast_amp
input{blst_prssr.inp}
**
** MATERIALS
**
*Material, name=al2024-t3
*Density
  2.78e-09,
*Elastic
  73084., 0.33
*Plastic, hardening=JOHNSON COOK
  369., 684., 0.73, 0., 0., 0.
*Rate Dependent, type=JOHNSON COOK
  0.0083,1.
*Material, name=s2-glass/fm94
*Damage Initiation, criterion=HASHIN
  2250.,2250., 32., 65., 50., 75.

```

```
*Damage Evolution, type=ENERGY
 12.5, 12.5, 1., 1.
*Density
 1.98e-09,
*Elastic, type=LAMINA
50600.,9900., 0.33,3750.,3750.,1650.
*Fail Strain
 0.045, -0.045, 0.0048, -0.0073, 0.045
**
** INTERACTION PROPERTIES
**
*Surface Interaction, name=IntProp-1
*Friction
0.,
*Surface Behavior, pressure-overclosure=HARD
**
** BOUNDARY CONDITIONS
**
** Name: bc_fix Type: Symmetry/Antisymmetry/Encastre
*Boundary
fix_bndry, ENCASTRE
** Name: bc_xsymm Type: Symmetry/Antisymmetry/Encastre
*Boundary
xsymm, XSYMM
** Name: bc_ysymm Type: Symmetry/Antisymmetry/Encastre
*Boundary
ysymm, YSYMM
** Name: bot_ref Type: Symmetry/Antisymmetry/Encastre
*Boundary
bot_ref, ENCASTRE
** Name: top_ref Type: Symmetry/Antisymmetry/Encastre
*Boundary
top_ref, ENCASTRE
** -----
**
** STEP: blast_step
**
*Step, name=blast_step
*Dynamic, Explicit
, 0.001
*Bulk Viscosity
0.06, 1.2
** Mass Scaling: Semi-Automatic
**           comp_panel
*Fixed Mass Scaling, elset=comp_panel, dt=2e-07, type=below min
**
** LOADS
**
** Name: blast_amp Type: Pressure
*Dload, amplitude=blast_amp
blast_surface, P, 1.
**
** INTERACTIONS
**
** Interaction: Int-1
```

```
*Contact, op=NEW
*Contact Inclusions, ALL EXTERIOR
*Contact Property Assignment
, , IntProp-1
**
** OUTPUT REQUESTS
**
*Restart, write, number interval=1, time marks=NO
**
** FIELD OUTPUT: F-Output-2
**
*Output, field
*Element Output, elset=glare3_panel-1.glare3_panel-1, directions=YES
2, 5, 8, 11, 14, 17, 20
DAMAGEFC, DAMAGEFT, DAMAGEMC, DAMAGENT, DAMAGESHR, DMICRT, STATUS
**
** FIELD OUTPUT: F-Output-1
**
*Output, field
*Node Output, nset=comp_panel, variable=PRESELECT
*Element Output, elset=comp_panel, directions=YES, variable=PRESELECT
*Integrated Output, elset=comp_panel, variable=PRESELECT
*Energy Output, elset=comp_panel, variable=PRESELECT
*Incrementation Output, variable=PRESELECT
**
** HISTORY OUTPUT: H-Output-2
**
*Output, history
*Node Output, nset=mid_node
U3, V3
**
** HISTORY OUTPUT: H-Output-1
**
*Output, history, variable=PRESELECT
*End Step
```

Appendix C

LS-DYNA - MMALE input files

Representative LS-DYNA input files are presented in this section and refer to the ConWep and MMALE models investigated in Chapter 3. Files created using the Hyprmesh and LS-Prepost preprocessor are large because all the elements and nodes of the model are listed. This information has therefore been omitted.

ConWep model

```
## LS-DYNA Keyword file created by LS-PREPOST 3.0(Beta) - 04Mar2010(08:36)
## Created on Mar-22-2010 (16:12:06)
*KEYWORD
*TITLE
$# title
GLARE3_75G_TIED
*CONTROL_ACCURACY
$$ OSU          INN      PIDOSU
$#   osu        inn      pidosu
      0          1          0
*CONTROL_BULK_VISCOSITY
$$      Q1      Q2      IBQ
$#      q1      q2      type      btype
      1.500000  0.060000      1          0
*CONTROL_CONTACT
$$ SLSFAC  RWPNAL  ISLCHK  SHLTHK  PENOPT  THKCHG  ORIEN  ENMASS
$# slsfac  rwpnal  islchk  shlthk  penopt  thkchg  orien  enmass
      1.000000  0.000      2          1          0          0          1          0
$# usrstr  usrfrc  nsbcs  interm  xpene  ssthk  ecdt  tiedprj
      0          0          0          0  4.000000  0          0          0
$# sfric  dfrc  edc  vfc  th  th_sf  pen_sf
      0.000  0.000  0.000  0.000  0.000  0.000  0.000
$# ignore  frceng  skiprwg  outseg  spotstp  spotdel  spothin
      1          0          0          0          0          0          0.000
$# isym  nserod  rwgaps  rwgth  rwksf  icov  swradf  ithoff
      0          0          0  0.000  1.000000  0          0.000  0
$# shldg
      0
```



```

*CONTROL_ENERGY
$$  HGEN      RWEN      SLNTEN      RYLEN
$$#  hgen      rwen      slnten      rylene
      1        2          1          1

*CONTROL_HOURLASS
$$  IHQ      QH
$$#  ihq      qh
      1  0.100000

*CONTROL_SHELL
$$  WRPANG    ESORT      IRNXX    ISTUPD    THEORY      BWC      MITER      PROJ
$$#  wrpang    esort      irnxx    istupd    theory      bwc      miter      proj
      20.000000      1          -1          0          2          2          1          0
$$#  rotasc1   intgrd    lamsht    cstyp6    tshell      nfail1   nfail4   psnfail
      1.000000      0          0          1          0          0          0          0
$$#  psstupd   irquad
      0          0

*CONTROL_TERMINATION
$$  ENDTIM    ENDCYC    DTMIN    ENDENG    ENDMAS
$$#  endtim    endcyc    dtmin    endeng    endmas
      0.020000      0          0.000    0.000    0.000

*DATABASE_ATDOUT
$$#  dt      binary      lcur      ioopt
      0.001000      0          0          1

*DATABASE_GLSTAT
$$#  dt      binary      lcur      ioopt
      0.001000      0          0          1

*DATABASE_NODOUT
$$#  dt      binary      lcur      ioopt      dthf      binhf
      1.0000E-4      1          0          1          0.000    0

*DATABASE_BINARY_D3PLOT
$$  DT/CYCL    LCDT      BEAM      NPLTC
$$#  dt      lcdt      beam      npltc      psetid
      0.001000      0          0          0          0
$$#  ioopt
      0

*DATABASE_BINARY_D3THDT
$$  DT/CYCL    LCID
$$#  dt      lcdt      beam      npltc      psetid
      0.001000      0          0          0          0

*DATABASE_HISTORY_NODE
$MNAME OUTPUTBLOCKS      1TimeHistory1
$$#  id1      id2      id3      id4      id5      id6      id7      id8
      53650    68450    78343    88236    98129    108022    117915    0

*DATABASE_HISTORY_NODE_SET
$$#  id1      id2      id3      id4      id5      id6      id7      id8
      9        10       0        0        0        0        0        0

*DATABASE_HISTORY_SHELL_SET
$MNAME OUTPUTBLOCKS      2press_shells
$$#  id1      id2      id3      id4      id5      id6      id7      id8
      5        0        0        0        0        0        0        0

*BOUNDARY_SPC_SET_ID
$$#  id      heading
      1bc_fix_bndry
$$#  nsid      cid      dofz      dofz      dofz      dofz      dofz      dofz
      8        0        1        1        1        1        1        1

```

```

*SET_NODE_LIST_TITLE
fix_nodes
$#      sid      da1      da2      da3      da4
      8      0.000      0.000      0.000      0.000
$#      nid1      nid2      nid3      nid4      nid5      nid6      nid7      nid8
      48      88      147      376      429      434      435      441
*BOUNDARY_SPC_SET_ID
$#      id
      2bolt_nodes
$#      nsid      cid      dofx      dofy      dofz      dofrx      dofry      dofrz
      7      0      1      1      1      1      1      1
*SET_NODE_LIST_TITLE
bolt_nodes
$#      sid      da1      da2      da3      da4
      7      0.000      0.000      0.000      0.000
$#      nid1      nid2      nid3      nid4      nid5      nid6      nid7      nid8
      59590      59591      59593      59595      59596      59597      59604      59609
*LOAD_BLAST
$#      wgt      xbo      ybo      zbo      tbo      iunit      isurf
      1.0300E-4      0.000      0.000      200.00000      0.000      5      2
$#      cfm      cfl      cft      cfp
      2204.6001      0.003281      1000.0000      145.03770
*LOAD_SHELL_SET
$HMNAME LOADCOLS      4LoadShellSet_3
$HWCOLOR LOADCOLS      4      3
$#      esid      lcid      sf      at
      3      -2      1.000000      0.000
*CONTACT_AUTOMATIC_ONE_WAY_SURFACE_TO_SURFACE_TIEBREAK_ID
$HMNAME GROUPS      1AutoOneWayTie_1
$HWCOLOR GROUPS      1      3
$#      cid
      11-2
$#      ssid      msid      sstyp      mstyp      sboxid      mboxid      spr      mpr
      2      5      3      3      0      0      1      1
$#      fs      fd      dc      vc      vdc      penchk      bt      dt
      0.000      0.000      0.000      0.000      0.000      1      0.0001.0000E+20
$#      sfs      sfm      sst      mst      sfst      sfmt      fsf      vsf
      1.000000      1.000000      0.400000      0.130000      1.000000      1.000000      1.000000      1.000000
$#      option      nfls      sfls      param      eraten      erates      ct2cn      cn
      11      50.000000      25.000000      1.000000      2.500000      2.500000      1.000000      0.000
$#      soft      sofscl      lcidab      maxpar      sbopt      depth      bsort      frcfrq
      1      0.100000      0      1.025000      2.000000      2      0      1
*CONTACT_AUTOMATIC_ONE_WAY_SURFACE_TO_SURFACE_TIEBREAK_ID
$HMNAME GROUPS      2AutoOneWayTie_2
$HWCOLOR GROUPS      2      4
$#      cid
      22-3
$#      ssid      msid      sstyp      mstyp      sboxid      mboxid      spr      mpr
      5      6      3      3      0      0      1      1
$#      fs      fd      dc      vc      vdc      penchk      bt      dt
      0.000      0.000      0.000      0.000      0.000      1      0.0001.0000E+20
$#      sfs      sfm      sst      mst      sfst      sfmt      fsf      vsf
      1.000000      1.000000      0.130000      0.130000      1.000000      1.000000      1.000000      1.000000
$#      option      nfls      sfls      param      eraten      erates      ct2cn      cn
      11      50.000000      25.000000      1.000000      2.500000      2.500000      1.000000      0.000

```

```

$#      soft      sofsc1      lcidab      maxpar      sbopt      depth      bsort      frcfrq
          1 0.100000          0 1.025000  2.000000          2          0          1
*CONTACT_AUTOMATIC_ONE_WAY_SURFACE_TO_SURFACE_TIEBREAK_ID
$HMNAME GROUPS          3AutoOneWayTie_3
$HWCOLOR GROUPS          3          5
$#      cid                                          title
          33-4
$#      ssid      msid      sstyp      mstyp      sboxid      mboxid      spr      mpr
          6          3          3          3          0          0          1          1
$#      fs      fd      dc      vc      vdc      penchk      bt      dt
          0.000      0.000      0.000      0.000      0.000          1      0.0001.0000E+20
$#      sfs      sfm      sst      mst      sfst      sfmt      fsf      vsf
          1.000000  1.000000  0.130000  0.400000  1.000000  1.000000  1.000000  1.000000
$#      option      nfls      sfls      param      eraten      erates      ct2cn      cn
          11 50.000000 25.000000  1.000000  2.500000  2.500000  1.000000      0.000
$#      soft      sofsc1      lcidab      maxpar      sbopt      depth      bsort      frcfrq
          1 0.100000          0 1.025000  2.000000          2          0          1
*CONTACT_AUTOMATIC_ONE_WAY_SURFACE_TO_SURFACE_TIEBREAK_ID
$HMNAME GROUPS          4AutoOneWayTie_4
$HWCOLOR GROUPS          4          6
$#      cid                                          title
          44-5
$#      ssid      msid      sstyp      mstyp      sboxid      mboxid      spr      mpr
          3          8          3          3          0          0          1          1
$#      fs      fd      dc      vc      vdc      penchk      bt      dt
          0.000      0.000      0.000      0.000      0.000          1      0.0001.0000E+20
$#      sfs      sfm      sst      mst      sfst      sfmt      fsf      vsf
          1.000000  1.000000  0.400000  0.130000  1.000000  1.000000  1.000000  1.000000
$#      option      nfls      sfls      param      eraten      erates      ct2cn      cn
          11 50.000000 25.000000  1.000000  2.500000  2.500000  1.000000      0.000
$#      soft      sofsc1      lcidab      maxpar      sbopt      depth      bsort      frcfrq
          1 0.100000          0 1.025000  2.000000          2          0          1
*CONTACT_AUTOMATIC_ONE_WAY_SURFACE_TO_SURFACE_TIEBREAK_ID
$HMNAME GROUPS          5AutoOneWayTie_5
$HWCOLOR GROUPS          5          7
$#      cid                                          title
          55-6
$#      ssid      msid      sstyp      mstyp      sboxid      mboxid      spr      mpr
          8          7          3          3          0          0          1          1
$#      fs      fd      dc      vc      vdc      penchk      bt      dt
          0.000      0.000      0.000      0.000      0.000          1      0.0001.0000E+20
$#      sfs      sfm      sst      mst      sfst      sfmt      fsf      vsf
          1.000000  1.000000  0.130000  0.130000  1.000000  1.000000  1.000000  1.000000
$#      option      nfls      sfls      param      eraten      erates      ct2cn      cn
          11 50.000000 25.000000  1.000000  2.500000  2.500000  1.000000      0.000
$#      soft      sofsc1      lcidab      maxpar      sbopt      depth      bsort      frcfrq
          1 0.100000          0 1.025000  2.000000          2          0          1
*CONTACT_AUTOMATIC_ONE_WAY_SURFACE_TO_SURFACE_TIEBREAK_ID
$HMNAME GROUPS          6AutoOneWayTie_6
$HWCOLOR GROUPS          6          8
$#      cid                                          title
          66-7
$#      ssid      msid      sstyp      mstyp      sboxid      mboxid      spr      mpr
          7          4          3          3          0          0          1          1
$#      fs      fd      dc      vc      vdc      penchk      bt      dt

```

```

0.000      0.000      0.000      0.000      0.000      1      0.0001.0000E+20
$#      sfs      sfm      sst      mst      sfst      sfmt      fsf      vsf
1.000000  1.000000  0.130000  0.400000  1.000000  1.000000  1.000000  1.000000
$# option      nfls      sfls      param      eraten      erates      ct2cn      cn
11 50.000000  25.000000  1.000000  2.500000  2.500000  1.000000  0.000
$#      soft      sofsc1      lcidab      maxpar      sbopt      depth      bsort      frcfrq
1 0.100000      0 1.025000  2.000000      2      0      1
*PART
$HMNAME COMPS      2AL-FRONT
$HWCOLOR COMPS      2      3
$# title
AL-FRONT
$#      pid      secid      mid      eosid      hgid      grav      adpopt      tmid
2      1      2      0      0      0      0      0
*SECTION_SHELL_TITLE
ALUMINIUM_SECTION_SHELL
$#      secid      elform      shrft      nip      propt      qr/irid      icomp      setyp
1      0      0.000      0      0      0      0      0
$#      t1      t2      t3      t4      nloc      marea      idof      edgset
0.400000  0.400000  0.400000  0.400000  0.000      0.000      0.000      0
*MAT_SIMPLIFIED_JOHNSON_COOK_TITLE
ALUMINIUM 2024-T3
$#      mid      ro      e      pr      vp
2 2.7800E-9 72400.000 0.300000 0.000
$#      a      b      n      c      psfail      sigmax      sigsat      epso
369.00000 684.00000 0.740000 0.0083001.0000E+171.0000E+281.0000E+28 0.001000
*PART
$HMNAME COMPS      3AL-MID
$HWCOLOR COMPS      3      4
$# title
AL-MID
$#      pid      secid      mid      eosid      hgid      grav      adpopt      tmid
3      1      2      0      0      0      0      0
*PART
$HMNAME COMPS      4AL-BACK
$HWCOLOR COMPS      4      5
$# title
AL-BACK
$#      pid      secid      mid      eosid      hgid      grav      adpopt      tmid
4      1      2      0      0      0      0      0
*PART
$HMNAME COMPS      5COMP_0_FRONT
$HWCOLOR COMPS      5      6
$# title
COMP_0_FRONT
$#      pid      secid      mid      eosid      hgid      grav      adpopt      tmid
5      2      1      0      0      0      0      0
*SECTION_SHELL_TITLE
S2/GLASS EPOXY
$#      secid      elform      shrft      nip      propt      qr/irid      icomp      setyp
2      2      0.000      0      1      0      0      0
$#      t1      t2      t3      t4      nloc      marea      idof      edgset
0.130000  0.130000  0.130000  0.130000  0.000      0.000      0.000      0
*MAT_COMPOSITE_FAILURE_SHELL_MODEL_TITLE
S2/GLASS-EPOXY

```

```

$#      mid      ro      ea      eb      ec      prba      prca      prcb
      1 1.9800E-9 55000.000 9500.0000 9500.0000 0.061300 0.061300 0.330000
$#      gab      gbc      gca      kf      aopt      maflag
5500.0000 5500.0000 3000.0000 0.000 2.000000 1.000000
$#      xp      yp      zp      a1      a2      a3
0.000 0.000 0.000 0.000 1.000000 0.000
$#      v1      v2      v3      d1      d2      d3      beta
0.000 0.000 0.000 1.000000 0.000 0.000 0.000
$#      tsize      alp      soft      fbrt      sr      sf
0.000 0.000 0.000 0.000 0.447000 0.000
$#      xc      xt      yc      yt      sc
2000.0000 2500.0000 150.00000 50.000000 75.000000
*PART
$HMNAME COMPS      6COMP_90_FRONT
$HWCOLOR COMPS      6      7
$# title
COMP_90_FRONT
$#      pid      secid      mid      eosid      hgid      grav      adpopt      tmid
      6      2      1      0      0      0      0      0
*PART
$HMNAME COMPS      7COMP_0_BACK
$HWCOLOR COMPS      7      8
$# title
COMP_0_BACK
$#      pid      secid      mid      eosid      hgid      grav      adpopt      tmid
      7      2      1      0      0      0      0      0
*PART
$HMNAME COMPS      8COMP_90_BACK
$HWCOLOR COMPS      8      9
$# title
COMP_90_BACK
$#      pid      secid      mid      eosid      hgid      grav      adpopt      tmid
      8      2      1      0      0      0      0      0
*MAT_POWER_LAW_PLASTICITY_TITLE
P-L(Aluminium 2024-T3)
$#      mid      ro      e      pr      k      n      src      srp
      3 2.7800E-9 72400.000 0.300000 690.00000 0.160000 0.000 0.000
$#      sigy      vp
340.00000 0.000
*DEFINE_CURVE_TITLE
LC1
$#      lcid      sidr      sfa      sfo      offa      offo      dattyp
      1      0 1.000000 1.000000 0.000 0.000 0
$#      a1      o1
0.000 0.000
1.000000 1.000000
*DEFINE_CURVE_TITLE
LC2
$#      lcid      sidr      sfa      sfo      offa      offo      dattyp
      2      0 1.000000 1.000000 0.000 0.000 0
$#      a1      o1
0.000 0.000
1.000000 1.000000
*SET_NODE_LIST_TITLE
GROUP1

```

```

          9      0.000      0.000      0.000      0.000
    117849  117989  118539  118731  118519  118466  118529      0
*SET_NODE_LIST_TITLE
GROUP2
          10     0.000     0.000     0.000     0.000
    117851  117755  115695  115725  115565  115591  115898  115887
*SET_SHELL_LIST_TITLE
blast_surface
          3      0.000      0.000      0.000      0.000
          1      2          3          4          5          6          7          8
*SET_SHELL_LIST
$HMSET
$HMNAME SETS      5pres_shells
          5      0.000      0.000      0.000      0.000
    48694  48834  49054  49659      0          0          0          0
*ELEMENT_SHELL
$#   eid     pid     n1     n2     n3     n4     n5     n6     n7     n8
      1       2     193     197     199     192     0       0       0       0
*NODE
$#   nid           x           y           z       tc       rc
      48    100.0000000    300.0000000           0.000       0       0
*END
*COMPONENT
$#   clid   color1   color2   color3   color4
      1  0.251000  0.627000  0.835000  0.000       0       0       0
$HMNAME COMPS      7COMP_0_BACK
$HWCOLOR COMPS      7      8
$# name
Assembly 1
*COMPONENT_PART
$HMNAME COMPS      7COMP_0_BACK
$HWCOLOR COMPS      7      8
$#   pid     clid
      2       1
$HMNAME COMPS      7COMP_0_BACK
$HWCOLOR COMPS      7      8
$#   pid     clid
      3       1
$HMNAME COMPS      7COMP_0_BACK
$HWCOLOR COMPS      7      8
$#   pid     clid
      4       1
$HMNAME COMPS      7COMP_0_BACK
$HWCOLOR COMPS      7      8
$#   pid     clid
      5       1
$HMNAME COMPS      7COMP_0_BACK
$HWCOLOR COMPS      7      8
$#   pid     clid
      6       1
$HMNAME COMPS      7COMP_0_BACK
$HWCOLOR COMPS      7      8
$#   pid     clid
      7       1
$#   pid     clid

```

8 1
*COMPONENT_END

MMALE Model

```

$# LS-DYNA Keyword file created by LS-PREPOST 3.1 (Beta) - 19Aug2010(08:33)
$# Created on Sep-22-2010 (22:30:46)
*KEYWORD MEMORY=300000000
*TITLE
$# title
LS-DYNA keyword deck by LS-PrePost
*CONTROL_ACCURACY
$#   osu       inn   pidosu
      0         1     0
*CONTROL_ALE
$#   dct       nadv   meth   afac   bfac   cfac   dfac   efac
      1         0     1   0.000  0.000  0.000  0.000  0.000
$#   start     end   aafac   vfact   prit   ebc   pref   nsidebc
      0.0001.0000E+20  1.000000  1.0000E-6     0     0     0.000     0
*CONTROL_BULK_VISCOSITY
$#   q1       q2     type   btype
      1.500000  0.060000     1     0
*CONTROL_ENERGY
$#   hgen     rwen   slnten   rylen
      1         2     1     1
*CONTROL_TERMINATION
$#   endtim   endcyc   dtmin   endeng   endmas
      5.000000     0     0.000   0.000   0.000
*CONTROL_TIMESTEP
$#   dtinit   tssfacc   isdo   tslimt   dt2ms   lctm   erode   msist
      0.000  0.900000     0     0.000   0.000     0     0     0
$#   dt2msf   dt2mslc   imslc
      0.000     0     0
*DATABASE_ELOUT
$#   dt       binary   lcur   ioopt
      0.001000     0     0     1
*DATABASE_GLSTAT
$#   dt       binary   lcur   ioopt
      0.010000     0     0     1
*DATABASE_NODOUT
$#   dt       binary   lcur   ioopt   dthf   binhf
      0.001000     0     0     1   0.000     0
*DATABASE_BINARY_D3PLOT
$#   dt       lcdt   beam   npltc   psetid
      0.250000     0     0     0     0
$#   ioopt
      0
*DATABASE_BINARY_D3THDT
$#   dt       lcdt   beam   npltc   psetid
      0.500000     0     0     0     0
*DATABASE_EXTENT_BINARY
$#   neiph   neips   maxint   strflg   sigflg   epsflg   rtlflg   engflg
      0         0     3     0     1     1     1     1
$#   cmpflg   ieverp   beamip   dcomp   shge   stssz   n3thdt   ialemat
      0         0     0     1     2     1     2     1

```

```

$# nintsld  pkp_sen      sclp      unused      msscl      therm      intout      nodout
      0          0  1.000000      0          0          OSTRESS      STRESS
*DATABASE_HISTORY_NODE_SET
$#   id1      id2      id3      id4      id5      id6      id7      id8
      5          0          0          0          0          0          0          0
*BOUNDARY_NON_REFLECTING
$#   ssid      ad      as
      1      0.000      0.000
      2      0.000      0.000
      3      0.000      0.000
*BOUNDARY_SPC_SET_ID
$#   id
      OBC_XSYMM
$#   nsid      cid      dofx      dofy      dofz      dofrx      dofry      dofrz
      1          0          1          0          0          0          0          0
*SET_NODE_LIST_TITLE
xsymm
$#   sid      da1      da2      da3      da4      solver
      1      0.000      0.000      0.000      0.000MECH
$#   nid1      nid2      nid3      nid4      nid5      nid6      nid7      nid8
      350      356      362      368      374      380      386      392
*BOUNDARY_SPC_SET_ID
$#   id
      OBC_YSYMM
$#   nsid      cid      dofx      dofy      dofz      dofrx      dofry      dofrz
      2          0          0          1          0          0          0          0
*SET_NODE_LIST_TITLE
ysymm
$#   sid      da1      da2      da3      da4      solver
      2      0.000      0.000      0.000      0.000MECH
$#   nid1      nid2      nid3      nid4      nid5      nid6      nid7      nid8
      203      350      356      362      368      374      380      386
*BOUNDARY_SPC_SET_ID
$#   id
      OBC_ZSYMM
$#   nsid      cid      dofx      dofy      dofz      dofrx      dofry      dofrz
      3          0          0          0          1          0          0          0
*SET_NODE_LIST_TITLE
zsymm
$#   sid      da1      da2      da3      da4      solver
      3      0.000      0.000      0.000      0.000MECH
$#   nid1      nid2      nid3      nid4      nid5      nid6      nid7      nid8
      288      2458      2465      2472      2479      2486      2493      2500
*BOUNDARY_SPC_SET_ID
$#   id
      OBC_FIX
$#   nsid      cid      dofx      dofy      dofz      dofrx      dofry      dofrz
      4          0          1          1          1          1          1          1
*SET_NODE_LIST_TITLE
FIX_NODES
$#   sid      da1      da2      da3      da4      solver
      4      0.000      0.000      0.000      0.000MECH
$#   nid1      nid2      nid3      nid4      nid5      nid6      nid7      nid8

```



```

196353 196384 196415 196446 196477 196508 196539 196570
*PART
$HMNAME COMPS      2air
$HWCOLOR COMPS      2      3
$# title
Air
$#   pid      secid      mid      eosid      hgid      grav      adpopt      tmid
      1        1        2        2        2        0        0        0
*SECTION_SOLID_ALE_TITLE
SOLID_ALE
$#   secid      elform      aet
      1        11        1
$#   afac      bfac      cfac      dfac      start      end      aafac
      0.000      0.000      0.000      0.000      0.000      0.000      0.000
*MAT_NULL_TITLE
MAT_AIR
$#   mid      ro      pc      mu      terod      cerod      ym      pr
      2 1.2000E-6 -0.010000 0.000 0.000 0.000 0.000 0.000
*EOS_LINEAR_POLYNOMIAL_TITLE
EOL_AIR
$#   eosid      c0      c1      c2      c3      c4      c5      c6
      2 -1.000E-6 0.000 0.000 0.000 0.400000 0.400000 0.000
$#   e0      v0
      0.250000 1.000000
*HOURLASS_TITLE
HRGLSS_AIR
$#   hgid      ihq      qm      ibq      q1      q2      qb/vdc      qw
      2        1 1.0000E-6 0 1.500000 0.060000 0.100000 0.100000
*PART
$HMNAME COMPS      2air
$HWCOLOR COMPS      2      3
$# title
Explosive
$#   pid      secid      mid      eosid      hgid      grav      adpopt      tmid
      2        2        1        1        1        0        0        0
*SECTION_SOLID_ALE_TITLE
SOLID_ALE
$#   secid      elform      aet
      2        11        1
$#   afac      bfac      cfac      dfac      start      end      aafac
      0.000      0.000      0.000      0.000      0.000      0.000      0.000
*MAT_HIGH_EXPLOSIVE_BURN_TITLE
MAT_HE
$#   mid      ro      d      pcj      beta      k      g      sigy
      1 0.001590 6930.0000 21000.000 0.000 0.000 0.000 0.000
*EOS_JWL_TITLE
EOL_HE
$#   eosid      a      b      r1      r2      omeg      e0      vo
      1 3.7120E+5 3231.0000 4.150000 0.950000 0.320000 7000.0000 1.000000
*HOURLASS_TITLE
HRGLSS_HE
$#   hgid      ihq      qm      ibq      q1      q2      qb/vdc      qw
      1        1 1.0000E-6 0 1.500000 0.060000 0.100000 0.100000
*PART_COMPOSITE
$# title

```



```

5      0      0      0      0      0      0      0
*SET_SEGMENT_TITLE
ZSEG
$#    sid      da1      da2      da3      da4      solver
      1      0.000      0.000      0.000      0.000MECH
$#    n1      n2      n3      n4      a1      a2      a3      a4
      128259  125894  125851  128216  0.000  0.000  0.000  0.000
*SET_SEGMENT_TITLE
XSEG
$#    sid      da1      da2      da3      da4      solver
      2      0.000      0.000      0.000      0.000MECH
$#    n1      n2      n3      n4      a1      a2      a3      a4
      61907  61914  61915  190825  0.000  0.000  0.000  0.000
*SET_SEGMENT_TITLE
YSEG
$#    sid      da1      da2      da3      da4      solver
      3      0.000      0.000      0.000      0.000MECH
$#    n1      n2      n3      n4      a1      a2      a3      a4
      71560  71561  73926  73925  0.000  0.000  0.000  0.000
*ALE_MULTI-MATERIAL_GROUP
$#    sid  idtype  gpname
      1      0Air
*ALE_MULTI-MATERIAL_GROUP
$#    sid  idtype  gpname
      2      0Explosive
*CONSTRAINED_LAGRANGE_IN_SOLID
$#    slave  master  sstyp  mstyp  nquad  ctype  direc  mcoup
      3      1      0      0      0      2      1      0
$#    start  end      pfac  fric  frcmin  norm  normtyp  damp
      0.0001.0000E+10  0.100000  0.000  0.500000  0      0      0.000
$#    cq      hmin  hmax  ileak  pleak  lcidpor  nvent  blockage
      0.000  0.000  0.000  2      0.200000  0      0      0
$#    iboxid  ipenchk  intforc  ialesof  lagmul  pfacmm  thkf
      0      0      0      0      0.000  0      0.000
*ELEMENT_SOLID
$#    eid  pid      n1      n2      n3      n4      n5      n6      n7      n8
      757  1  192943  1283  1326  192983  192944  1284  1327  192984
*ELEMENT_SHELL
$#    eid  pid      n1      n2      n3      n4      n5      n6      n7      n8
      176005  5  196323  196354  196355  196324  0      0      0      0
*NODE
$#    nid      x      y      z      tc      rc
*END
*COMPONENT
$#    clid  color1  color2  color3  color4
      1  0.769000  0.004000  0.110000  0.000  0      0      0
$# name
Part 1
*COMPONENT_PART
$#    pid  clid
      1      1
$#    pid  clid
      2      1
$#    pid  clid
      5      1

```

*COMPONENT_END

Appendix D

LS-DYNA - Scaled fuselage input files

Representative LS-DYNA input files are presented in this section and refer to the scaled fuselage models investigated in Chapter 4. Files created using the Hyprmesh and LS-Prepost preprocessor are large because all the elements and nodes of the model are listed. This information has therefore been omitted.

Metallic demonstrator model subjected to an internal explosion of 20 gr Semtex

```
## LS-DYNA Keyword file created by LS-PrePost 3.2 (Beta) - 30May2011(14:54)
## Created on Aug-26-2011 (16:19:24)
*KEYWORD MEMORY=30000000
*TITLE
$# title
LS-DYNA keyword deck by LS-PrePost
*CONTROL_ACCURACY
      0      1      0
*CONTROL_BULK_VISCOSITY
$$      Q1      Q2      IBQ
      1.500000  0.060000      1      0
*CONTROL_CONTACT
$$  SLSFAC  RWPNAL  ISLCHK  SHLTHK  PENOPT  THKCHG  ORIEN  ENMASS
      0.100000  0.000      1      0      0      0      1      0
$$  USRSTR  USRFRC  NSBCS  INTERM  XPENE  SSTHK  ECDT  TIEDPRJ
      0      0      0      0      4.000000  0      0      0
$$  SFRIC  DFRIC  EDC  INTVFC  TH  TH_SF  PEN_SF
      0.000  0.000  0.000  0.000  0.000  0.000  0.000
$$  IGNORE  FRCENG
      0      0      0      0      0      0      0.000
$$  ISYM  NSEROD  RWGAPS  RWGDTH  RWKSF  ICOV
      0      0      0      0.000  1.000000  0      0.000  0
      0
*CONTROL_DYNAMIC_RELAXATION
$$  NRCYCK  DRTOL  DRFCTR  DRTERM  TSSFDR  IRELAL  EDTTL  IDRFLG
      250  0.001000  0.995000  0.000  0.000  0  0.040000  0
```

```

*CONTROL_SHELL
 20.000000      0      -1      0      2      2      1      0
  1.000000      0      0      1      0      0      0      0
    0      0      0

*CONTROL_TERMINATION
$$  ENDTIM      ENDCYC      DTMIN      ENDENG      ENDMAS
  1.000000      0      0.000      0.000      0.000

*CONTROL_TIMESTEP
$$  DTINIT      TSSFAC      ISDO      TSLIMIT      DT2MS      LCTM      ERODE      MSIST
  0.000  0.900000      0      0.000      0.000      0      0      0
  0.000      0      0

*DATABASE_MATSUM
  0.050000      0      0      1

*DATABASE_BINARY_D3PLOT
  0.100000      0      0      0      0
    0

*BOUNDARY_SPC_SET_ID
  1bc_fix
    7      0      1      1      1      1      1      1

*SET_NODE_LIST_TITLE
fix_nodes
    7      0.000      0.000      0.000      0.000
 151751  151752  151753  151754  151755  151756  151757  151758

*BOUNDARY_SPC_SET_ID
  1bc_fix_frms_skn
    9      0      1      1      1      1      1      1

*SET_NODE_LIST_TITLE
frms_spprt
    9      0.000      0.000      0.000      0.000MECH
 404114  404115  404116  404117  404118  404119  404120  404121

*BOUNDARY_SPC_SET_ID
  1bc_fix_skn_tp_bttm
   10      0      1      1      1      1      1      1

*SET_NODE_LIST_TITLE
skn_tp_nds
   10      0.000      0.000      0.000      0.000MECH
202065  209080  210647  211016  211049  211070  211075  211076

*LOAD_BLAST
33.299999-302.00000-302.00000      0.000      0.000      5      2
  0.002205  0.003280  1.000000 145.03770

*LOAD_SHELL_SET_ID
  1
    1      1  1.000000      0.000

*CONTACT_TIEBREAK_NODES_ONLY_ID
  1clts_frms
    1      11      4      0      0      0      0      0
  0.000      0.000      0.000      0.000      0.000      0      0.0001.0000E+20
  1.000000  1.000000      0.000      0.000  1.000000  1.000000  1.000000  1.000000
2160.0000 2580.0000  1.000000  1.000000

*SET_NODE_LIST_TITLE
clts_tp
    1      0.000      0.000      0.000      0.000MECH
 25383  25387  25455  25464  25478  25490  25582  25594

*SET_SEGMENT_TITLE
frms

```

```

11      0.000      0.000      0.000      0.000MECH
149625  149706  149724  149645  0.000      0.000      0.000      0.000
*CONTACT_TIEBREAK_NODES_ONLY_ID
3strngrs_skn
3      12      4      0      0      0      0      0
0.000      0.000      0.000      0.000      0.000      0      0.0001.0000E+20
1.000000  1.000000      0.000      0.000  1.000000  1.000000  1.000000  1.000000
2160.0000 2580.0000  1.000000  1.000000
*SET_NODE_LIST_TITLE
strngrs
3      0.000      0.000      0.000      0.000
70901    70916    70934    70949    70965    70974    70989    71004
*CONTACT_TIEBREAK_NODES_ONLY_ID
4dblrs_ntrnl
4      12      4      0      0      0      0      0
0.000      0.000      0.000      0.000      0.000      0      0.0001.0000E+20
1.000000  1.000000      0.000      0.000  1.000000  1.000000  1.000000  1.000000
2160.0000 2580.0000  1.000000  1.000000
*SET_NODE_LIST_TITLE
dblrs_ntrnl
4      0.000      0.000      0.000      0.000
50841    50856    50874    50889    50905    50914    50929    50944
*CONTACT_TIEBREAK_NODES_ONLY_ID
5dblrs_xtrnl
5      12      4      0      0      0      0      0
0.000      0.000      0.000      0.000      0.000      0      0.0001.0000E+20
1.000000  1.000000      0.000      0.000  1.000000  1.000000  1.000000  1.000000
2160.0000 2580.0000  1.000000  1.000000
*SET_NODE_LIST_TITLE
dblrs_xtrnl
5      0.000      0.000      0.000      0.000
62306    62326    62350    62370    62398    62418    62442    62462
*CONTACT_AUTOMATIC_SINGLE_SURFACE
0      0      0      0      0      0      0      0
0.000      0.000      0.000      0.000      0.000      0      0.0001.0000E+20
1.000000  1.000000      0.000      0.000  1.000000  1.000000  1.000000  1.000000
*PART
$HMNAME COMPS      1blkhd
$HWCOLOR COMPS      1      3
blkhd
1      1      2      0      0      0      0      0
*SECTION_SHELL_TITLE
blkhd
1      16  1.000000      2      1      0      0      0
2.200000  2.200000  2.200000  2.200000      0.000      0.000      0.000      0
*MAT_POWER_LAW_PLASTICITY_TITLE
Aluminium 7178-T62
2      0.002780 71700.000  0.330000 200.00000  0.200000      0.000      0.000
538.00000      0.000
*PART
$HMNAME COMPS      2blkhd_nnr
$HWCOLOR COMPS      2      4
blkhd_nnr
2      2      2      0      0      0      0      0
*SECTION_SHELL_TITLE

```



```

blkhd_nnr
      2      16  1.000000      2      1      0      0      0
28.000000 28.000000 28.000000 28.000000  0.000  0.000  0.000  0
*PART
$HMNAME COMPS      3blkhd_tr
$HWCOLOR COMPS      3      5
blkhd_tr
      3      3      2      0      0      0      0      0
*SECTION_SHELL_TITLE
blkhd_tr
      3      16  1.000000      2      1      0      0      0
33.000000 33.000000 33.000000 33.000000  0.000  0.000  0.000  0
*PART
$HMNAME COMPS      11cleats
$HWCOLOR COMPS      11      6
cleats
      11      11      2      0      0      0      0      0
*SECTION_SHELL_TITLE
clts
      11      16  1.000000      3      1      0      0      0
2.200000  2.200000  2.200000  2.200000  0.000  0.000  0.000  0
*PART
$HMNAME COMPS      12dblrs_frms_tp
$HWCOLOR COMPS      12      7
dblrs_frms_tp
      12      12      4      0      0      0      0      0
*SECTION_SHELL_TITLE
dblrs_frms_tp
      12      16  1.000000      2      1      0      0      0
2.200000  2.200000  2.200000  2.200000  0.000  0.000  0.000  0
*MAT_RIGID_TITLE
RIGID_SUPPORTS
      4  0.002780 71700.000  0.330000  0.000  0.000  0.000
1.000000      7      7
0.000  0.000  0.000  0.000  0.000  0.000
*PART
$HMNAME COMPS      13dblrs_frms_bttm
$HWCOLOR COMPS      13      8
dblrs_frms_bttm
      13      13      4      0      0      0      0      0
*SECTION_SHELL_TITLE
dblrs_frms_bttm
      13      16  1.000000      2      1      0      0      0
2.200000  2.200000  2.200000  2.200000  0.000  0.000  0.000  0
*PART
$HMNAME COMPS      21frms
$HWCOLOR COMPS      21      7
frms
      21      21      5      0      0      0      0      0
*SECTION_SHELL_TITLE
frms
      21      16  1.000000      2      1      0      0      0
2.200000  2.200000  2.200000  2.200000  0.000  0.000  0.000  0
*MAT_SIMPLIFIED_JOHNSON_COOK_TITLE
AL2024_JC

```

```

      5  0.002780 72400.000  0.330000  0.000
369.00000 684.00000  0.730000  0.083000  0.140000 484.000001.0000E+28  1.000000
*PART
$HMNAME COMPS      31dblrs_ntrnl
$HWCOLOR COMPS      31      13
dblrs_ntrnl
      31      31      5      0      0      0      0      0
*SECTION_SHELL_TITLE
dblrs_ntrnl
      31      16  1.000000      2      1      0      0      0
      1.700000  1.700000  1.700000  1.700000  0.000  0.000  0.000  0
*PART
$HMNAME COMPS      32dblrs_xtrnl
$HWCOLOR COMPS      32      17
dblrs_xtrnl
      32      32      5      0      0      0      0      0
*SECTION_SHELL_TITLE
dblrs_xtrnl
      32      16  1.000000      2      1      0      0      0
      4.000000  4.000000  4.000000  4.000000  0.000  0.000  0.000  0
*PART
$HMNAME COMPS      41skn_1a
$HWCOLOR COMPS      41      20
skn_1a
      41      41      7      0      0      0      0      0
*SECTION_SHELL_TITLE
skn_1a
      41      16  1.000000      3      1      0      0      0
      2.200000  2.200000  2.200000  2.200000  0.000  0.000  0.000  0
*MAT_SIMPLIFIED_JOHNSON_COOK_TITLE
AL7178_JC
      7  0.002780 71700.000  0.330000  0.000
538.00000 200.00000  0.200000  0.000  0.100000 607.000001.0000E+28  1.000000
*PART
$HMNAME COMPS      42skn_1b
$HWCOLOR COMPS      42      21
skn_1b
      42      42      7      0      0      0      0      0
*SECTION_SHELL_TITLE
skn_1b
      42      16  1.000000      3      1      0      0      0
      2.200000  2.200000  2.200000  2.200000  0.000  0.000  0.000  0
*PART
$HMNAME COMPS      43skn_1c
$HWCOLOR COMPS      43      24
skn_1c
      43      43      7      0      0      0      0      0
*SECTION_SHELL_TITLE
skn_1c
      43      16  1.000000      3      1      0      0      0
      2.200000  2.200000  2.200000  2.200000  0.000  0.000  0.000  0
*PART
$HMNAME COMPS      44skn_1d
$HWCOLOR COMPS      44      25
skn_1d

```

```

          44          44          7          0          0          0          0          0
*SECTION_SHELL_TITLE
skin_id
          44          16  1.000000          3          1          0          0          0
    2.200000  2.200000  2.200000  2.200000  0.000  0.000  0.000  0.000
*PART
$HMNAME COMPS      51strngrs
$HWCOLOR COMPS      51      28
strngrs
          51          51          6          0          0          0          0          0
*SECTION_SHELL_TITLE
strngrs
          51          16  1.000000          2          1          0          0          0
    2.300000  2.300000  2.300000  2.300000  0.000  0.000  0.000  0.000
*MAT_SIMPLIFIED_JOHNSON_COOK_TITLE
AL7075_JC
          6  0.002780  71000.000  0.330000  0.000
    434.00000  303.57999  0.390000  0.968000  0.170000  484.000001.0000E+28  1.000000
*PART
$HMNAME COMPS      61frms_tp_bttm
$HWCOLOR COMPS      61      29
frms_tp_bttm
          61          61          3          0          0          0          0          0
*SECTION_SHELL_TITLE
frms_tp_bttm
          61          16  1.000000          2          1          0          0          0
    4.000000  4.000000  4.000000  4.000000  0.000  0.000  0.000  0.000
*MAT_POWER_LAW_PLASTICITY_TITLE
Aluminium 2024-T3
          3  0.002780  71700.000  0.330000  200.00000  0.200000  0.000  0.000
    345.00000  0.000
*MAT_POWER_LAW_PLASTICITY_TITLE
Aluminium 7075-T3511
          1  0.002780  71700.000  0.330000  200.00000  0.200000  0.000  0.000
    400.00000  0.000
*DEFINE_CURVE_TITLE
rfrnc
          1          0  1.000000  1.000000  0.000  0.000  0
          0.000  0.000
          1.000000  1.000000
*DEFINE_CURVE_TITLE
rfrnc
          2          0  1.000000  1.000000  0.000  0.000  0
          0.000  0.000
          1.000000  1.000000
*SET_NODE_LIST_TITLE
clts_frms
          6  0.000  0.000  0.000  0.000
    419983  420002  420018  420037  420280  420299  420315  420334
*SET_NODE_LIST_TITLE
dblrs_xtrnl_skn
          8  0.000  0.000  0.000  0.000MECH
    332535  365910  366018  332460  332473  332897  332803  340170
*SET_SHELL_LIST_TITLE
blst_srfc

```

1	0.000	0.000	0.000	0.000				
544214	544215	544216	544217	544218	544219	544220	544221	
734802	734803	734804	734805	0	0	0	0	
*ELEMENT_SHELL								
108661	21	120126	120137	120119	120119	0	0	0
*NODE								
25207	-395.7245178	-463.9636536	-478.9009094		0	0		
*END								

Appendix E

RADIOSS - MMALE simulations

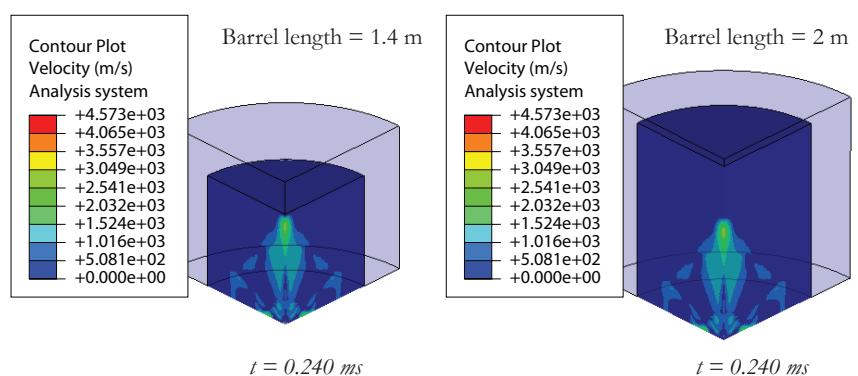
E.1 Interaction of pressurised cylindrical structures subjected to TNT blast loading

This Appendix gives an overview of a study on the dynamic behaviour of Glare pressurised barrels subjected to internal blast loadings using the fluid structure interaction approach (ALE) within the explicit finite element software RADIOSS. The barrel setup was based on well-controlled and minimal dynamic fracture tests, which aim to emulate conditions on-board a commercial aircraft. The effects of length and static pre-pressurisation were investigated to determine the interaction between barrel deformation and reflected shock waves. In this paper, it is shown that the length of the barrel may significantly induce severe vibration modes as a result of shock reflection waves from the top surface of the barrel. Finally the effect of pre-pressurisation was proven to alter the structural response to an internal explosion by providing additional internal energy to propagate the blast wave. As a result, it has been concluded that pre-pressurization of an aircraft fuselage will increase the structural damage due to the detonation of an on-board explosive device and must be included in all future studies to model the dynamic crack growth and structural integrity of typical aircraft structures.

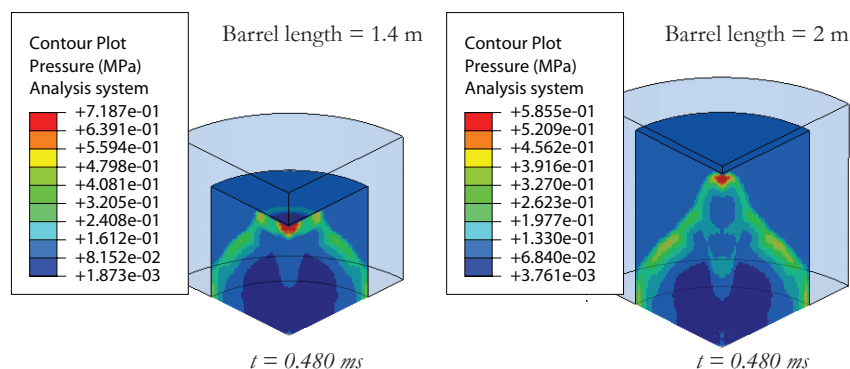
E.2 Influence of Barrel Length

To determine the effect of barrel length on the shock wave behaviour of a 54g TNT charge, a numerical study was performed on closed atmospheric GLARE barrels with the following respective lengths: 1.4 and 2 m, which will be referred to as Barrel A and B, respectively. The shock wave front for Barrel A reaches the top of the barrel at

approximately $t=0.24\text{ms}$. At this time the shock wave velocity profile for both barrels is approximately the same, as shown in Fig. E.1(a). The pressure which impinges on the top surface will depend on the rate of which the blast wave dissipates as a function of time and space. Therefore Barrel A experiences a larger blast pressure, as you would expect, indicating that damage would be more pronounced in this barrel configuration particularly as this would have a higher bending stiffness, as shown in Fig. E.1(a). The higher bending stiffness will cause Barrel A to offer more of a resistance to the blast wave, dissipating more energy through irreversible damage processes such as plastic deformation in the aluminium layers and damage energy within the GFRP layers.



(a) Velocity contour



(b) Pressure contour

FIGURE E.1: Distribution of blast (a) velocity (m/s) and (b) pressure shock wave at the same time for 1.4 and 2 m GLARE barrels for a 54g TNT charge (Pressure is in MPa)

Monitoring the pressure profile experienced at the lower perimeter of the GLARE barrel shows that there are two instantaneous rises in pressure, or peaks, see Fig. E.2. The first peak represents the contact with the initial reflected shock wave, which is clearly independent of barrel length. The second peak is a result of the shock wave reflecting from the top boundary of the barrel, giving a second 'blast' effect. This second peak

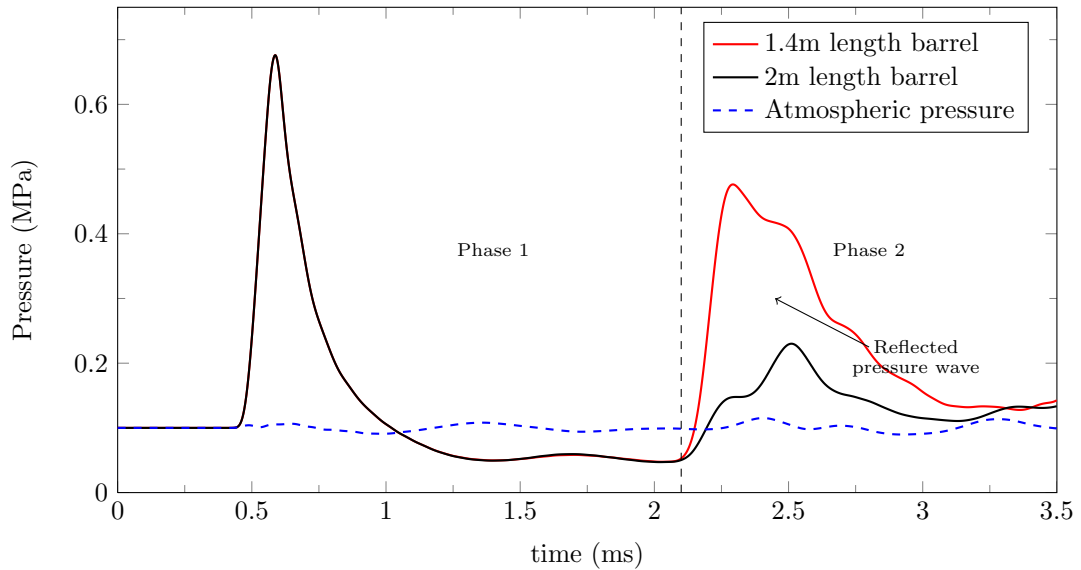


FIGURE E.2: Pressure profile extracted from lower perimeter for 1.4 and 2m GLARE barrels for a 54g TNT charge

is more severe for Barrel A than B, since the blast shock wave has expanded further and longer in the latter case, dissipating more energy. This second pressure peak is crucial in assessing the damage tolerance of the barrel, as further damage can occur and accumulate longer after initial detonation of explosion, as a result of shock wave reflection from adjacent boundaries.

Monitoring the global internal energy of the system provides an insight into the physical instability of the fluid-structure interaction. There is evidence to show that as the shock waves propagates along the length of the barrel; the structure is experiencing out-of-plane bending in an oscillatory manner, as illustrated in Fig. E.3.

Although the internal energy for both models are initially identical, they begin to deviate at approximately $t = 1.25$ ms. During this time there are two significant peaks where the amplitude of the second peak depends on the barrel length. The first apparent peak occurs during the initial detonation and propagation of the explosive, whose amplitude is independent of the barrel length. After the initial decay of the explosive, a second rise in internal energy is shown, with Barrel A experiencing a larger amplitude than Barrel B. It appears that less energy is dissipated in flexural deformation which is evident in Table E.1 where the longer barrel B deflects 30% more than A. This is expected as Barrel A has a larger bending stiffness than Barrel B, indicating that blast effects would be more pronounced in the former model.

The internal energy profile beyond this phase indicates a recovery of some stability, which is abruptly interrupted by the second reflected blast wave for Barrel A, as discussed

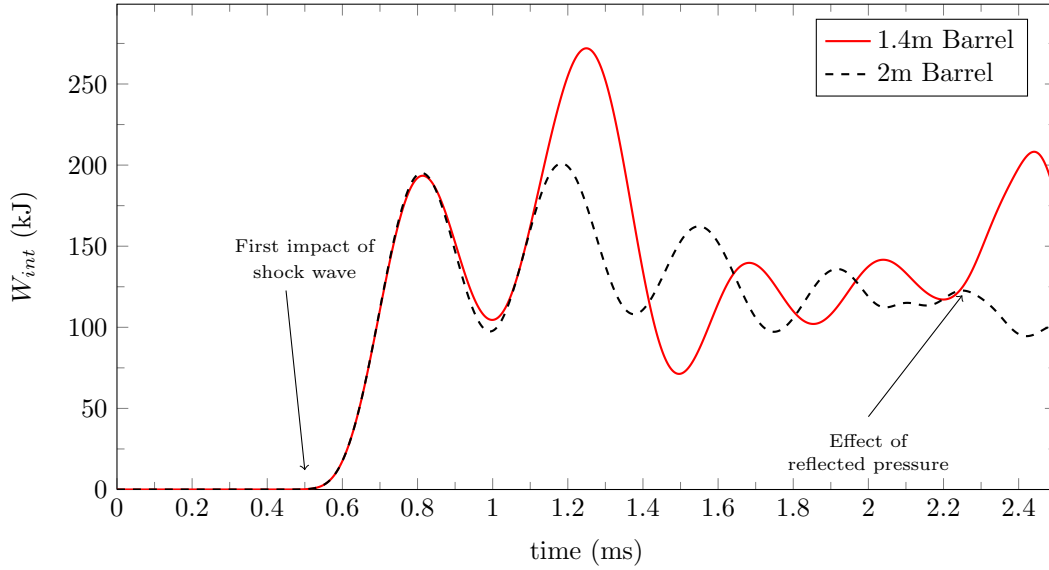


FIGURE E.3: Internal energy profile for 1.4 and 2 m GLARE barrels for a 54g TNT charge

TABLE E.1: Influence of GLARE barrel lengths on the maximum displacement, Von Mises and strain for a 54g TNT charge

	δ_{max} (mm)	$\sigma_{max,vm}$ (MPa)
Barrel A	2.99	366
Barrel B	4.13	502
Difference (%)	27	27

previously. This induces a further increase in internal energy, which in the presence of damage will propagate it further, resulting in a weaker structure.

E.3 Effect of pressurisation

The parameters within the interior Eulerian mesh (air) were changed to apply a pre-stress of 0.2 MPa to take into account the effect of pressurisation. This method proved more computationally efficient and accurate than applying an external stress to simulate the circumferential (hoop) stresses. Figure E.4 illustrates the influence of pressurization on the blast shock wave phenomena, which clearly shows an acceleration of the second reflected pressure compared to the non-pressurised case. The global energy of the system, as shown in Fig. E.5, shows that the pressurised barrel absorbs more energy than the non-pressurised case. This is an important factor to consider when studying the dynamic crack growth of the pressurised barrel tests, as the combined effects of inertia and cabin pressurisation will help drive the crack long after the initial dissipation of the explosion.

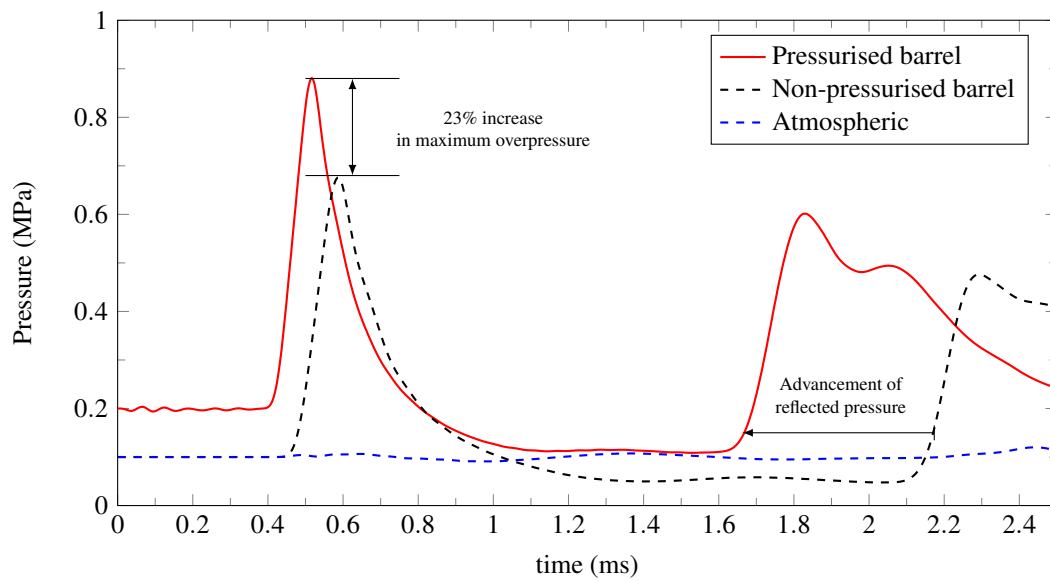


FIGURE E.4: Effect of pressurisation on the blast pressure profile for 1.4 m GLARE barrel for a 54g TNT charge

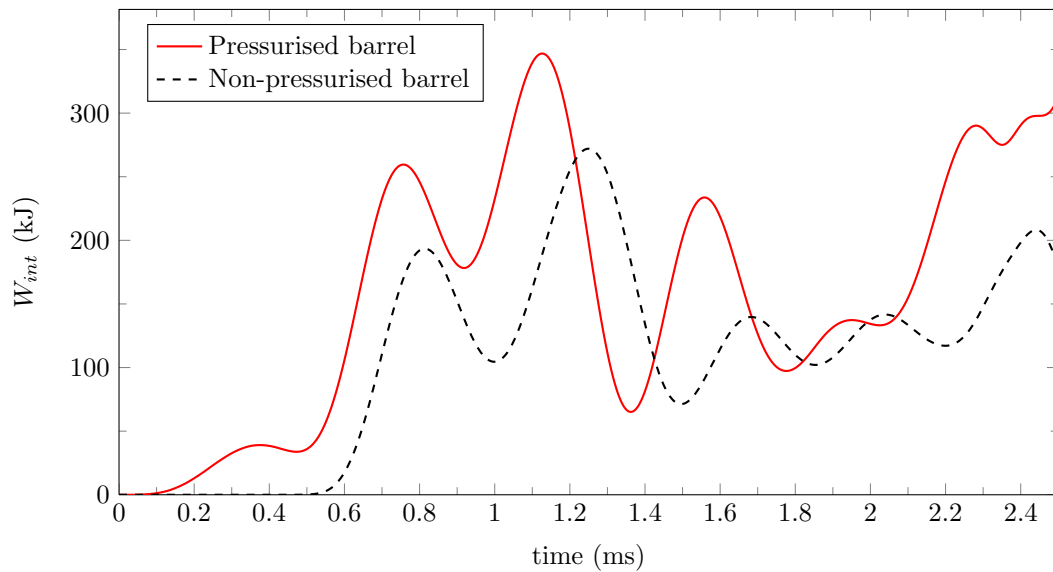


FIGURE E.5: Effect of pressurisation on the internal energy of 1.4 m GLARE barrel for a 54g TNT charge

Appendix F

LS-DYNA - Dynamic fracture files

Representative LS-DYNA input files are presented in this section and refer to the dynamic fracture models investigated in Chapter 6. Due to the size of the files, only the rate-dependent models are given here for Mode I crack growth. Input files are available upon request and may be found on the accompanied DVD.

```
## LS-DYNA Keyword file created by LS-PREPOST 3.1 (Beta) - 19Aug2010(08:33)
## Created on Feb-21-2011 (20:42:52)
*KEYWORD
*TITLE
$# title
LS-DYNA keyword deck by LS-PrePost
*CONTROL_ACCURACY
$$ OSU          INN      PIDOSU
$#   osu        inn      pidosu
      0          1          0
*CONTROL_BULK_VISCOSITY
$$      Q1      Q2      IBQ
$#      q1      q2      type      btype
      1.500000  0.060000      1          0
*CONTROL_SHELL
$$  WRPANG  ESORT  IRNXX  ISTUPD  THEORY  BWC  MITER  PROJ
$#  wrpang  esort  irnxx  istupd  theory  bwc  miter  proj
      20.000000      0      -1          0          2          2          1          0
$#  rotasc1  intgrd  lamsht  cstyp6  tshell  nfail1  nfail4  psnfail
      1.000000      0          0          1          0          0          0          0
$#  psstupd  irquad  cntco
      0          0          0
*CONTROL_TERMINATION
$$  ENDTIM  ENDCYC  DTMIN  ENDENG  ENDMAS
$#  endtim  endcyc  dtmin  endeng  endmas
      5.000000      0          0.000      0.000      0.000
*CONTROL_TIMESTEP
$$  DTINIT  TSSFAC  ISDO  TSLIMIT  DT2MS  LCTM  ERODE  MSIST
```

```

$# dtinit      tssfacc      isdo      tslimt      dt2ms      lctm      erode      ms1st
    0.000  0.900000      0      0.000      0.000      0      0      0
$# dt2msf      dt2mslc      imsc1
    0.000      0      0
*DATABASE_GLSTAT
$# dt      binary      lcur      ioopt
    0.010000      0      0      1
*DATABASE_MATSUM
$# dt      binary      lcur      ioopt
    0.010000      0      0      1
*DATABASE_BINARY_D3PLOT
$# dt      lcdt      beam      npltc      psetid
    0.100000      0      0      0      0
$# ioopt
    0
*DATABASE_EXTENT_BINARY
$# neiph      neips      maxint      strflg      sigflg      epsflg      rltflg      engflg
    0      0      3      0      1      1      1      1
$# cmpflg      ieverp      beamip      dcomp      shge      stssz      n3thdt      ialemat
    0      0      0      1      2      1      2      1
$# nintsld      pkp_sen      sclp      unused      mssc1      therm      intout      nodout
    0      0  1.000000      0      0      OSTRESS      STRESS
*DATABASE_HISTORY_NODE_SET
$# id1      id2      id3      id4      id5      id6      id7      id8
    1037      0      0      0      0      0      0      0
*BOUNDARY_SPC_SET_ID
$HMSET
$HMNAME SETS      51Set_51
$# id      heading
    1BC_ZSYMM
$# nsid      cid      dofz      dofz      dofz      dofz      dofz      dofz
    1035      0      0      0      1      1      1      0
*SET_NODE_LIST_TITLE
ZSYMM
$# sid      da1      da2      da3      da4      solver
    1035      0.000      0.000      0.000      0.000MECH
$# nid1      nid2      nid3      nid4      nid5      nid6      nid7      nid8
    1      2      3      4      5      6      7      8
    167058      167060      167061      167062      167063      167064      167065      167066
*BOUNDARY_SPC_SET_ID
$HMSET
$HMNAME SETS      51Set_51
$# id      heading
    1BC_FIX_NODES
$# nsid      cid      dofz      dofz      dofz      dofz      dofz      dofz
    1036      0      1      1      1      1      1      1
*SET_NODE_LIST_TITLE
FIX_NODES
$# sid      da1      da2      da3      da4      solver
    1036      0.000      0.000      0.000      0.000MECH
$# nid1      nid2      nid3      nid4      nid5      nid6      nid7      nid8
    4097      4098      4099      4100      4101      4102      4103      4104
*LOAD_SHELL_SET_ID
$# id      heading
    1PRESSURE_SHELL
    
```

```

$#      esid      lcid      sf      at
      1037      55  1.000000  0.000
*LOAD_SHELL_SET_ID
$#      id                                     heading
      2PRESSURE_SHELL
$#      esid      lcid      sf      at
      1037      65  1.000000  1.000000
*PART
$HMNAME COMPS      11bulk_mesh
$HWCOLOR COMPS      11      3
$# title
bulk_mesh
$#      pid      secid      mid      eosid      hgid      grav      adpopt      tmid
      11      11      11      0      0      0      0      0
*SECTION_SHELL_TITLE
bulk shells
$#      secid      elform      shrff      nip      propt      qr/irid      icomp      setyp
      11      16      0.000      0      1      0      0      0
$#      t1      t2      t3      t4      nloc      marea      idof      edgset
      1.000000  1.000000  1.000000  1.000000  0.000      0.000      0.000      0
*MAT_SIMPLIFIED_JOHNSON_COOK_TITLE
MAT_JOHNSON_COOK
$#      mid      ro      e      pr      vp
      11  0.002780  72400.000  0.330000  0.000
$#      a      b      n      c      psfail      sigmax      sigsat      epso
      369.00000  684.00000  0.730000  0.0083001.0000E+171.0000E+281.0000E+28  0.001000
*PART
$HMNAME COMPS      21connecting_shells_low
$HWCOLOR COMPS      21      5
$# title
connecting_shells_low
$#      pid      secid      mid      eosid      hgid      grav      adpopt      tmid
      21      11      11      0      0      0      0      0
*PART
$HMNAME COMPS      22connecting_shells_high
$HWCOLOR COMPS      22      5
$# title
connecting_shells_high
$#      pid      secid      mid      eosid      hgid      grav      adpopt      tmid
      22      11      11      0      0      0      0      0
*PART
$HMNAME COMPS      23cohesive zones ag
$HWCOLOR COMPS      23      6
$# title
cohesive zones ag
$#      pid      secid      mid      eosid      hgid      grav      adpopt      tmid
      23      23      23      0      0      0      0      0
*SECTION_SOLID_TITLE
cohesive zones layer ag
$#      secid      elform      aet
      23      19      0
*MAT_COHESIVE_GENERAL_TITLE
MAT_COHESIVE_GENERAL
$#      mid      ro      roflg      intfall      tes      tslc      gic      giic
      23  0.002780      0  1.000000  0.000      45  19.000000  19.000000

```

```

$#      xmu      t      s      stfsf
    1.000000 931.50000 931.50000 0.000
*PART
$HMNAME COMPS      24mat_0 sandwich_low
$HWCOLOR COMPS      24      7
$# title
mat_0 sandwich_low
$#      pid      secid      mid      eosid      hgid      grav      adpopt      tmid
          24      21      21      0      0      0      0      0
*SECTION_SHELL_TITLE
mat_0 sandwich layer shells
$#      secid      elform      shrf      nip      propt      qr/irid      icip      setyp
          21      16      0.000      0      1      0      0      0
$#      t1      t2      t3      t4      nloc      marea      idof      edgset
    0.100000 0.100000 0.100000 0.100000 0.000 0.000 0.000 0
*MAT_NULL_TITLE
MAT_NULL
$#      mid      ro      pc      mu      terod      cerod      ym      pr
          212.7800E-35      0.000      0.000      0.000      0.000      0.000      0.000      0.000
*PART
$HMNAME COMPS      25mat_0 sandwich_high
$HWCOLOR COMPS      25      7
$# title
mat_0 sandwich_high
$#      pid      secid      mid      eosid      hgid      grav      adpopt      tmid
          25      21      21      0      0      0      0      0
*PART
$HMNAME COMPS      11bulk_mesh
$HWCOLOR COMPS      11      3
$# title
initial_notch_low
$#      pid      secid      mid      eosid      hgid      grav      adpopt      tmid
          26      21      21      0      0      0      0      0
*PART
$HMNAME COMPS      11bulk_mesh
$HWCOLOR COMPS      11      3
$# title
initial_notch_high
$#      pid      secid      mid      eosid      hgid      grav      adpopt      tmid
          27      21      21      0      0      0      0      0
*DEFINE_CURVE_TITLE
traction_separation_curve
$#      lcid      sidr      sfa      sfo      offa      offo      dattyp
          45      0 1.000000 1.000000 0.000 0.000 0
$#
          a1      o1
          0.000      0.000
          0.0031100      0.5251600
          0.0062200      0.8569900
          0.0093300      0.9954800
          0.0100000      1.0000000
          0.7500000      1.0000000
          0.7772900      0.9668500
          0.8083800      0.8618600
          0.8394800      0.7074100
          0.8705700      0.5265900

```

```

0.9016600      0.3424700
0.9327500      0.1781500
0.9638400      0.0567100
0.9949300      0.0012200
1.0000000      0.000

*DEFINE_CURVE_TITLE
pressurised_load_case
$#   lcid      sidr      sfa      sfo      offa      offo      dattyp
      55        0  1.000000  1.000000  0.000      0.000      0
$#           a1           o1
      0.000           0.000
      0.5000000      0.2000000
      1.0000000      0.2000000

*DEFINE_CURVE_TITLE...% One of five pressure curves
pressurised_blast
$#   lcid      sidr      sfa      sfo      offa      offo      dattyp
      65        0  1.000000  1.000000  0.000      0.000      0
$#           a1           o1
      0.0399000      0.2000000
      0.0800000      0.1990000

*DEFINE_CURVE_TITLE
critical_damping
$#   lcid      sidr      sfa      sfo      offa      offo      dattyp
      75        0  1.000000  1.000000  0.000      0.000      0
$#           a1           o1
      0.000           1.0000000
      1.0000000      1.0000000
      1.0010000      0.000
      100.0000000      0.000

*SET_NODE_LIST
$HMSET
$HMNAME SETS      11Set_11
$#   sid      da1      da2      da3      da4      solver
      11      0.000      0.000      0.000      0.000MECH
$#   nid1      nid2      nid3      nid4      nid5      nid6      nid7      nid8
      1        2        0        0        0        0        0        0

*SET_NODE_LIST
$HMSET
$HMNAME SETS      12Set_12
$#   sid      da1      da2      da3      da4      solver
      12      0.000      0.000      0.000      0.000MECH
$#   nid1      nid2      nid3      nid4      nid5      nid6      nid7      nid8
      3        4        0        0        0        0        0        0

*SET_SHELL_LIST_TITLE
PRESSURE_SHELL
$HMSET
$HMNAME SETS      1037pressure_shells
$#   sid      da1      da2      da3      da4
      1037      0.000      0.000      0.000      0.000
$#   eid1      eid2      eid3      eid4      eid5      eid6      eid7      eid8
      159205  159206  159209  159235  159236  159237  159238  159239

*CONSTRAINED_SHELL_TO_SOLID
$HMNAME COMPS      26ConstrndShelToSolid
$HWCOLOR COMPS      26      4
$#   nid      nsid

```



```

          5          11
*CONSTRAINED_SHELL_TO_SOLID
$HMNAME COMPS          26ConstrndShelToSolid
$HWCOLOR COMPS          26          4
$#      nid      nsid
          6          12
*DAMPING_GLOBAL
$#      lcid      valdmp      stx      sty      stz      srx      sry      srz
          75      1.000000      10.000000      10.000000      10.000000      10.000000      0.000      0.000
*ELEMENT_SOLID
$#      eid      pid      n1      n2      n3      n4      n5      n6      n7      n8
          2077      23      225      233      234      226      227      235      236      228
*ELEMENT_SHELL
$#      eid      pid      n1      n2      n3      n4      n5      n6      n7      n8
          1      21      5      7      15      13      0      0      0      0
*NODE
$#      nid      x      y      z      tc      rc
          1      612.0000000      -0.0500000      0.000      0      0
          2      613.0000000      -0.0500000      0.000      0      0
*END
*COMPONENT
$#      clid      color1      color2      color3      color4
          1      0.769000      0.004000      0.110000      0.000      0      0      0
$HMSET
$HMNAME SETS          19Set_19
$# name
Part 1
*COMPONENT_PART
$HMSET
$HMNAME SETS          19Set_19
$#      pid      clid
          11      1
$HMSET
$HMNAME SETS          19Set_19
$#      pid      clid
          21      1
$HMSET
*COMPONENT_END

```

Bibliography

- [1] A. Kamoulakos, V.L. Chen, E. Mestreau, and R. Lohner. Finite element modelling of structure/fluid interaction in explosively loaded aircraft fuselage panels using pamshock/pamflow coupling. In *Presented at the Conference on Spacecraft Structures, Materials and Mechanical Testing, ESA/CNES/DARA, Noordwijk, The Netherlands*, 1996.
- [2] M.A. Meyers. *Dynamic behavior of materials*. John Wiley and Sons-Interscience, 1994.
- [3] DM Owen, S. Zhuang, AJ Rosakis, and G. Ravichandran. Experimental determination of dynamic crack initiation and propagation fracture toughness in thin aluminum sheets. *International Journal of Fracture*, 90(1):153–174, 1998.
- [4] MF Kanninen, SJ Hudak, HR Couque, RJ Dexter, and PE O’Donoghue. Viscoplastic-dynamic crack propagation: Experimental and analysis research for crack arrest applications in engineering structures. *International Journal of Fracture*, 42(3):239–260, 1990. ISSN 0376-9429.
- [5] RL Veldman, J. Ari-Gur, C. Clum, A. DeYoung, and J. Folkert. Effects of prepressurization on blast response of clamped aluminum plates. *International journal of impact engineering*, 32(10):1678–1695, 2006.
- [6] Civil Aviation Authority. Aircraft Hardening research Programme: Final Overview Report. Technical Report Report no. 2001/9, Civil Aviation Authority, 2001.
- [7] Y Moon, W Patterson, G Bharatram, S Schimmels, and V Venkayya. Vulnerability and survivability analysis of aircraft fuselage subjected to internal detonations. In *MSC 1995 World Users’ Conference Proceedings*, 1995.
- [8] K. Ravi-Chandar. *Dynamic fracture*. Elsevier Science, 2004.
- [9] A. Vlot and J.W. Gunnink. *Fibre metal laminates: An Introduction*. Springer, 2001. ISBN 1402003919.

-
- [10] T.J. De Vries. *Blunt and sharp notch behaviour of Glare laminates*. PhD thesis, Delft University of Technology, The Netherlands, 2001.
- [11] Associated Press library photo. Aloha airlines flight 243, April 28 1988. URL http://en.wikipedia.org/wiki/Aloha_Airlines_Flight_243.
- [12] U.K. Accidents Investigation Branch. Report on the accident to boeing 747-121-w739pa at lockerbie, dumfriesshire, scotland on 21 december 1988. aircraft accident report 2/90, hms0, london. Technical report, U.K. Accidents Investigation Branch, 1990.
- [13] HJ. Fleisher. Design and explosive testing of a blast resistant luggage container. In *In: Proc. structures under shock and impact conference IV*, page p. 519., 1996.
- [14] G. Langdon, W. Cantwell, and G. Nurick. The blast response of novel thermoplastic-based fibre-metal laminates - some preliminary results and observations. *Composites Science and Technology*, 65:861–872, 2005. ISSN 02663538.
- [15] A. Vlot. Impact loading on fibre metal laminates. *International journal of impact engineering*, 18(3):291–307, 1996.
- [16] G. S. Langdon, Y. Chi, G. N. Nurick, and P. Haupt. Response of GLARE© panels to blast loading. *Engineering Structures*, 31:3116–3120, 2009. ISSN 01410296.
- [17] J Ndambi, K Dewolf, and J Vantomme. VULCAN Deliverable 2.4: Experimental results for blast behaviour of flat panels. Technical report, Royal Military Academy (Belgium), 2008.
- [18] D. Karagiozova, GS Langdon, GN Nurick, and S. Chung Kim Yuen. Simulation of the response of fibre-metal laminates to localised blast loading. *International Journal of Impact Engineering*, 37(6):766–782, 2010.
- [19] G. Mohamed, C. Soutis, and A. Hodzic. Numerical investigation of fibre-metal laminates subjected to blast loadings. In *2nd ECCOMAS Thematic Conference on the Mechanical Response of Composites, Imperial College London, UK*, 2009.
- [20] V.B. Chalivendra, S. Hong, I. Arias, J. Knap, A. Rosakis, and M. Ortiz. Experimental validation of large-scale simulations of dynamic fracture along weak planes. *International Journal of Impact Engineering*, 36(7):888–898, 2009.
- [21] O.R. van der Meulen. Modeling of dynamic ductile fracture propagation using cohesive zone elements. Master’s thesis, Department of Civil Engineering, TU Delft: Delft., 2009.

- [22] S. Li, MD Thouless, AM Waas, JA Schroeder, and PD Zavattieri. Use of a cohesive-zone model to analyze the fracture of a fiber-reinforced polymer-matrix composite. *Composites science and technology*, 65(3-4):537–549, 2005.
- [23] T.W. Bjerke and J. Lambros. Theoretical development and experimental validation of a thermally dissipative cohesive zone model for dynamic fracture of amorphous polymers. *Journal of the Mechanics and Physics of Solids*, 51(6):1147–1170, 2003.
- [24] ABAQUS Users Manual. 6.10-1. *Dassault Systmes Simulia Corp., Providence, RI, USA*, 2010.
- [25] JO Hallquist. LS-DYNA. Keyword Users Manual. Version 971. *Livermore Software Technology Corporation*, 2007.
- [26] J. Mediavilla Varas and F. Soetens. Failure of pressurised barrel tests under explosive loading. Technical report, TNO Defence, Security and Safety. Vulcan Memorandum, August 2009.
- [27] C. Soutis. Recent advances in building with composites. *Plastics, Rubber and Composites*, 9(10):359–366, 2009.
- [28] R Marissen. *Fatigue crack growth in Arall a hybrid aluminium aramid composite material*. PhD thesis, Delft University of Technology, Delft, The Netherlands., 1988.
- [29] G.H.J.J. Roebroeks. *Towards GLARE: The development of a fatigue insensitive and damage tolerant aircraft material*. PhD thesis, Delft University of Technology, The Netherlands, 1991.
- [30] R.C. Alderliesten. *Fatigue crack propagation and delamination growth in Glare*. PhD thesis, Delft University of Technology, The Netherlands, 2005.
- [31] A. Vlot, LB Vogelesang, and TJ De Vries. Towards application of fibre metal laminates in large aircraft. *Aircraft Engineering and Aerospace Technology*, 71(6):558–570, 1999.
- [32] A. Vlot, E. Kroon, and G. La Rocca. Impact response of fiber metal laminates. *Key Engineering Materials*, 141:235–276, 1997.
- [33] H. Fatt, C. Lin, DM Revilock, and D.A. Hopkins. Ballistic impact of GLARE; fiber-metal laminates. *Composite Structures*, 61(1):73–88, 2003.
- [34] C. Vermeeren. An historic overview of the development of fibre metal laminates. *Applied Composite Materials*, 10(4):189–205, 2003.

- [35] N. Jacob, GN Nurick, and GS Langdon. The effect of stand-off distance on the failure of fully clamped circular mild steel plates subjected to blast loads. *Engineering Structures*, 29(10):2723–2736, 2007.
- [36] GS Langdon, SL Lemanski, GN Nurick, MC Simmons, WJ Cantwell, and GK Schleyer. Behaviour of fibre-metal laminates subjected to localised blast loading: Part I—Experimental observations. *International journal of impact engineering*, 34(7):1202–1222, 2007.
- [37] M.S. Hoo Fatt and L. Palla. Analytical modeling of composite sandwich panels under blast loads. *Journal of Sandwich Structures and Materials*, 11(4):357, 2009.
- [38] D. Bonorchis and GN Nurick. The influence of boundary conditions on the loading of rectangular plates subjected to localised blast loading—importance in numerical simulations. *International Journal of Impact Engineering*, 36(1):40–52, 2009.
- [39] MA McCarthy, JR Xiao, N. Petrinic, A. Kamoulakos, and V. Melito. Modelling of bird strike on an aircraft wing leading edge made from fibre metal laminates—part 1: material modelling. *Applied composite materials*, 11(5):295–315, 2004.
- [40] A Vlot. High Strain Rate Tests on Fibre Metal Laminates, Series 07. Technical report, Delft University Press, The Netherlands, 1998.
- [41] M Hagenbeek. *Characterisation of Fibre Metal Laminates under Thermo-mechanical Loadings*. PhD thesis, Delft University of Technology, Delft, The Netherlands, 2005.
- [42] P. Linde and H. de Boer. Modelling of inter-rivet buckling of hybrid composites. *Composite Structures*, 73(2):221–228, 2006.
- [43] F.K. Chang and K.Y. Chang. Post-failure analysis of bolted composite joints in tension or shear-out mode failure. *Journal of Composite Materials*, 21(9):809, 1987. ISSN 0021-9983.
- [44] M. Kashtalyan and C. Soutis. Analysis of composite laminates with intra-and interlaminar damage. *Progress in Aerospace Sciences*, 41(2):152–173, 2005. ISSN 0376-0421.
- [45] M.Y. Kashtalyan and C. Soutis. Mechanisms of internal damage and their effect on the behavior and properties of cross-ply composite laminates. *International applied mechanics*, 38(6):641–657, 2002. ISSN 1063-7095.
- [46] C. Soutis, P.W.R. Beaumont, and Inc ebrary. *Multi-scale modelling of composite material systems: the art of predictive damage modelling*. Woodhead, 2005. ISBN 1855739364.

- [47] Z. Hashin. Failure criteria for unidirectional fiber composites. *Journal of applied mechanics*, 47:329, 1980.
- [48] I. Lapczyk and J.A. Hurtado. Progressive damage modeling in fiber-reinforced materials. *Composites Part A: Applied Science and Manufacturing*, 38(11):2333–2341, 2007.
- [49] G.R. Johnson and W.H. Cook. A constitutive model and data for metals subjected to large strains, high strain rates and high temperatures. In *Proceedings of the 7th International Symposium on Ballistics*, pages 541–547. the hague, Netherlands, 1983.
- [50] G. Ravichandran, A.J. Rosakis, J. Hodowany, and P. Rosakis. On the conversion of plastic work into heat during high-strain-rate deformation. *American Institute of Physics*, pages 557–562, 2002.
- [51] Murat Buyuk, Steve Kan, and Matti J. Loikkanen. Explicit Finite-Element Analysis of 2024-T3/T351 Aluminum Material under Impact Loading for Airplane Engine Containment and Fragment Shielding. *Journal of Aerospace Engineering*, 22(3): 287–295, 2009.
- [52] GN Nurick and JB Martin. Deformation of thin plates subjected to impulsive loading—a review Part II: Experimental studies. *International journal of impact engineering*, 8(2):171–186, 1989.
- [53] W. Johnson. *Impact strength of materials*. Edward Arnold (Publishers) Ltd., 25 Hill St., London W 1 X 8 LL., 1972.
- [54] N. Jacob, S.C.K. Yuen, D. Bonorchis, GN Nurick, SA Desai, and D. Tait. Quadrangular plates subjected to localised blast loads—an insight into scaling. *Int J Impact Eng*, 30(8-9):1179–1208, 2004.
- [55] C.N. Kingery, G. Bulmash, and US Army Ballistic Research Laboratory. *Air blast parameters from TNT spherical air burst and hemispherical surface burst*. Ballistic Research Laboratories, 1984.
- [56] G Randers-Pehrson and K.A Bannister. Airblast loading model for dyna2d and dyna3d, arl-tr- 1310. Technical report, DTIC Document, 1997.
- [57] A. Neuberger, S. Peles, and D. Rittel. Scaling the response of circular plates subjected to large and close-range spherical explosions. part i: Air-blast loading. *International journal of impact engineering*, 34(5):859–873, 2007.

- [58] A. Forghani and R. Vaziri. Computational modeling of damage development in composite laminates subjected to transverse dynamic loading. *Journal of Applied Mechanics*, 76:051304, 2009.
- [59] G Mohamed, C Soutis, and A Hodzic. Modelling the damage tolerance of composites to blast loading in pressurised cylindrical structures. In *ECCM14, 14th European Conference on Composite Materials, 7-10 June 2010, Budapest, Hungary*, 2010.
- [60] Suri Bala. Tie-break contacts in LS-DYNA, Livermore Software. Technical report, Livermore Software Technology Corporation, Livermore, CA, USA, 2010.
- [61] M. Loikkanen, G. Praveen, and D. Powell. Simulation of Ballistic Impact on Composite Panels. In *10th International LS-DYNA Users Conference*, 2008.
- [62] Po-Yu Chang and Jenn-Ming Yang. Modeling of fatigue crack growth in notched fiber metal laminates. *International Journal of Fatigue*, 30(12):2165 – 2174, 2008. ISSN 0142-1123.
- [63] DW Hyde. ConWep, Conventional Weapons Effects Program. *US Army Engineer Waterways Experiment Station, Vicksburg, MS*, 1992.
- [64] A. Alia and M. Souli. High explosive simulation using multi-material formulations. *Applied thermal engineering*, 26(10):1032–1042, 2006. ISSN 1359-4311.
- [65] P.D. Smith, J.G. Hetherington, PD Smith, and Hetherington. *Blast and ballistic loading of structures*. Butterworth-Heinemann Oxford: Boston, 1994.
- [66] M. Souli and L. Olovson. Fluid-structure interaction in ls-dyna: Industrial applications. In *Proceedings of the 4th European LS-DYNA Users Conference. Ulm, Germany, DYNAmore GmbH*, 2003.
- [67] N. Aquelet, M. Souli, J. Gabrys, and L. Olovson. A new ALE formulation for sloshing analysis. *Structural Engineering and Mechanics*, 16(4):423–440, 2003.
- [68] J. Mediavilla Varas. Blast tests on Aluminium and CFRP demonstrators. Technical report, TNO Defence, Security and Safety. Vulcan Memorandum, 2011.
- [69] Aerospace Specification Metals (ASM) Inc. Metals handbook, vol.2. *Properties and Selection: Nonferrous Alloys and Special-Purpose Materials*, ASM International 10th Ed:1166–1168, 1990.
- [70] Y. Yang, DH Li, HG Zheng, XM Li, and F. Jiang. Self-organization behaviors of shear bands in 7075 T73 and annealed aluminum alloy. *Materials Science and Engineering: A*, 527(1-2):344–354, 2009.
- [71] LB Freund. *Dynamic fracture mechanics*. Cambridge Univ Pr, 1998.

- [72] D. Hull and P. Beardmore. Velocity of propagation of cleavage cracks in tungsten. *International Journal of Fracture*, 2(2):468–487, 1966. ISSN 0376-9429.
- [73] MF Kanninen. Research in progress on unstable crack propagation in pressure vessels and pipelines. *International Journal of Fracture*, 6(1):94–96, 1970. ISSN 0376-9429.
- [74] C.A.J.R. Vermeeren. *The Residual Strength of Fibre Metal Laminates*. PhD thesis, Faculty of Aerospace Engineering, Delft University of Technology, The Netherlands, 1995.
- [75] Michael Janssen, Jan Zuidema, and Russell Wanhill. *Fracture Mechanics: Second Edition*. Spon Press, 2002.
- [76] I. Scheider and W. Brocks. Residual strength prediction of a complex structure using crack extension analyses. *Engineering Fracture Mechanics*, 76(1):149–163, 2009.
- [77] U. Zerbst, M. Heinemann, C.D. Donne, and D. Steglich. Fracture and damage mechanics modelling of thin-walled structures-An overview. *Engineering Fracture Mechanics*, 76(1):5–43, 2009.
- [78] V. Tvergaard and J.W. Hutchinson. The relation between crack growth resistance and fracture process parameters in elastic-plastic solids. *Journal of the Mechanics and Physics of Solids*, 40(6):1377–1397, 1992. ISSN 0022-5096.
- [79] O. Nguyen, EA Repetto, M. Ortiz, and RA Radovitzky. A cohesive model of fatigue crack growth. *International Journal of Fracture*, 110(4):351–369, 2001.
- [80] F. Zhou, J.F. Molinari, and T. Shioya. A rate-dependent cohesive model for simulating dynamic crack propagation in brittle materials. *Engineering fracture mechanics*, 72(9):1383–1410, 2005.
- [81] DS Dugdale. Yielding of steel sheets containing slits. *Journal of the Mechanics and Physics of Solids*, 8(2):100–104, 1960. ISSN 0022-5096.
- [82] GI Barenblatt. The mathematical theory of equilibrium cracks in brittle fracture. *Advances in applied mechanics*, 7(55-129):104, 1962.
- [83] K-H. Schwalbe, I. Scheider, and A. Cornec. SIAM CM 09 The SIAM method for applying cohesive models to the damage behaviour of engineering materials and structures. Technical report, GKSS, 2009.
- [84] A. Hillerborg, M. Modéer, and P.E. Petersson. Analysis of crack formation and crack growth in concrete by means of fracture mechanics and finite elements. *Cement and concrete research*, 6(6):773–781, 1976. ISSN 0008-8846.

- [85] T. Siegmund and A. Needleman. A numerical study of dynamic crack growth in elastic-viscoplastic solids. *International Journal of Solids and Structures*, 34(7): 769–787, 1997. ISSN 0020-7683.
- [86] A. Needleman. An analysis of decohesion along an imperfect interface. *International Journal of Fracture*, 42(1):21–40, 1990. ISSN 0376-9429.
- [87] I. Scheider and W. Brocks. The effect of the traction separation law on the results of cohesive zone crack propagation analyses. *Key Engineering Materials*, 251-252: 313–318, 2003.
- [88] A. Needleman. A continuum model for void nucleation by inclusion debonding. *Journal of Applied Mechanics*, 54:525, 1987.
- [89] I. Scheider and W. Brocks. Simulation of cup-cone fracture using the cohesive model. *Engineering Fracture Mechanics*, 70(14):1943–1961, 2003. ISSN 0013-7944.
- [90] B.C. Simonsen and R. Tornqvist. Experimental and numerical modelling of ductile crack propagation in large-scale shell structures. *Marine Structures*, 17(1):1–27, 2004. ISSN 0951-8339.
- [91] T.J. de Vries and C.A.J.R. Vermeeren. R-curve test data: 2024-T3, 7075-T6, GLARE 2 & GLARE 3. Technical report, LR M-705. Technical report, TU-Delft, 1995.
- [92] S. Roychowdhury, Y.D. Arun Roy, R.H. Dodds, et al. Ductile tearing in thin aluminum panels: experiments and analyses using large-displacement, 3-D surface cohesive elements. *Engineering Fracture Mechanics*, 69(8):983–1002, 2002. ISSN 0013-7944.
- [93] W. Li and T. Siegmund. An analysis of crack growth in thin-sheet metal via a cohesive zone model. *Engineering Fracture Mechanics*, 69(18):2073–2093, 2002. ISSN 0013-7944.
- [94] P.D. Zavattieri. Modeling of crack propagation in thin-walled structures using a cohesive model for shell elements. *Transaction -American Society of Mechanical Engineers Journal of Applied Mechanics*, 73(6):948, 2006.
- [95] G Mohamed, C Soutis, and A Hodzic. Interaction of hybrid pressurised cylindrical structures subjected to blast loading. *Plastics, Rubber and Composites: Macromolecular Engineering*, 2011.
- [96] M. Anvari, I. Scheider, and C. Thaulow. Simulation of dynamic ductile crack growth using strain-rate and triaxiality-dependent cohesive elements. *Engineering fracture mechanics*, 73(15):2210–2228, 2006. ISSN 0013-7944.

-
- [97] X. Zhang, Y.W. Mai, and R.G. Jeffrey. A cohesive plastic and damage zone model for dynamic crack growth in rate-dependent materials. *International journal of solids and structures*, 40(21):5819–5837, 2003.
- [98] P. Perzyna. Fundamental problems in viscoplasticity. *Advances in applied mechanics*, 9:243–377, 1966.

Publications

Refereed Journal Publications

1. Mohamed G, Soutis C, Hodzic A, Craveur J.C., Pormente S Interaction of hybrid pressurised cylindrical structures subjected to blast loading, *Plastics, Rubber and Composites: Macromolecular Engineering*, 2010.
2. Mohamed G, Soutis C, Hodzic A. A fluid-structure interaction model of pressurised composite structures subjected to blast loading. *Advanced Composite Letters*, 2010.
3. Mohamed G, Soutis C, Hodzic A. Modelling the structural deformation of metallic and hybrid GLARE panels to blast load, *International Journal of Composite Structures*, March 2010.
4. Mohamed G, Soutis C, Hodzic A. Performance of GLARE panels subjected to intense pressure pulse loading, *The Aeronautical Journal*, 2011.
5. Atas A, Mohamed G, Soutis C. Modelling delamination onset and growth in pin loaded composite laminates, *Composite Science and technology*, 2011.

Submitted Journal Publications

1. Mohamed G, Soutis C, Hodzic A. Blast resistance and damage modelling of fibre metal laminates to blast loads, *Applied Composite Materials*, Springer, 2011.
2. Mohamed G, Soutis C, Hodzic A. Multi-material ALE formulation for blast-induced fluid-structure interaction in fibre metal laminates, *American Institute of Aeronautics and Astronautics*, 2010.
3. Mohamed G, Soutis G, Hodzic A. Ballistic projectile perforation and blast response of thin Aluminium 2024-T3 plates, *International Journal of Structural Integrity*, 2011.

Conference Proceedings

1. Mohamed G, Soutis C, Hodzic A. Dynamic Analysis of GLARE structures: An Experimental-Numerical Approach. In: RAeS 2nd Aircraft Structural Design Conference, 26-28 October 2010.
2. Mohamed G, Soutis C, Hodzic A. Modelling the damage tolerance of composites to blast loading in pressurised cylindrical structures. In: ECCM-14 Conference Proceedings; Budapest, June 7-11, 2010
3. Mohamed G, Soutis C, Hodzic C. A Finite element analysis of aircraft materials subjected to blast. In: ICCES'10, 28 March -1 April, Las Vegas, USA
4. Mohamed G, Soutis G, Hodzic A. Numerical analysis of FMLs subjected to blast loadings. In: 2nd ECCOMAS Thematic Conference on the Mechanical Response of Composites, 1-3 April 2009, Imperial College London, UK.

Papers in Preparation

1. Mohamed G, Soutis C, Hodzic A. Energy partition for ballistic penetration of hybrid composite panels. *Composite Science and Technology*, 2011.
2. Mohamed G, Soutis C, Hodzic A. Simulation of dynamic ductile crack growth using strain-rate dependent cohesive elements. *International Journal of Impact Engineering*, 2011.
3. Mohamed G, Soutis C, Hodzic A. Dynamic behaviour of fibre metal laminates: An Overview. Book, Publisher, Year
4. Mohamed G, Soutis C, Hodzic A. A combined experimental-numerical approach of GLARE 3 pressurised cylindrical structures subjected to intense blast loading, Russian, 2011.

Curriculum Vitae

Galal Mohamed was born in Rotherham on September 4th 1985. In October 2004, after successfully completing his A-levels at Thomas Rotherham College, he began a 4 year Masters degree course in *Mechanical Engineering with Spanish* at University of Sheffield. During his studies, he actively took part in *Engineers without Borders* in transferring knowledge to the wider local community through Outreach by visiting schools, run practical workshops and seminars. In 2006-2007 he was awarded an ERASMUS grant to study at the Faculty of Engineering at the Universidad de Sevilla. Galal eventually graduated with a first class honours MEng degree in 2008.

In the same year, he started a Ph.D. research under supervision of Prof C. Soutis and Dr. Hodzic from the now-named *Composite Systems Innovation Centre* in the Department of Mechanical Engineering. His PhD was sponsored by the EU-FP6 VULCAN Project, a consortium of leading academia and industry partner's in Europe. His research involved investigating the dynamic behaviour of fibre metal laminates, such as GLARE, relative to monolithic metallic structures through a combined experimental-numerical approach. Blast mitigation methods were proposed based on the energy absorption of these structures and their dynamic fracture characteristics in the presence of multi-site damage (MSD).